



©2009 ESA/ARIANESPACE / Opéque Vidéo du CSG - S. MARTIN

This thesis was typeset with L<sup>A</sup>T<sub>E</sub>X, using a modified version of the University of California Ph.D. dissertation class file, `ucthesis.cls`. Unless otherwise noted, all figures in this thesis were created by the author using IDL<sup>®</sup> or CorelDraw<sup>®</sup>.

**Cover photograph** An Ariane 5 ECA launcher, carrying the Herschel and Planck spacecraft on-board, lifts-off from the Ariane launch pad at the European spaceport in Kourou, French Guiana on 14 May 2009 (*Photo: ESA-CNES-Arianespace*).

IMAGING FOURIER TRANSFORM SPECTROSCOPY FROM A SPACE  
BASED PLATFORM – THE HERSCHEL/SPIRE FOURIER  
TRANSFORM SPECTROMETER

LOCKE DEAN SPENCER

B.Sc. in Engineering Physics With Distinction, University of Alberta, 2003  
M.Sc. Physics, University of Lethbridge, 2005

A Thesis

Submitted to the School of Graduate Studies  
of the University of Lethbridge  
in Partial Fulfilment of the  
Requirements of the Degree

PHILOSOPHIÆ DOCTOR

IN

EARTH, SPACE, AND PHYSICAL SCIENCE

Department of Physics & Astronomy  
University of Lethbridge  
LETHBRIDGE, ALBERTA, CANADA

© Locke Dean Spencer, 2009

## Dedication

Among other mathematical subjects, Optics and Astronomy came in turn, and when I read of the many charming discoveries that had been made by means of the telescope, I was so delighted with the subject that I wished to see the heavens and Planets with my own eyes thro' one of those instruments.

---

William Herschel [1, p. 59]

To J & K, who definitely come before L.



## Abstract

The Herschel Space Observatory (Herschel), a flagship mission of the European Space Agency (ESA), is comprised of three cryogenically cooled instruments commissioned to explore the far-infrared/submillimetre universe. Herschel's remote orbit at the second Lagrangian point (L2) of the Sun-Earth system, and its cryogenic payload, impose a need for thorough instrument characterization and rigorous testing as there will be no possibility for any servicing after launch.

The Spectral and Photometric Imaging Receiver (SPIRE) is one of the instrument payloads aboard Herschel and consists of a three band imaging photometer and a two band imaging spectrometer. The imaging spectrometer on SPIRE consists of a Mach-Zehnder (MZ)-Fourier transform spectrometer (FTS) coupled with bolometric detector arrays to form an imaging FTS (IFTS). This thesis presents experiments conducted to verify the performance of an IFTS system from a space based platform, i.e. the use of the SPIRE IFTS within the Herschel space observatory. Prior to launch, the SPIRE instrument has undergone a series of performance verification tests conducted at the Rutherford Appleton Laboratory (RAL) near Oxford, UK. Canada is involved in the SPIRE project through provision of instrument development hardware and software, mission flight software, and support personnel. Through this thesis project I have been stationed at RAL for a period spanning fifteen months to participate in the development, performance verification, and characterization of both the SPIRE FTS and photometer instruments.

This thesis discusses Fourier transform spectroscopy and related FTS data process-

ing (Chapter 2). Detailed discussions are included on the spectral phase related to the FTS beamsplitter (Chapter 3), the imaging aspects of the SPIRE IFTS instrument (Chapter 4), and the noise characteristics of the SPIRE bolometer detector arrays as measured using the SPIRE IFTS (Chapter 5). This thesis presents results from experiments performed both on site at the RAL Space Science and Technology Department (SSTD) Assembly Integration Verification (AIV) instrument test facility as well as from the Astronomical Instrumentation Group (AIG) research laboratories within the Department of Physics & Astronomy at the University of Lethbridge.

## Acknowledgements

First, I need to thank Prof. David Naylor for providing me the opportunity to stay with the group and complete a Ph.D. I still remember being in the office at RAL that afternoon when David first suggested that I consider a Ph.D. Seeing SPIRE through to launch in this capacity has been very rewarding, and continues to be so. I also must thank David for his sense of humour, work ethic, and especially for all of his efforts helping the group get on with our work. I don't think that I have caused that many of them, but I have noticed more grey hair on David's head since I first joined the group.

I am incredibly grateful to my beautiful wife, Jill, for her love, support, and encouragement throughout this effort. From my experience preparing my M.Sc. thesis, I knew what I was getting into with this one, Jill did not. A thesis is much more enjoyable after it is completed, and I know that the writing process was difficult on her, perhaps even more than it was on myself. Thank you Jill, for helping me through this process and helping me make some of the best decisions that I have ever made. And thank you to Don and Ruth Ann Anderson, for trusting me to care for their *favourite*, and to all of the Andersons for welcoming me into their family. I owe my parents, Kevin and Sharon Spencer, and siblings, Mark, Sheryl, Shauna, and Shannon, many thanks for their love and support throughout all of my life; the same is true for my siblings-in-law as they have entered the family. My parents provided me many opportunities to make independent decisions from an early age and otherwise learn how to think, solve problems, and be creative; that has been a huge advantage to me.

My daughter, Kay, was born on 15 December 2008, not too long after I started

writing. Thank you, Kay, for being such a good girl and sleeping through the night at such an early age. Thank you for your bright smiles in the morning that would stay with me the whole day. I cannot picture our family without you. Although there were many times that I returned from school late and hungry, it was always a tremendous joy to see your smile welcome me home and hold you in my arms before attending to anything else.

Thank you to David Naylor, Regan Dahl, Scott Jones, Richard Querel, and Jill for all of your help in the thesis proofreading and editing process. I am not sure that it is possible to look at a thesis without finding some sort of typographical error, but it is now harder to do in this thesis than before your collective eyes were set upon it. I also need to thank Scott for putting up with me in the office. I couldn't have asked for a better student to share an office with during the writing process.

Dr. Jin Zhang of Cardiff University has provided a great service in the HFSS beamsplitter simulations (Chapter 3). These efforts greatly helped in our understanding of beamsplitter effects in observation data. Dr. Pete Hargrave of Cardiff University provided helpful guidance on the fabrication of the blackbody sources that were used in the beamsplitter emission study (Chapter 3). The theoretical bolometer model of Chapter 5 was based heavily upon the Mathcad simulations performed by Prof. Matt Griffin, also of Cardiff University.

This work would not be complete without the efforts of the University of Lethbridge Astronomical Instrumentation Group (AIG), both past and present. The AIG has absolutely lived up to the statement, "it takes a family to raise a grad student." Brad Gom has provided assistance on so many fronts throughout the years, as has Peter Davis,

Trevor Fulton, Greg Tompkins, Ian Schofield, Baoshe Zhang, Robin Phillips, John Lindner, Margaret Tahic, Frank Klassen, and Sheila Matson. There have been many co-op and summer students while I have been at the U of L that have made an impression and have been great to work with: Kris Dyke, Andres Rebolledo, Dan Handford, Dan Closson, Tony Gong, Brandon Wong, and Jamil Shariff to name a few. Thank you to Edward Polehampton, who was also a great office-mate and friend, for all of the assistance on so many levels. Edward has been an invaluable member of our group over the years and is always cheerful and ready to provide information or otherwise lend a hand. I am also grateful that Ed allowed the Canadian flag to fly from the window of the *Canadian* office at RAL; the Union Jack which Ed delivered on his visit to Lethbridge is still in the window of the SPIRE lab at the U of L. In mentioning the AIG, I must also thank all of the AIG members who started up Blue Sky Spectroscopy; Lethbridge is very fortunate to have such a company. It has been great to continue to work with Peter and Trevor on SPIRE.

I would like to thank Matt Griffin, Bruce Swinyard, Tanya Lim, Samuel Ronayette, Ken King, Marc Ferlet, Sunil Sidher, Dave Smith, Steve Guest, Judy Long, Alan Pierce, Mike Trower, Peter Ade, Jin Zhang, Asier & Mercedes Aramburu, Sarah Leeks, Pete Hargrave, Adam Woodcraft, Bruce Sibthorpe, Ivan Valtchanov, Tim Waskett, Jean-Paul Baluteau, along with the remainder of the SPIRE team in the UK and Europe for their training, support, and assistance while I was staying in the UK. I thoroughly enjoyed the time I spent at RAL. On that note, I would also like to thank the hospitable staff at the SPIRE B&B which helped to make my time in Oxford enjoyable.

Thank you to Ian Chapman for introducing me to Prof. Naylor, setting me on the

graduate studies path, and for being such a great friend.

This research has been funded in part by the Natural Sciences and Engineering Research Council (NSERC), Alberta Ingenuity (AI), the University of Lethbridge, the Canadian Institute for Photonics Innovation (CIPI), the Canadian Space Agency (CSA), the European Space Agency (ESA), and the UK Science and Technology Facilities Council (STFC, formerly Particle Physics and Astronomy Research Council - PPARC).

Finally, I need to acknowledge the external examiner and members of my committee for their very useful comments. Profs. Boéré and Siminovitch have been very supportive and encouraging throughout my graduate studies. Prof. Ade spent almost as many hours stuck in traffic on the M4 as he did on the plane getting here from the UK. Not surprisingly, after the initial submission to the committee, I identified several minor errors in this thesis in preparing for the defense. In addition to the more obvious ones, each committee member also spotted a few subtle errors or improvements that I am not sure I would have noticed myself. This thesis is substantially improved by the thorough review provided by Profs. Naylor, Siminovitch, Boéré, and Ade prior to final approval. Thank you also to Prof. Roussel for chairing the examination.

# Contents

Dedication	iii
Abstract	iv
Acknowledgements	vi
Table of Contents	x
List of Tables	xiii
List of Figures	xiv
List of Abbreviations	xvi
List of Equations	xix
Thesis Format	xxii
<b>1 Introduction</b>	<b>1</b>
1.1 Herschel . . . . .	2
1.2 SPIRE . . . . .	5
1.3 My Contribution to SPIRE . . . . .	9
1.3.1 PFM Testing Participation . . . . .	10
1.3.2 Data Analysis . . . . .	12
1.3.3 Publications . . . . .	14
1.4 SAG-4 . . . . .	16
1.5 Thesis Summary . . . . .	19
<b>2 Fourier Transform Spectroscopy</b>	<b>22</b>
2.1 A Brief History . . . . .	23
2.2 Fourier Series . . . . .	25
2.3 Fourier Integrals . . . . .	26
2.4 Properties of Fourier Transforms . . . . .	27
2.5 The Michelson Interferometer . . . . .	31
2.5.1 Monochromatic Input Sources . . . . .	33
2.5.2 Polychromatic/Broad Input Sources . . . . .	34
2.6 FTS Advantages . . . . .	35

2.6.1	The Jacquinot Advantage . . . . .	35
2.6.2	The Fellgett Advantage . . . . .	36
2.6.3	The Connes Advantage . . . . .	37
<b>2.7</b>	<b>Practical Considerations . . . . .</b>	<b>38</b>
2.7.1	Sampling and Spectral Resolution . . . . .	38
2.7.2	Noise . . . . .	40
2.7.3	Natural Apodization . . . . .	42
<b>2.8</b>	<b>Conclusions . . . . .</b>	<b>44</b>
<b>3</b>	<b>FTS Beamsplitter Emission . . . . .</b>	<b>45</b>
3.1	Dual Input/Output FTS . . . . .	46
3.2	FTS Port Compensation . . . . .	51
3.3	Beamsplitter Emission Theory . . . . .	59
3.4	SPIRE Beamsplitter Emission . . . . .	64
3.5	Beamsplitter Emission Simulations . . . . .	66
3.6	Beamsplitter Emission Study . . . . .	78
3.7	Beamsplitter Emission Correction . . . . .	87
3.8	Conclusions . . . . .	92
<b>4</b>	<b>Imaging FTS . . . . .</b>	<b>94</b>
4.1	IFTS Advantages . . . . .	98
4.2	IFTS Practical Considerations . . . . .	100
4.3	Obliquity Theory . . . . .	101
4.3.1	Off-Axis Alignment . . . . .	103
4.3.2	Finite FOV . . . . .	103
4.3.3	Finite FOV & Off-Axis . . . . .	104
4.3.4	Spectral Resolution . . . . .	107
4.3.5	IFTS ILS . . . . .	108
4.3.6	Detector Optical Alignment . . . . .	110
4.4	The SPIRE IFTS . . . . .	112
4.4.1	The SPIRE Detector Arrays . . . . .	112
4.4.2	The Theoretical SPIRE IFTS ILS . . . . .	114
4.5	Spectral Line Sources for Ground Testing . . . . .	122
4.6	SPIRE ILS Characterization Results . . . . .	123
4.7	A Case Study of IFTS in Astronomy . . . . .	128
4.7.1	The Starburst Galaxy M82 . . . . .	131
4.8	Conclusions . . . . .	135
<b>5</b>	<b>Signal and Noise in the SPIRE FTS . . . . .</b>	<b>136</b>
5.1	Bolometer Theory . . . . .	138
5.1.1	Determination of Incident Optical Power, $Q$ . . . . .	142
5.1.2	Bolometer Dynamic Response . . . . .	144
5.1.3	Sources of Noise . . . . .	145
5.2	SPIRE Optical Efficiencies . . . . .	148
5.3	SPIRE Optical Input Configurations . . . . .	153



5.4	<b>SPIRE Bolometer Models</b> . . . . .	<b>157</b>
5.5	<b>Performance of the SPIRE FTS</b> . . . . .	<b>165</b>
5.5.1	Observations Viewing the SPIRE Test Facility . . . . .	165
5.5.2	Observations Viewing the CBB . . . . .	170
5.5.3	In-Flight Sensitivity Predictions . . . . .	177
5.6	<b>Conclusions</b> . . . . .	<b>183</b>
<b>6</b>	<b>Conclusions</b> . . . . .	<b>185</b>
6.1	<b>FTS Beamsplitter Phase</b> . . . . .	<b>186</b>
6.2	<b>IFTS Obliquity Corrections</b> . . . . .	<b>187</b>
6.3	<b>SPIRE Bolometer Detector Performance</b> . . . . .	<b>188</b>
6.4	<b>Current Status of Herschel</b> . . . . .	<b>189</b>
6.5	<b>Future Work</b> . . . . .	<b>190</b>
	<b>Bibliography</b> . . . . .	<b>191</b>
	<b>Appendices</b> . . . . .	<b>219</b>
A	<b>Off-Axis OPD Correction</b> . . . . .	<b>219</b>
B	<b>Derivation of Beamsplitter Phase <math>\Phi</math></b> . . . . .	<b>222</b>
B.1	<b>Dual Input Interferogram Outputs, Eqs. 3.1 &amp; 3.2</b> . . . . .	<b>222</b>
B.2	<b>Derivation of Ideal Beamsplitter <math>\Phi</math>, Eq. 3.6</b> . . . . .	<b>225</b>
C	<b>Off-Axis Natural Apodization Integral</b> . . . . .	<b>226</b>
D	<b>Bolometer Theory Derivations</b> . . . . .	<b>231</b>
D.1	$G_S(T, T_o)$ , Eq. 5.7 . . . . .	231
D.2	$G_E(T, T_o)$ , Eq. 5.9 . . . . .	232
D.3	$Z_D$ , Eq. 5.16 . . . . .	234
D.4	$S$ , Eq. 5.17 . . . . .	235
D.5	Phonon NEP, Eq. 5.21 . . . . .	239
D.6	Photon NEP, Eq. 5.27 . . . . .	240
D.7	NEP <sub>measured</sub> , Eq. 5.31 . . . . .	242

# List of Tables

1.1	Summary of SPIRE Instrument Testing . . . . .	12
2.1	Symmetry properties of Fourier transform pairs . . . . .	29
2.2	Fourier theorems . . . . .	30
3.1	Measured SPIRE beamsplitter $\Phi$ . . . . .	66
3.2	MZ-FTS beamsplitter $\Phi$ . . . . .	81
4.1	Hyper-spectral imaging instruments . . . . .	97
4.2	SPIRE detector $\alpha$ & $\beta$ . . . . .	114
4.3	SPIRE detector expected and measured $\beta$ . . . . .	115
4.4	PFM FTS laser spectra . . . . .	123
4.5	Effective Doppler vel. for uncorrected SPIRE detector axial orientation ( $\beta$ ). . . . .	131
4.6	Expected Doppler velocity of CO lines in M82 . . . . .	135
5.1	SPIRE optics efficiencies . . . . .	150
5.2	SPIRE detector coupling efficiency factors . . . . .	152
5.3	SPIRE FTS background power levels . . . . .	157
5.4	SPIRE bolometer model inputs . . . . .	159
5.5	SPIRE bolometer simulation results . . . . .	164
5.6	Observed SPIRE FTS NEP values . . . . .	177
5.7	Observed M82 CO line intensities . . . . .	178
5.8	Predicted S/N for SPIRE FTS observations of M82 . . . . .	180
5.9	Predicted $t_{req}$ to achieve S/N of 1000 for SPIRE FTS observations of M82 . . . . .	180
5.10	Simulated CO integrated line intensities . . . . .	181

# List of Figures

1.1	The Herschel Space Observatory . . . . .	3
1.2	SPIRE, PACS, and HIFI on the Herschel optical bench . . . . .	4
1.3	The SPIRE FTS instrument . . . . .	6
1.4	The SPIRE instrument . . . . .	7
2.1	Diagram of a classical Michelson interferometer . . . . .	32
2.2	Natural apodization due to a finite entrance aperture . . . . .	43
3.1	Diagram of a Mach-Zehnder interferometer . . . . .	47
3.2	Complementary FTS input/output. . . . .	50
3.3	SPIRE spectrometer calibration source SCAL. . . . .	52
3.4	SPIRE observation holding CBB constant and cooling SCAL_A. . . . .	53
3.5	Spectral input for constant CBB/cooling SCAL_A SPIRE observations. . . . .	54
3.6	Peak interferogram power with constant CBB and cooling SCAL_A. . . . .	57
3.7	Interferograms recorded while holding CBB constant and cooling SCAL_A. . . . .	58
3.8	Range of acceptable $\Phi$ values . . . . .	61
3.9	Spectral phase for SCAL_A cooling observations. . . . .	65
3.10	SPIRE port compensation interferograms. . . . .	65
3.11	Input A and B dominant scans illustrating deviation from $2\Phi = \pi$ . . . . .	67
3.12	SPIRE beamsplitter emission interferograms. . . . .	67
3.13	Monochromatic model of port compensation . . . . .	70
3.14	Broad-band basic model of port compensation . . . . .	71
3.15	Empirical beamsplitter model . . . . .	73
3.16	Interferogram components resulting from the empirical beamsplitter model . . . . .	74
3.17	HFSS simulation results for beamsplitter $R$ , $T$ , $\Phi$ , and $\mathcal{A}$ . . . . .	76
3.18	HFSS beamsplitter model interferograms . . . . .	77
3.19	Picture of MZ-FTS . . . . .	78
3.20	Picture of MZ-FTS infrared blackbody radiation source . . . . .	80
3.21	Infrared picture of MZ-FTS blackbody radiation sources . . . . .	80
3.22	Series of MZ-FTS interferograms investigating port compensation . . . . .	82
3.23	MZ-FTS interferograms used to determine port compensation phase shift $\Phi$ . . . . .	83
3.24	MZ-FTS interferograms with a heated beamsplitter . . . . .	85
3.25	MZ-FTS beamsplitter thermalization time constant . . . . .	86
3.26	Correction of MZ-FTS port compensation interferograms. . . . .	89
3.27	Correction of SPIRE beamsplitter emission for SLW . . . . .	90
3.28	Correction of SPIRE beamsplitter emission for SSW . . . . .	91

4.1	Various spatial scanning schemes which produce a hyper-spectral image . . .	97
4.2	Various off-axis ILS integration configurations . . . . .	102
4.3	Off-Axis spectral considerations neglecting FOV . . . . .	104
4.4	Natural apodization ILS . . . . .	105
4.5	Finite FOV spectral considerations . . . . .	105
4.6	Off-axis spectral resolution, $\Delta\sigma$ , normalized . . . . .	108
4.7	Various off-axis normalized ILS profiles . . . . .	109
4.8	Off-axis line shift $\sigma'_o$ . . . . .	111
4.9	SPIRE SLW and SSW array position on sky . . . . .	113
4.10	SPIRE SLW ILS functions, $\Delta\sigma = \infty$ . . . . .	116
4.11	SPIRE SSW ILS functions, $\Delta\sigma = \infty$ . . . . .	117
4.12	SPIRE SLW ILS functions, various $\Delta\sigma$ . . . . .	119
4.13	SPIRE SSW ILS functions, various $\Delta\sigma$ . . . . .	120
4.14	SPIRE SLW ILS functions, $\Delta\sigma = 0.04 \text{ cm}^{-1}$ . . . . .	121
4.15	SPIRE SSW ILS functions, $\Delta\sigma = 0.04 \text{ cm}^{-1}$ . . . . .	121
4.16	Measured SPIRE ILS function . . . . .	125
4.17	SPIRE SLW frequency shift . . . . .	126
4.18	SPIRE SSW frequency shift . . . . .	127
4.19	Minimum resolvable Doppler velocity shift for SPIRE . . . . .	130
4.20	X-Ray, visible, IR, & submm image of the starburst galaxy M82 . . . . .	133
5.1	SPIRE Bolometer . . . . .	140
5.2	Optical configuration of the SPIRE FTS . . . . .	149
5.3	Throughput ( $A\Omega$ ) of the SPIRE FTS . . . . .	151
5.4	Various modeled inputs to the SPIRE FTS . . . . .	154
5.5	Photograph of the Herschel telescope . . . . .	155
5.6	Photograph of the telescope simulator . . . . .	156
5.7	Photograph of the CBB housing . . . . .	156
5.8	Incident background spectra for various configurations of the SPIRE FTS .	158
5.9	SPIRE FTS DC NEP contributions for CBB configuration . . . . .	160
5.10	Total DC NEP for the various flight/lab configurations of the SPIRE FTS .	161
5.11	DC responsivity for the flight/lab configurations of the SPIRE FTS . . . .	163
5.12	Residual noise extraction for laboratory NEP determination . . . . .	169
5.13	Spectral NEP for SLW-D2 viewing the lab . . . . .	171
5.14	$NEP_{elec}$ & $NEP_{total}$ for both arrays while viewing the laboratory . . . . .	172
5.15	Residual noise extraction from CBB observations for NEP determination . .	174
5.16	NEP for the SPIRE FTS detectors viewing the laboratory . . . . .	175
5.17	Variation of photon NEP with CBB temperature . . . . .	176
5.18	Expected S/N of CO lines in high-resolution spectra of M82 . . . . .	182
A.1	FTS obliquity derivation . . . . .	221
C.1	Coordinate system for off-axis IFTS obliquity derivation . . . . .	227
C.2	Constant $\theta$ integration used in IFTS ILS derivation . . . . .	228

# List of Abbreviations

<b>ADC</b>	analog to digital conversion
<b>ADU</b>	arbitrary data unit
<b>AIG</b>	Astronomical Instrumentation Group
<b>AIV</b>	RAL spacecraft assembly integration verification facility
<b>AOT</b>	astronomical observation template
<b>CBB</b>	SPIRE test facility cold blackbody source
<b>CEA</b>	Commissariat a l'Energie Atomique (Atomic Energy Commission) in Grenoble France
<b>CO</b>	carbon monoxide
<b>CQM</b>	SPIRE cryogenic qualification model
<b>ESA</b>	the European Space Agency
<b>FFT</b>	fast Fourier transform algorithm developed by Cooley and Tukey [2]
<b>FIR</b>	far-infrared radiation
<b>FOV</b>	field-of-view
<b>FTS</b>	Fourier transform spectrometer/spectroscopy
<b>FWHM</b>	full width at half maximum
<b>GTKP</b>	guaranteed time key project
<b>HCP</b>	hexagonal close packed
<b>HDPE</b>	high density polyethylene
<b>Herschel</b>	Herschel Space Observatory
<b>HFSS</b>	High Frequency Structural Simulator software package developed by Ansoft Corp.
<b>HIFI</b>	Heterodyne Instrument for the Far-Infrared
<b>ICC</b>	instrument control centre

---

<b>IDL</b>	Interactive Data Language software package developed by Research Systems Inc. used in scientific data reduction
<b>IEEE</b>	Institute of Electrical and Electronics Engineers
<b>IFTS</b>	imaging Fourier transform spectrometer / spectroscopy
<b>ILS</b>	instrumental line-shape
<b>IR</b>	Infrared radiation
<b>IRMMW-THZ</b>	Infrared Millimetre Waves – Terahertz IEEE conference series
<b>ISM</b>	interstellar medium
<b>ISM</b>	stellar initial mass function
<b>ISO</b>	Infrared Space Observatory
<b>ITT</b>	SPIRE performance verification instrument test team
<b>JCMT</b>	James Clerk Maxwell Telescope
<b>LWS</b>	long wavelength sensor of the Infrared Space Observatory
<b>M82</b>	the starburst galaxy Messier 82, also known as NGC 3034
<b>MZ</b>	Mach-Zehnder
<b>NEP</b>	noise equivalent power
<b>NSERC</b>	Natural Sciences and Engineering Research Council of Canada
<b>NTD</b>	neutron transmutation doped
<b>OPD</b>	optical path difference, the linear difference between two beampaths in an interferometer
<b>OSA</b>	the Optical Society of America
<b>PACS</b>	the photoconductor array camera and spectrometer
<b>PDR</b>	photo-dissociation region
<b>PFM</b>	SPIRE instrument Proto-flight model
<b>PID</b>	proportional - integral - derivative control loop
<b>PV</b>	performance verification
<b>RAL</b>	the Rutherford Appleton Laboratory space science research centre located in the UK
<b>rms</b>	root-mean-square
<b>RSRF</b>	SPIRE photometer relative spectral response function
<b>S/N</b>	signal-to-noise ratio

---

<b>SAG</b>	SPIRE Specialist Astronomy Group
<b>SAG-4</b>	SPIRE Interstellar Medium specialist astronomy group
<b>SCAL</b>	SPIRE spectrometer calibrator source
<b>SCUBA</b>	Submillimetre Common User Bolometer Array
<b>SDAG</b>	SPIRE data analysis group
<b>SED</b>	spectral energy distribution
<b>SI</b>	Système International d'Unités / International System of Units
<b>SLW</b>	long wavelength array of the SPIRE spectrometer
<b>SMEC</b>	SPIRE mechanism composed of rooftop mirrors on a frictionless translation stage
<b>SPIE</b>	The International Society for Optical Engineering, formerly known as the Society of Photo-Optical Instrumentation Engineers
<b>SPIRE</b>	the Spectral and Photometric Imaging Receiver instrument on the Herschel telescope
<b>SSTD</b>	RAL Space Science and Technology Department
<b>SSW</b>	short wavelength array of the SPIRE spectrometer
<b>submm</b>	submillimetre
<b>SVR</b>	SPIRE instrument science verification review
<b>TFTS</b>	Test facility Fourier transform spectrometer
<b>ZPD</b>	point of zero optical path difference in an interferometer/interferogram

# List of Equations

2.1	Trigonometric Fourier series . . . . .	25
2.2	Fourier series fundamental frequency . . . . .	25
2.3	Fourier series $a_o$ . . . . .	26
2.4	Fourier series $a_n$ . . . . .	26
2.5	Fourier series $b_n$ . . . . .	26
2.6	Fourier series in exponential form . . . . .	26
2.7	Exponential Fourier series $d_n$ . . . . .	26
2.8	Reverse complex Fourier transform . . . . .	27
2.9	Forward complex Fourier transform . . . . .	27
2.10	Sample cosine function . . . . .	28
2.11	Fourier transform of a cosine function . . . . .	28
2.12	Dirac Delta Function . . . . .	28
2.13	Dirac Delta Integral . . . . .	28
2.14	Sample Sine function . . . . .	28
2.15	Fourier transform of a sine function . . . . .	28
2.16	Boxcar function . . . . .	29
2.17	Cardinal sine (sinc) function . . . . .	29
2.18	Electric field propagation through a Michelson FTS . . . . .	33
2.19	Irradiance of monochromatic source propagation through a Michelson FTS . . . . .	34
2.20	Monochromatic interferogram expression . . . . .	34
2.21	Broad-band source interferogram . . . . .	35
2.22	Cosine Fourier transform of a broad-band interferogram . . . . .	35
2.23	Nyquist Sampling condition . . . . .	38
2.24	Nyquist frequency $\sigma_{Nq}$ . . . . .	38
2.25	Spectral resolution $\Delta\sigma$ . . . . .	39
2.26	FTS ILS FWHM . . . . .	39
2.27	Photon noise $\varsigma_{\text{photon}}$ . . . . .	40
2.28	Johnson noise voltage $V_{J \text{ rms}}$ . . . . .	41
2.29	$1/f$ noise current $i_{1/f \text{ rms}}$ . . . . .	41
2.30	Natural apodization interferogram for a monochromatic source . . . . .	42
2.31	Evaluation of natural apodization interferogram for a monochromatic source . . . . .	43
2.32	Natural apodization interferogram including small angle approximation . . . . .	43
2.33	FTS resolving power ( $R$ ) . . . . .	44
2.34	Jacquinot resolution criterion . . . . .	44



3.1	Measured irradiance at output 1 for a MZ-FTS . . . . .	48
3.2	Measured irradiance at output 2 for a MZ-FTS . . . . .	48
3.3	Ideal output at output 1 for dual input FTS interferograms . . . . .	48
3.4	Ideal output at output 2 for dual input FTS interferograms . . . . .	48
3.5	Conservation of energy via summation of both FTS outputs . . . . .	49
3.6	Ideal beamsplitter phase shift $\Phi$ determined through conservation of energy .	49
3.7	Geometric fill ratio of SCAL . . . . .	55
3.8	Hamy phase parameter . . . . .	59
3.9	Reflectance, transmittance, and absorption . . . . .	60
3.10	Range restriction on $2\Phi$ for two port optical device . . . . .	60
3.11	Range restriction on $2\Phi$ for two port optical device including absorption . . .	60
3.12	Range restriction on $\Phi$ for $r_1 = r_2$ . . . . .	60
3.13	Complex interferogram including beamsplitter emission for output 1 . . . . .	62
3.14	Complex interferogram including beamsplitter emission for output 2 . . . . .	62
3.15	Sinusoidal interferogram including beamsplitter emission for output 1 . . . . .	62
3.16	Sinusoidal interferogram including beamsplitter emission for output 2 . . . . .	62
4.1	FTS obliquity correction factor . . . . .	103
4.2	Off-axis effective frequency . . . . .	104
4.3	Natural apodization ILS for off-axis detectors . . . . .	105
4.4	Obliquity ILS integral . . . . .	106
4.5	Values of $\int d\phi$ for obliquity integration . . . . .	106
4.6	Differential form of Equation 4.2 . . . . .	106
4.7	Imaging FTS ILS, $\psi(\sigma)$ . . . . .	107
4.8	Obliquity integration with respect to $\sigma$ . . . . .	107
4.9	Expression relating a monochromatic interferogram to the FTS ILS . . . . .	107
4.10	Off-axis spectral resolution . . . . .	108
4.11	Off-axis spectral line centre . . . . .	110
4.12	Off-axis line centre . . . . .	110
4.13	Conversion between $\theta_{\text{sky}}$ and $\theta_{\text{FTS}}$ . . . . .	114
4.14	Uncertainty in spectral line centre . . . . .	124
5.1	Bolometer power absorption/dissipation $W$ . . . . .	139
5.2	Bolometer resistance $R(T)$ . . . . .	141
5.3	Bolometer temperature coefficient of resistance $\alpha$ . . . . .	141
5.4	Bolometer heat capacity $C(T)$ . . . . .	141
5.5	Bolometer heat equation . . . . .	141
5.6	Bolometer steady state equation . . . . .	141
5.7	Bolometer static thermal conductance $G_S(T, T_o)$ . . . . .	141
5.8	Bolometer dynamic thermal conductance $G_D(T, T_o)$ . . . . .	142
5.9	Bolometer effective dynamic conductance $G_E(T, T_o)$ . . . . .	142
5.10	Bolometer resistance determination for FTS measurements, $R(z)$ . . . . .	142
5.11	Bolometer bias current determination for FTS measurements, $I(z)$ . . . . .	142
5.12	Bolometer temperature determination for FTS measurements, $T(z)$ . . . . .	143
5.13	Bolometer electrical power determination for FTS measurements, $P(z)$ . . . . .	143

5.14	Bolometer total power dissipation for FTS measurements, $W(z)$ . . . . .	143
5.15	Bolometer incident radiant power for FTS measurements, $Q(z)$ . . . . .	143
5.16	Bolometer dynamic impedance $Z_D$ . . . . .	144
5.17	Bolometer DC responsivity $S$ . . . . .	144
5.18	Bolometer effective time constant $\tau_E$ . . . . .	144
5.19	Bolometer physical time constant $\tau_D$ . . . . .	145
5.20	Johnson NEP, $NEP_J$ . . . . .	146
5.21	Phonon NEP, $NEP_{phonon}$ . . . . .	146
5.22	Load resistor NEP, $NEP_{load}$ . . . . .	146
5.23	Amplifier NEP, $NEP_{amp}$ . . . . .	147
5.24	Total electronic/thermal (i.e. non-optical) NEP, $NEP_{elec}$ . . . . .	147
5.25	Absorbed radiant power $Q_i$ . . . . .	147
5.26	Total absorbed radiant power $Q$ . . . . .	148
5.27	Photon NEP, $NEP_{\nu-i}$ . . . . .	148
5.28	Total photon NEP, $NEP_{photon}$ . . . . .	148
5.29	Overall optical transmission efficiency for SPIRE . . . . .	152
5.30	Bolometer bias current, $I(Q, T, T_o)$ . . . . .	157
5.31	Derivation of NEP from a measured spectrum, $NEP_{measured}$ . . . . .	167
5.32	Effective FTS antenna temperature $T_{eff}$ . . . . .	178
5.33	FTS velocity resolution $\Delta v$ . . . . .	178
5.34	FTS S/N in temperature units $S/N_T$ . . . . .	179
5.35	FTS noise in temperature units $\zeta_T$ . . . . .	179
5.36	FTS observation time as a function of desired S/N, $t_{req}$ . . . . .	179
A.1	Derivation of OPD obliquity correction . . . . .	221
B.1	Derivation of Equation 3.1, $I_1(\sigma_o)$ . . . . .	224
B.2	Derivation of Equation 3.2, $I_2(\sigma_o)$ . . . . .	224
B.3	Ideal beamsplitter phase difference $\Phi$ . . . . .	225
C.1	Derivation of $\sin \phi$ for IFTS obliquity considerations . . . . .	230
C.2	Derivation of $\cos \phi'$ for IFTS obliquity considerations . . . . .	230
D.1	Bolometer thermal conductivity, $k(T)$ . . . . .	232
D.2	Derivation of Eq. 5.7, $G_S(T, T_o)$ . . . . .	232
D.3	Derivation of Eq. 5.9, $G_E(T, T_o)$ . . . . .	234
D.4	Derivation of Eq. 5.16, $Z_D$ . . . . .	235
D.5	Dimensionless $H$ in derivation of bolometer $S$ . . . . .	235
D.6	Relation between $dV/dI$ and $R_L$ . . . . .	236
D.7	Derivation of responsivity $S$ . . . . .	238
D.8	Derivation of Eq. 5.21, $NEP_{phonon}$ . . . . .	240
D.9	Spectral density of absorbed radiation, $\chi$ . . . . .	241
D.10	Photon mode occupation used in derivation of photon NEP, $\kappa(\nu)$ . . . . .	241
D.11	Bolometer absorbed radiant power used in photon NEP determination, $Q_\nu$ . . . . .	241
D.12	Derivation of Eq. 5.27, $NEP_\nu$ . . . . .	242
D.13	Derivation of Eq. 5.31, $NEP_{measured}$ . . . . .	243

# Thesis Format

This thesis uses the following conventions:

**Equations** Equation units are included in square brackets after the equation (e.g., [cm/s] indicates that an equation has units of centimetres per second). Those units which are not given, to avoid confusion, are listed here. If the units of a numbered equation are not given, and the type of equation is not discussed here, the equation is unitless. The units for an FTS interferogram in this work will typically be one of three representations. The first possibility of interferogram units is the Volt (V), as the detector electronics measure the changes in voltage of a current biased bolometer. Another interferogram unit is the arbitrary data unit (ADU). The ADU is the raw number output as digitized by the FTS detector electronics' analog to digital conversion (ADC). The final interferogram unit is the Watt (W), which arises from converting the measured detector voltage into the optical power incident on the detector during the interferogram measurement. If other source factors are known, then the interferogram may also be expressed in terms of [unit]/m<sup>2</sup> or [unit]/(m<sup>2</sup> sr). Other variants of these units may also be used such as mV (10<sup>-3</sup> V) and pW (10<sup>-12</sup> W). The spectrum will be in units reciprocal to the interferogram. Therefore, the

spectrum may be in units of  $\text{ADU}/\sqrt{\text{cm}^{-1}}$ ,  $\text{V}/\sqrt{\text{cm}^{-1}}$ ,  $\text{W}/\sqrt{\text{cm}^{-1}}$ , etc. The actual units of the interferogram/spectrum are not necessarily important provided there is consistency between the two, i.e. the correct reciprocal units are used for both. In some equations, the units are not important; for example, a Fourier series may be calculated for a function with units of height, dollars, Volts, Watts, etc. where the operation is the same regardless of the unit. The units of such generic equations will not be listed with the equation.

**Units** An attempt has been made to use *Système International d’Unités* (SI) units and constants. There are exceptions where non-SI units are more commonly used in this field. One example of this is the use of cm and  $\text{cm}^{-1}$  (wavenumber) for optical path difference and frequency. Another exception is the units used for angles. Radians (rad.), degrees ( $\text{deg./}^\circ$ ), arcminutes ( $'$ ), and arcseconds ( $''$ ) will all be used depending on the context of the discussion. In Chapter 3, the reference to some angles such as  $\pi, \pi/2$ , etc. in radians provides greater clarity than the use of degrees, especially when referring to their use in trigonometric functions. In other aspects, such as discussing small deviations from  $\pi, \pi/2$ , etc. the use of degrees as units seems to be more clear. Although some may find this interchanging of units frustrating it is the author’s view that it makes the content easier to read. This is a very subjective choice. In Chapter 4, the units for angles are more consistently  $''$ ,  $'$ , and degrees. If the unit of an angle is not stated in an equation, and the angular units do not cancel out, the angle is assumed to be in radians. Non-SI units will be introduced as necessary.

## Chapter 1

# Introduction

Ah, but a man's reach should exceed his grasp, or what's a  
heaven for?

---

Robert Browning [3, p. 157]

---

In this chapter a brief introduction to Herschel and SPIRE is provided along with a summary of the ground based performance verification testing of SPIRE conducted at the Rutherford Appleton Laboratory. A summary of the work performed during the completion of the Ph.D. degree requirements is provided. Finally, some of the scientific motivations for this work are introduced.

## 1.1 The Herschel Space Observatory

Herschel is one of the cornerstone missions in the ESA science Horizon 2000 plan [4] designed to study the far-infrared (FIR)/submillimetre (submm) region of the electromagnetic spectrum. Contrary to Herschel's uninhibited view of the FIR/submm, the Earth's atmosphere is highly opaque in this region of the spectrum; this is primarily due to water vapour absorption. Although the best astronomical observatory sites in the world enjoy a small number of narrow spectral windows during nights when the atmosphere above them is particularly dry, the majority of the FIR/submm astronomical spectrum is unexplored [5]. The 3.5 m diameter Herschel primary mirror is the largest of its kind possible for a space mission [4]. A photograph of Herschel, taken during the final stages of ground based spacecraft integration testing, is shown in Figure 1.1. The three instruments on Herschel (Spectral and Photometric Imaging Receiver(SPIRE), the photoconductor array camera and spectrometer (PACS), and the Heterodyne Instrument for the Far-Infrared (HIFI)), shown in Figure 1.2, are complementary and provide astronomers access to the full FIR/submm band at a variety of spectral resolutions ranging from the low- to medium-resolution provided by PACS and SPIRE, to the high-resolution provided by HIFI. Herschel's main scientific objectives,



Figure 1.1: Photograph of the fully assembled Herschel Space Observatory. *Photo: ESA*

in our own and nearby galaxies, are spectroscopy of both star forming regions and stellar evolution [4]. For more distant sources, Herschel's main objectives are galactic and deep extragalactic imaging surveys [4].

The Herschel primary mirror is passively cooled during flight to  $\sim 80$  K and is expected to have an emissivity of  $\sim 1\%$  (the temperature and emissivity are to be confirmed following launch). The fact that emission from the Herschel primary mirror is the principle source of noise for the SPIRE bolometer detectors [6] (see Chapter 5) is a testament to their sensitivity. The Herschel optical bench, which is cryogenically cooled with a superfluid liquid helium cryostat, is expected to maintain the Herschel instruments at operating temperatures

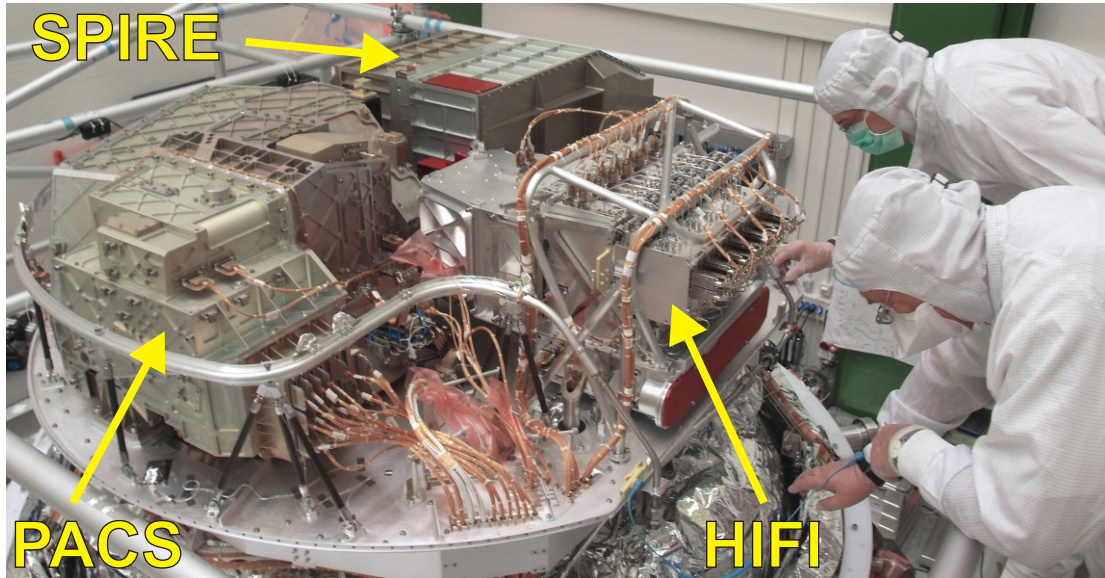


Figure 1.2: The three instruments (HIFI (front-right), PACS (front-left) and SPIRE (back)) on the Herschel optical bench undergoing telescope assembly and integration testing. *Photo: Astrium*

for 3 – 5 years of observation time.

Herschel's operational orbit is about a location in the Sun-Earth system called the second Lagrangian point (L2), some  $\sim 1.5$  million km from the Earth [7]. This orbit provides a cool/dark environment, uninterrupted access to the full FIR/submm spectrum, and access to virtually the entire sky over the course of a year, providing Herschel the low background needed for photometry and the uninterrupted wavelength coverage ideal for spectroscopy. There is strong motivation to verify instrument performance fully and conduct a comprehensive instrument calibration during ground based instrument performance verification testing prior to launch because the L2 orbit is not accessible to any type of service mission.



## 1.2 The Spectral and Photometric Imaging Receiver (SPIRE)

SPIRE comprises an IFTS covering wavelengths between  $194 - 672 \mu\text{m}$ , and a three-band imaging photometer operating over the same spectral region with bands centred at approximately  $250, 350$  and  $500 \mu\text{m}$  [8]. The SPIRE FTS instrument is shown in Figure 1.3. A photograph of the fully assembled, flight-qualified SPIRE instrument, taken just prior to Herschel instrument integration testing, is shown in Figure 1.4. Both the SPIRE photometer and spectrometer use feedhorn coupled bolometer arrays [9]. The individual bolometers are composite detectors using a neutron transmutation doped (NTD) germanium thermistor element attached to a Silicon Nitride micromesh spider-web substrate [10, 11], coated with a metallic film to match the impedance of free space, as the absorbing layer [12]. Spatial modulation of the telescope signal is provided to both instruments either by a two axis beam steering mirror, or by scanning the telescope across the sky [13].

The IFTS found within SPIRE is of the Mach-Zehnder configuration [14], containing two novel broadband intensity beamsplitters [15]. The SPIRE IFTS has a field-of-view (FOV) of  $2.6'$  and two spectral pass-bands of wavelengths  $194 - 324 \mu\text{m}$  (spectrometer short wavelength (SSW)) and  $316 - 672 \mu\text{m}$  (spectrometer long wavelength (SLW)) [16], each observed by an array of bolometer detectors. A schematic diagram of the SPIRE FTS is shown in Figure 3.1 (Chapter 3). One of the two SPIRE FTS optical input ports admits radiation incident from the astronomical source while the other optical input port of the FTS contains a calibration source (the Spectrometer Calibrator (SCAL)) which is in place to compensate for emission from the telescope primary mirror (see Chapter 3).

Frequency modulation of the source signal is provided by the SPIRE FTS mech-

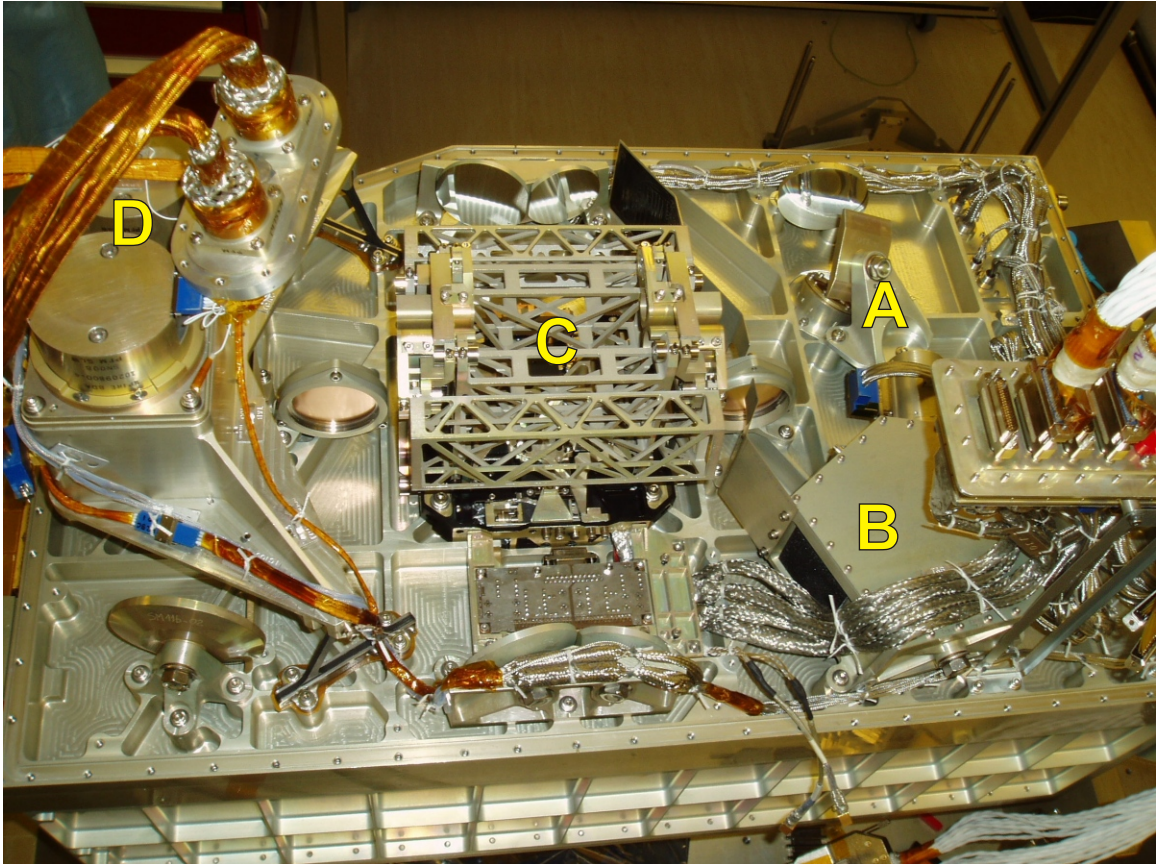


Figure 1.3: Photograph of the SPIRE FTS instrument. Light incident on the telescope enters the SPIRE FTS in the upper right corner of the figure (A). The internal blackbody source (SCAL) is in the lower right portion of the figure (B). The SPIRE FTS mechanism is in the centre of the image (C) and the SPIRE FTS detector arrays are on the left hand side (D). *Photo: SPIRE Consortium, RAL*

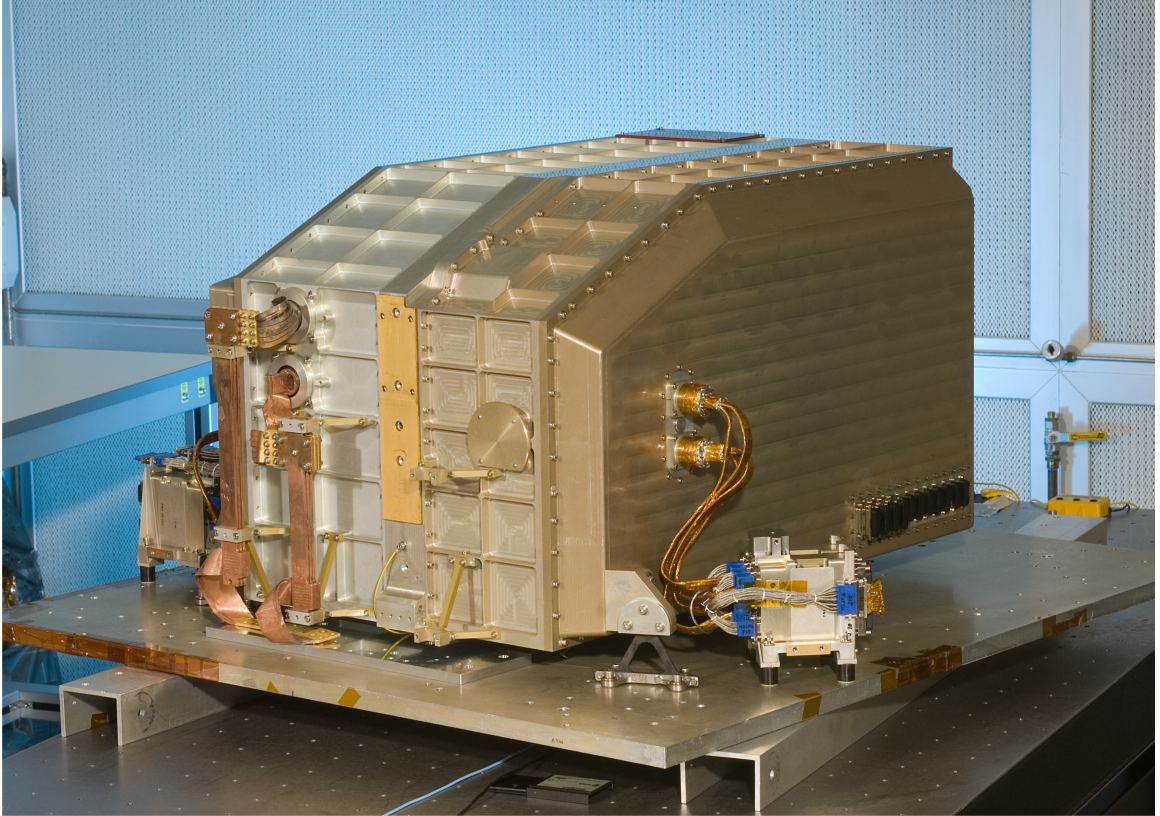


Figure 1.4: Photograph of the SPIRE instrument prior to integration on the optical bench of the Herschel cryostat. *Photo: SPIRE Consortium, RAL*

anism (SMEC), which modulates the optical path difference (OPD) between the two optical paths of the FTS instrument [17]. The SPIRE FTS astronomical observation templates (AOTs) provide three standard spectral resolutions: low, medium, and high (i.e.  $\Delta\sigma = 1.0, 0.25, 0.04 \text{ cm}^{-1}$ ) [18]. Low-resolution mode is ideal for continuum spectrophotometry while high-resolution mode is optimal for mapping regions of broad molecular rotational transitions, e.g. CO rotational dynamics in a molecular cloud.

The SPIRE science program consists of two primary themes: extragalactic and galactic surveys. The goal of the SPIRE extragalactic deep survey is to cover a large area

---

of sky to a depth that is at the confusion limit for galaxies [19]. For the galactic portion, SPIRE will survey nearby molecular clouds to detect complete samples of pre-stellar, proto-stellar, and young-stellar objects. Therefore, SPIRE must be sensitive enough to detect faint objects and cover large areas in a reasonable time while having sufficient dynamic range to measure bright and faint sources simultaneously. Similar sensitivity requirements exist for SPIRE extragalactic observations; for these, the available spatial resolution of SPIRE precludes the same level of cloud dynamic analysis, however, given SPIRE's broad spectral coverage and sensitive detectors, it is hoped that important spectral features, such as molecular rotational transition lines, will be observed at a variety of redshifts.

Prior to the launch of Herschel, the performance of the SPIRE instrument was verified and calibrated during a series of pre-vibration, vibration, and post-vibration ground-based tests. These tests are referred to as cryogenic qualification model (CQM) and Proto-flight model (PFM) test campaigns; the CQM model of the SPIRE instrument, with a limited functionality, was verified prior to the development of the fully functional PFM of SPIRE. Vibration testing is performed in order to simulate the expected acceleration environment of a rocket launch. Pre- and post- vibration testing are conducted to verify that the instrument will survive launch, and that instrument performance is not affected by the adverse launch environment. Shortly after launch, the Herschel mission undergoes its performance verification (PV) phase of operations where the instrument performance capabilities under the actual observatory space background environment are tested for the first time.

### 1.3 My Contribution to SPIRE

During the defence of my M.Sc. thesis [20], one of the examiners asked how much of the work presented in the thesis was my own. While somewhat surprised by the question, I stated that all of the work presented was my own. It is somewhat difficult to define strict boundaries on the division of efforts in a project such as Herschel/SPIRE, where individuals and teams perform specific tasks that contribute towards a much greater whole. While the work presented in this thesis is, in fact, my own, there are many research teams, each with several expert scientists and engineers, collaboratively working on the SPIRE project. This section is included to outline my level of involvement with the project and the work I did towards the completion of this thesis. §1.3.1 & §1.3.2 outline my participation in SPIRE PFM testing and subsequent data analysis, respectively. An overview of the publications that have resulted from my participation in this work is provided in §1.3.3. At the end of the chapter, the work I have done in the context of each subsequent thesis chapter is summarized in §1.5.

My participation in the SPIRE project is in partial fulfillment to the Canadian contribution to Herschel/SPIRE which provides Canadian astronomers access to the Herschel/SPIRE guaranteed time observation program. As a more direct recognition for my personal contribution to the project thus far, I have been awarded the title of SPIRE *Associate Scientist* and have priority access to SPIRE observation data through the SPIRE interstellar medium specialist astronomy group (SAG-4) guaranteed time key project (GTKP) (see §1.4).



### 1.3.1 Participation in SPIRE Ground Based Performance Verification Testing

I first became involved in the SPIRE project after completing my B.Sc. in Engineering Physics at the University of Alberta, Edmonton in the spring of 2003. Initially, I worked in Dr. Naylor's laboratory as an employee of the University of Lethbridge under a Natural Sciences and Engineering Research Council (NSERC) Undergraduate Student Research Award (USRA) for a semester long work-term to get my feet wet in preparation for graduate studies. During this work-term our research group developed, constructed, tested, and delivered a test-facility FTS (TFTS) to the SPIRE AIV facility at RAL; developed control software for the Test FTS (TFTS); and developed an FTS data processing toolkit software package [21] in the Interactive Data Language (IDL). Throughout my graduate studies I have regularly used both the TFTS and its associated control software, and the IDL data processing toolkit.

From September 2003 to August 2005 I worked towards my M.Sc. in Physics on the spectral characterization of the SPIRE photometer. As part of my studies, I was stationed at RAL, in the UK, for a six month period from January to June 2004 during the performance verification testing of the SPIRE instrument CQM. During this time I used the TFTS coupled with the SPIRE photometer detectors to characterize the spectral performance of the SPIRE photometer. I was also serving as a full time member of the Instrument Control Centre (ICC) staff on the Instrument Test Team (ITT). Incidentally, the SPIRE cryo-cooler, which contains pressurized Helium and needs special certification in order to be transported via air courier, needed to return to Commissariat a l'Energie

Atomique (CEA) between the CQM-1 and CQM-2 test campaigns. Sending me with the cooler by rail was much simpler than flying it, so I spent an entire day on various trains making sure that a key component of SPIRE remained safe during transport, and had an opportunity to see the CEA facility in Grenoble, France.

Upon completion of my M.Sc. I was again stationed at RAL between September and December of 2005 as an ICC staff member on the ITT. During this time the PFM-2 instrument test campaign was conducted. I also participated in the SPIRE/PACS parallel mode testing at EADS/Astrium in Munich, Germany, conducted shortly after the completion of PFM-2 testing.

Under an NSERC postgraduate scholarship, I began my Ph.D. research project in January 2006. While the focus of my M.Sc. research project was on using the calibrated TFTS to evaluate the performance of the SPIRE photometer, this Ph.D. research project focuses on the performance and calibration of the SPIRE FTS itself. I was again stationed at RAL between November 2006 and February 2007, which included the PFM-4 instrument test campaign. During PFM-4, in addition to my standard duties in the ITT, I was responsible for developing, implementing, and analyzing all of the tests related to development of the photometer relative spectral response function (RSRF) calibration data product for each of the three photometer detector arrays of the SPIRE flight model. I was also heavily involved in the implementation and analysis of the series of experiments verifying the spectral performance of the SPIRE IFTS, including studies of: instrumental line-shape (ILS) across both detector arrays, obliquity effects, input port compensation, and detector noise performance.

Table 1.1: Summary of SPIRE instrument testing.

Test	Dates
CQM-1	2/2/2004 – 13/2/2004
CQM-2	25/8/2004 – 14/10/2004
SPIRE/PACS parallel mode	7/11/2005 – 9/11/2005
PFM-1	22/2/2005 – 8/4/2005
PFM-2	17/8/2005 – 20/10/2005
PFM-3	15/3/2006 – 13/4/2006, 25/4/2006 – 5/7/2006
PFM-4	20/10/2006 – 29/1/2007
PFM-5	2/2/2007 – 16/3/2007

While there are many aspects of the PFM test campaigns that have not been discussed, the timeline presented here is intended to put my participation in the project in perspective with the progression of my graduate studies. A summary of the SPIRE instrument test campaigns is provided in Table 1.1. In short, I have been stationed full time at RAL to participate in instrument performance verification testing for a period spanning 15 months since joining the project. While I was stationed in the UK, my time was primarily devoted to instrument testing itself; notwithstanding, significant effort on the data analysis side was also required. Although some analysis was performed on site in the UK, much of the subsequent data analysis took place off-line, upon returning to Lethbridge, and is discussed in §1.3.2.

### 1.3.2 Data Analysis

For every hour spent collecting data in the laboratory, another several hours are often needed in the analysis of the collected data. Many of the experiments that I performed in SPIRE PFM testing involved generating scripts that would be initiated at the conclusion



of the evening shift in the lab and left to run all night until the morning shift started up the following day, generating a significant amount of data to work with. As a quick measure, a properties search of the “SPIRE” directory where I store all of the CQM/PFM raw and analyzed data on my desktop computer reveals 32,391 files within 678 Folders occupying a total of 74.4 GB of hard disk space. A search of my “IDL” directory reveals 2,931 files within 109 folders occupying 80.4 MB of disk space; this corresponds to  $\sim 10^6$  lines of scripting code (with a reasonably large error bar on this number). Although there is some redundancy in the storage system that I have adopted, and the true measure of data stored and created in various formats would take more time to generate than it is worth, the approximate numbers above speak to the sheer volume of data and analysis that I have become intimately familiar with over the years that my efforts have been dedicated to this project.

As part of my involvement in SPIRE, I am an active participant of the SPIRE data analysis group (SDAG). SDAG meetings provide the principle discussion forum for PFM test analysis progress and results among the instrument teams. I prepared and presented material related to many aspects of both the SPIRE photometer and spectrometer for SDAG meetings. I also worked in collaboration with many others on data processing and analysis, data archiving and distribution, interpretation of results, creation of additional experiments, etc.

As mentioned above, I was responsible for the determination of the RSRF for each of the three photometer detector arrays. In addition to the design and execution of the experiments required to obtain such data, I was responsible for its subsequent analysis. This involved processing many nights worth of FTS interferogram scans, sorting high, medium,

and low quality observations, looking for any significant differences and/or trends across each array, and finally averaging the results to provide one calibration file per array.

SPIRE instrument development progression requires a series of science verification reviews (SVR), the passing of which represent significant milestones in the instrument development progress. In preparation for an SVR, technical reports on many aspects of the instrument performance and development are required. I participated as a co-author of the SVR reports on the SPIRE instrument throughout [22–24].

Much of the SPIRE CQM and PFM data that I have analyzed will contribute to the analysis of SPIRE flight astronomical observation data in one form or another. The beamsplitter emission and port compensation work (Chapter 3) provides valuable instrument characterization data and guides the requirements for calibration observations during the flight PV phase. Chapter 3 also provides input for a specific module which has been added to the SPIRE data processing pipeline software to correct for port compensation anomalies. The obliquity effect results (Chapter 4) contribute important information for the removal of instrumental effects from the final spectra. The sensitivity and noise results (Chapter 5) provide verification of the theoretical bolometer model using ground-based performance verification measurements, which in turn allows prediction of the detector noise performance once the final space environment is known.

### 1.3.3 Publications

While working with the SPIRE project, I have had valuable opportunities to present my work to a variety of audiences. Although the majority of this dissemination of knowledge comes in the form of conference submissions, I have also submitted work in

the form of: journal manuscript submissions, internal technical reports, telescope observation proposals, and departmental and graduate student colloquia presentations.

As mentioned above, my M.Sc. thesis [20] presents the use of an FTS external to the SPIRE cryostat to determine the spectral characterization of the SPIRE photometer detector arrays.

The International Society for Optical Engineering (SPIE) Astronomical Telescopes and Instrumentation conference series is held every two years and represents the main conference for presenting current progress on large space and astronomy projects currently under development. I am the lead author on three submissions to SPIE conferences: one paper discussing the use of the TFTS in SPIRE instrument testing [25], and two discussing performance of the SPIRE FTS [16, 26]. I am also a co-author on several other SPIE submissions discussing progress on FTS analysis and SPIRE test results [8, 27–29].

In alternate years to the SPIE conference, the Optical Society of America (OSA) holds a topical meeting on Fourier transform spectroscopy. I have been the lead author on three OSA-FTS submissions: a paper on the optimization of FTS phase correction [30], FTS OPD metrology calibration [31], and a paper discussing a study of FTS beamsplitter anomalies [32]; I was also a co-author on another OSA-FTS submission [33].

Our research group has also presented work at the Institute of Electrical and Electronics Engineers (IEEE) Infrared Millimetre Waves – Terahertz (IRMMW-THZ) conference series. I presented results on SPIRE FTS port compensation [34] and beamsplitter emission [35], in 2007 and 2008, respectively. I have also presented work at the Canadian Astronomy Society (CASCA) [36–38] and the Canadian Remote Sensing Society annual

meetings [39, 40].

Within the project environment, I am a co-author on several technical reports submitted for instrument SVR meetings [22–24], and am a proposer on the SAG-4 GTKP observation proposal [41]. A manuscript submission on FTS metrology calibration has been published in *Applied Optics* [42], and, at the time of thesis submission, several manuscripts are in preparation for submission based upon work presented in this thesis. I have also been personally acknowledged in two published journal articles [43, 44]. In all, I have been the lead author on four oral and seven poster presentations given at international conferences, have been co-author on five international conference submissions, and have presented my work on campus and in the community many times. I have also published in a peer reviewed research journal and reviewed articles submitted to research journals as part of the peer review process. Although Herschel was initially scheduled for launch in early 2007 [45], the complexity in developing and testing each instrument, integrating all of the instruments with the telescope, and the pioneering nature of the project, led to delays which pushed the launch to 14 May 2009. An unfortunate consequence of these delays is that no Herschel flight data is presented in this thesis. I am, however, still involved with the project and plan to be working with Herschel data as part of my post-doctoral research.

## 1.4 Interstellar Medium Specialist Astronomy Group

As mentioned above, I have been given the title of associate scientist for my contribution to the SPIRE project. This title provides access to guaranteed time observation data once Herschel is in flight. In this section, the science goals of the SAG-4 GTKP, of

which I am a member, are introduced.

Herschel observation time is primarily divided into open time and guaranteed time. Approximately 64% of observation time is open time which is available to the entire astronomical community. Guaranteed time, which is given to the instrument teams to compensate for contributions to the project, is allocated 32% of observation time. The remaining 4% is discretionary time. The SPIRE guaranteed time program is divided into specialty areas with access to guaranteed time observations given to the various instrument and science project teams in return for their contributions to the project. Guaranteed time program priorities include: high redshift galaxies, galaxies in the local Universe, galactic star formation, the interstellar medium, and local solar system objects. The SAG-4 interstellar dust evolution proposal [41], submitted April 2007, has been accepted into the SPIRE GTKP observation program.

The SAG-4 observations utilize both SPIRE and PACS mapping and imaging spectroscopy to build on, with greater spatial resolution, previous surveys such as those performed by IRAS [46, 47] and DIRBE [48]; SAG-4 will also compliment ISO [49–51] and Spitzer [52] observations. The dust evolution observations are divided into several categories: shock-processed dust [53], cirrus and molecular clouds [54,55], photo-dissociation regions (PDR) [51, 56, 57], and star forming regions [58–61]. The high spatial resolution provided by SPIRE observations of the physical and chemical conditions prevailing in the cold phases of the interstellar medium (ISM) will enable study of the behavior of interstellar gas and dust both before and during star formation.

Stars form through the collapse of fragmented dense cloud cores in the ISM [62].

---

At each stage of the star formation process physical conditions can be traced through dust emission; dynamical dust processes govern the stellar initial mass function (IMF) [63]. While the SPIRE specialist astronomy group (SAG)-3 GTKP will map star forming regions, SAG-4 will follow up on these mappings with FTS observations which will be used to derive changes in dust properties and gas conditions. The dust spectral energy distribution (SED) will be constrained more precisely, an unbiased spectral survey of the lines in the FIR/submm will be available, and a measure of gas temperature and density will be possible with appropriate spectral lines (e.g. CO). Spectroscopy of star forming regions will be performed on pre-stellar cores, Class 0 and Class 1 protostars, and hot PDRs surrounding galactic H II regions. Sources selected also have low-resolution Infrared Space Observatory (ISO)/ long wavelength sensor (LWS) spectra available. In a discussion comparing theoretical models of ISM molecular cloud dynamics with observations, Goldsmith [64] states, *“This has not been an area in which much success has been achieved at longer wavelengths, which suggests that there is still something fairly basic missing in our understanding . . . It is possible that the multiple [spectral] lines available with Herschel will provide critical new information, since the different lines will have a large range of optical depths and thus sample different portions of the cloud.”* These high priority programs for Herschel require sensitive continuum imaging in several bands to carry out surveys, a low-resolution spectroscopic mode to obtain detailed SEDs of selected objects, and a high-resolution spectroscopic mode to measure key spectral lines.

## 1.5 Thesis Summary

An introductory review of FTS is provided in Chapter 2. This chapter includes a discussion of Fourier theory including relevant mathematics, and an introduction to FTS instrumentation.

Chapter 3 includes a study of FTS beamsplitter phase and emission. While analyzing SPIRE spectrometer data after the conclusion of all PFM testing, a unique effect was noticed within the recorded data. In this effect, an odd symmetry attributed to the FTS beamsplitter is observed in FTS interferograms when both spectral inputs are well balanced. Although there was not an opportunity to study this effect further with the SPIRE FTS as testing was completed and the instrument team no longer had access to the instrument, further experimentation was performed locally in University of Lethbridge AIG laboratories with an FTS instrument similar to SPIRE. I designed and constructed two identical, temperature controlled, blackbody sources for the two inputs of the FTS. I assisted in the rebuilding of a single pixel submm cryogenic detector to use with our laboratory FTS. Subsequently, I conducted a series of experiments to further investigate the effects of beamsplitter emission. As a result of this study, the SPIRE FTS observing modes were fundamentally redesigned and an additional process was included in the SPIRE FTS data processing software pipeline [65].

The imaging aspects of the SPIRE IFTS are discussed in Chapter 4. While at RAL, I participated in experiments designed to explore the obliquity effects associated with an IFTS. These experiments included the use of a molecular laser and photonic mixer as unresolved spectral line sources incident on the SPIRE FTS detector arrays. In Chapter

4, the results are presented for an investigation of the change in ILS and shift in observed source frequency as a function of axial detector position. Although some experiments were performed during earlier PFM test campaigns, the results presented in Chapter 4 are from the PFM-4 tests alone as some instrument changes took place prior to PFM-4. The observations with the molecular laser used to produce these results were recorded at RAL over a period of several days and involved several hours of preparatory work getting the laser operational each day. The photonic mixer was provided on loan from another group at RAL and was only available one day during PFM-4 testing. The molecular laser scans comprise ~1 GB of raw data and ~7 GB of processed data products while the photonic mixer data is comprised of ~233 MB of raw data and ~2 GB of processed data products; the processed data products mentioned above include both intermediate data products such as interferograms interpolated onto an evenly spaced OPD grid and low-resolution phase correction spectra, and the desired final data products such as co-added, high-resolution, spectra.

A study of the performance of the SPIRE bolometer detectors is provided in Chapter 5. The analysis presented in Chapter 5 includes both simulation work and observational data analysis. I performed all of the theoretical bolometer simulation work presented in the IDL language, although it was heavily based on simulations performed by Dr. Matt Griffin in the SPIRE Sensitivity Models document [6]. The IDL model which I developed did add to Dr. Griffin's theoretical model, as I simulated the background radiation from the laboratory and cryostat environment in addition to the expected in-flight telescope environment radiation which was included in the original model [6]. I conducted all of the FTS analysis presented in Chapter 5 and I also performed all of the rotational carbon monoxide (CO)



analysis and simulations.

Conclusions, the current status of Herschel, and future work are presented in Chapter 6.

## Chapter 2

# Fourier Transform Spectroscopy and FTS Data Processing

The major laws of spectral lines ... as well as their significance for chemistry appeared to me like a miracle ... This is the highest form of musicality in the sphere of thought.

---

Albert Einstein [66, p. 115]

---

The popularity of Fourier transform spectroscopy (FTS) as a diagnostic tool in the physical sciences owes much to the astronomical community which pioneered many of the important developments in this field [67, 68]. This chapter gives an overview of FTS and its underlying mathematical principles. Fourier series and integrals are introduced. A description of a classical Michelson interferometer is provided. The principal advantages of a Fourier transform spectrometer (also abbreviated as FTS) are reviewed including the Jacquinot, Fellgett, and Connes advantages. Practical considerations in the use of an FTS such as sampling the interferogram, natural apodization arising from the optical design of the interferometer, and the impact of various noise contributions to the interferogram on the derived spectrum are also discussed. Chapters 3 & 4 provide further details on beamsplitters and imaging FTS, respectively.

## 2.1 A Brief History

A technique for analyzing periodic functions was developed by Jean Baptiste Joseph Fourier (1768 – 1830), now known as *Fourier's Theorem* [69, 70]. This method expresses any function as a linear combination of orthogonal sinusoids and cosinusoids. Originally developed to analyze heat flow in solids [71], it was not until a century later that Fourier's theorem became appreciated as the powerful analytical tool that it is today. Indeed, one is hard pressed to find a branch of the physical sciences in which this theorem is not applied. Other scientists contemporary to Fourier, including Euler, Lagrange, and Gauss, also made contributions to the field of Fourier/trigonometric series as it was emerging [72].

The roots of Fourier transform interferometry date back to the 1880's when Dr. Albert Michelson [73] invented the interferometer and realized the basic concepts of Fourier transform spectroscopy while attempting to detect the Earth's motion through the proposed *luminiferous ether* [74]. Interferometry and Fourier analysis were not exploited at that time due to the lack of computational power and extremely poor detector sensitivity [75–77]. Michelson invented a mechanical analog computer, called a harmonic analyzer [78], capable of performing Fourier transforms of about 80 data points, but this was not extensively used for Fourier transform spectroscopy. Michelson measured 'visibility curves' [79] with his eye and made crude estimates of the spectrum. The Michelson interferometer is described in detail in §2.5 of this chapter.

The first interferogram (see §2.5) was recorded in 1911 by Rubens and Wood [67] who used a microradiometer to record the interference signal. Lacking the computational power to compute the Fourier transform of the recorded signal directly, Rubens and Wood computed the Fourier transform of educated guesses of simple spectra for comparison with the measured signal. It was not until 1958 that the first Fourier transform was computed numerically by Fellgett [80], who was also the first to recognize the multiplex advantage of Fourier transform spectrometers (§2.6.2). In 1960, Jaquinot recognized that an FTS conveys a significant throughput advantage over other types of spectrometer (§2.6.1) [81]. The breakthrough that took FTS from the domain of a very few scientists to a common diagnostic tool found in every chemistry undergraduate laboratory was the rediscovery of the fast Fourier transform (FFT) algorithm by Cooley and Tukey in 1965 [2]. The FFT algorithm was subsequently introduced to Fourier spectroscopy by Forman [82] in 1966.

History has shown that an algorithm similar to the FFT developed by Carl F. Gauss was found in an unpublished manuscript amongst his collected works, although its existence was not known to Cooley and Tukey [72]. In fact, it is also possible that Gauss' work on Fourier series coefficient analysis pre-dates the original work of Fourier [72]. An algorithm similar to the FFT was published in 1942 by Danielson and Lanczos [83, 84], who give credit to Runge and König [85] as the source of their method [86]. The first application of FTS to astronomy was published in 1969 by Janine & Pierre Connes [68]. Now in the 21st century, FTS systems have been selected as the spectrometer of choice in several current and future space astronomy missions [87–94].

## 2.2 Fourier Series

Fourier's theorem states that a periodic function,  $f(z)$ , of period  $Z_o$ , can be expressed as a series of harmonic functions whose periods are integer submultiples of  $Z_o$  (i.e.  $Z_o/n$  where  $n = 1, 2, 3 \dots$ ). The trigonometric form of the Fourier Series representation is given by

$$f(z) = \frac{a_o}{2} + \sum_{n=1}^{\infty} [a_n \cos(n\omega_o z) + b_n \sin(n\omega_o z)] , \quad (2.1)$$

where

$$\omega_o = \frac{2\pi}{Z_o} \quad (2.2)$$

is the fundamental frequency and the functions  $\cos(n\omega_o z)$  and  $\sin(n\omega_o z)$  form a set of mutually orthogonal basis vectors. The constants  $a_o$ ,  $a_n$ , and  $b_n$  are given by

$$a_o = \frac{2}{Z_o} \int_{z_1}^{z_1+Z_o} f(z) dz , \quad (2.3)$$

$$a_n = \frac{2}{Z_o} \int_{z_1}^{z_1+Z_o} f(z) \cos(n\omega_o z) dz \quad n = 1, 2, 3, \dots , \quad (2.4)$$

and,

$$b_n = \frac{2}{Z_o} \int_{z_1}^{z_1+Z_o} f(z) \sin(n\omega_o z) dz \quad n = 1, 2, 3, \dots . \quad (2.5)$$

Using Euler's formula [95], the Fourier series may be expressed in an exponential form given by

$$f(z) = \sum_{n=-\infty}^{\infty} d_n e^{in\omega_o z} , \quad (2.6)$$

where

$$d_n = \frac{1}{Z_o} \int_{z_1}^{z_1+Z_o} f(z) e^{-in\omega_o z} dz , \quad (2.7)$$

and the amplitudes of the spectral components are split between positive frequencies (+ $n$ ), and negative frequencies ( $-n$ ).

The Dirichlet conditions [96] must be met in order for a Fourier series to exist (weak condition) and be convergent (strong conditions). The weak Dirichlet condition states that in order for a function,  $f(z)$ , to have a Fourier series it must be absolutely integrable over one period, i.e.  $\int_{Z_o} |f(z)| dz < \infty$ . The two strong conditions require a finite number of 1) finite discontinuities, and, 2) extrema, in one period. Thus, any periodic waveform that can be generated in the laboratory automatically satisfies the strong Dirichlet conditions, and hence possesses a convergent Fourier series.

## 2.3 Fourier Integrals

As the spacing between harmonic frequencies decreases and the limits of the Fourier series are extended to infinity, the Fourier series representation (Equation 2.6) can be re-

placed by the Fourier integral representation given by

$$f(z) = \int_{-\infty}^{\infty} F(\sigma) e^{i2\pi\sigma z} d\sigma , \quad (2.8)$$

where the expression is known as the reverse (or inverse) complex Fourier transform [97,98].

In this case, optical path difference, i.e.  $z$  (cm), and wavenumber, i.e.  $\sigma$  ( $\text{cm}^{-1}$ ), are reciprocal Fourier transform variables. Another common Fourier pair is time ( $t$ ), measured in seconds, and frequency ( $\nu$ ), measured in Hz. The spectrum, i.e.  $F(\sigma)$ , is given by

$$F(\sigma) = \int_{-\infty}^{+\infty} f(z) e^{-i2\pi\sigma z} dz , \quad (2.9)$$

and is known as the forward complex Fourier transform. Euler's formula may be used on either forward or reverse complex Fourier transforms to obtain sine and cosine Fourier transform expressions.

## 2.4 Properties of Fourier Transforms

In this section, some of the important Fourier transform properties which are relevant to this thesis will be introduced. Table 2.1 outlines the symmetry properties of Fourier transforms and a summary of Fourier Theorems is provided in Table 2.2. For a full review of the Fourier transform properties summarized in Table 2.2, the reader is referred to the literature [98–100]. This section will discuss aspects of symmetry, Fourier transform pairs, and Fourier Theorems. Due to their importance, specific functions such as the Dirac Delta function, the boxcar function, and the cardinal sine function (i.e. the *sinc* function [99]), are introduced directly.

Consider a cosinusoid of spatial frequency  $\sigma_o$  ( $\text{cm}^{-1}$ ) defined over the range  $z \in$

$(-\infty, +\infty)$  of the form

$$f(z) = \cos(2\pi\sigma_0 z) . \quad (2.10)$$

The Fourier transform of  $f(z)$  is expressed as

$$F(\sigma) = \frac{1}{2}\delta(\sigma - \sigma_0) + \frac{1}{2}\delta(\sigma + \sigma_0) , \quad (2.11)$$

where

$$\delta(\sigma') = \begin{cases} \infty & \text{for } \sigma' = 0 \\ 0 & \text{for } \sigma' \neq 0 \end{cases} \quad (2.12)$$

and

$$\int_{-\infty}^{+\infty} \delta(\sigma') d\sigma' = 1 \quad (2.13)$$

represents the Dirac delta function [99]<sup>1</sup>, and  $\sigma' = \sigma \pm \sigma_0$ . The Fourier transform of an even cosine results in two delta functions of equal magnitude at  $\pm\sigma_0$ . The Fourier transform of a real valued even function produces a real valued result with even symmetry with respect to the positive and negative frequencies.

Similarly, the Fourier transform of an odd function in  $z \in (-\infty, +\infty)$  of the form

$$f(z) = \sin(2\pi\sigma_0 z) \quad (2.14)$$

is given by

$$F(\sigma) = \frac{-i}{2}\delta(\sigma - \sigma_0) + \frac{i}{2}\delta(\sigma + \sigma_0) . \quad (2.15)$$

The Fourier transform of a real valued odd function produces an imaginary valued result with odd symmetry with respect to the positive and negative frequencies. Since an arbitrary function can be decomposed into a linear combination of symmetric and antisymmetric

---

<sup>1</sup>Any reference to the *delta function* in this thesis refers to the Dirac Delta function unless otherwise stated.



components, there is no loss of generality in this approach. Fourier transform symmetry properties for a variety of functions are shown in Table 2.1.

Table 2.1: Symmetry properties of Fourier transform pairs, where  $z$  and  $\sigma$  represent the spatial and spectral domains, respectively.

$f(z)$		$F(\sigma)$	
Real	Imaginary	Real	Imaginary
even	0	even	0
odd	0	0	odd
0	even	0	even
0	odd	odd	0
asymmetric	0	even	odd
0	asymmetric	odd	even
even	odd	asymmetric	0
odd	even	0	asymmetric
even	even	even	even
odd	odd	odd	odd
asymmetric	asymmetric	asymmetric	asymmetric

The boxcar function is encountered frequently in both the spatial and frequency domains in Fourier analysis and is given by

$$\Pi(z) = \begin{cases} 1 & |z| \leq L \\ 0 & |z| > L \end{cases}, \quad (2.16)$$

where  $2L$  is the range of the function, centred about 0. The Fourier transform of  $f(z) = \Pi(z)$  is the well known *sinc* function

$$F(\sigma) = 2L \operatorname{sinc}(2\pi\sigma L) = 2L \frac{\sin(2\pi\sigma L)}{2\pi\sigma L}. \quad (2.17)$$

Table 2.2: Fourier theorems [100, 101].

Theorem	$f(z)$	$F(\sigma)$
Addition/Superposition	$f_1(z) + f_2(z)$	$\Rightarrow F_1(\sigma) + F_2(\sigma)$
Scalar multiplication	$kf(z)$	$\Rightarrow kF(\sigma)$
Parseval's	$\int_{-\infty}^{+\infty}  f(z) ^2 dz$	$= \int_{-\infty}^{+\infty}  F(\sigma) ^2 d\sigma$
Wiener-Khintchine	$f^*(z) * f(-z)$	$\Rightarrow  F(-\sigma) ^2$
Reversal	$f(-z)$	$\Rightarrow F(-\sigma)$
Symmetry	$F(z)$	$\Rightarrow 2\pi f(-\sigma)$
Scaling ( $a$ real)	$f(az)$	$\Rightarrow \frac{1}{ a } F\left(\frac{\sigma}{a}\right)$
OPD shift	$f(z - z_o)$	$\Rightarrow F(\sigma)e^{-i2\pi\sigma z_o}$
Frequency shift ( $\sigma_o$ real)	$f(z)e^{i2\pi\sigma_o z}$	$\Rightarrow F(\sigma - \sigma_o)$
OPD convolution	$f_1(z) * f_2(z)$	$\Rightarrow F_1(\sigma)F_2(\sigma)$
Frequency convolution	$f_1(z)f_2(z)$	$\Rightarrow F_1(\sigma) * F_2(\sigma)$
OPD modulation	$f(z) \times \cos(2\pi\sigma_o z)$	$\Rightarrow \frac{1}{2}F(\sigma - \sigma_o) + \frac{1}{2}F(\sigma + \sigma_o)$
OPD differentiation	$\frac{d^n f(z)}{dz^n}$	$\Rightarrow (i2\pi\sigma)^n F(\sigma)$
OPD integration	$\int_{-\infty}^z f(z') dz'$	$\Rightarrow \frac{F(\sigma)}{i2\pi\sigma} + \pi F(0)\delta(\sigma)$

## 2.5 The Michelson Interferometer

The simplest form of an FTS is a Michelson interferometer [76] which operates on the principles of the division and subsequent interference of light. The path that light travels through a Michelson interferometer from the source to detector (Figure 2.1) is as follows:

1. Light from a source enters the interferometer (and is collimated by a lens or mirror if required) resulting in a plane wave.
2. The resulting plane wave is then split (ideally into two equal amplitude waves) by the beamsplitter.
3. These waves travel and reflect from the FTS mirrors (one fixed (3a) and one movable (3b)) and are directed back on themselves towards the beamsplitter.
4. The reflected waves are recombined at the beamsplitter where two resultant waves are formed, one traveling back to the source, and the other one to the detector.
5. A detector placed at the focus of the final optics records the interference of the combined waves of light, resulting in an intensity variation that depends on the phase difference between the interfering waves known as an interferogram.

An FTS spectrometer may also be constructed in a Mach-Zehnder (MZ) configuration. The MZ-FTS operates under the same principles as the Michelson FTS and is introduced in §3.1.

In the case of an ideal interferometer, when the OPD between the two paths is zero, all frequency components exhibit zero phase difference and constructive interference occurs simultaneously for all wavelengths; this position of the FTS translation stage is referred to as the position of zero optical path difference (ZPD). The variation of optical path difference by the motion of the moving mirror from one limit, through the point of ZPD, to the other limit constitutes a scan (e.g.  $-L \rightarrow ZPD \rightarrow +L$ ). The optical signal recorded by the detector for the duration of a scan is called the interferogram. The relationship between

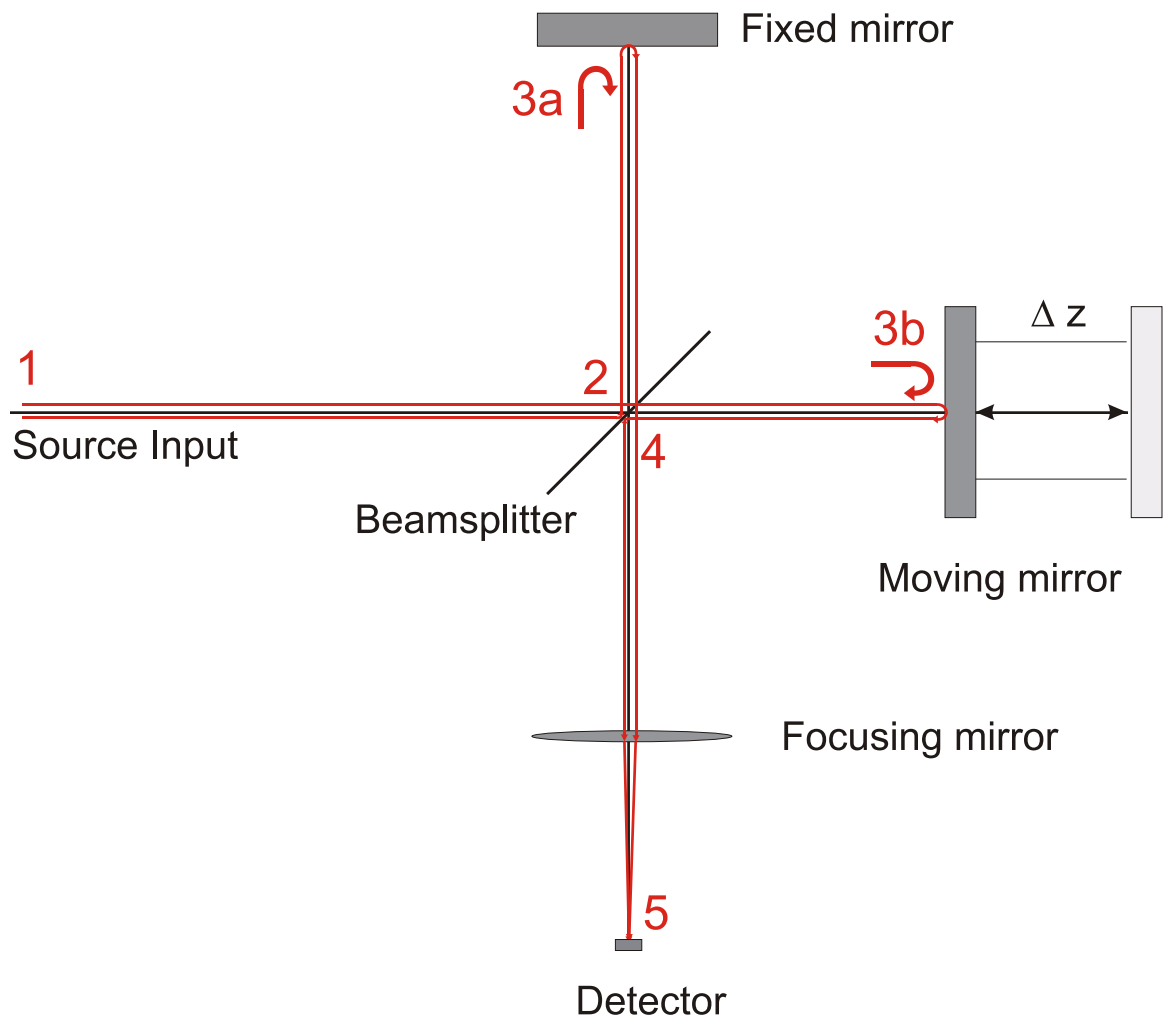


Figure 2.1: Diagram of a classical Michelson interferometer [102].

the interferogram and spectrum is most easily explained using a monochromatic source; the extension to general spectral sources is straightforward and follows.

### 2.5.1 Monochromatic Input Sources

Consider a monochromatic beam of frequency  $\sigma_o$  entering the interferometer. The input beam is divided in two by the beamsplitter. The electric fields describing these two beams, starting in phase at the point just prior to the beamsplitter, can be written as

$$\begin{aligned} E_1(z_1, t') &= E_0 r e^{i\rho} r_m e^{i2\pi(\sigma_o z_1 - \nu t')} t e^{i\tau} \quad [\text{V/m}] \\ E_2(z_2, t') &= E_0 t e^{i\tau} r_m e^{i2\pi(\sigma_o z_2 - \nu t')} r e^{i\rho} \quad [\text{V/m}] \end{aligned}, \quad (2.18)$$

where:  $E_0$  is the amplitude of the incident electromagnetic wave of angular frequency  $\omega = 2\pi\sigma_o$ ,  $t'$  is the propagation time,  $t e^{i\tau}$  is the beamsplitter transmission,  $r e^{i\rho}$  is the beamsplitter reflection,  $r_m$  is the reflection coefficient of each mirror which is taken to be real valued, and  $z_1$  and  $z_2$  are the lengths of the optical paths traveled by the two beams, respectively. The total electric field at the detector ( $E_D$ ) is given by adding the two individual electric fields from Equation 2.18. Since the detector is unable to respond fast enough, the detector measures the intensity of incident radiation rather than the oscillation of the electric field. For example, a typical bolometer has a frequency response of less than or equal to 100 Hz while a wavelength of 100  $\mu\text{m}$  corresponds to a frequency of 3 THz. Thus, a detector placed at the output of an FTS measures a total intensity at the detector which is proportional to the square of the magnitude of the total electric field [76] and is given by

$$I_o(z) = \frac{c\epsilon_o}{2} |E_T|^2 = c\epsilon_o E_0^2 R_m R T [1 + \cos(2\pi\sigma_o z)] \quad [\text{W/m}^2], \quad (2.19)$$

where  $c$  is the speed of light,  $\epsilon_o$  is the permittivity of free space,  $z = z_1 - z_2$  is the OPD,  $R_m = r_m^2$  is the reflectance of the mirrors, and  $R = r^2$  and  $T = t^2$  are the reflectance and transmittance of the beamsplitter, respectively. In the case of an ideal interferometer, the beamsplitter reflects and transmits 50% of the incident light, and the mirrors are perfect reflectors. The interferogram is seen to be composed of a constant term and a modulation term, which is given by the cosine function. It is customary to ignore the constant term as it contains no spectral information. Considering only the modulated term, the above expression is simplified by substituting  $B(\sigma_o) = c\epsilon_o|E_o|^2$  to describe the intensity of the monochromatic source and may be given by

$$I_o(z) = R_mRTB(\sigma_o)[\cos(2\pi\sigma_o z)] . \quad (2.20)$$

The Fourier transformation of Equation 2.20 is comprised of two symmetric delta functions at  $\pm\sigma_o$ , i.e.  $B(\sigma_o)\delta(\sigma \pm \sigma_o)/2$ , neglecting for the moment the constant amplitude terms  $R_mRT$ . In the monochromatic example, the spectrum  $B(\sigma)$  is only nonzero at frequencies  $\pm\sigma_o$  and is zero elsewhere.

### 2.5.2 Polychromatic/Broad Input Sources

When a spectral source contains more than one frequency component, the linear transform properties of the Fourier transform (Table 2.2) guarantee that the resultant interferogram can be expressed as a superposition of interferograms for many monochromatic sources of different frequencies, i.e.

$$I(z) = R_mRT \int_{-\infty}^{+\infty} B(\sigma) \cos(2\pi\sigma z) d\sigma . \quad (2.21)$$

The above expression, neglecting the constant  $R_m RT$  term for the moment, is simply the cosine Fourier transform of the source spectrum  $B(\sigma)$ . The spectrum can be recovered by the inverse cosine Fourier transform of the interferogram as follows

$$B(\sigma) = \frac{1}{R_m RT} \int_{-\infty}^{+\infty} I(z) \cos(2\pi\sigma z) dz . \quad (2.22)$$

In the ideal case,  $B(\sigma)$  and  $I(z)$  are real valued, allowing a savings of a factor of two by measuring from ZPD to  $+L$  rather than  $-L \leq z \leq +L$ . In practical applications, optical, electronic, mechanical, and sampling effects break the symmetry of the interferogram. Analysis of the resulting asymmetric interferogram requires the use of the complex Fourier transform (Equations 2.9 & 2.8) and the process known as phase correction [20, 30]. Phase correction is discussed in detail in my M.Sc. thesis [20].

## 2.6 FTS Advantages

The FTS possesses several advantages when compared with other types of spectrometer. These include: high throughput (Jacquinot advantage), broad simultaneous spectral coverage ( Fellgett advantage), and intrinsic frequency calibration (Connes advantage), which are discussed in turn below.

### 2.6.1 The Jacquinot Advantage

The high throughput of the FTS is known as the Jacquinot advantage [81]. FTS throughput is defined as the product of the area of the input light beam  $A$  ( $\text{m}^2$ ) and the solid angle  $\Omega$  (sr) contained within the beam; this quantity is also known as the *étendue* or light-grasp. The controlling factor for the throughput is usually the most expensive component of

the spectrometer; in the case of an FTS this is typically the beamsplitter. All interferometers possessing circular symmetry (eg. FTS or Fabry Perot interferometers) have significantly higher throughput, compared with dispersive spectrometers such as grating spectrometers, where the throughput is determined by the narrow entrance and exit slits, whose width can only be increased at the expense of lower resolution. A similar relationship between throughput and resolution exists for an FTS, but it is far less severe as will be shown in §2.7.3.

### 2.6.2 The Fellgett Advantage

The multiplex advantage [80] of an FTS, also known as the Fellgett advantage, is due to the exposure of an interferometer to all spectral components of a signal simultaneously. By comparison, in a dispersive spectrometer [102] only a narrow range of wavelengths are measured by a single detector.

For the case in which the noise is independent of the signal amplitude, the ratio of the FTS signal-to-noise ratio (S/N) compared to that of a grating spectrometer is proportional to the square root of the number of resultant spectral elements [103]. *Ceteris paribus*, an FTS will have a much higher S/N than a grating spectrometer. Moreover, it should be noted that due to the narrow entrance and exit slits of a grating spectrometer [102], the throughput of an FTS is typically two orders of magnitude larger than a grating spectrometer, which leads to an even greater increase in S/N.

Advances in detector array technology allow grating spectrometers to observe entire spectral ranges simultaneously. An FTS, however, can use the same detector arrays to observe, simultaneously, many spatial components of the source, thus retaining a multiplex



advantage [75], which is now spatial rather than spectral. Such a system is known as an imaging FTS (see Chapter 4).

The multiplex advantage of an FTS becomes a multiplex disadvantage when detectors are background limited, i.e. photon or source noise is the dominant noise source. Even under such conditions the FTS retains the Jacquinot advantage (§2.6.1).

### 2.6.3 The Connes Advantage

The Connes advantage [104] is that the intrinsic frequency scale calibration of an FTS spectrum is uniquely determined from the OPD sampling of the interferogram. In comparison, dispersive spectrometers have nonlinear frequency scales which are determined by the fabrication limitations of the dispersive element. Wavelength calibration of such systems requires high-resolution observations of several monochromatic sources and fitting a polynomial to these data which is subsequently used to establish the nonlinear scale. Although it is not required, FTS frequency scale calibration can be verified by a single observation of a monochromatic source such as a laser.

In addition to the absolute frequency calibration, the FTS also presents the best instrumental line-shape of any spectrometer. The FTS ILS is determined by the maximum OPD recorded and is independent of frequency. It is practical to compare, or even subtract, standard reference spectra taken with different FTS instruments. This is even true for very complex reference spectra. By comparison, the same is not true for grating spectrometers, where the ILS is dependent on the fabrication of the dispersive element, the detector size and position within the focal plane, and the wavelength.

## 2.7 Practical Considerations

There are many situations in which the performance of an FTS is less than ideal. This section discusses some of the considerations required in the use of real world FTS instruments.

### 2.7.1 Sampling and Spectral Resolution

The Nyquist sampling theorem [105, 106] states that a DC band-limited signal may be perfectly reconstructed if the data sampling frequency is twice that of the highest spectral content of the signal being sampled. Other conditions on the Nyquist sampling theorem are similar to convergence requirements in a Fourier series and are satisfied given that the interferogram is actually measured. For the sampling of an interferogram, the OPD sampling interval must satisfy the following

$$\Delta z \leq \frac{1}{2\sigma_{band}} \quad [\text{cm}] , \quad (2.23)$$

where  $\Delta z$  is the optical sampling interval (in cm) and  $\sigma_{band}$  is the spectral bandwidth of the signal (in  $\text{cm}^{-1}$ ). For DC band-limited spectra,  $\sigma_{band}$  is equivalent to  $\sigma_{max}$ , the highest spectral frequency component ( $\text{cm}^{-1}$ ). The maximum observable or Nyquist frequency,  $\sigma_{Nq}$ , is given by the relation:

$$\sigma_{Nq} = \frac{1}{2\Delta z} \quad [\text{cm}^{-1}] . \quad (2.24)$$

It is common practice to measure the interferogram in equal increments of optical path difference, which allows use of the FFT algorithm. The FFT algorithm [2] computes the discrete Fourier transform of  $N$  data points on the order of  $N \log_2 N$  operations, as compared

to an order of  $N^2$  operations for the discrete Fourier transform algorithm. Therefore, the FFT provides a time savings on the order of  $\frac{\log_2 N}{N}$ . Proper use of the FFT algorithm in FTS data processing requires at least one unique data point at ZPD. Failure to sample the position of ZPD exactly results in phase errors in the spectrum [20].

The derivation presented in §2.5 for determining the spectrum from the interferogram involved integrating the OPD from  $-\infty$  to  $+\infty$ . In practice, interferograms cannot be measured out to infinity in either direction of OPD and are measured, rather, to a finite maximum OPD, i.e.  $L$ . As a result, independent spectral data points are evenly spaced by a finite interval,  $\Delta\sigma$ , which is given by

$$\Delta\sigma = \frac{1}{2L} \quad [\text{cm}^{-1}]. \quad (2.25)$$

The ILS of an FTS is actually wider than  $\Delta\sigma$ , however, again due to the finite OPD measurement in the interferogram. A finite interferogram can be thought to be an ideal interferogram extended out to  $\pm\infty$ , multiplied by a rectangular function  $\Pi(L)$ . The convolution theorem (Table 2.2) illustrates that the finite truncation of the interferogram results in a sinc function being convolved across the spectrum in the reciprocal Fourier domain [75].

The full width at half maximum (FWHM) of the FTS ILS is given as follows

$$\Delta\sigma_{\text{FTS-FWHM}} \simeq \frac{1.207}{2L} \quad [\text{cm}^{-1}]. \quad (2.26)$$

Thus, FTS spectra have an inherent sinc ILS and the resolution of an FTS is variable depending on the OPD length  $L$  selected for an interferogram.

### 2.7.2 Noise

There are many different sources of noise introduced into the measurement of interferograms. These noise sources can typically be categorized as optical, electrical, mechanical, thermal, and perhaps catastrophic.

Optical noise consists of photon noise and source noise. Photon noise ( $\varsigma_{\text{photon}}$ ) is due to statistical fluctuations in photon arrival which is proportional to the square root of the average rate of photons arrival ( $\bar{n}$  [photons/s]), modified by the Bose-Einstein factor as follows [107,108]

$$\varsigma_{\text{photon}} = \sqrt{\bar{n} \left( \frac{e^{hc\sigma/k_b T}}{e^{hc\sigma/k_b T} - 1} \right)} \quad [\text{photons/s}] , \quad (2.27)$$

where  $h$  is the Planck constant,  $c$  is the speed of light,  $k_b$  is the Boltzmann constant, and  $T$  is the source temperature. The Bose-Einstein correction factor becomes particularly important at long wavelengths. Source noise arises from periodic and random variations in source intensity over time, e.g. the proportional-integral-derivative (PID) oscillations of a controlled blackbody source, and can have contributions of either flat,  $1/f$  spectral distribution, or both [76]. Other sources of optical noise include any optical contribution that does not originate from the desired source such as cosmic rays, spacecraft pointing errors, etc.

Other noise sources can be categorized as Johnson noise, phonon noise, shot noise, and  $1/f$  noise [109]. Johnson noise, which has a flat spectral profile, is associated with the thermal motion of charge carriers in a resistive device, and has a root-mean-square (rms) noise voltage given by

$$V_{J \text{ rms}} = \sqrt{4k_b T R \Delta f} \quad [\text{V}] , \quad (2.28)$$

where  $T$  [K] is the temperature of the resistive component,  $R$  [ $\Omega$ ] is the component resistance, and  $\Delta f$  is the signal bandwidth [Hz]. Thus, Johnson noise can be minimized by narrowing the bandwidth, lowering the temperature of the resistive element, or both. Phonons are quantized lattice vibrations within any solid state device. The statistical variation in phonon distribution effects the thermal conductivity and thus the bolometer operating point. Any variations in phonon flux are thus sensed by the bolometer circuit and result in another electrical noise component [109, 110]. Shot noise results from time-dependent fluctuations in electrical current caused by the quantized electron charge, and occurs frequently in solid-state devices such as tunnel junctions, Schottky diodes, and p-n junctions.  $1/f$  noise, which is known for its  $1/f$  spectral profile, is perhaps the most studied and least understood detector noise source [107]. Poor electrical contacts between a detector and connecting electrodes is a partial explanation of  $1/f$  noise. An empirical expression for  $1/f$  noise is given by [107]

$$i_{1/f \text{ rms}} = a \sqrt{\frac{i_D^\alpha \Delta f}{f^\beta}} \quad [\text{A}] , \quad (2.29)$$

where  $a$  is a proportionality constant,  $\alpha$  and  $\beta$  are constant of value  $\sim 2$  and  $\sim 1$ , respectively,  $i_D$  is the detector current (A), and  $\Delta f$  and  $f$  are the bandwidth and frequency (Hz). The most common method to overcome  $1/f$  noise is to increase the signal modulation frequency such that the  $1/f$  noise falls off.

Ideally, an FTS is designed such that all noise is reduced to the point where photon noise dominates through careful alignment and proper choice of detectors, optics, and readout electronics. Random noise levels may be reduced through improving interferometer stage metrology, source stability (if possible), signal averaging, and reducing digitization

errors. The random noise contribution to the interferogram can never be completely removed but can be minimized through careful FTS design, observation planning, and data processing techniques.

### 2.7.3 Natural Apodization

In the case of a point source located at the input focus of an interferometer, the resulting collimated beam has no divergence and thus the overlap of the recombined beams from the interferometer is independent of OPD. In reality, however, all interferograms suffer from some degree of distortion due to the divergence of radiation within the interferometer. In a real interferometer the entrance aperture has a finite size, meaning that a beam entering the interferometer is divergent and the overlap between the recombined beams depends upon OPD; this leads to the phenomenon known as natural apodization.

Consider light entering an interferometer at an angle  $\alpha$  from the optical axis (see Figure 2.2). Whereas the OPD for on-axis light is simply  $z$ , the off-axis OPD becomes  $z \cos(\alpha)$  (see Appendix A). The resulting interferogram intensity is determined by integrating over the solid angle  $\Omega$ . For a monochromatic source, the interferogram may be given by

$$I(z) = \int_0^{\Omega_M} \cos [2\pi\sigma_o z \cos(\theta)] d\Omega, \quad (2.30)$$

where  $\theta$  ranges from 0 to  $\alpha$  and  $\Omega_M$  is the total solid angle. Using  $d\Omega = \sin\theta d\theta d\phi$  in a spherical coordinate system, the above expression may be evaluated analytically for any  $\alpha$  as follows

$$I(z) = 2\pi [1 - \cos(\alpha)] \text{sinc} \left[ 2\pi\sigma_o z \left( \frac{1 - \cos(\alpha)}{2} \right) \right] \cos \left[ 2\pi\sigma_o z \left( \frac{1 + \cos(\alpha)}{2} \right) \right]. \quad (2.31)$$

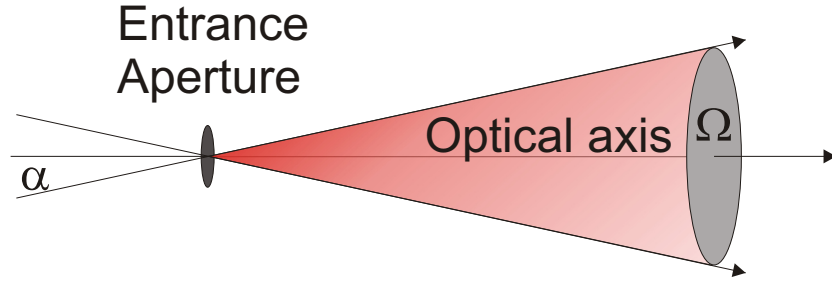


Figure 2.2: Diagram of off-axis light due to a finite sized entrance aperture on an FTS.

In the case where  $\alpha$  is small, two approximations can be made: first, the small angle approximation,  $\cos(\alpha) \approx 1 - \frac{\alpha^2}{2}$ , and, second, a circular aperture at the focus of a collimating mirror has solid angle  $\Omega = \pi\alpha^2$ . The following simplification of Equation 2.31 results in

$$I(z) \approx \Omega \operatorname{sinc} \left[ 2\pi\sigma_o z \left( \frac{\Omega}{4\pi} \right) \right] \cos \left[ 2\pi\sigma_o z \left( 1 - \frac{\Omega}{4\pi} \right) \right]. \quad (2.32)$$

The finite entrance aperture of an interferometer results in the interferogram being multiplied by a sinc function, which is equivalent to the shape of the ILS changing and a shift in the frequency scale of the corresponding spectrum. For a monochromatic source at frequency  $\sigma_o$ , the spectral line appears to be at  $\sigma_o$  for the on-axis signal, but for the most oblique rays with the shortest OPD ( $z' = z \cos(\alpha)$ ) the spectral line will be shifted to  $\sigma_o[1 - \Omega/(2\pi)]$ . Thus the observed line will be centred at  $\sigma_o[1 - \Omega/(4\pi)]$  and will have a width increase of  $\Omega\sigma_o/(2\pi)$ . Therefore, spectral resolution greater than  $\Omega\sigma_o/(2\pi)$  cannot be achieved as the rectangular convolution has broadened all spectral features. Resolving power of an interferometer is given as

$$R = \frac{\sigma}{\Delta\sigma}. \quad (2.33)$$

The limit on spectral resolution can be related to resolving power as follows:

$$R \leq \frac{\sigma}{\left(\frac{\sigma\Omega}{2\pi}\right)} = \frac{2\pi}{\Omega}, \quad (2.34)$$

where the inequality above is known as the Jacquinot criterion [76]. The Jacquinot criterion places an upper limit on the attainable resolving power of an interferometer for a given  $\Omega$ , which in turn is determined from the entrance aperture and feed optics of the interferometer.

For a single pixel FTS in which the detector is placed on-axis, the ILS including divergence is a sinc function convolved with a rectangle function. The situation for off-axis detectors becomes far more complex and is discussed in Chapter 4.

## 2.8 Conclusions

This chapter has introduced the mathematics behind the operation of an FTS. The classical Michelson interferometer design was introduced and the Jacquinot, Fellgett, and Connes advantages of the FTS have been explored. Practical limitations in the application of the FTS in areas such as natural apodization, sampling, noise, symmetry, resolution, finite travel, and finite aperture size have been discussed. The FTS, with its simple opto-mechanical design, broad spectral coverage, high throughput and variable resolution make it the spectrometer of choice for measurements of weak astronomical signals at submillimetre wavelengths as witnessed by the selection of FTS instruments for active missions such as AKARI [89], SCUBA-2 [111], and Herschel [8], and planned missions such as SPICA [90], FIRI [91], and SPIRIT [112].



## Chapter 3

# Fourier Transform Spectrometer

## Beamsplitter Emission

When we are listening to several different tones we can tell them apart, but when we look with our eyes at a mixture of colors we cannot tell the parts from which it was made, because the eye is nowhere near as discerning as the ear in this connection.

However, with a spectroscope we *can* analyze the frequencies of the light waves and in this way we can see the very tunes of the atoms that are in the different stars.

In Chapter 2, key practical aspects of Fourier spectroscopy were reviewed. In this chapter, I explore the effects of beamsplitter phase and emission on the measured interferogram signal; these effects become particularly important at long wavelengths. It is not widely appreciated that in the Mach-Zehnder design, the input beamsplitter can itself be a source of emission which produces a modulated signal component at the output of the interferometer. If this is not properly accounted for in FTS data processing, it will lead to errors in the resulting spectrum. This chapter discusses the theory behind the contribution of FTS beamsplitter emission to the interferogram. A model based on this theory has been developed to allow comparison with experimental data obtained with two FTS instruments that have been shown to exhibit a modulated component of the interferogram due to beamsplitter emission. One of these instruments is the SPIRE FTS [17], and the other is an astronomical MZ-FTS which was developed for ground based observations from the James Clerk Maxwell Telescope (JCMT) [114] similar in design to SPIRE. Unless otherwise stated, the SPIRE FTS will be referred to as SPIRE and the other FTS will be referred to as the MZ-FTS.

### 3.1 Dual Input/Output FTS

All FTS interferometers have two input ports and two output ports. In the case of a Michelson interferometer, each port is a superposition of both an input and an output port. One consequence of the Michelson interferometer is that 50% of the input flux is returned to the source. By comparison, the MZ-FTS instrument design [14] ensures independent access to all four ports of the interferometer. Figure 3.1 illustrates an MZ-FTS where the

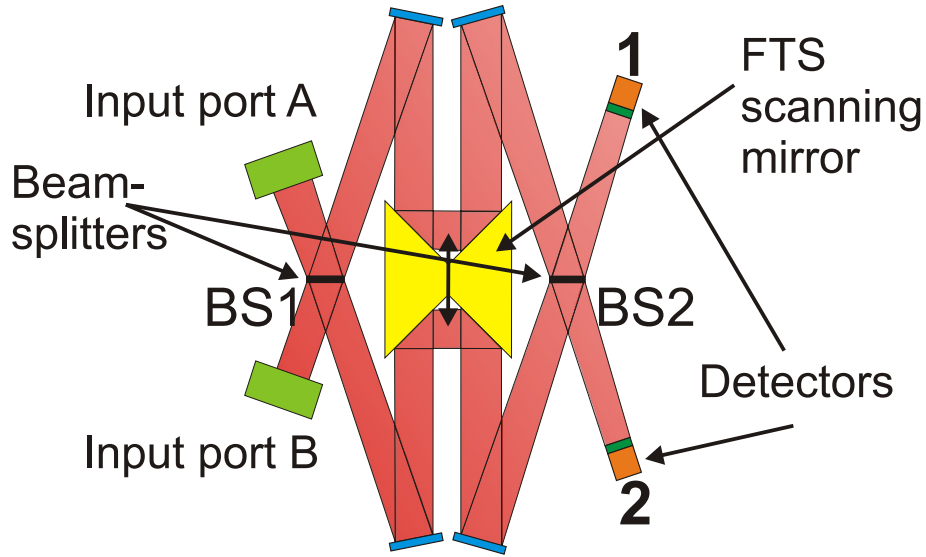


Figure 3.1: Diagram of a Mach-Zehnder FTS [14].

input ports are labeled A and B, and the output ports are labeled 1 and 2. In practice, this design is implemented using two beamsplitters [115], however the same result could be implemented with one large beamsplitter. A key advantage of the MZ-FTS design is that all input radiation reaches the output ports with none returning to the source. A schematic of the SPIRE FTS is shown in Figure 3.1, where input A represents the input port viewing the sky and a spectrometer calibration source is positioned at the second input port (B).

Suppose sources of frequency  $\sigma_o$  with electric field intensity  $E_A$  at input A and  $E_B$  at input B are incident on the FTS shown in Figure 3.1. The input irradiance of A is  $I_A = \frac{c\epsilon_o}{2}|E_A|^2$  while that of B is  $I_B = \frac{c\epsilon_o}{2}|E_B|^2$  (Equation 2.19). Each output port of the FTS sees each of the input ports through one of two combinations of optical paths, either a symmetric or an asymmetric combination. The symmetric modulation involves each of the interfering beams being both reflected and transmitted by a beamsplitter once. The

asymmetric modulation involves one beam being reflected by a beamsplitter twice whereas the other interfering beam is transmitted by a beamsplitter twice. The irradiance at each output port due to the symmetric optical paths, i.e. output port 1 due to input B and that of output port 2 due to input A, is comparable to that given by Equation 2.19. The output irradiance observed for the asymmetric optical paths, however, differs from the form of Equation 2.19. The total irradiance at either output for frequency  $\sigma_o$  including both inputs is the superposition of that expected from either source independently and is given by

$$I_1(z, \sigma_o) = I_A R_m [R^2 + T^2 + 2RT \cos(2\pi\sigma_o z + 2\Phi)] + 2I_B R_m RT [1 + \cos(2\pi\sigma_o z)] \quad , \quad (3.1)$$

and

$$I_2(z, \sigma_o) = I_B R_m [R^2 + T^2 + 2RT \cos(2\pi\sigma_o z - 2\Phi)] + 2I_A R_m RT [1 + \cos(2\pi\sigma_o z)] \quad , \quad (3.2)$$

where the substitution of  $\Phi = \rho - \tau$  is made (see Equations B.1 & B.2, Appendix B.1 for further details). The extension of Equations 3.1 & 3.2 to all frequencies is given by

$$I_1(z) = \int_{-\infty}^{+\infty} E_A^2(\sigma) RT e^{+i2\Phi} e^{i2\pi\sigma z} d\sigma + \int_{-\infty}^{+\infty} E_B^2(\sigma) RT e^{i2\pi\sigma z} d\sigma \quad , \quad (3.3)$$

and

$$I_2(z) = \int_{-\infty}^{+\infty} E_B^2(\sigma) RT e^{-i2\Phi} e^{i2\pi\sigma z} d\sigma + \int_{-\infty}^{+\infty} E_A^2(\sigma) RT e^{i2\pi\sigma z} d\sigma \quad , \quad (3.4)$$

where the  $c\epsilon_o/2$ ,  $R_m$ , and unmodulated terms have been omitted for clarity.

Conservation of energy dictates that the total irradiance of any one source should be found to propagate through the FTS, provided that there is no absorption within it.

Hence, the sum of the interferogram components at each output should be equivalent to the irradiance, if measured, at the input as follows

$$\begin{aligned} [I_1(z) + I_2(z)] \Big|_{E_B=0} &= I_A \\ [I_1(z) + I_2(z)] \Big|_{E_A=0} &= I_B \end{aligned} \quad , \quad (3.5)$$

where it is assumed that the other input is not contributing to the signal. Following the derivation of Carli et al. [116] which assumes perfect mirrors and beamsplitters, i.e.  $R_m = 1$  and  $R + T = 1$ , conservation of energy (Equation 3.5) may be used to determine the beamsplitter phase shift  $\Phi$  as follows

$$\Phi = n\pi + \pi/2 \quad , \quad (3.6)$$

where  $n$  is any integer (see Equation B.3, Appendix B.2 for further details). The phase difference between signals at each output port for a given input, i.e.  $2\Phi$  (Equations 3.3 & 3.4), is ideally  $\pi$ ; hence, while at ZPD, one output exhibits total *constructive* interference, while the other output exhibits total *destructive* interference. The complementary nature of the input and output ports is shown in Figure 3.2. This figure presents measurements obtained with the SPIRE FTS viewing blackbody sources at different temperatures. The upper row of the figure demonstrates the complementary nature of the two output ports for interferograms in which the input B (SCAL) is the dominant radiant source. It can be clearly seen that the SLW (left) and SSW (right) interferograms exhibit a  $\sim\pi$  phase difference, as expected. The lower row in Figure 3.2 shows the corresponding data for interferograms in which the input A (Cold Blackbody) is the dominant radiant source, again showing the  $\sim\pi$  phase difference. The columns of the figure demonstrate the complementary nature of the output as a function of input port dominance, and again show the  $\sim\pi$  phase difference.

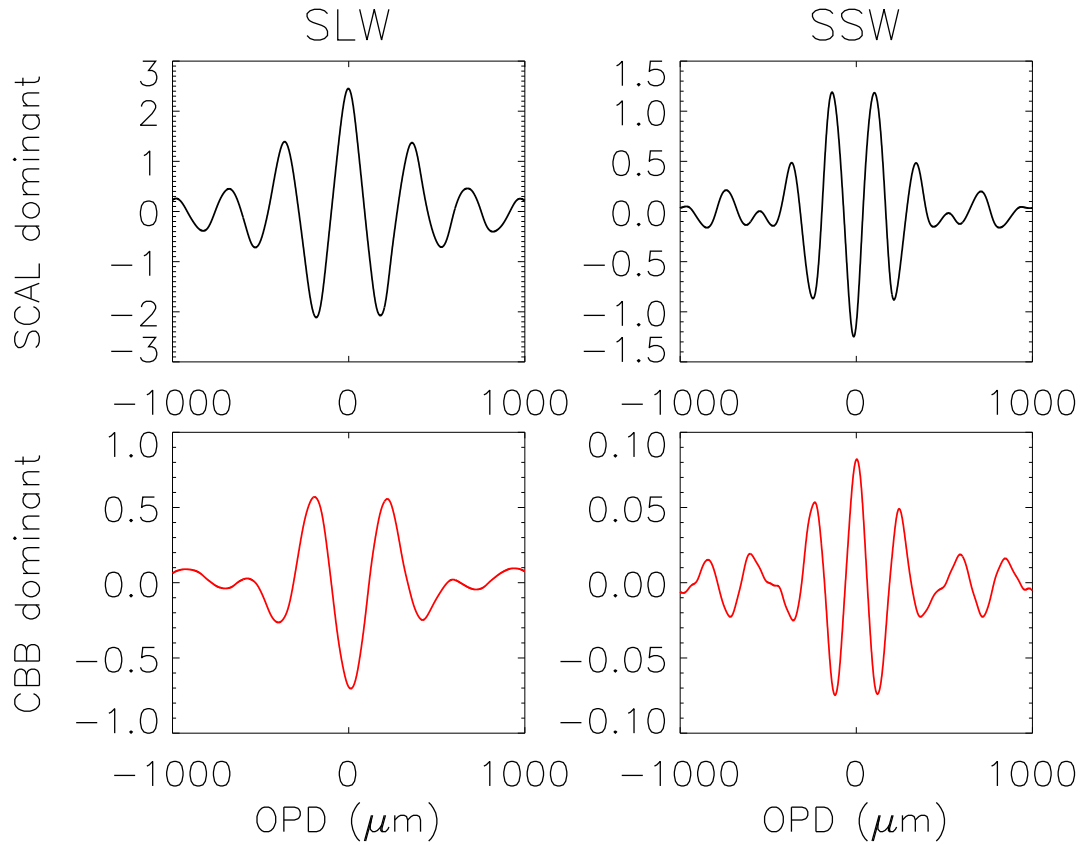


Figure 3.2: FTS interferograms with either input A dominant (top row) or input B dominant (bottom row) for output 1 (left column) and output 2 (right column). These interferograms were recorded during SPIRE PFM testing and illustrate the complementary input/output of an FTS.

## 3.2 FTS Port Compensation

The reciprocal nature of the source modulation for each input port at a given output port lends itself to an FTS technique known as port compensation or port balancing. For broad-band/continuum observations, the challenging dynamic range requirements of the interferogram signal near ZPD can be reduced by placing a broadband spectral source at the second, complementary, FTS input port. Port compensation is particularly advantageous in cases where blackbody emission from the focusing optics of an instrument produces a radiative background which dominates a much weaker source signal, as is often the case in FIR and submm astronomy. Ground based observations are limited by the background emission from the Earth's atmosphere. Although space based observations are performed above the atmosphere, they may still be compromised by the thermal emission from the telescope which imposes a photon noise limit; such is the case for Herschel [34].

Ideally, the second FTS input port of SPIRE would view the Herschel telescope looking at a dark region of sky, providing a background nearly identical to the undesired background of the primary input port. However, the requirement of having the second input looking at the dark sky would limit the observation range for the SPIRE FTS. One could argue that no such dark reference position exists, especially for deep galactic observations. Moreover, due to the volume limited confines of a space instrument, this configuration is not practical for Herschel. To provide a suitable compensating background, the SPIRE design calls for use of an internal calibration source (SCAL), located at the pupil, whose radiant flux can be adjusted in flight to compensate for the emission from the passively cooled telescope optics. The application of port compensation through the use of SCAL

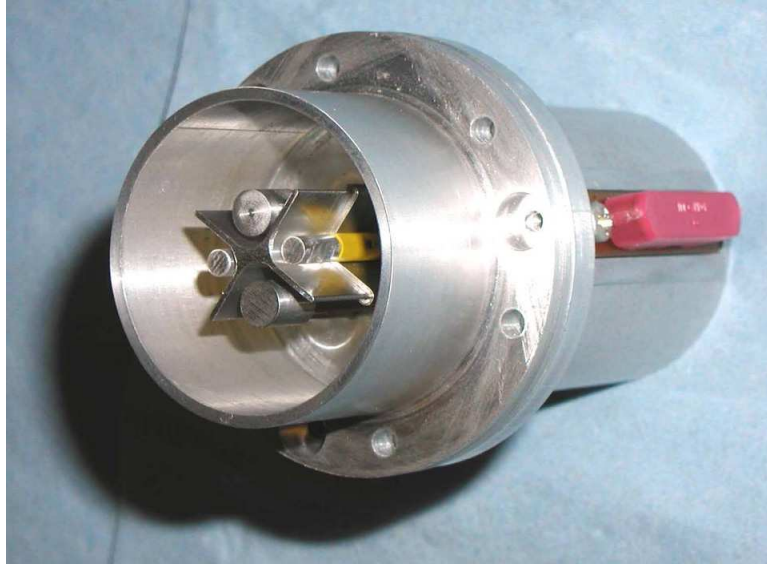


Figure 3.3: Image of an SCAL prototype. *Image: Cardiff School of Physics and Astronomy.*

allows the interferogram dynamic range to be optimized for measurements of astronomical sources.

Although the Herschel primary mirror is manufactured to tight performance specifications, it will not be possible to determine the temperature and emissivity of the telescope accurately until after launch. The passively cooled telescope primary mirror is expected to have a temperature of 80 K and an emissivity of 0.02 [6]. A telescope of higher emissivity will radiate more efficiently than one of lower emissivity, and thus will cool to a lower equilibrium temperature. However, even at the higher temperature, the lower emissivity telescope is preferred due to the fact that the total flux emitted in this case is lower than for the high emissivity, low temperature, telescope. Regardless, a radiative background power of several pW is expected to be incident on the SPIRE FTS from the telescope primary mirror emission in the SPIRE spectral band [13, 117] (see Chapter 5). Therefore, SCAL



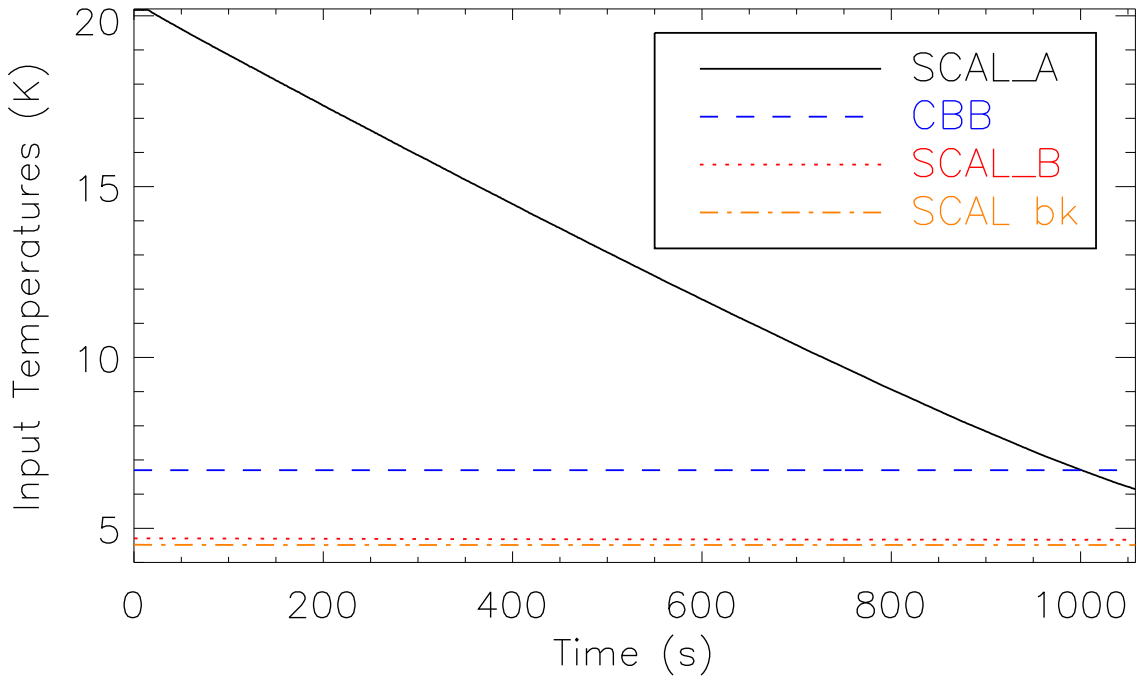


Figure 3.4: Input temperatures of the CBB and SCAL (SCAL\_A, SCAL\_B, and SCAL background) while medium-resolution ( $\Delta\sigma = 0.25 \text{ cm}^{-1}$ ) interferograms were recorded with SPIRE.

must have sufficient variability to accommodate this uncertainty. The SCAL input port is located at a SPIRE pupil, where its effective emissivity is determined by a geometric fill factor. SCAL employs two sources, SCAL\_A and SCAL\_B, that fill 4% and 2% of the pupil area, respectively. The two redundant sources fill 6% of the pupil and the remaining 88% of the pupil area is filled by the background, both at the ambient instrument background temperature [117]. An image of an SCAL prototype is shown in Figure 3.3.

One of the experiments performed during SPIRE PFM testing was to hold the CBB, illuminating the primary input port, at a constant temperature while heating/cooling SCAL across its range of temperature settings. Figure 3.4 illustrates the input temperatures for one such experiment where the CBB was maintained at 6.7 K (dashed curve) and

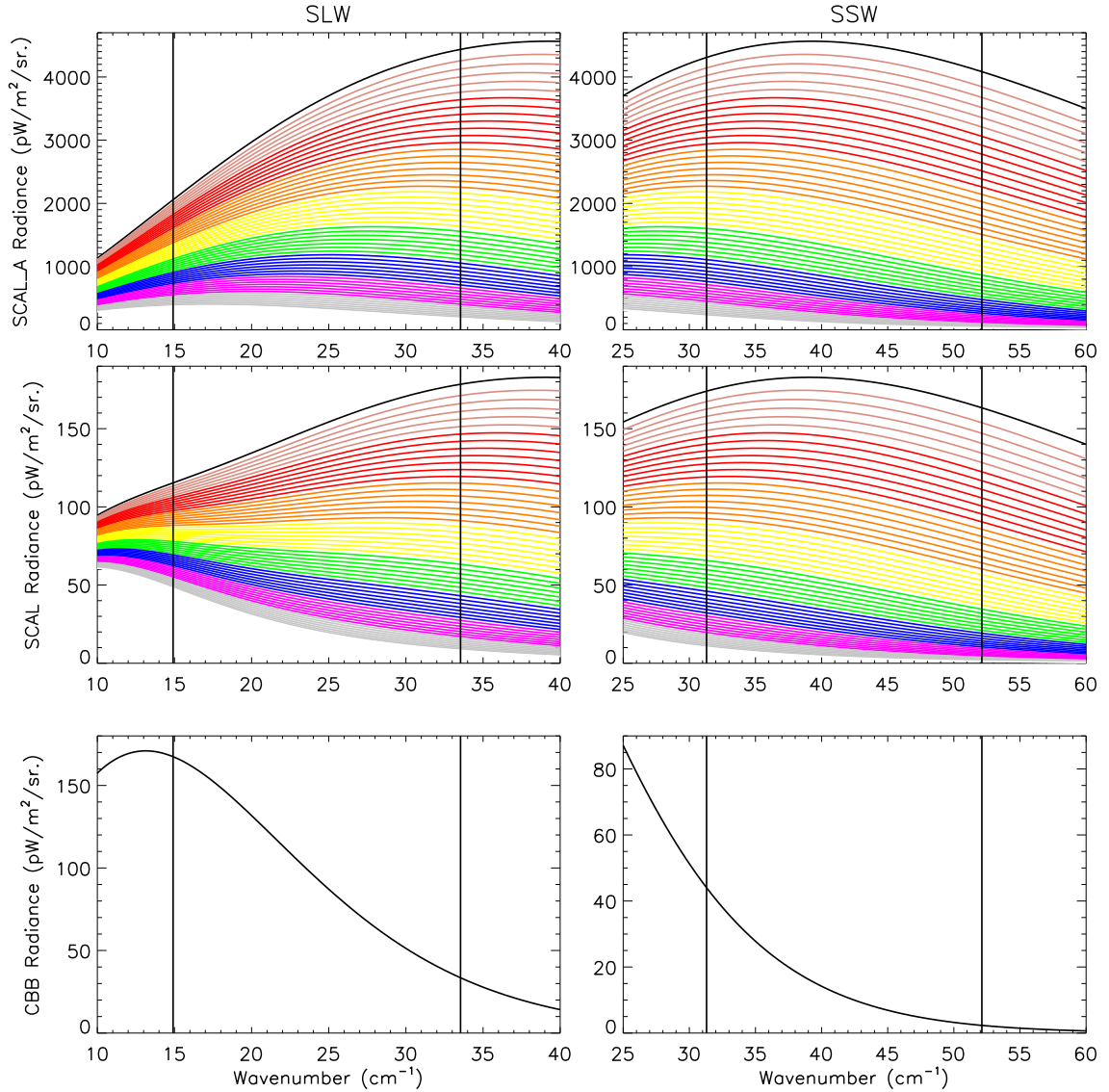


Figure 3.5: Calculated spectral radiance for the CBB and SCAL temperatures shown in Figure 3.4. The upper row shows the radiance for a 100% emissive SCAL\_A. The middle row shows the proportional sum of SCAL\_A, SCAL\_B, and the SCAL background (4%, 2%, and 94%, respectively) which is input to the secondary input port of SPIRE. The lower plot shows the radiance for the CBB which is input to the sky input port of SPIRE.

SCAL\_A was cooled from 20.2 K to 6.1 K (solid curve) while medium-resolution interferograms were recorded. The calculated spectral radiances for each input source, and for each scan, based on these temperatures, are shown in Figure 3.5. The spectral radiance for the SCAL input port (middle row of Figure 3.5) is determined via a geometric ratio of the blackbody contributions of SCAL\_A, SCAL\_B, and the SCAL background (BK), respectively, as follows

$$\begin{aligned}
 B_{SCAL}(\sigma) = & 0.04 \times P(\sigma, T_{SCAL\_A}) \\
 & + 0.02 \times P(\sigma, T_{SCAL\_B}) \ , \\
 & + 0.94 \times P(\sigma, T_{BK})
 \end{aligned}
 \tag{3.7}$$

where the coefficients represent the geometric pupil fill ratios for each component of SCAL, and  $P(\sigma, T_x)$  represents the Planck blackbody radiance evaluated over the frequency interval of interest at the SCAL A, B, and background temperatures. As the flux difference between the two input ports of the FTS under port compensation decreases (i.e. while SCAL\_A cools such that the radiant flux from SCAL matches that of the CBB, cf. the middle and lower row of Figure 3.5) the interferogram modulation amplitude is expected to decrease. Due to differences in the total spectral radiance of each SPIRE input during PFM testing, interferogram amplitude under port compensation is not expected to reach zero. The effectiveness of port compensation in SPIRE is shown in Figure 3.6 which depicts the maximum amplitude of the modulated component of the interferogram corresponding to the input configurations depicted in Figures 3.4 & 3.5, for both modeled and measured data sets. As expected, interferogram modulation does not reach zero for any of the SCAL settings shown and the optimal SCAL settings for one SPIRE array are not the optimal settings for the other array; this is indicated by the horizontal displacement between the

vertical bars in the figure.

The central regions of the interferograms recorded while SCAL\_A cooled are shown in Figure 3.7, where a loss of even symmetry and non-zero modulation amplitude in the recorded interferograms under port compensation are seen. Imperfect spectral nulling or an additional component not associated with either FTS input port are two potential causes of the observed residual interferogram modulation under port compensation. Differences between the spectral radiance of each FTS input may easily explain the non-zero modulation amplitude, but they cannot explain the loss of even symmetry in the recorded interferogram. Non-ideal beamsplitter characteristics provide the explanation for both the non-zero modulation amplitude and loss of symmetry under port compensation. In the case of SPIRE, both a spectral input mismatch and non-ideal beamsplitter phase are observed to effect the symmetry of recorded interferograms. To investigate this phenomena, I undertook a detailed study of the effects of non-ideal beamsplitter characteristics on FTS port compensation. These characteristics and results of this study are discussed in detail in §3.3 – §3.6.

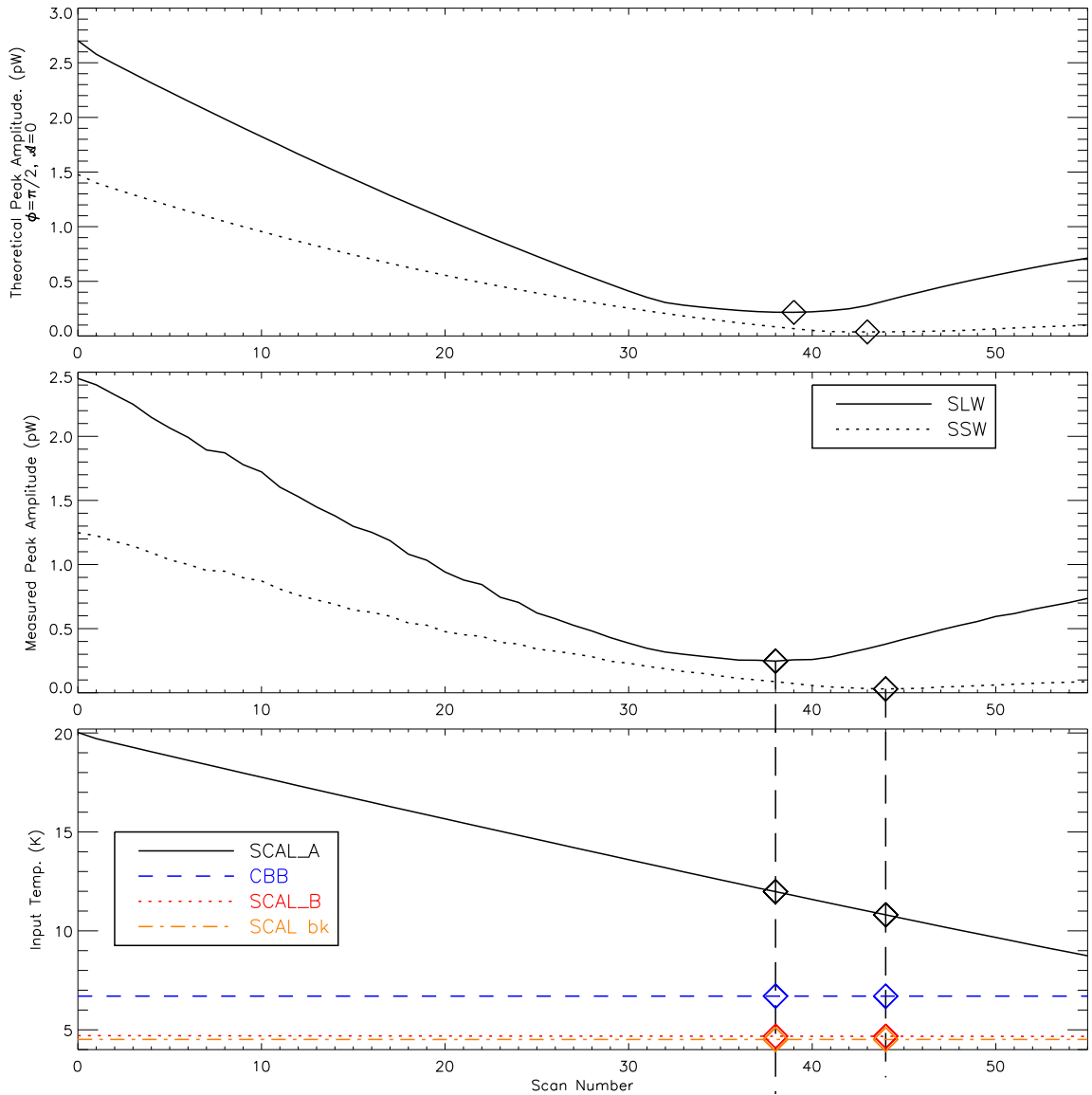


Figure 3.6: Theoretical model (top) and measured peak interferogram modulation (middle) for SCAL\_A cooling and constant CBB temperature. The bottom plot shows the temperatures corresponding to each of the above cases in the top and middle. The diamonds in the upper and middle plots represent the minimum amplitude of each curve, i.e. optimal port compensation. The diamonds in the lower plot show the input temperatures corresponding to the optimal port compensation measurement for each detector array, with dashed vertical bars connecting the temperatures with the interferogram measurement. In both the theoretical model and the measured data, optimal port compensation occurs at different input settings for each detector array.

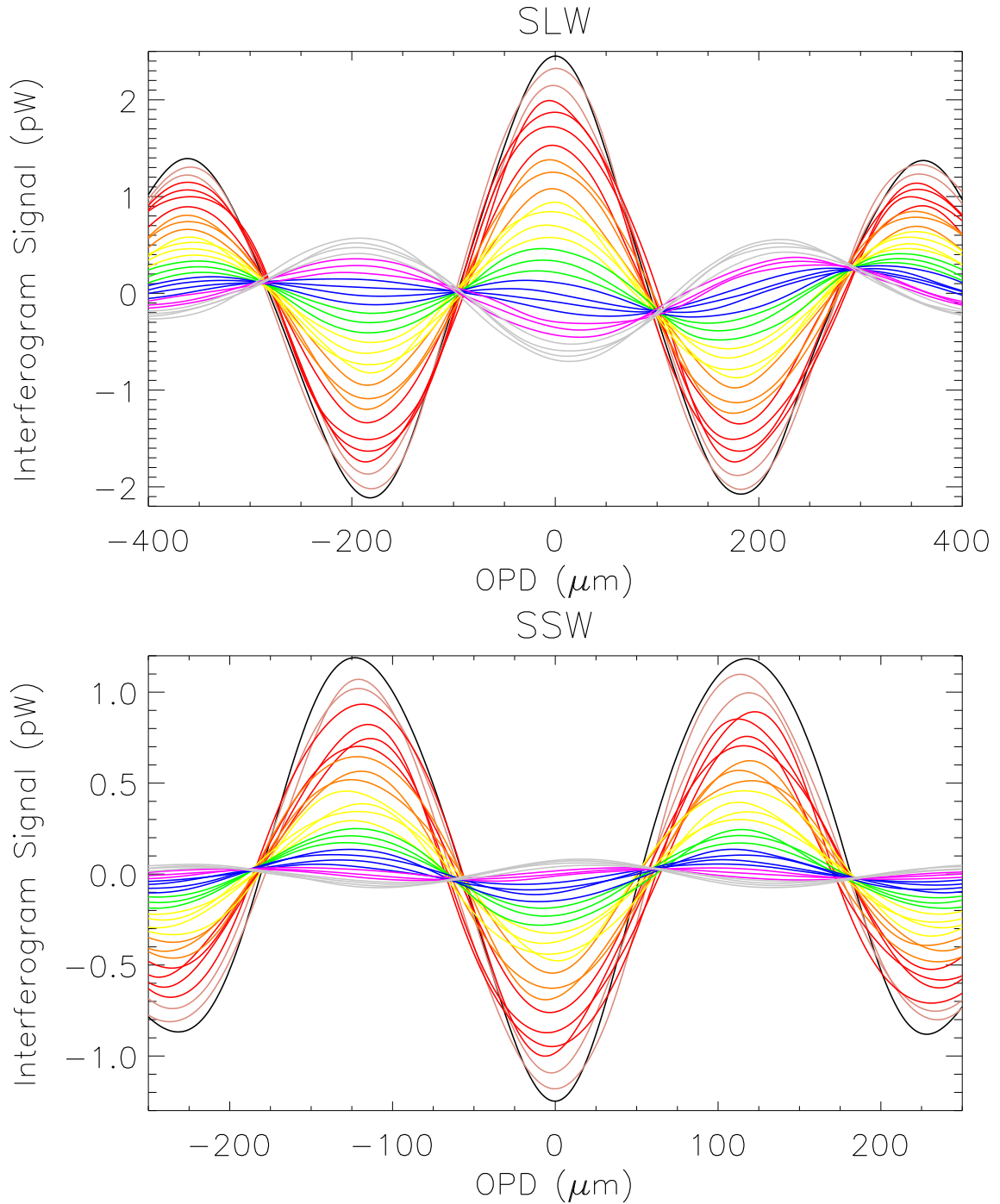


Figure 3.7: Interferogram signal observed while cooling SCAL-A and holding the CBB at constant temperature. As the interferograms modulation amplitude decreases, optimal port compensation is approached. Under optimal port compensation (see Figure 3.10) the even symmetry of the interferogram is lost and the interferogram amplitude is seen to be non-zero.

### 3.3 Beamsplitter Emission Theory

Using silvered glass as an optical medium, Hamy [118] demonstrated the importance of the phase components of an optical device's reflection and transmission coefficients on the symmetry of transmission and reflection fringes. While the following discussion is restricted to FTS beamsplitters, other devices such as mirrors, optical filters, semi-transparent metal films, combinations of mirrors and prisms, etc., may be considered under a similar framework [119]. Consider a beamsplitter with transmission and reflection coefficients given by  $r_1 e^{i\rho_1}$  and  $t_1 e^{i\tau_1}$  for one side and  $r_2 e^{i\rho_2}$  and  $t_2 e^{i\tau_2}$  for the other. The Hamy phase parameter (expressed here as  $2\Phi$  for the convenience of this discussion) is important in evaluating the reflection and transmission fringe distribution, and is given by

$$2\Phi = (\rho_1 - \tau_1) + (\rho_2 - \tau_2) . \quad (3.8)$$

For identical behaviour on both sides of the beamsplitter, Equation 3.8 reduces to  $\Phi = \rho - \tau$  (explaining the use of  $2\Phi$  notation). The application of conservation of energy arguments allowed Dufour to determine restrictions on the range of allowed values of  $2\Phi$ , and hence restrictions on the allowed values of  $\Phi$ , for given reflection and transmission amplitudes using a graphical method in 1950 [120]. This restriction was refined and expressed analytically by Cownie in 1957 [121]. More recently, Troitskii (2002) has extended this work for generic optical two-port devices [122]. For a given optical surface, reflectance ( $R$ ), transmittance ( $T$ ), and absorption ( $\mathcal{A}$ ), are related as follows

$$R_n + T_n + \mathcal{A}_n = 1 , \quad (3.9)$$

where the subscript  $n$  indicates an optical surface or element,  $R_n = r_n^2$ , and  $T_n = t_n^2$ . Assuming that  $t_1 = t_2 = t$ , i.e. that a device is optically reciprocal [102], a restriction on  $2\Phi$  is given by the following inequality [123]

$$\cos(2\Phi) \leq \frac{t^4 - 2t^2 + (1 - r_1^2)(1 - r_2^2)}{2t^2(r_1 r_2)}. \quad (3.10)$$

A knowledge of some of the parameters in Equation 3.10 grants exploration of the allowed range for  $\Phi$ . Equation 3.10 may also be expressed including absorption as follows [121]

$$\cos(2\Phi) \leq \frac{\mathcal{A}_1 \mathcal{A}_2 - (r_1^2 + r_2^2)t^2}{2t^2(r_1 r_2)}. \quad (3.11)$$

In the special case of  $r_1 = r_2$ , it follows that  $\mathcal{A}_1 = \mathcal{A}_2$  and

$$|\cos(\Phi)| \leq \frac{\mathcal{A}}{2tr}. \quad (3.12)$$

This result agrees with Carli et al. [116] who use a conservation of energy argument for an isothermal FTS instrument. Figure 3.8 illustrates the allowed values of  $\Phi$  for symmetric beamsplitters ( $\mathcal{A}_1 = \mathcal{A}_2$ ) over a range of transmittance values typical of an FTS instrument. If a beamsplitter has zero absorption both Figure 3.8 and Equation 3.11 confirm that  $\Phi = \pi/2$ .

By its very nature, an ideal beamsplitter has a reflectance and transmittance of 50%, and zero absorption. In practice, however, some absorption will occur within the beamsplitter. Following Kirchoff's law of thermal radiation [124], any radiation absorbed by a beamsplitter must be re-radiated. While absorption and radiative emission from both beamsplitters in the MZ-FTS design contribute to the total flux received at either output, it is only the emission from the first beamsplitter that can contribute to the modulated interferogram signal [116]. While at visible wavelengths there is essentially zero emission at



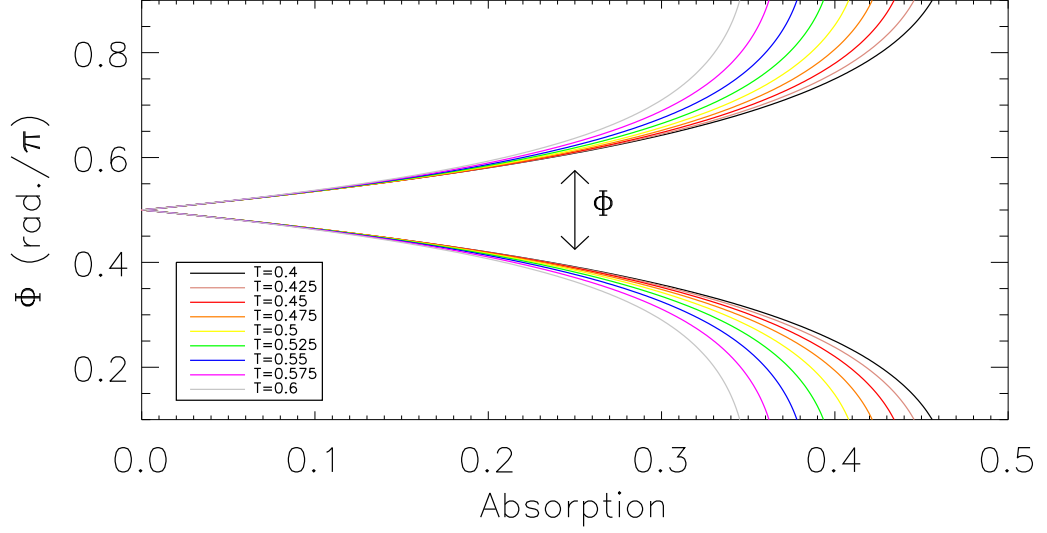


Figure 3.8: Range of acceptable values of  $\Phi$  for  $\mathcal{A}_1 = \mathcal{A}_2$  and  $0.4 \leq T \leq 0.6$ . Angles shown are in radians divided by  $\pi$ , i.e.  $\pi/2$  is shown as 0.5.

room or cryogenic temperatures, a study of the Planck function at these temperatures shows that there is non-zero emission at submm wavelengths. Indeed, the cosmic background radiation ( $T_{\text{CBR}} = 2.728$  K) peaks at 1.062 mm [125].

For spectra  $E_A(\sigma)$  in input port A,  $E_B(\sigma)$  in input port B, and  $E_{\text{BS1}}(\sigma)$  from BS1, the modulated interferogram observed at either output port of the FTS is no longer accurately expressed by Equations 3.3 & 3.4 [35]. The correct representation must include the beamsplitter emission and phase as follows

$$\begin{aligned}
 I_1(z) = & \int_{-\infty}^{+\infty} E_B^2(\sigma) RT e^{i2\pi\sigma z} d\sigma \\
 & + \int_{-\infty}^{+\infty} E_A^2(\sigma) RT e^{+i2\Phi} e^{i2\pi\sigma z} d\sigma \quad , \\
 & + \int_{-\infty}^{+\infty} E_{\text{BS1}}^2(\sigma) \sqrt{RT} e^{+i\Phi} e^{i2\pi\sigma z} d\sigma
 \end{aligned} \tag{3.13}$$

and

$$\begin{aligned}
I_2(z) = & \int_{-\infty}^{+\infty} E_A^2(\sigma)RT e^{i2\pi\sigma z} d\sigma \\
& + \int_{-\infty}^{+\infty} E_B^2(\sigma)RT e^{-i2\Phi} e^{i2\pi\sigma z} d\sigma \quad , \\
& + \int_{-\infty}^{+\infty} E_{BS1}^2(\sigma)\sqrt{RT} e^{-i\Phi} e^{i2\pi\sigma z} d\sigma
\end{aligned} \tag{3.14}$$

where, again, the  $c\epsilon_o/2$ ,  $R_m$ , and unmodulated terms have been omitted for clarity. For a well-balanced interferometer (i.e.  $E_A(\sigma) \approx E_B(\sigma)$ ), the  $E_B$  integral complements the  $E_A$  integral, because of the  $2\Phi$  term (ideally  $\pi$ ). In this situation, the  $E_{BS1}(\sigma)$  term may dominate the observed signal, producing an interferogram with odd symmetry. Equations 3.13 & 3.14 may be expressed in terms of sinusoidal Fourier transforms as follows

$$\begin{aligned}
I_1(z) = & \int_{-\infty}^{+\infty} E_B^2(\sigma)RT \cos(2\pi\sigma z) d\sigma \\
& + \int_{-\infty}^{+\infty} E_A^2(\sigma)RT \cos[2\Phi(\sigma)] \cos(2\pi\sigma z) d\sigma \\
& - \int_{-\infty}^{+\infty} E_A^2(\sigma)RT \sin[2\Phi(\sigma)] \sin(2\pi\sigma z) d\sigma \quad , \\
& + \int_{-\infty}^{+\infty} E_{BS1}^2(\sigma)\sqrt{RT} \cos[\Phi(\sigma)] \cos(2\pi\sigma z) d\sigma \\
& - \int_{-\infty}^{+\infty} E_{BS1}^2(\sigma)\sqrt{RT} \sin[\Phi(\sigma)] \sin(2\pi\sigma z) d\sigma
\end{aligned} \tag{3.15}$$

and

$$\begin{aligned}
I_2(z) = & \int_{-\infty}^{+\infty} E_A^2(\sigma)RT \cos(2\pi\sigma z) d\sigma \\
& + \int_{-\infty}^{+\infty} E_B^2(\sigma)RT \cos[2\Phi(\sigma)] \cos(2\pi\sigma z) d\sigma \\
& + \int_{-\infty}^{+\infty} E_B^2(\sigma)RT \sin[2\Phi(\sigma)] \sin(2\pi\sigma z) d\sigma \quad . \\
& + \int_{-\infty}^{+\infty} E_{BS1}^2(\sigma)\sqrt{RT} \cos[\Phi(\sigma)] \cos(2\pi\sigma z) d\sigma \\
& + \int_{-\infty}^{+\infty} E_{BS1}^2(\sigma)\sqrt{RT} \sin[\Phi(\sigma)] \sin(2\pi\sigma z) d\sigma
\end{aligned} \tag{3.16}$$

Phase, by definition, is of odd symmetry in the frequency domain, which means that the  $\sin[n\Phi(\sigma)] \sin(2\pi\sigma z)$  integrals above (where  $n = 1, 2$ ) are non-zero, i.e. the symmetry is even

in  $\sigma$ , but remains odd in  $z$ . In the event that  $\Phi \neq \pi/2$ , the interferogram has two sources of odd symmetry. The input component with a  $\pm 2\Phi$  phase term will have both even and odd contributions with amplitudes proportional to  $\cos(\pm 2\Phi)$  and  $\sin(\pm 2\Phi)$ , respectively. The beamsplitter contribution will also have both even and odd interferogram contributions with amplitudes proportional to  $\cos(\pm\Phi)$  and  $\sin(\pm\Phi)$ , respectively. For  $\Phi \gtrsim \pi/2$ ,  $\sin \Phi > 0$  and  $\sin 2\Phi < 0$  whereas for  $\Phi \lesssim \pi/2$ ,  $\sin \Phi > 0$  and  $\sin 2\Phi > 0$ . Therefore, the odd interferogram components due to the secondary output port and beamsplitter will be of opposing sign only if  $\Phi \gtrsim \pi/2$ .

Although zero absorption implies zero emission and a beamsplitter with zero absorption must have  $\Phi = \pi/2$  according to Equation 3.6, it does not necessarily follow that  $\Phi = \pi/2$  implies zero absorption in the beamsplitter. It is evident from Figure 3.8 that  $\Phi = \pi/2$  is a valid solution for all beamsplitter  $\mathcal{A}$  values considered practical for an FTS, and a beamsplitter emission component may be present in interferograms where  $\Phi = \pi/2$ . Importantly, the only component of odd symmetry in the interferogram when  $\Phi = \pi/2$  is due to the beamsplitter emission. Although the interferogram will appear asymmetric, the imaginary component of the spectrum may be used to perform a preliminary correction, and remove this component from the spectrum, if the Fourier transform is computed with a correct knowledge of ZPD. This becomes increasingly difficult if other phase errors are also present in the spectrum.

### 3.4 SPIRE Beamsplitter Emission

As discussed earlier, beamsplitter phase/emission has been observed in port compensation interferograms recorded with the SPIRE FTS during PFM testing. This section will identify interferogram and spectral features indicative of non-ideal beamsplitter performance in SPIRE. §3.7 discusses the removal of beamsplitter phase/emission from these interferograms.

Figure 3.9 shows the spectral phase for the SPIRE interferograms shown in Figure 3.7. The phase for the SCAL dominated interferograms is seen to be flat and centred about  $0^\circ$ , but the spectral phase for the CBB dominated scans, i.e. those interferograms from the end of the test run after SCAL had cooled, has clearly not reached  $180^\circ$ . Moreover, the phase for interferograms approaching optimal port compensation is at intermediate values between  $0^\circ$  and  $180^\circ$  and is slowly varying. As stated in §3.2, inspection of the interferogram signal under conditions approaching optimal port compensation (see Figure 3.7) reveals a loss of the even symmetry characteristic of FTS interferograms. This is demonstrated in Figure 3.10 where only the input dominant and optimal port compensation interferograms of Figure 3.7 are shown. As discussed in §3.3, in addition to the symmetric interferogram contributions from both input ports, there are two potential interferogram contributions having odd symmetry. One component is from the  $\pm 2\Phi$  phase shifted input port, and the other is caused by emission from the FTS beamsplitter.

Interferograms relating to the SCAL dominant and CBB dominant cases do not appear to be symmetric about the same ZPD. Figure 3.11 illustrates the OPD shift observed between input A and input B dominant interferograms. Using a mean wavelength for each

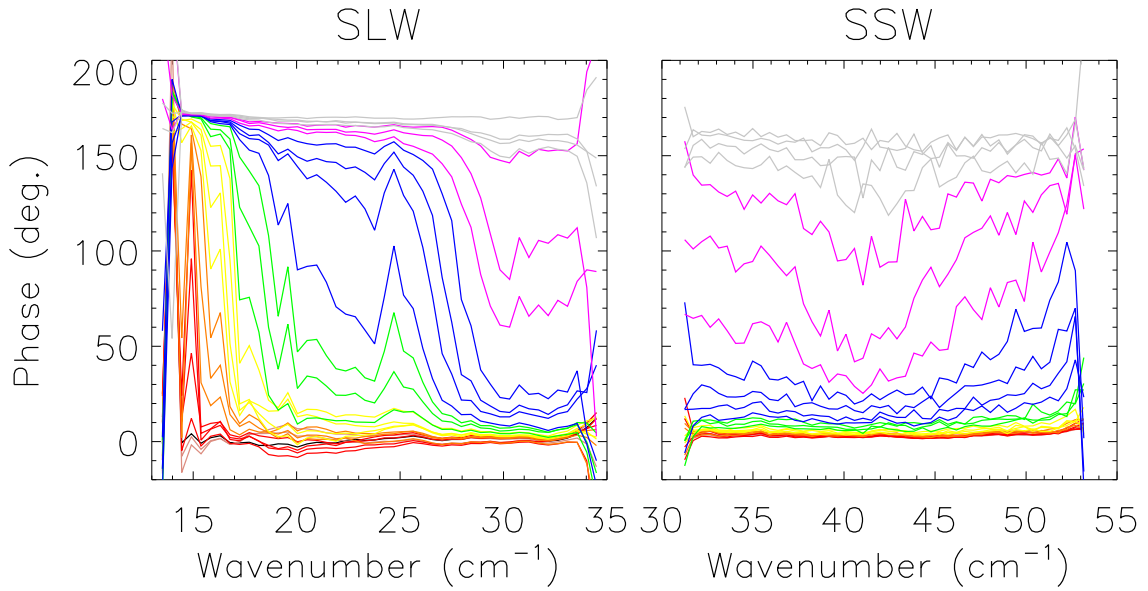


Figure 3.9: Spectral phase for interferograms recording the port compensation transition shown in Figure 3.7 using the same identification scheme.

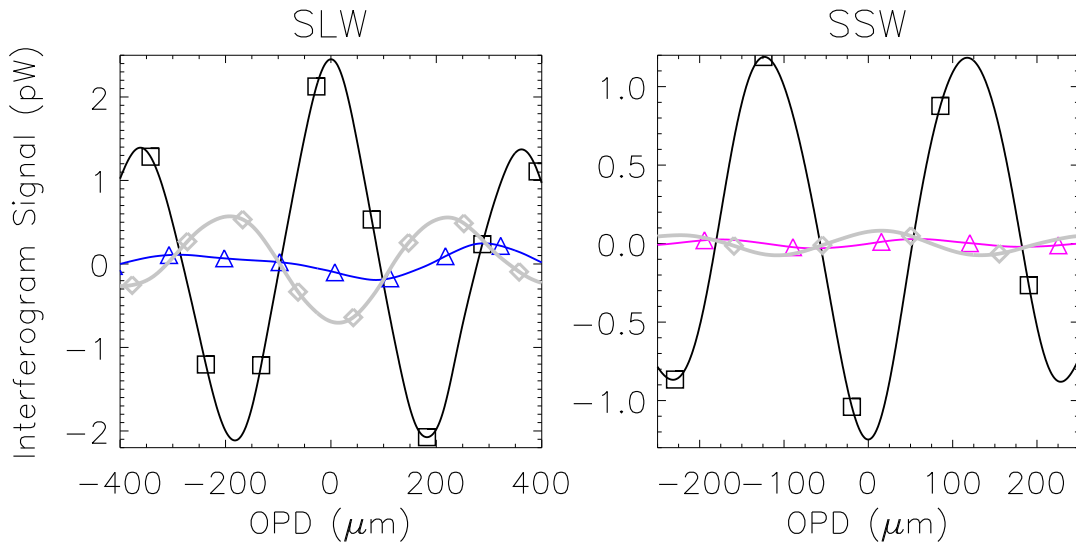


Figure 3.10: Interferograms 0, 38, and 54 (SLW) and 0, 44, and 54 (SSW) from Figure 3.7 illustrating SCAL dominance (squares, scan 0), CBB dominance (diamonds, scan 54), and port compensation (triangles, scan 38–SLW, 44–SSW) in SPIRE FTS observations.

Table 3.1: Experimentally determined beamsplitter  $\Phi$  and  $\mathcal{A}$  for the SPIRE FTS. The values shown are obtained from analysis of interferograms recorded with 13 SLW detectors and 31 SSW detectors.

Array	$\Phi$	$2\Phi/2$	$\mathcal{A}_{\min}$
SLW	$99.6^\circ \pm 7.0^\circ$	$95.1^\circ \pm 2.7^\circ$	$0.04 \pm 0.03$
SSW	$97.2^\circ \pm 9.2^\circ$	$100.5^\circ \pm 4.0^\circ$	$0.09 \pm 0.04$

band determined by the frequency centroid of the spectrum, the shift in interferogram OPD can be used to determine a mean value for  $2\Phi$ . Using this method, values of  $\Phi = 95.5^\circ \pm 3.4^\circ$  for SLW detector C3, and  $\Phi = 101.6^\circ \pm 5.3^\circ$  for SSW detector D4 were determined (i.e. the determined values of  $2\Phi$  were halved). Similarly, as illustrated in Figure 3.12, the OPD shift between an SCAL dominant scan and an optimal port compensation scan yields values for  $\Phi$  directly. With observations of  $\Phi$  taken from measured FTS data, a minimum value for beamsplitter absorption can be determined using Equation 3.11. This analysis was performed for all available detectors from both arrays, i.e. 13 detectors for the SLW array and 31 detectors for the SSW array; results are given in Table 3.1. The uncertainty associated with the  $\Phi$  values in Table 3.1 reflects both the uncertainty in the OPD shift measurement and the standard deviation from  $\Phi$  values across the entire array. The uncertainty in the  $\mathcal{A}$  values is determined via error propagation through Equation 3.12.

### 3.5 Beamsplitter Emission Simulations

Computer simulations based on a variety of models were performed in order to better understand port compensation interferogram symmetry, the phase associated with

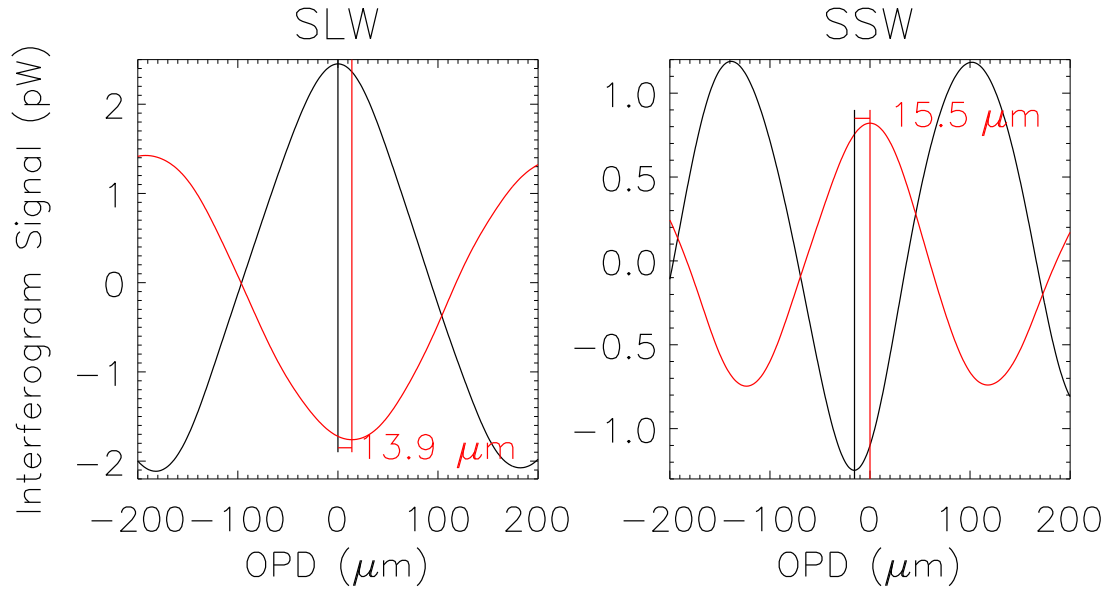


Figure 3.11: Input A and B dominant scans illustrating deviation from  $2\Phi = \pi$ .

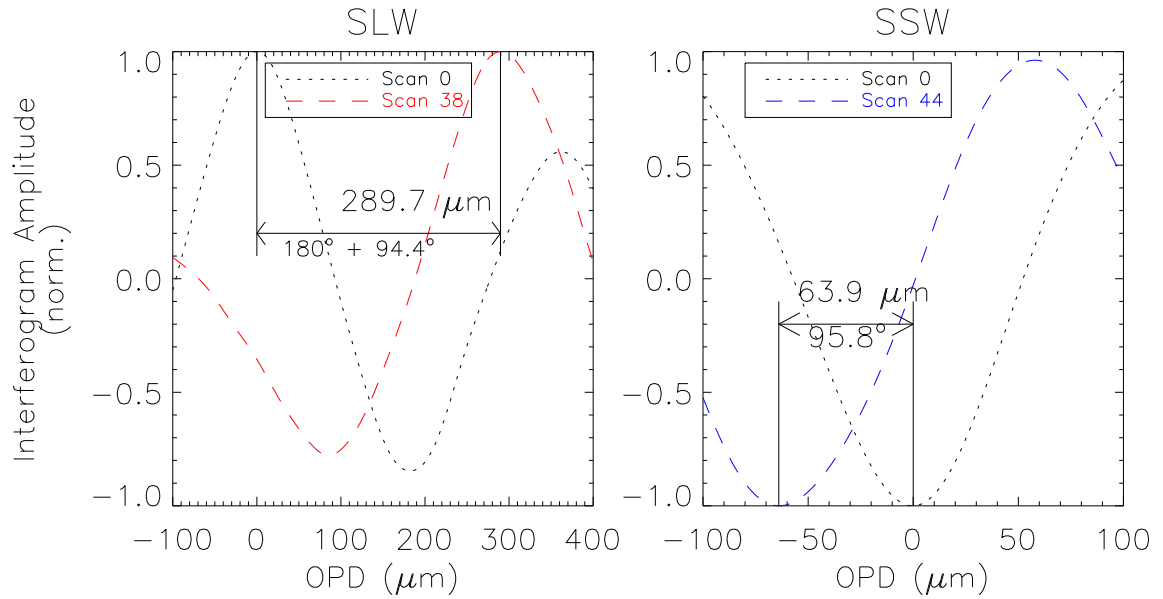


Figure 3.12: Normalized interferograms 0 and 38 (SLW) and 0 and 44 (SSW) illustrating the  $\sim 90^\circ$  phase shift associated with FTS beamsplitter emission.

beamsplitter absorption and emission, and their effects on FTS experiments. This section introduces a progression of simulations which begin with simple assumptions and inputs and moves towards more complex models and realistic cases. Empirical beamsplitter models, beamsplitter calibration measurements, and High Frequency Structural Simulator (HFSS) [126] simulation data were provided by Dr. Zhang at Cardiff University School of Physics & Astronomy [127].

The first two simulations are shown in Figure 3.13. The first simulation is shown in the left hand column of the figure and uses constant and ideal values of  $R$  and  $T$ , i.e.  $R = T = 0.5$ , and a monochromatic spectral input. The source is set to a wavelength of  $400 \mu\text{m}$  ( $25 \text{ cm}^{-1}$  frequency) with equal amplitude at both FTS inputs. The right hand column of Figure 3.13 illustrates the case of  $R = T = 0.45$  and  $\mathcal{A} = 0.1$  for the same spectral input. As expected, there is a shift in the local minima for the secondary input interferogram component related to its  $2\Phi$  phase term. The phase variation from the ideal value of  $\pi$  is demonstrated by the  $14.2 \mu\text{m}$  OPD shift in the apparent position of ZPD for  $I_B$ . This shift corresponds to a beamsplitter phase of  $\Phi = 96.4^\circ$  which originates from  $\mathcal{A} = 0.1$ . While it is convenient to measure a shift in the apparent ZPD for symmetric interferograms, the shift for interferogram components with odd symmetry is measured by the shift of the zero crossing away from ZPD. The observed shift in the ZPD zero crossing of the beamsplitter emission interferogram ( $I_{BS}$ ) is exactly half of the shift observed in the  $2\Phi$  interferogram, i.e.  $7.1 \mu\text{m}$ , corresponding to the  $\Phi$  phase term. The  $\pi$  phase shift between the overall interferogram ( $I_A + I_B + I_{BS}$ ; bottom row of the second column of Figure 3.13) and the beamsplitter emission component ( $I_{BS}$ ; fourth row of the second column of Figure



3.13) is caused by  $\Phi > \pi/2$ ; this phase difference is not present for  $\Phi < \pi/2$ .

The second set of simulations use the same two beamsplitter models as above with a rectangular input spectrum in place of the monochromatic source. Using the central in-band frequency for phase calculations, the observed shifts of interferogram features in OPD still correspond to the beamsplitter phase,  $\Phi$ , as they do for the monochromatic case. Figure 3.14 illustrates the resultant interferograms for the rectangular input spectrum. All of the observed OPD shifts of each interferogram component are as expected.

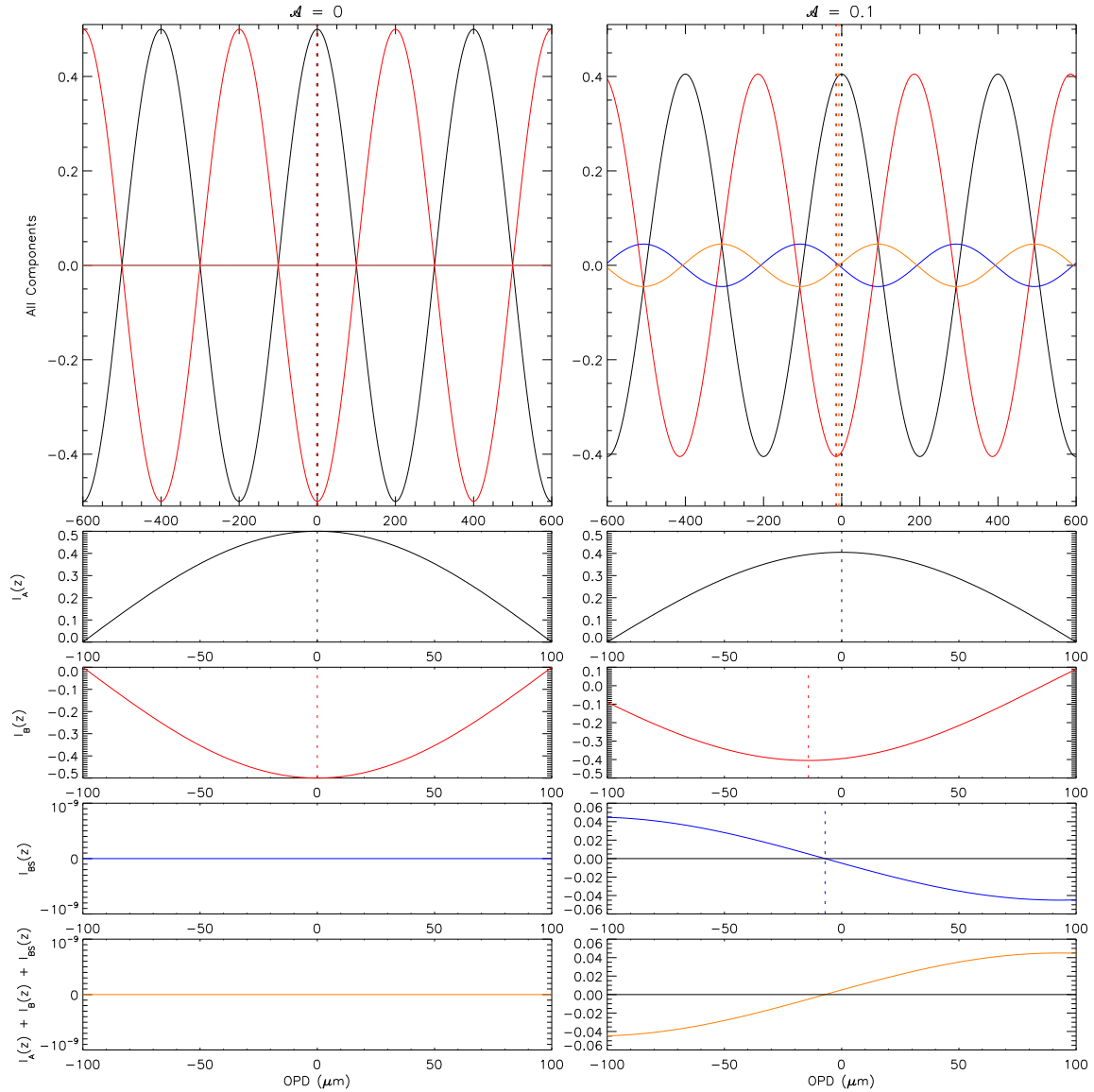


Figure 3.13: Basic model of port compensation/beamsplitter emission using  $R = T = 0.5$  (left column) and  $R = T = 0.45$  and  $\mathcal{A} = 0.1$  (right column) for a monochromatic source. The top row shows all interferogram components  $I_A(z)$ ,  $I_B(z)$ ,  $I_{BS}(z)$ , and their summation with zero absorption (left) and 10% absorption (right). The components are shown individually in subsequent rows as follows  $I_A(z)$  – second row,  $I_B(z)$  – third row,  $I_{BS}(z)$  – fourth row, and the total interferogram ( $I_1(z) + I_2(z) + I_{BS}(z)$ ) – bottom row. Vertical dotted lines illustrate the expected local extrema or zero-crossings. The left column illustrating the  $\mathcal{A} = 0$  case demonstrates perfect port compensation.

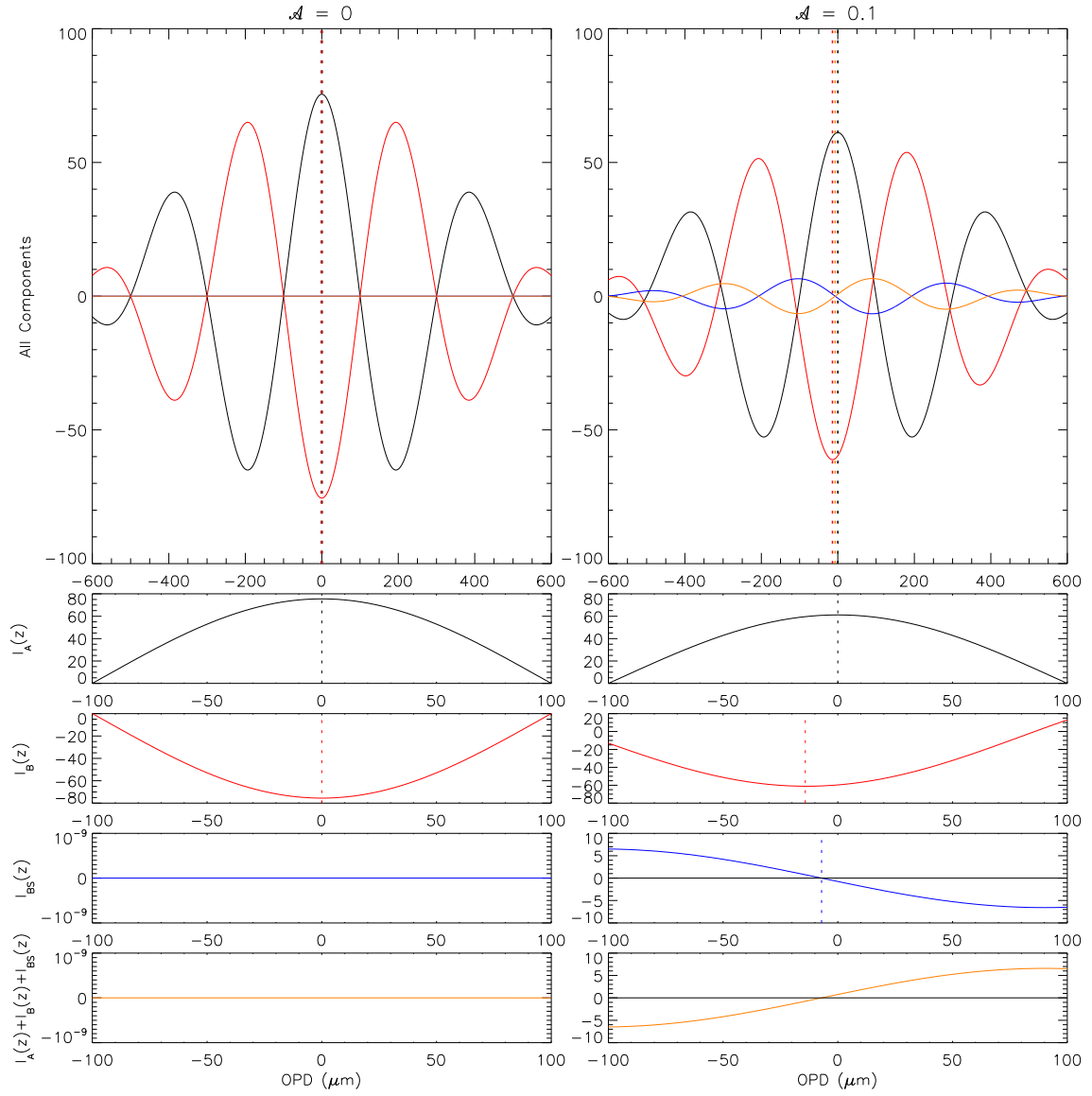


Figure 3.14: Basic model of port compensation/beamsplitter emission for a broadband input spectrum. The layout of this figure is similar to that of Figure 3.13.

Figure 3.15 illustrates the reflectance ( $R$ ), transmittance ( $T$ ), absorption ( $\mathcal{A}$ ), and phase ( $\Phi$ ) resultant from the empirical beamsplitter model provided by Dr. Zhang, all of which are frequency dependent. The model corresponds to the beamsplitters used in the MZ-FTS discussed in Section 3.6. The spectral band of interest for this beamsplitter model is  $\sim 6 - 34 \text{ cm}^{-1}$ . These simulation results, as shown in Figure 3.16, are similar to the basic beamsplitter models shown previously (Figures 3.13 & 3.14). The absorption in these more realistic models, however, is on the order of 1%, so the observed OPD shifts due to beamsplitter phase are much smaller than the  $\mathcal{A} = 0.1$  examples above. The resultant simulated OPD shift of the beamsplitter emission component is  $0.58 \mu\text{m}$  and that of the secondary input port is twice that,  $1.16 \mu\text{m}$ .

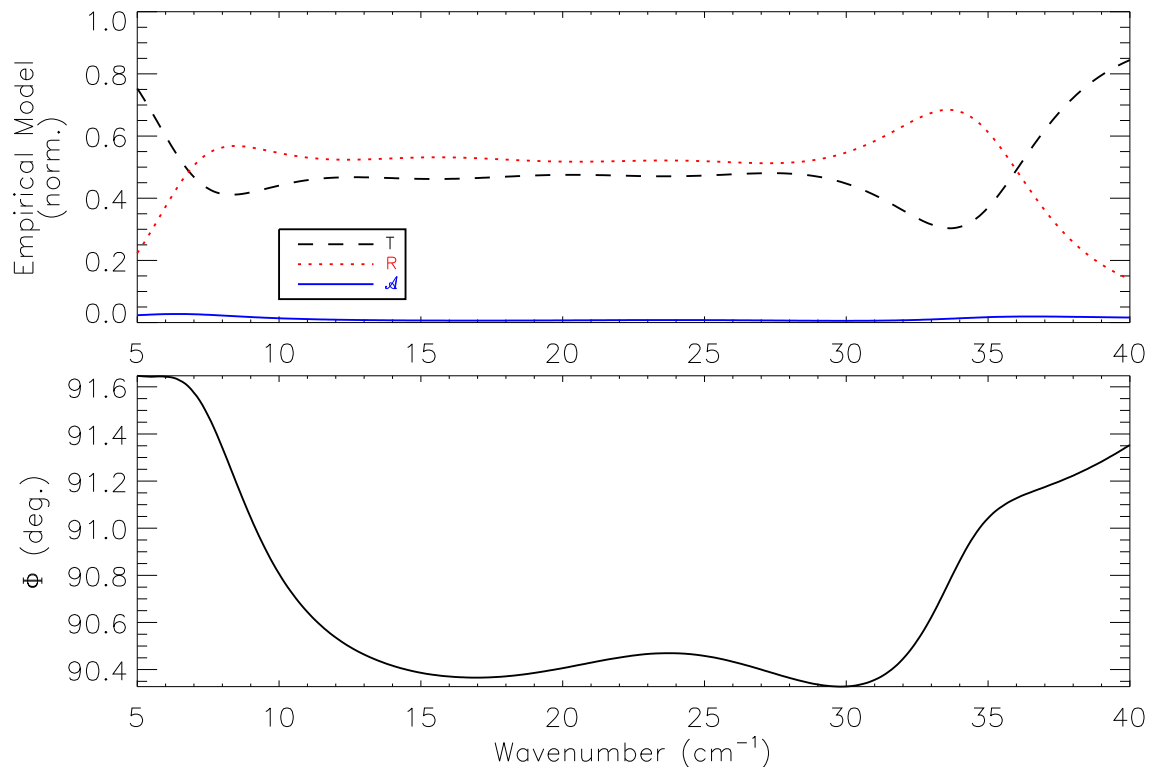


Figure 3.15: Empirical values for reflectance ( $R$ ), transmittance ( $T$ ), absorption ( $\mathcal{A}$ ), and phase ( $\Phi$ ) for the MZ-FTS beamsplitters.

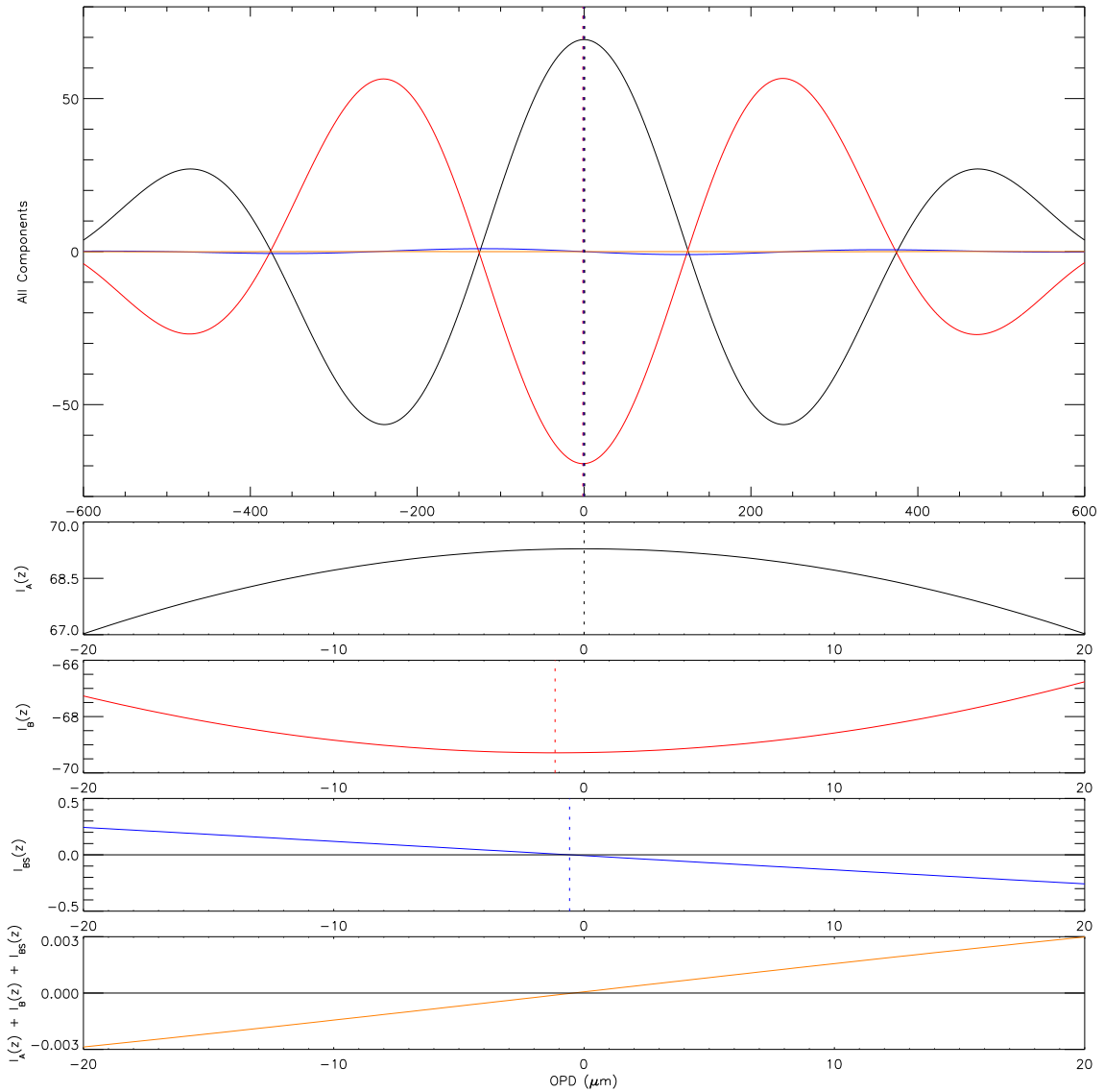


Figure 3.16: Interferogram components resulting from the empirical model of port compensation/beamsplitter emission for the MZ-FTS. The top row shows all of the individual interferogram components  $I_A(z)$ ,  $I_B(z)$ ,  $I_{BS}(z)$ , and their summation. The components are shown individually in subsequent rows as follows  $I_A(z)$  – second row,  $I_B(z)$  – third row,  $I_{BS}(z)$  – fourth row, and the total interferogram ( $I_1(z) + I_2(z) + I_{BS}(z)$ ) – bottom row. Vertical dotted lines illustrate the expected local extrema or zero-crossings.

In addition to the empirical values for the MZ-FTS beamsplitters, HFSS simulations [126] also provided  $R$ ,  $T$ ,  $\Phi$ , and  $\mathcal{A}$ . Beamsplitter properties for two simulations are shown in Figure 3.17. The first simulation assumes perfect structure and infinite metal conductivity, while the other includes the finite conductivity of copper, a finite thickness for the copper grids, and frequency dependent substrate absorption. Figure 3.18 illustrates the results from the HFSS interferogram simulation. Interferogram features are shifted in OPD in accordance with the  $\Phi$  and  $2\Phi$  phase as expected.

Although the claim was made in §3.3 that deviations from  $\Phi = \pi/2$  were the result of beamsplitter absorption, it is evident from the HFSS simulations that beamsplitter phase is deviating from  $\pi/2$  even without any absorption (cf. the left and right hand columns of Figure 3.18). Brasunas has noted that an absorbing beamsplitter is not necessary for such phase anomalies to occur [128]. This behaviour is the result of the metamaterial properties of the capacitive and inductive metal mesh subcomponents of the beamsplitters [127]. Since the analysis of §3.4 assumes that all observed deviation from  $\pi/2$  in  $\Phi$  is due to beamsplitter absorption, the values reported for  $\mathcal{A}$  in Table 3.1 are likely to be exaggerated; the actual beamsplitter  $\mathcal{A}$  is expected to be lower than the values reported in Table 3.1.

The analysis of §3.4 assumes that  $\Phi$  is constant across the entire band, and that observed shifts in interferogram OPD provide an estimate of  $\Phi$  for the entire interferogram. This section demonstrates that the OPD shift in the isolated interferogram components can be used to infer  $\Phi$ ; this, however, is not necessarily the case for observed interferograms. In the beamsplitter emission simulations, one has the luxury of calculating each interferogram component separately, and combining them to form the final interferogram. In practice,

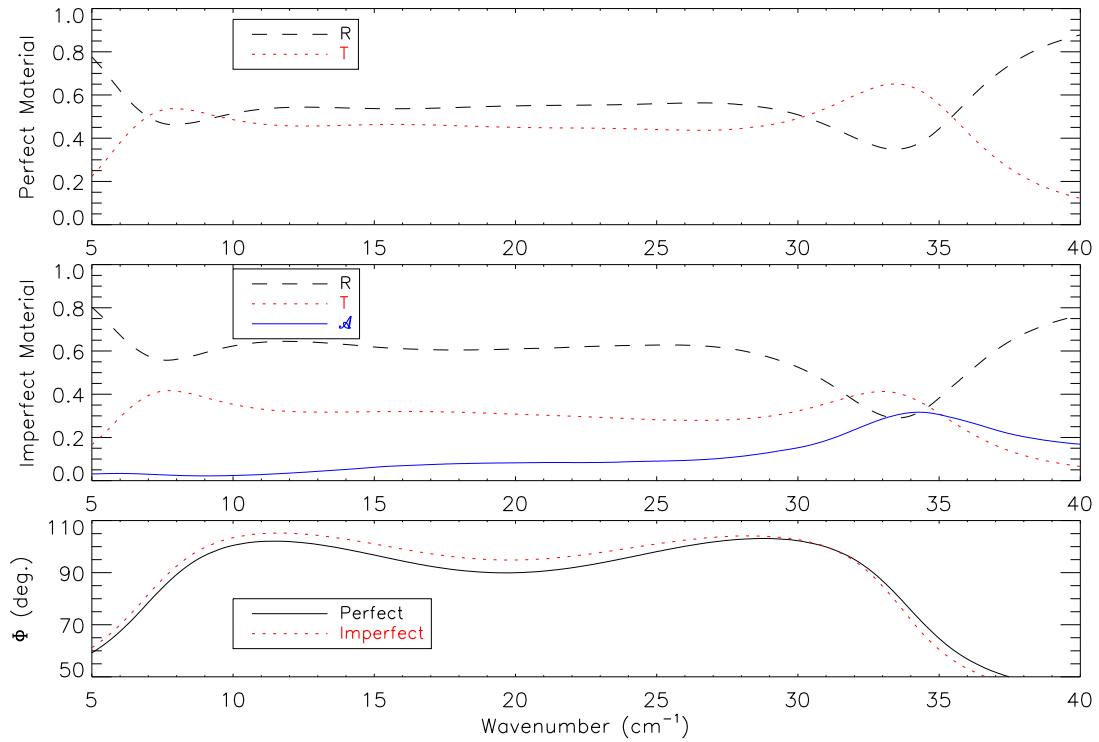


Figure 3.17: HFSS simulation results for  $R$ ,  $T$ ,  $\Phi$ , and  $\mathcal{A}$ . The higher than expected absorption in the centre plot is caused by a limitation in the HFSS software which is unable to model accurately ultra-thin substrates.

only the final interferogram is available to the experimentalist. It is evident from the HFSS simulations, shown in Figure 3.18, that the OPD shift of the total interferogram (bottom row of Figure 3.18) is not exactly the same as the OPD shift for the isolated beamsplitter emission component (fourth row of Figure 3.18). In §3.4 & §3.6, the OPD shift of the measured interferogram at optimal port compensation is assumed to be similar to that of the beamsplitter emission component, and is thus used to obtain an estimate of  $\Phi$ . The uncertainty of  $\Phi$  obtained in this manner is therefore relatively large when no additional information is available on the relationship between each interferogram component.



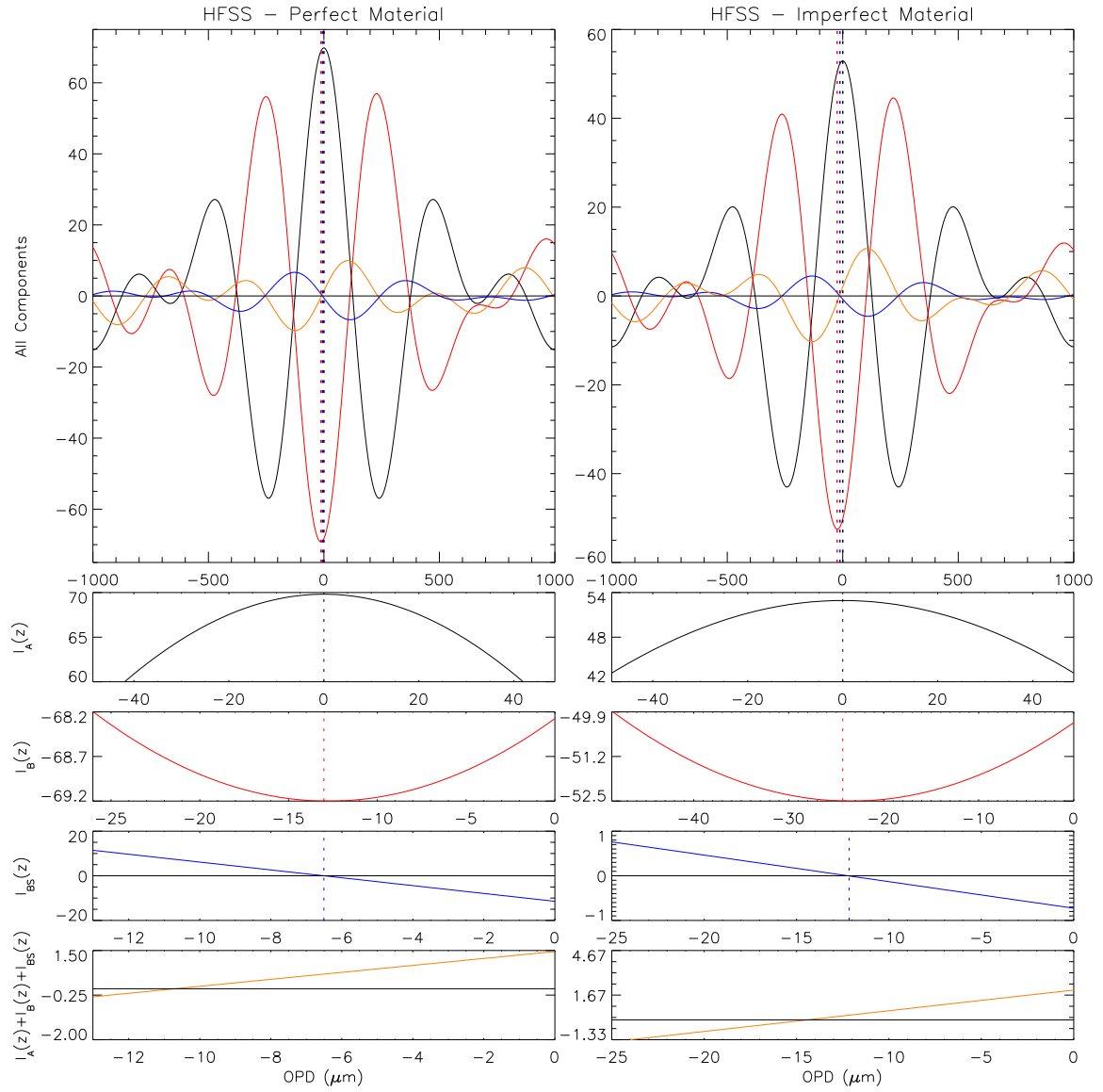


Figure 3.18: Simulated interferograms for HFSS models. The left column shows results for a perfect structure and the right column shows results that include the simulation of finite metal conductivity and substrate absorption.

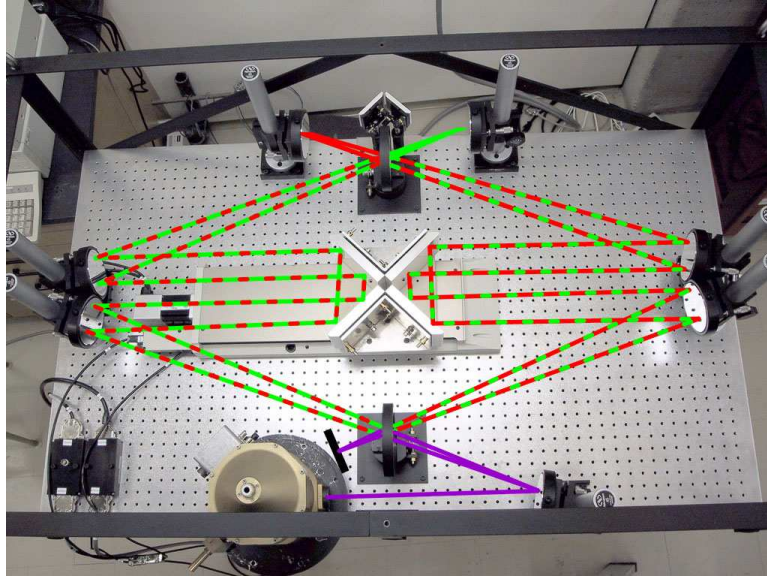


Figure 3.19: Image of the MZ-FTS used to verify beamsplitter emission characteristics.

### 3.6 Beamsplitter Emission Study

The effect of beamsplitter emission, and non-ideal beamsplitter phase, in SPIRE interferograms was not realized until final analysis of PFM test data, after all of the SPIRE pre-flight calibration testing had been completed. An independent study using an FTS of design similar to that of SPIRE, using beamsplitters of similar construction to those used in SPIRE (although of a slightly different band-pass), was performed in order to quantify the effects of beamsplitter self-emission in a balanced FTS. Although SPIRE is tested under vacuum at cryogenic temperatures, similar effects were observed with an MZ-FTS at room temperature under atmospheric pressure (see Figure 3.19).

In this study I designed and built two identical, independently controlled, black-body sources (see Figure 3.20) to be used at both FTS input ports (A & B, Figure 3.1).

Each blackbody source was constructed using Minco [129] heaters bonded to the surface of a 5 mm thick copper disk using Epo-Tek-920 thermal epoxy [130]. The exposed side of the heater was then coated with a mixture of thermal epoxy, graphite (~3% by mass), and carborundum grains of various sizes (~5% by mass) to improve the source emission and reduce specular reflections. The heat source was insulated from its machined aluminum housing by three ~1 cm long delrin [131] rods attached to the copper disks using brass machine screws. Two temperature sensors are mounted to the back of the copper disk to provide temperature readings to the blackbody electronics, for temperature control, and also to the FTS control server, for temperature logging. The copper disks provide additional thermal mass to the heat source and thus allow for greater temperature uniformity across the surface. An Infrared (IR) image of the two blackbody sources, demonstrating the temperature uniformity across the surface, is shown in Figure 3.21. The blackbody sources are PID temperature controlled and operate at ambient temperature up to 100°C (above which the delrin loses mechanical stability and may melt). With great caution, a heat gun was used to warm the beamsplitter above ambient temperature.

To investigate the effects of beamsplitter emission, two experiments were performed. In the first experiment, highly-oversampled ( $\delta z = 16 \mu\text{m}$  OPD), low-resolution, interferograms were recorded with one input held at a constant temperature,  $T_c$ , while the other was allowed to cool from  $T > T_c$  to  $T < T_c$  (typically spanning a range of  $T_c \pm 3$  K). In the second experiment, the beamsplitter itself was heated above ambient temperature and allowed to cool while both input sources were maintained at the same temperature, again while recording highly-oversampled, low-resolution, interferograms. These experiments are

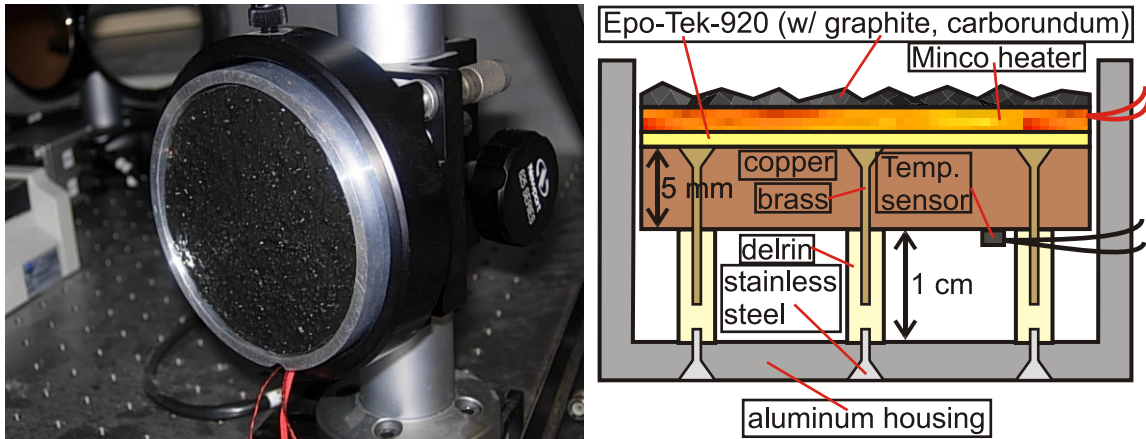


Figure 3.20: Image (left), and schematic diagram (right), of the identical IR blackbody sources constructed for investigation of FTS port compensation and beamsplitter emission.

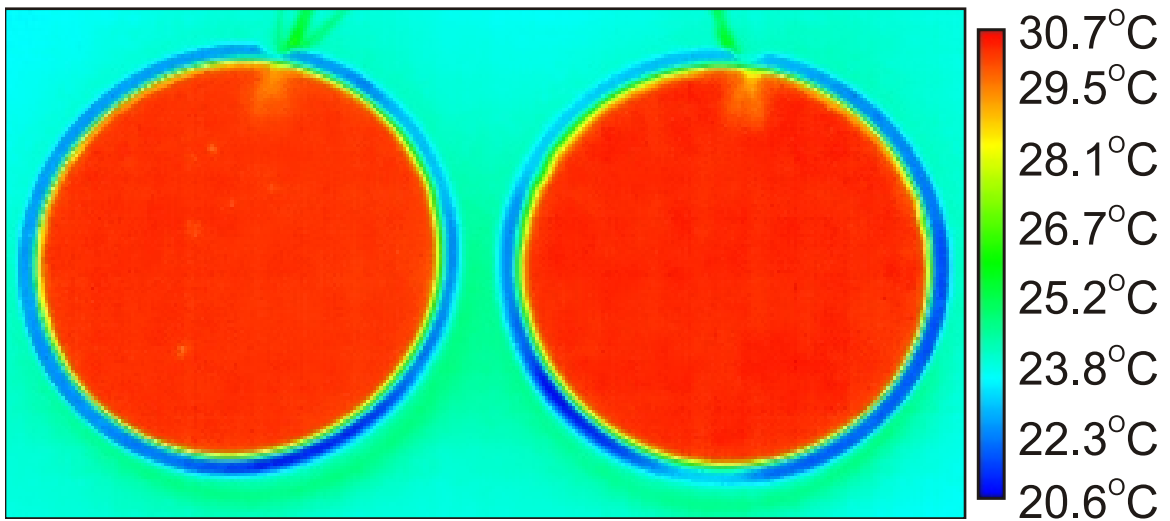


Figure 3.21: Infrared image of both of the identical blackbody sources set to 30°C. The image was recorded using a FLIR A320 [132] IR camera.

Table 3.2: Experimentally derived beamsplitter  $\Phi$  and  $\mathcal{A}$  for the MZ-FTS.

Frequency Band	$\Phi$	$\mathcal{A}_{\min}$
Open (513 $\mu\text{m}$ )	$101.4^\circ \pm 9.9^\circ$	$0.16 \pm 0.17$
350 $\mu\text{m}$	$95.8^\circ \pm 14.1^\circ$	$0.09 \pm 0.24$
450 $\mu\text{m}$	$102.9^\circ \pm 11.3^\circ$	$0.18 \pm 0.19$
450 $\mu\text{m}$ – wide	$90.1^\circ \pm 11.3^\circ$	$0.001 \pm 0.19$
850 $\mu\text{m}$	$99.7^\circ \pm 5.9^\circ$	$0.14 \pm 0.10$
Average (all)	$98.0^\circ \pm 5.1^\circ$	$0.12 \pm 0.09$

performed in the FIR with several narrow and wide band filters employed to characterize this effect at a variety of frequencies and bandwidths. The first experiment is designed to determine the point of optimal port balancing, and demonstrate the range of temperature over which beamsplitter self-emission in a balanced FTS is significant. The second experiment verifies directly that the source of the asymmetric component of the port-balanced interferogram is in fact beamsplitter emission.

Figure 3.22 illustrates data similar to that of Figure 3.7 recorded with the MZ-FTS. The figure demonstrates the transition between interferograms dominated by one input port to interferograms dominated by the other input port, with optimal port compensation occurring intermediately. A loss of symmetry under optimal port compensation similar to that of SPIRE is observed for each of the 5 frequency bands of the detector. The optimal compensation interferogram from each data set is normalized to the amplitude of an input dominant interferogram in Figure 3.23. As was observed with SPIRE, the maximum amplitude of the optimal port compensation interferogram occurs near the zero-crossings of the primary interferogram in each case, indicating a phase shift of  $\sim\pi/2$ . An analysis similar to that of the SPIRE port-compensation interferograms was performed in this work for the MZ-FTS beamsplitters with results shown in Table 3.2.

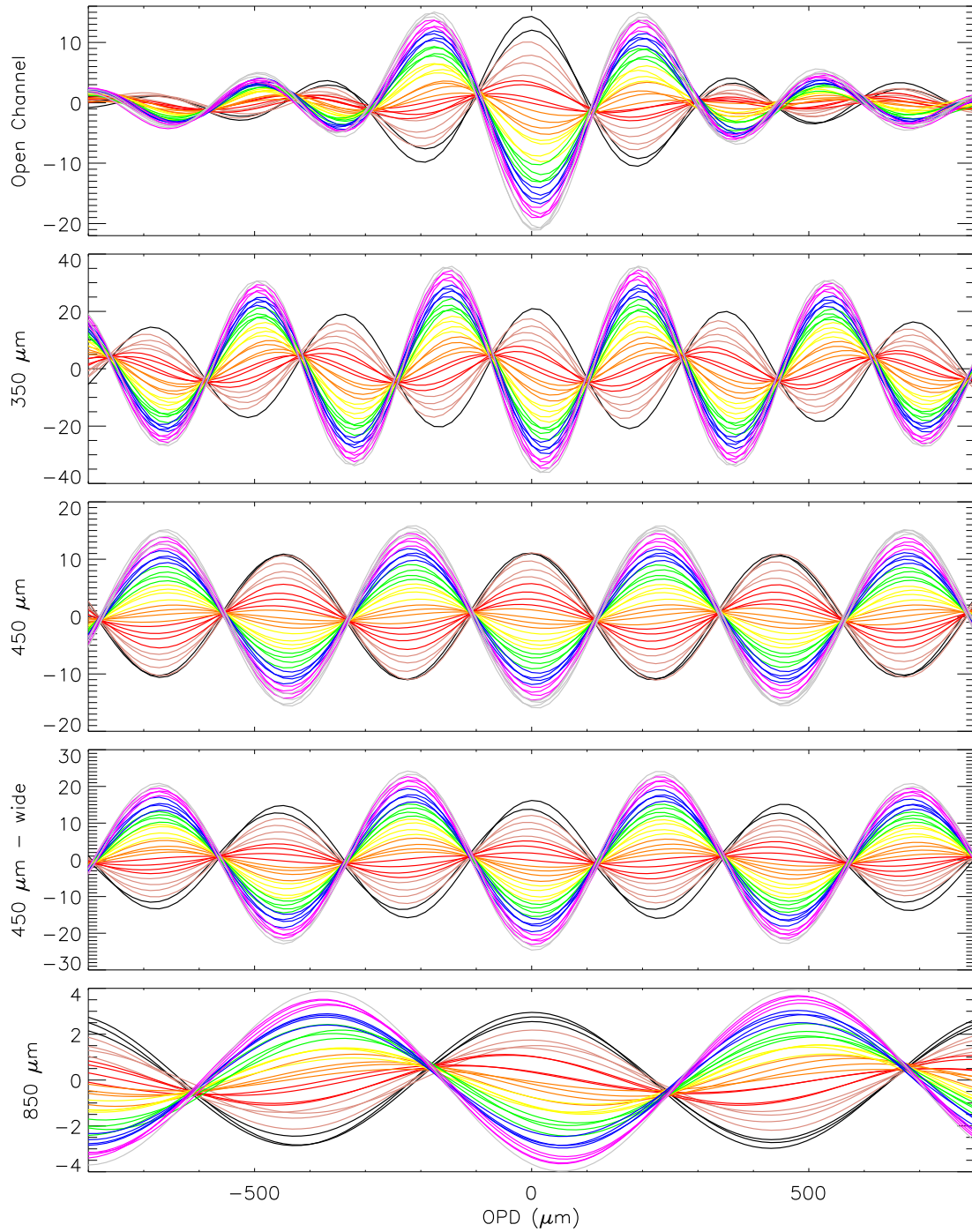


Figure 3.22: Interferograms measured with the MZ-FTS verifying that port compensation characteristics are similar to those of the SPIRE FTS. While these interferograms were recorded, one input was held at 303 K while the other input was cooled from 306 K to 300 K. The change in temperature between each individual scan is  $\sim 0.2$  K.

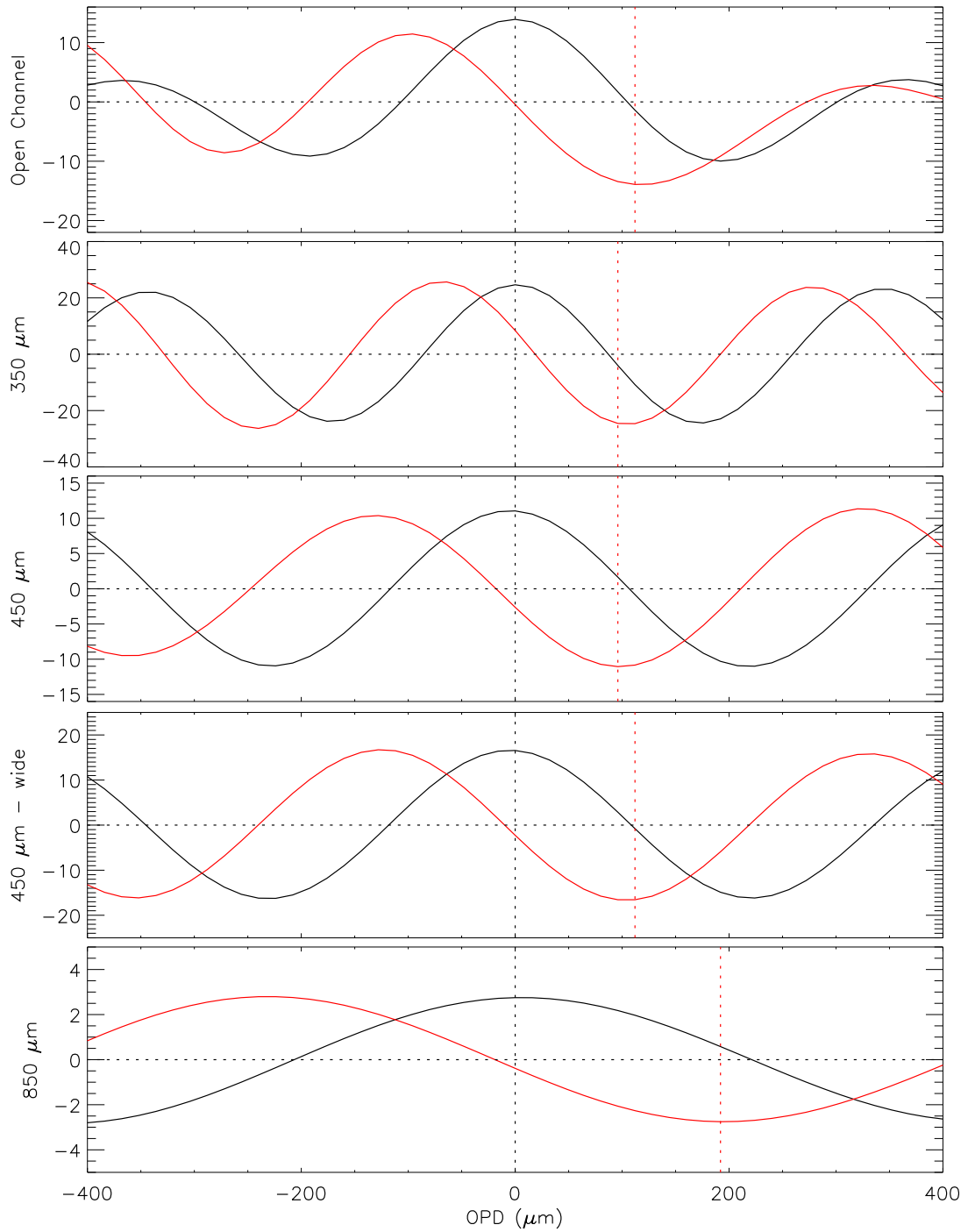


Figure 3.23: Normalized port compensation interferograms investigating the phase shift  $\Phi$  used to derive the values shown in Table 3.2.

The above measurements provide verification that the MZ-FTS behaves in a similar fashion to the SPIRE FTS under port compensation. The next phase of the study was to artificially heat the first beamsplitter to enhance this effect. Several low-resolution interferograms were recorded with both input sources at the same temperature, i.e. optimal port compensation. During this time, the beamsplitter was heated with an external convection source and allowed to return to ambient temperature with the heat source removed from the system. This heating of the beamsplitter produced an immediate and dramatic effect. Results are shown in Figure 3.24, where a separate window is used for each frequency band. In each sub-figure, the upper curve (circles) is an input A dominant scan, the lower curve (triangles) is an input B dominant scan, and the two central curves show the beamsplitter emission dominant interferogram. The low amplitude central curve (squares) is the resultant interferogram with port compensation and an ambient beamsplitter, and the central curve of larger magnitude (diamonds) is the heated beamsplitter interferogram. The dashed lines are included for reference and help to illustrate the  $\sim\pi/2$  phase shift present for the beamsplitter emission signal. Whereas the beamsplitter emission signal is normalized in Figure 3.23, no normalization is performed on the data presented in Figure 3.24. The beamsplitter emission interferogram approaches the amplitude of the input dominant case when there is a  $\sim 2$  K temperature difference between the two identical input sources. As is expected for  $\Phi > \pi/2$ , there is an  $\sim\pi$  phase difference between the port compensation interferogram with an ambient beamsplitter and the interferogram heavily dominated by heated beamsplitter emission.

The low thermal mass of the beamsplitter together with the coupling of the em-



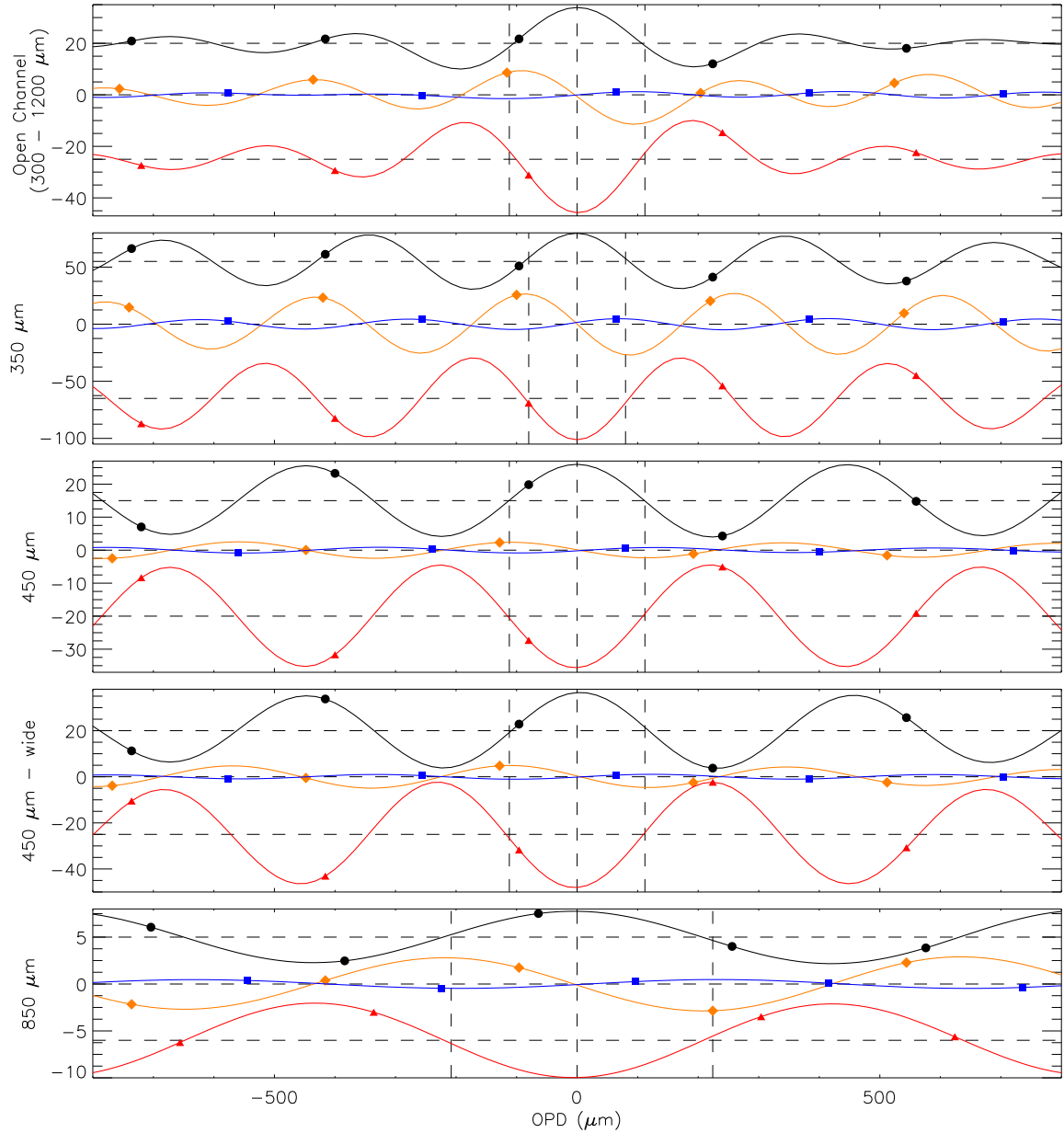


Figure 3.24: Interferograms measured with the MZ-FTS while the first beamsplitter was heated and allowed to cool. The upper curve (circles) in each plot shows the input A dominant interferogram. The lower curve (triangles) in each plot shows the input B dominant interferogram. The two central curves show interferograms with balanced input ports. The central curve of low amplitude (squares) shows the ambient beamsplitter interferogram while the greater amplitude curve (diamonds) shows the heated beamsplitter case.

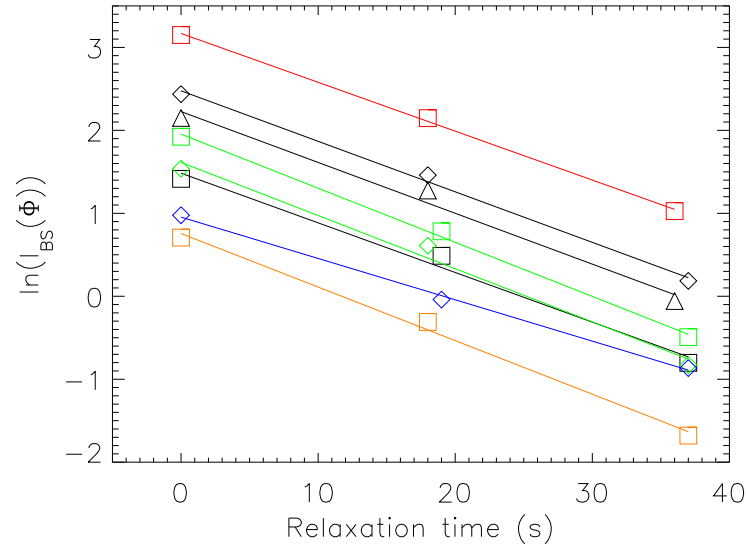


Figure 3.25: Linearization of beamsplitter cooling used in determination of the beamsplitter relaxation time constant.

bedded metal grids to the large beamsplitter frame allows the beamsplitter to reach thermal equilibrium quickly. A study of the beamsplitter thermal relaxation was performed using the interferograms recorded when the beamsplitter was heated and allowed to cool. Figure 3.25 plots the natural logarithm of the peak interferogram amplitude against time such that the inverse of the slope yields the thermalization time constant. The intercept for each curve is different because the beamsplitter was not heated to exactly the same temperature at the start of each trial. The rate of cooling however, should be consistent regardless of the starting point; therefore, the individual  $\mathcal{T}$ 's may be averaged. The beamsplitter thermal relaxation time constant,  $\mathcal{T}$ , was determined to be  $16.6 \pm 1.5$  s.

It can be seen from Figures 3.4 & 3.6 that the time to record each scan in the SPIRE port compensation interferograms was approximately 15 s. As the beamsplitters used in SPIRE are very similar to those used in the MZ-FTS study, a thermal relaxation

time constant of  $\sim 16$  s can be assumed for the SPIRE beamsplitters also. If the thermal relaxation time constant were significantly longer than the time to record a single interferogram, the beamsplitter emission could be assumed to be constant. If the time constant were significantly less than the scan time, then the beamsplitter emission could be assumed to be negligible. Since each of these SPIRE interferograms was recorded on the order of one thermal relaxation time constant, the beamsplitter emission cannot be ignored, nor can it be assumed constant over the period in which each interferogram is recorded. Although the exact contribution to the interferogram from the beamsplitter under these conditions is difficult to measure, this can be considered as a systematic effect, and thus removal of beamsplitter emission can be performed by subtraction of calibration measurements from a stable instrument.

### 3.7 Beamsplitter Emission Correction

As discussed in Section 3.3, interferograms recorded under conditions of port compensation are potentially comprised of asymmetric components in addition to the typical symmetric components resulting from the input sources (see Equations 3.13 & 3.14). These interferogram asymmetries are in addition to those causing standard FTS phase errors as expected for single input FTS observations [20] and must be corrected for independently of standard phase correction. FTS port compensation is employed under conditions of an instrument or its environment producing a radiative background which dominates a much weaker source signal. In such cases, the contribution from the beamsplitter emission to the total interferogram may thus be considered to be a constant component which must

be removed prior to phase correction and Fourier analysis. Thus, port compensation calibration observations should be performed under nominal instrument operating conditions. These calibration observations can be used to remove the undesired spectral components, and standard phase correction and Fourier analysis may then be performed on the port compensation corrected interferograms.

Removal of the asymmetric component of the MZ-FTS interferograms is shown in Figure 3.26. The left-hand column shows interferograms with either input port dominant, and the interferogram of the optimal port compensation case. The right-hand column of the figure shows the correction of the input port dominant interferograms where even symmetry is observed to be restored.

Figures 3.27 & 3.28 illustrate the improvement in the spectral phase across the 15–33.5  $\text{cm}^{-1}$  (SLW) and 31–52  $\text{cm}^{-1}$  (SSW) bands that result when the beamsplitter emission component is removed from the SPIRE port compensation interferograms. The upper plots show the raw interferograms and subsequent spectral phase when the beamsplitter emission and phase terms are present. The lower plots show the interferograms after the subtraction of this effect; the resulting spectral phase is centered on zero or  $\pm 180^\circ$ , as expected.

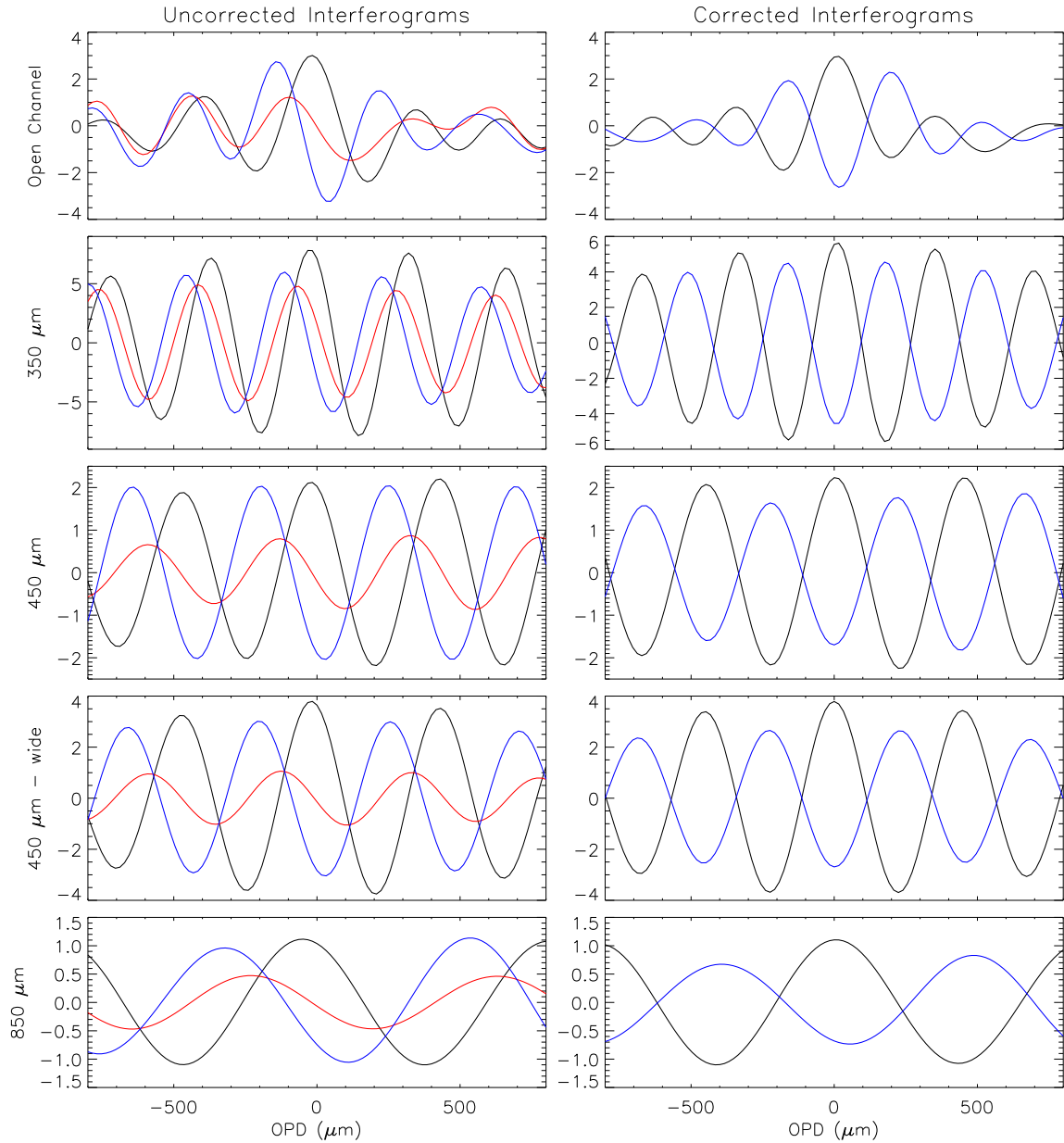


Figure 3.26: Removal of the asymmetric components of port compensation/beamsplitter emission interferograms for the MZ-FTS. The left hand column shows three uncorrected interferograms per frequency channel, the two input port dominant scans, and the optimal compensation scan. The right hand column shows the two input dominant scans after the removal of asymmetry.

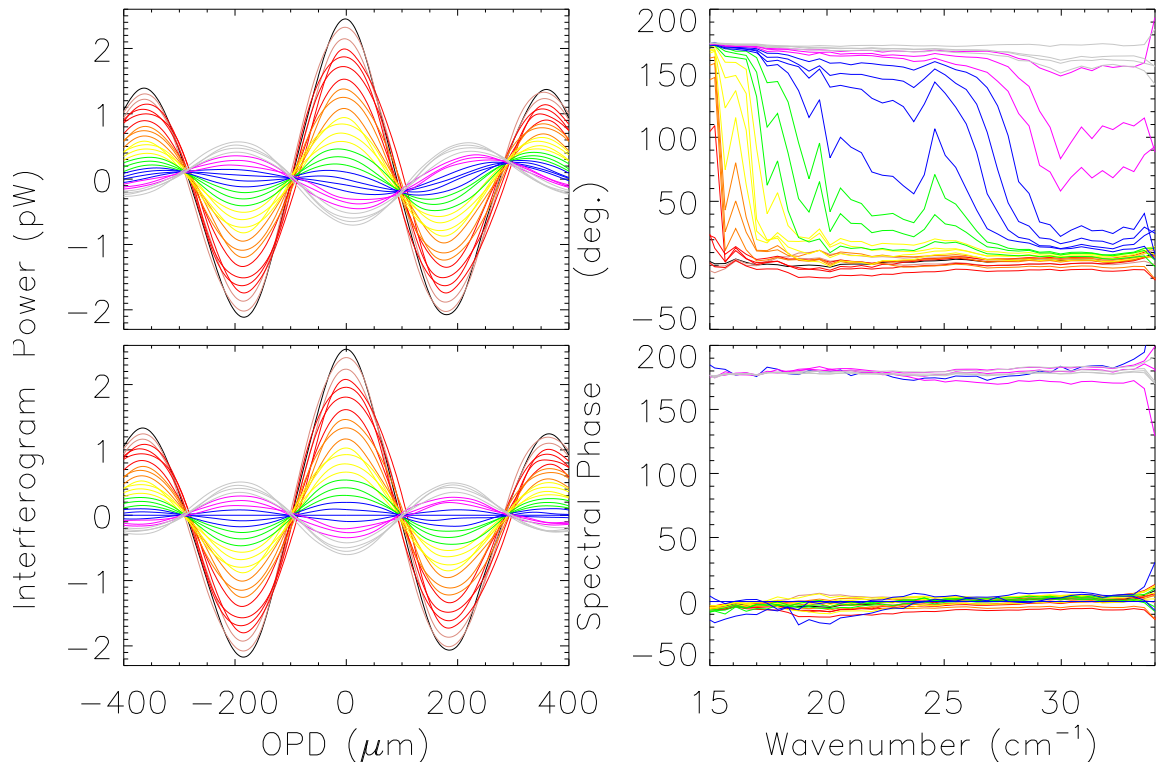


Figure 3.27: Removal of the beamsplitter emission component of SPIRE SLW interferograms. The upper row illustrates the interferograms (left) and spectral phase (right) for the data shown in Figure 3.7. The lower row shows the same interferograms after the removal of the asymmetric component.

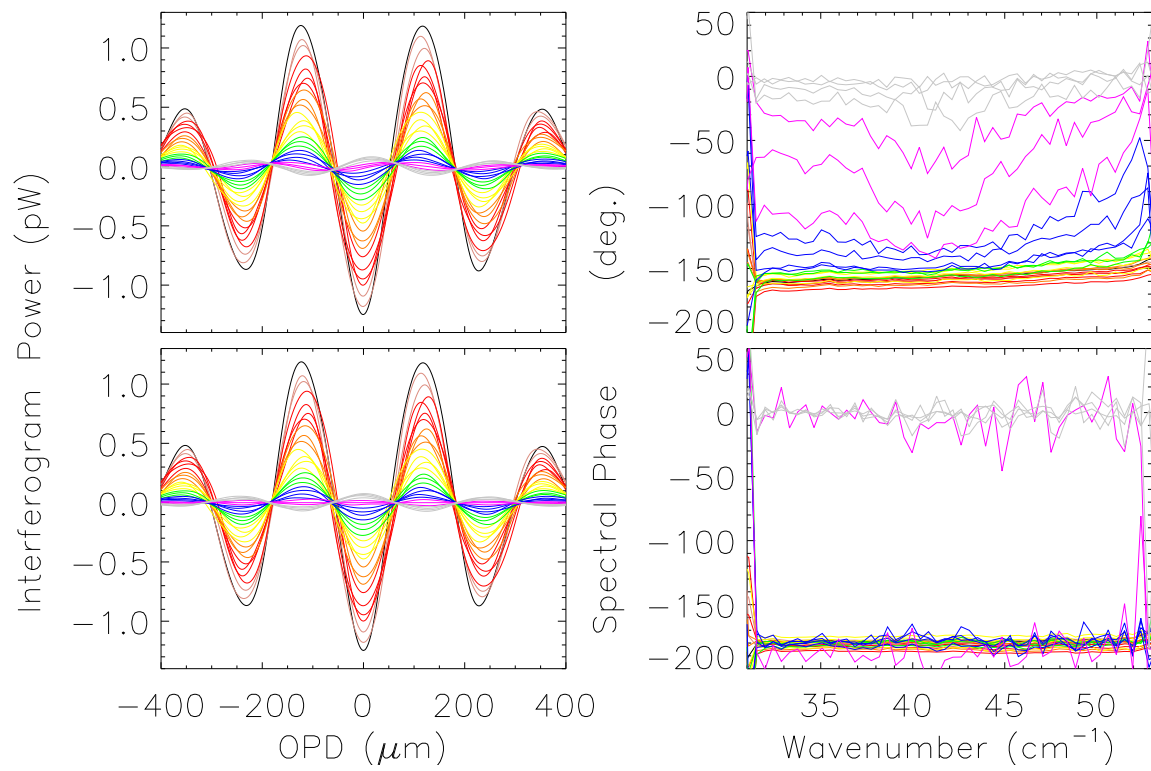


Figure 3.28: Removal of the beamsplitter emission component of SPIRE SSW interferograms (see Figure 3.27 caption for more details).

### 3.8 Conclusions

It has been shown that an interferogram recorded under conditions of port compensation may appear asymmetric if the beamsplitter phase  $\Phi$  deviates from the ideal value of  $\pi/2$ . In this case the corresponding phase shift of the secondary FTS input deviates from  $\pi$ , which causes amplitude and phase errors in the resultant spectrum [133–135]. If there is any absorption in the beamsplitter, a non-zero beamsplitter emission component may also be present in the recorded interferogram [34, 35, 133, 134, 136–139]. In the best-case scenario, this component has odd symmetry, but will generally be a linear combination of even and odd components. Moreover, if the location of ZPD is not known, then isolation of the individual interferogram components (i.e. from each input port and the beamsplitter emission itself) is difficult and phase correction will not restore the symmetry of the measured interferogram.

Results are included from a study of the effect of beamsplitter emission on port-balanced FTS interferograms. The theory of port compensation and beamsplitter emission, along with results from computer simulations of this effect in ideal and realistic instrumentation, has also been presented. This effect has been observed in an FTS operating under vacuum at cryogenic temperatures and in one operating at room temperature where the temperatures of the beamsplitters and input sources have been controlled directly. While the presence of beamsplitter phase/emission effects in the SPIRE instrument were only detected during the testing of the flight-model, they are, in fact, unavoidable at these long wavelengths. It is a testament to the sensitivity of the SPIRE detectors that the contribution to the interferograms shown in Figure 3.7, which arises from a beamsplitter of



---

temperature less than 10 K, can be observed easily. Since this effect is systematic, once determined, it can be readily removed from the raw data. In light of these developments, a specific module has been added to the SPIRE data processing pipeline to account for beamsplitter phase/emission.

Beamsplitter emission is not usually seen in the visible or near-IR because of the small number of photons emitted at these wavelengths for typical instrumental temperatures. In the submm, however, this effect becomes evident, and perhaps even dominant, even for instruments at cryogenic temperatures. According to Wien's law, the peak wavelength of emission of an object at cryogenic temperatures lies in the submm spectral region, and the effect of beamsplitter emission from an object at such temperatures cannot be ignored. Although simple in theory, port compensation of the SPIRE FTS is non-trivial since it is not possible to match precisely the spectral signature of the Herschel optics over their possible temperature and emissivity parameter space. Typically, only partial spectral cancellation can be expected, which causes complications in the subsequent data processing and spectral analysis. SPIRE FTS port compensation observations are scheduled early in the performance verification phase after launch, while the Herschel telescope primary mirror is cooling. This will provide important data on Herschel's thermal properties as well as produce calibration measurements of SPIRE beamsplitter emission in order to refine its removal using data processing software.

## Chapter 4

# Imaging Fourier Transform

# Spectroscopy

Science is built up with facts, as a house is with stones. But a collection of facts is no more a science than a heap of stones is a house.

---

Jules Henri Poincaré [140, p. 127]

An investigation of the physics of a scene often requires both spectral and spatial information, i.e. a hyper-spectral image. In the case of an astronomical source such as a star forming region, information on the composition and dynamics of a source is provided by the spectrum while the scene morphology is interpreted from spatial information. A non-imaging spectrometer provides spectral information of a single point in a scene; with such an instrument, any required spatial information must be obtained by some mode of spatial scanning over time to build up a hyper-spectral image. With the availability of detector arrays, data in two dimensions, which may be applied either spectrally or spatially, is acquired simultaneously. Dispersive spectrometers using a two-dimensional detector array may use either one dimension for spectral information and the other for spatial information, or both dimensions for spectral information. The IFTS, i.e. an FTS coupled with a two-dimensional detector array, on the other hand, obtains two dimensions of spatial information simultaneously while acquiring spectra.

The FTS instrument has a rich heritage in astronomy [141] and related applications where the multiplex advantage provides efficient use of limited photons in many regions of the electromagnetic spectrum [68]. In the infrared, initial developments in radiation detectors produced one-of-a-kind hand-made devices. Any desired imaging or astronomical mapping with such a device requires that pointed observations be rastered across the image plane/sky, a process which is both tedious and time consuming, moreover, measurements are further complicated by changes in the atmosphere over the long periods of time required to build up a hyper-spectral image. Recent advances in detector technology have led to the development of infrared detector arrays [12, 142, 143]. With the availability of detector

arrays, a trade-off exists in the application of the dimensions of the array; the two dimensions can be applied either to obtain spatial information, spectral information, or a combination of both.

There are a variety of spectroscopic instruments capable of obtaining a hyper-spectral image. A detector array coupled with an  $n$ -colour filter wheel can obtain  $n$ -colour images for each detector. A detector array coupled with a diffraction grating uses one dimension of the array for spectral information while the other dimension may be used to collect spatial information; a pushbroom [144] type raster is required to build up the second spatial dimension. An Echelle spectrograph [145] uses both array dimensions for spectral resolution (course and fine), and therefore a two-dimensional raster is required to build up a spatial image. An FTS coupled with a detector array uses both array dimensions for spatial information and the spectral dimension is built up over time as the FTS translation stage is scanned across its range of OPD. A Fabry-Pérot interferometer [146], which is capable of levels of throughput similar to that of an FTS, provides higher spectral resolution over a narrower spectral band than that of an FTS. A detector array may be coupled with a Fabry-Pérot interferometer to perform hyper-spectral imaging. Similar to the IFTS, an imaging Fabry-Pérot interferometer records spatial information on the detector array and scans spectral information over time. A summary of obtaining hyper-spectral images with the instruments described above is provided in Table 4.1. Examples of the two-, one-, or zero-dimensional scanning required to build up a hyper-spectral image are shown in Figure 4.1.

This chapter discusses the use of FTS instruments in imaging spectroscopic appli-

Table 4.1: Spatial and Spectral resolution provided by various hyper-spectral imaging systems with a  $m \times n$  detector array and a scan time,  $t$ .

Instrument	Simultaneous dimensions		Scanned dimension	Resolution	
	Spatial	Spectral		Spatial	Spectral
Filter wheel ( $a$ filters)	2	0	spectral	$m \times n$	$a$
Diffraction grating	1	1	spatial	$m \times t$ $n \times t$	$n$ $m$
Echelle	0	2	spatial	$t$	$m \times n$
Imaging Fabry-Pérot (plate spacing = $d$ , mirror reflectivity = $R$ )	2	0	spectral	$m \times n$	$\frac{1}{2d} \left( \frac{1-R}{\pi\sqrt{R}} \right)$
IPTS ( $OPD_{max} = L$ )	2	0	spectral	$m \times n$	$1/2L$

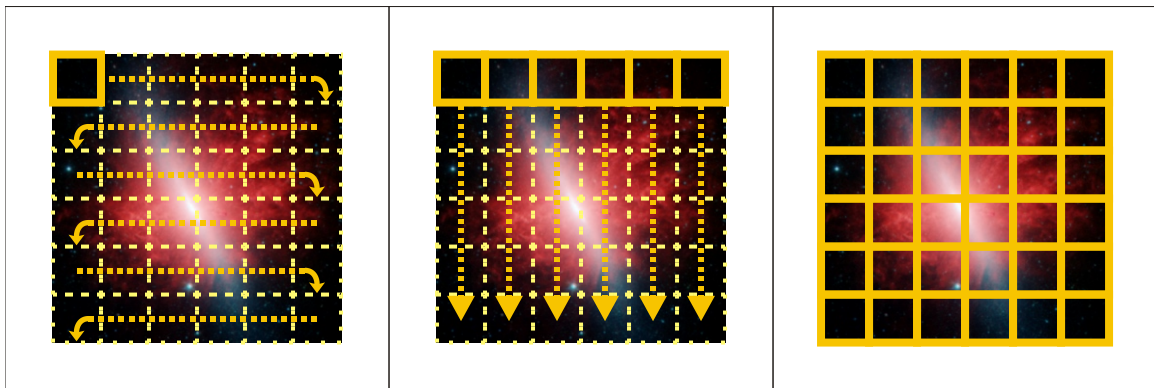


Figure 4.1: Various spatial scanning methods which generate a hyper-spectral image. The left panel illustrates the raster scan required when a spectrometer provides spectral information for only one pointing at a time, e.g. a single pixel grating spectrometer or an Echelle spectrograph. The central panel illustrates pushbroom scanning where spectral/spatial information is available in one dimension and the instrument must sweep out the other dimension in time, e.g. a grating spectrometer with a two dimensional detector array. The right panel illustrates an imaging spectrometer which records spectral information in two spatial dimensions simultaneously, e.g. an imaging FTS or a detector array coupled with a filter wheel. The inset photo is a Spitzer infrared image of the starburst galaxy M82. *Inset Photo: NASA/JPL-Caltech/Univ. of AZ/C. Engelbracht*

cations. Advantages of IFTS systems are discussed in §4.1 and the practical considerations required in the application of an IFTS are found in §4.2. The relevant theory involved in the extension of FTS into spatial dimensions is introduced in §4.3 where alignment, field-of-view, resolution, and ILS effects are discussed. This discussion is related to the specifics of the SPIRE IFTS in §4.4. The experiments performed to verify the imaging aspects of the SPIRE IFTS are described in §4.5 and the observed characteristics of the SPIRE IFTS, including PFM test results, are given in §4.6. The application of IFTS in astronomy using Messier 82 (M82) as a case study example is presented in §4.7.

## 4.1 IFTS Advantages

The Fourier transform spectrometer, with its high throughput, broad spectral coverage, variable resolution, intrinsic calibration, and simple design, has proven to be the spectrometer of choice in many applications. By combining an infrared detector array with a Fourier transform spectrometer, all of the benefits of a single pixel FTS are now extended to an imaging FTS system – an IFTS. The use of IFTS is particularly advantageous for applications involving narrow spectral features spread over a large frequency range. In fact, many other imaging spectrometers are not able to provide the high spectral resolution required across a large pass-band, so IFTS is the only viable option.

The Fellgett advantage for IFTS remains the same as for the FTS (see §2.6.2). Considering single pixel spectrometers, the FTS has a multiplex advantage over other spectrometers in that all spectral components of a source are recorded simultaneously. A grating spectroscopic system coupled with an array of detectors may regain the spectral multiplex

advantage as it measures every frequency component of a target simultaneously, albeit across different detectors. The multiplex advantage in an FTS, however, is regained in a spatial sense as it is able to simultaneously measure all spectral content of a source using a single detector, so the multiple detectors in an array provide the advantage that each detector views a different target. Depending on the nature of the noise present in an observation, one system may perform better than another, e.g. the photon noise per detector in a grating spectrometer is less because of the reduced number of photons within each spectral resolution element (see §4.2).

In FTS, all spectral channels are recorded simultaneously on a single detector, allowing the multiple detectors in an array to be dedicated to imaging directly. Hence, in IFTS, a full 2-D image is acquired per frame where successive frames are associated with a unique translation stage OPD. Spectral resolution is determined not by the available number of detectors in an array, but by the range of OPD in the recorded frames. With IFTS, applications only requiring low spectral resolution, where high spectral resolution may be a disadvantage, do not need to record any greater resolution than necessary, and can save acquisition time in the process. For example, low-resolution spectra are required to obtain spectral energy distribution values for dust emission in the interstellar medium. In a given amount of observation time, a higher S/N of the dust SED continuum is achieved with many low-resolution interferograms rather than a small number of high-resolution interferograms. Instantaneous spectral resolution for a grating spectrometer is fixed a priori by the number of detector elements in an array, limiting any flexibility in spectral resolution of any such instrument. Contrary to other imaging spectrometers, the IFTS is unique in that spectral

resolution can be varied during operation. This allows the observed spectral resolution to match the science goals of a particular application, with the added benefit that a reduction in spectral resolution scanned yields observation time savings or improved S/N.

Intrinsic spectrometer wavelength calibration, i.e. the Connes advantage, of FTS is generally preserved for IFTS applications because of the single valued wavelength correction factor (see Equation 4.1). As discussed in §4.3.3, there may be frequency dependent contributions to the overall ILS, but the sinc nature of the ILS remains frequency independent, and the frequency independence of off-axis IFTS ILS is a reasonably accurate assumption in most practical cases [147].

## 4.2 Imaging FTS Practical Considerations

Instrument sensitivity is an important consideration in any spectroscopic study. As FTS instruments view all spectral components of the source at all times, they are also subject to all of the in-band noise at all times. Observations taken to significantly higher spectral resolution than required then encounter diminishing returns on observation time as more noise enters the spectrum. This is especially true for photon noise limited observations where the Fellgett advantage can become a disadvantage. Thus, where high-resolution spectral features will see improvement in S/N with increased spectral resolution, typically much better than a grating spectrometer or a filter wheel, relatively broad spectral features, where the grating resolution is adequate, may see the FTS achieve a lower S/N than a dispersive spectrometer.

A significant challenge to IFTS is that of temporal source fluctuations. Any varia-



tions in source intensity while FTS interferograms are recorded result in additional Fourier components in the final spectrum. The changing OPD of the FTS translation stage produces the modulation of the source spectrum under study. Any significant temporal fluctuations in the source under observation, within the frequency range of interest, i.e. the interferogram modulation frequency, are analogous to the application of an apodization kernel to the interferogram – one which does not have a functional dependence on OPD and is almost certain to be asymmetric. Thus, periodic/temporal source fluctuations are likely to give rise to line-shifting and line-broadening in the resultant spectral features.

Although the IFTS may not be the instrument of choice for some dynamic scenes, the derived spectra from other imaging spectrometers are not immune to detrimental effects caused by temporal source fluctuations either. As mentioned above, grating spectrometers do not record more than one spatial dimension simultaneously and therefore must scan an image in at least one direction given a two-dimensional detector array. Thus, the spectra for adjacent pixels in the scanning direction are not recorded over the same time interval. This may cause difficulties in time-resolved imaging spectroscopy where the resultant hyperspectral images are not representative of the same period of time.

### 4.3 Obliquity Theory

This section identifies the differences between ideal, single pixel, and imaging FTS. The analysis in this section is for circular detectors, with  $\alpha$  and  $\beta$  representing the FOV half-angle and off-axis alignment, respectively. Within the FTS instrument, these angles represent the divergence of coherent radiation. Within this section several angles will be

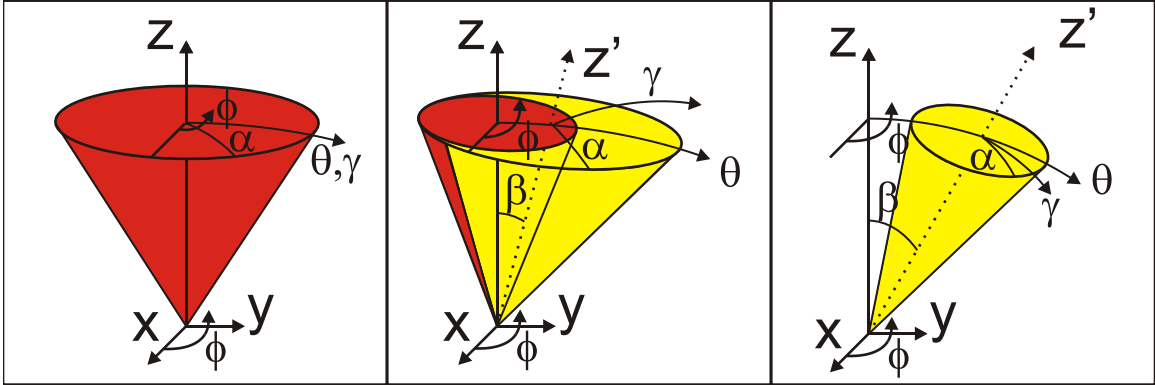


Figure 4.2: Various configurations for finite FOV and off-axis detector alignment. The on-axis case is shown in the left panel ( $\beta = 0$ ), the slightly off-axis case is shown in the centre panel ( $\alpha > \beta$ ), and the fully off-axis case is shown in the right panel ( $\beta > \alpha$ ).

incorporated into the discussion:  $\alpha, \beta, \gamma, \theta$ , and  $\phi$ . Unless otherwise stated,  $\alpha$  represents the detector FOV half-angle,  $\beta$  represents deviation of the detector optical axis with respect to the FTS optical axis,  $\gamma$  represents the instantaneous angle between the FTS optical axis and the detector/detector element under consideration, and  $\theta$  and  $\phi$  represent the usual angles in the standard spherical coordinate system with  $z$  as the optical axis (see Figure 4.2).

There is potentially some confusion with the use of the symbol  $\Phi$  to represent beamsplitter phase in Chapter 3, and the symbol  $\phi$  to represent an angle in the spherical coordinate system in this chapter. The angle  $\phi$  is only used in intermediate calculations here (and relevant appendices), with the angle  $\psi$  being used to express the angle of the detector FOV boundary condition (see Equation 4.5). The use of  $\phi$  in this chapter is explicitly as a spherical coordinate angle. In subsequent chapters,  $\Phi$  refers to a beamsplitter phase term.

### 4.3.1 Off-Axis Alignment

Oblique rays in an FTS instrument encounter a modified OPD,  $z'$ , with respect to the on-axis OPD,  $z$ , given by [148]

$$z' = z \cos \gamma \quad [\text{cm}] , \quad (4.1)$$

where  $\gamma$  is the angle between the ray and optical axis. This OPD modification has several consequences in Fourier analysis. As the effective sampling rate,  $\Delta z$ , and maximum OPD,  $L$ , are both reduced by  $\cos \gamma$ , this effects the resultant spectral resolution ( $\Delta\sigma$ ), Nyquist frequency ( $\sigma_{Nq}$ ), and observed spectral line centre ( $\sigma'_o$ ). For parallel rays within the interferometer, the entire interferogram is modified by the same  $\cos \gamma$  factor, and it is thus easily taken into account. Figure 4.3 illustrates the effect of varying the off-axis angle for perfectly collimated light in an FTS. In this section, the angle  $\beta$  is used to represent the alignment of the optical axis of a detector, and thus Figure 4.3 displays the spectrometer divergence angle as  $\beta$  rather than  $\gamma$  (Equation 4.1). As illustrated in Figure 4.2, the angle  $\gamma$  is used to represent the angle away from the detector's optical axis, while  $\beta$  is used specifically for the alignment of the detector's central axis;  $\alpha$  represents the maximum divergence angle from the detector's central axis.

### 4.3.2 Finite Entrance Aperture/Field-of-View

As discussed in §2.7.3, a finite detector FOV, i.e.  $\Omega \neq 0$ , results in a broadening of features in the corresponding FTS spectrum. For a detector which is centred on the FTS optical axis and has a FOV half-angle of  $\alpha$ , the on-axis rays within the detector FOV have no spectral shift while the most oblique rays accepted have a spectral shift of  $\sigma_o \cos \alpha$ . For

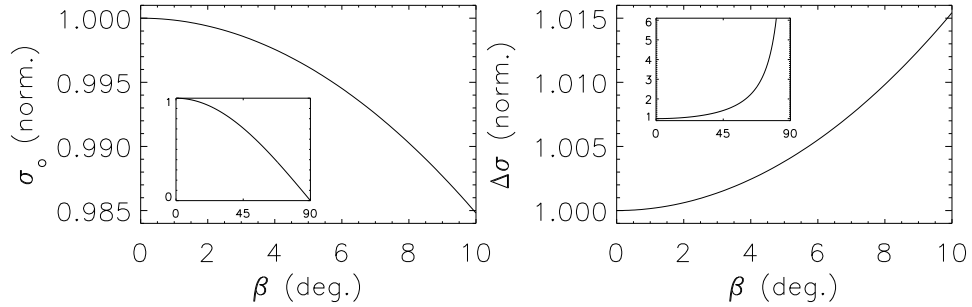


Figure 4.3: Change in observed spectral line centre (left), and resolution (right), as a function of off-axis detector alignment  $\beta$ . The insets each show the effect over an extended range.

intermediate axial angles of  $\gamma$ , the observed frequency,  $\sigma$ , is related to the source frequency,  $\sigma_o$ , as follows

$$\sigma = \sigma_o \cos \gamma \quad [\text{cm}^{-1}]. \quad (4.2)$$

Figure 4.4 illustrates the rectangular line-shape which results from a finite, non-zero, FOV. For a monochromatic source of frequency  $\sigma_o$ , the observed line centre is shifted from  $\sigma_o$  to  $\sigma_o(1 + \cos \alpha)/2$ . Although the frequency width of the source signal may be infinitesimally narrow, it is observed to have a width of  $\sigma_o(1 - \cos \alpha)$  (for an infinite resolving power FTS instrument). Since interferograms cannot be measured to infinite OPD, there is a convolution of the spectrum with a sinc ILS (Equation 2.32) in addition to the line-broadening effects discussed here. Figure 4.5 illustrates the effect of non-zero detector FOV on spectral line centre and resolution.

### 4.3.3 Finite Field-of-View and Off-Axis Alignment

When an off-axis detector is considered, account must be taken not only of the non-zero pixel FOV of half-angle  $\alpha$ , but also the off-axis angle with which it views the

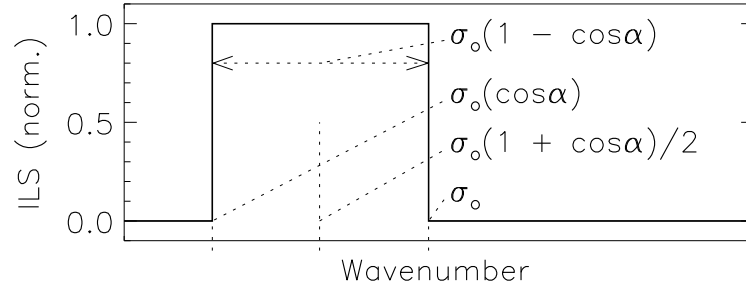


Figure 4.4: Rectangular ILS caused by finite FOV for an FTS instrument of infinite resolving power.

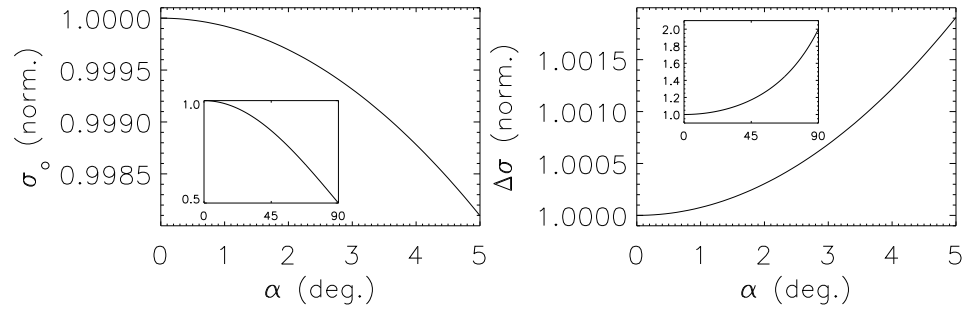


Figure 4.5: Change in observed spectral line centre (left) and resolution (right) as a function of FOV half-angle  $\alpha$ . The insets each show the effect over an extended range.

FTS,  $\beta$  [149]. The combination of detector axial alignment and non-zero FOV,  $\beta$  and  $\alpha$ , respectively, is more complicated than the superposition of their effects individually. For a detector viewing a monochromatic source off-axis by an angle  $\beta$  with a FOV half-angle  $\alpha$ , the net interferogram (similar to Equation 2.30) is given by solving the equation

$$I(z, \sigma_o) = \int_{\Omega} \cos(2\pi\sigma_o z \cos \gamma) d\Omega, \quad (4.3)$$

where  $\gamma$  is the off-axis angle of the finite element  $d\Omega$  (Figure 4.2). Using  $z$  as the optical axis, the above expression may be expressed in spherical coordinates as follows

$$I(z, \sigma_o) = \iint \sin \theta \cos(2\pi\sigma_o z \cos \theta) d\theta d\phi, \quad (4.4)$$

where  $d\Omega = \sin\theta d\theta d\phi$ , and  $\cos\gamma = \cos\theta$  by virtue of the coordinate system selected. Figure 4.2 illustrates three cases to consider in the evaluation of Equation 4.4 [150], namely  $\beta = 0$ ,  $\alpha > \beta$ , and finally  $\beta > \alpha$ .

Let  $\psi(\theta)$  represent the integration of the  $\phi$  portion of Equation 4.4. Using the result of Equation C.1 (as derived in Appendix C),  $\psi(\theta)$  is expressed as follows

$$\psi(\theta) = \int d\phi = \begin{cases} 0 & , \beta > \alpha, \theta < |\alpha - \beta| \\ 2\pi & , \alpha > \beta, \theta < |\alpha - \beta| \\ 2 \cos^{-1} \left( \frac{\cos \alpha - \cos \beta \cos \theta}{\sin \beta \sin \theta} \right) & , \theta > |\beta - \alpha| \\ 0 & , \theta > \beta + \alpha \end{cases} , \quad (4.5)$$

where  $\psi$  is a function of  $\theta$  for  $|\alpha - \beta| < \theta < (\alpha + \beta)$ , and constant (either 0 or  $2\pi$ ) outside of that range. For  $\beta = 0$  (the left panel of Figure 4.2), the result is simply that derived in §2.7.3, i.e.  $\psi = 2\pi$ . For  $\beta > \alpha$ ,  $\psi$  is a function of  $\theta$  for its entire range. The final case of  $\alpha > \beta$ ,  $\beta \neq 0$  is a combination of the two other cases, where  $\psi$  is constant for the initial values of  $\theta$  near the optical axis and becomes a function of  $\theta$  once  $\theta > |\beta - \alpha|$ .

The differential form of Equation 4.2 is given by [151]

$$d\sigma = -\sigma_o \sin\theta d\theta \quad [\text{cm}^{-1}] . \quad (4.6)$$

The above expression may be used to transform  $\psi$  into a function of  $\sigma$  as follows

$$\psi(\sigma) = \begin{cases} 0 & , \beta > \alpha, \sigma > \sigma_o \cos(\alpha - \beta) \\ 2\pi & , \alpha > \beta, \sigma > \sigma_o \cos(\alpha - \beta) \\ 2 \cos^{-1} \left( \frac{\sigma_o \cos \alpha - \sigma \cos \beta}{\sigma_o \sin \beta \sqrt{\sigma_o^2 - \sigma^2}} \right) & , \sigma_o \cos(\beta + \alpha) < \sigma < \sigma_o \cos(\beta - \alpha) \\ 0 & , \sigma < \sigma_o \cos(\beta + \alpha) \end{cases} . \quad (4.7)$$

The above relation then allows Equation 4.4 to be integrated across  $\sigma$  instead of  $\theta$  as follows

$$I(z, \sigma_o) = \int \psi(\sigma) \cos(2\pi\sigma z) d\sigma, \quad (4.8)$$

where the integration limits depend on the axial configuration of the detector (see Figure 4.2). For  $\alpha > \beta$ ,  $\sigma \in [\sigma_o \cos(\alpha + \beta), \sigma_o]$ , and for  $\beta > \alpha$ ,  $\sigma \in [\sigma_o \cos(\alpha + \beta), \sigma_o \cos(\beta - \alpha)]$ .

Equation 4.8 is a representation of the cosine Fourier transform of  $\psi(\sigma)$ . An FTS ILS,  $\Pi(\sigma)$ , corresponds to the interferogram of a monochromatic source (e.g. frequency  $\sigma_o$ ),  $I(z, \sigma_o)$ , through the inverse Fourier transform as follows

$$I(z, \sigma_o) = \int \Pi(\sigma) \cos(2\pi\sigma z) d\sigma. \quad (4.9)$$

Therefore, the expression  $\psi(\sigma)$  within Equation 4.8 is simply a representation of the FTS ILS at frequency  $\sigma_o$ .

#### 4.3.4 Axial Variation of Spectral Resolution

Figure 4.4 illustrates the frequency shift of a spectral feature due to natural apodization for an on-axis detector. The ILS is uniformly broadened from  $\sigma_o$  on-axis to  $\sigma_o \cos \alpha$  off-axis, where the FOV half-angle is  $\alpha$ . It has been shown that the line-shape is always confined to  $[\sigma_o \cos \theta_{max}, \sigma_o \cos \theta_{min}]$ , where  $\theta_{min}$  and  $\theta_{max}$  are the minimal and maximal angles accepted by a detector [151]. The detector spectral resolution is therefore expressed as

$$\begin{aligned} \Delta\sigma_{\text{off-axis}}(\alpha, \beta) &= \sigma_o(\theta_{min}) - \sigma_o(\theta_{max}) \\ &= \sigma_o \begin{cases} 1 - \cos(\alpha + \beta) & , \quad \alpha > \beta \\ 2 \sin \alpha \sin \beta & , \quad \beta > \alpha \end{cases} \quad [\text{cm}^{-1}], \quad (4.10) \end{aligned}$$

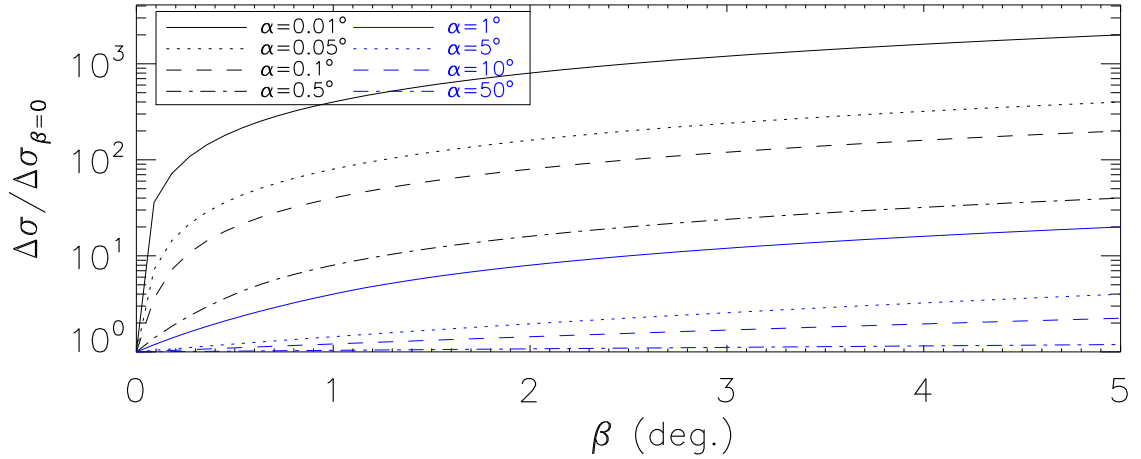


Figure 4.6: Variation of spectral resolution with detector off-axis position,  $\beta$ , for detector FOV values of  $\alpha = [0.01^\circ, 0.05^\circ, 0.1^\circ, 0.5^\circ, 1^\circ, 5^\circ, 10^\circ, 50^\circ]$ . The resolution shown has been normalized to the on-axis case, i.e.  $\beta=0$ .

where the spectral width  $\Delta\sigma_{\text{off-axis}}$  is taken as the full-width to zero amplitude. The reason that the FWHM should not be used in this description is discussed in §4.3.5. Figure 4.6 illustrates the change in spectral resolution, normalized to the on-axis case (i.e.  $\beta = 0$ ), as  $\alpha$  &  $\beta$  vary.

#### 4.3.5 Axial Variation of Instrument Line-Shape

As discussed in §4.3.3, the ILS across an IFTS detector array, neglecting finite OPD considerations for the moment, is given by  $\psi(\sigma, \alpha, \beta)$  for circular detectors (Equation 4.7). Finite OPD effects require that the infinite OPD ILS discussed here be convolved with a sinc function; this will be included in §4.4.2 but is not important for the discussion here. Figure 4.7 illustrates examples of the IFTS ILS, i.e.  $\psi(\sigma)$ , for each of the three cases shown in Figure 4.2.

An approximation of the observed spectral line centre ( $\sigma'_o$ ) may be obtained as the



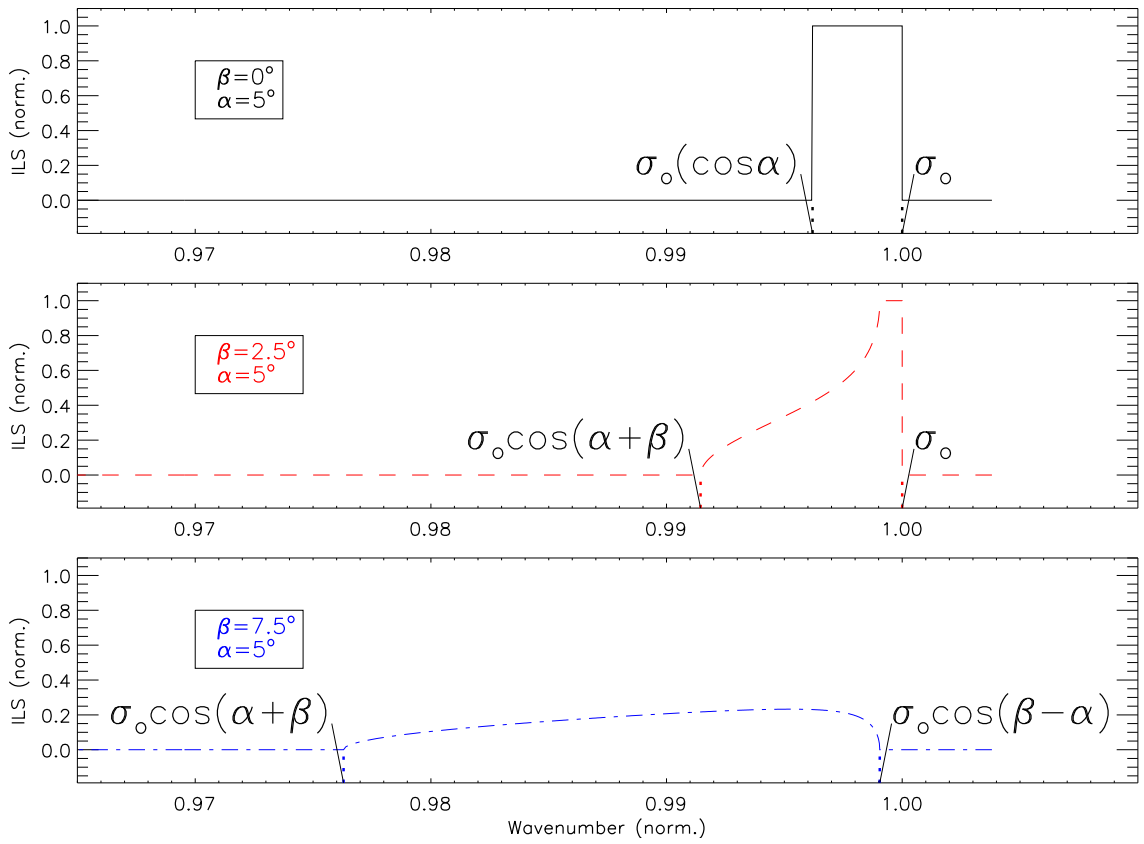


Figure 4.7: Normalized ILS profiles for  $\alpha = 5^\circ$  and  $\beta = 0^\circ$  (top),  $\beta = 2.5^\circ$  (middle), and  $\beta = 7.5^\circ$  (bottom). These ILS profiles are examples of each of the three detector configurations shown in Figure 4.2.

intermediate frequency of the ILS as follows

$$\begin{aligned}\sigma'_o &= \frac{\sigma_o(\theta_{min}) + \sigma(\theta_{max})}{2} \\ &= \sigma_o \begin{cases} 1/2 + \cos(\alpha + \beta)/2 & , \alpha > \beta \\ \cos \alpha \cos \beta & , \beta > \alpha \end{cases} \quad [\text{cm}^{-1}], \end{aligned} \quad (4.11)$$

where the ILS is assumed to be relatively flat in order for the above approximation to be considered valid. To account for the structure of the ILS, the effective line centre may be identified as the area centroid of  $\psi(\sigma)$  as follows

$$\sigma'_o = \frac{\int \sigma \psi(\sigma) d\sigma}{\int \psi(\sigma) d\sigma} \quad [\text{cm}^{-1}]. \quad (4.12)$$

The above expression is difficult to evaluate analytically but is easily evaluated numerically for a given  $\alpha$  &  $\beta$ . It is clear from Figure 4.7 that an equivalent rectangle ILS is easily defined for on-axis detectors, and detectors where  $\alpha \ll \beta$ , but is not a practical approximation for intermediate locations in an array where  $\alpha \approx \beta$ . This is particularly important in the context of misalignment of the on-axis detector, where the off-axis angle  $\beta$  may be thought of as a misalignment. Figure 4.8 illustrates the shift in  $\sigma'_o$  across a detector array for various  $\alpha$  and  $\beta$ .

#### 4.3.6 Detector Optical Alignment

One important consideration in IFTS is that the central pixel should be on-axis, while no other pixels will be on-axis for a given detector array. Therefore, for the central pixel,  $\beta = 0$  ideally, and, by definition,  $\beta < \alpha$  should hold true. For all off-axis pixels  $\beta > \alpha$ . Therefore, any of the equations above (e.g. Equations 4.8, 4.10, & 4.11) describing conditions where  $\alpha > \beta$  should be thought of as addressing optical alignment of the central

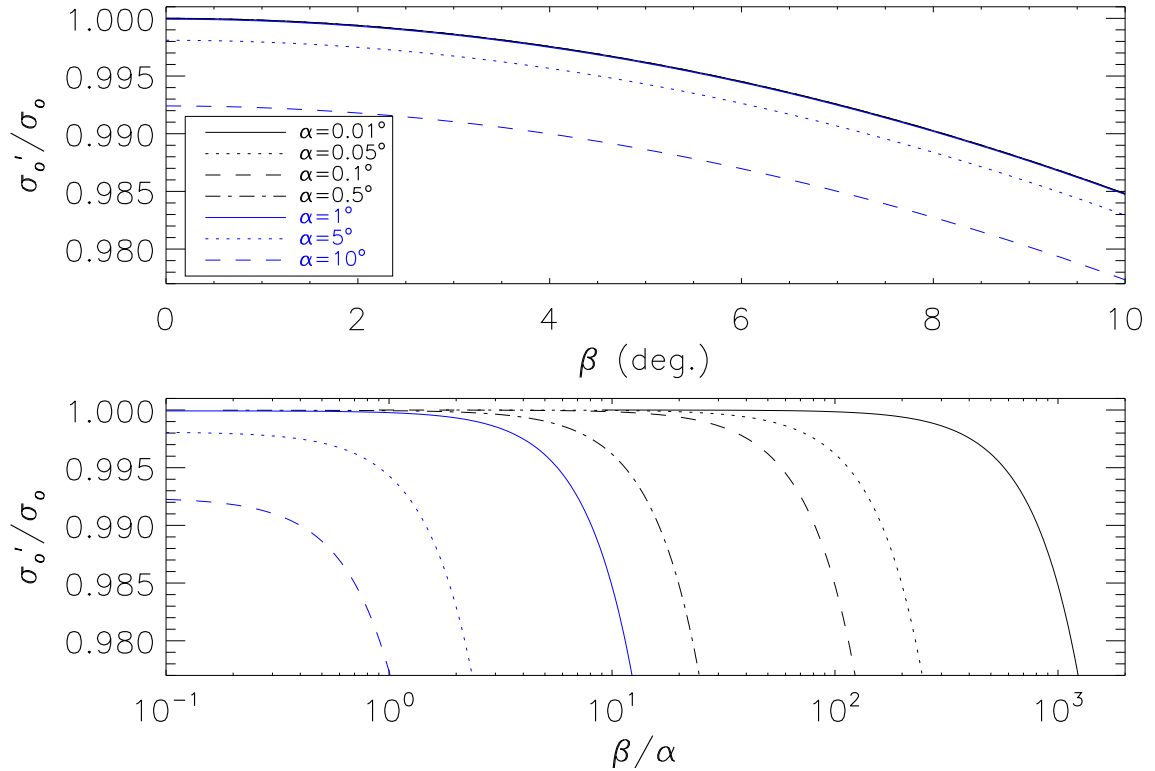


Figure 4.8: Variation of expected line centre as a function of detector off-axis position,  $\beta$ , for detector FOV values of  $\alpha = [0.01^\circ, 0.05^\circ, 0.1^\circ, 0.5^\circ, 1^\circ, 5^\circ, 10^\circ]$ . The line centre has been normalized to the on-axis case, i.e.  $\beta = 0$ . The upper plot shows the line centre variation with  $\beta$  expressed in degrees. The  $\alpha = [0.01^\circ, 0.05^\circ, 0.1^\circ, 0.5^\circ, 1^\circ]$  cases are virtually identical in the  $\beta \in [0^\circ, 10^\circ]$  range. The lower plot illustrates the same trend for  $\beta$  normalized with respect to  $\alpha$ , where differences in the small  $\alpha$  curves are more evident.

pixel, and  $\beta$  can be thought of as error in optical alignment. The  $\beta > \alpha$  condition addresses all remaining off-axis pixels.

## 4.4 The SPIRE IFTS

This section discusses the extended FOV and off-axis effects expected and observed within the SPIRE IFTS. The term obliquity effects will be used hereafter to refer to either effect individually or their combined effect. The two output ports of the SPIRE IFTS each contain detector arrays covering separate frequency ranges across the SPIRE band to allow greater spatial sampling and detection efficiency [13]. This section will look at the expected variation of instrument performance across the SPIRE IFTS detector arrays. The following section (§4.7) will discuss the astronomical implications of axial variation and obliquity effects in spectral performance for the SPIRE IFTS.

### 4.4.1 The SPIRE Detector Arrays

The SLW array covers a frequency range of  $14.9 - 33.6 \text{ cm}^{-1}$  ( $298 - 671 \text{ }\mu\text{m}$ ) [16], and has 19 detectors arranged in a hexagonal close packed (HCP) configuration distributed in three concentric rings about the central detector. The SLW beams are  $\sim 48''$  apart on the sky, while the FOV of each detector is frequency dependent and varies between  $\sim 32''$  near the band centre and  $\sim 40''$  near the band edges [152]. A nominal value for the FOV half-angle of  $20''$  will be used for the SLW FOV. A  $2.6'$  instrument FOV causes partial vignetting of the peripheral detectors in both the SLW and SSW arrays [153].

The SSW array covers a frequency range of  $31.3 - 52.1 \text{ cm}^{-1}$  ( $191 - 323 \text{ }\mu\text{m}$ ), and

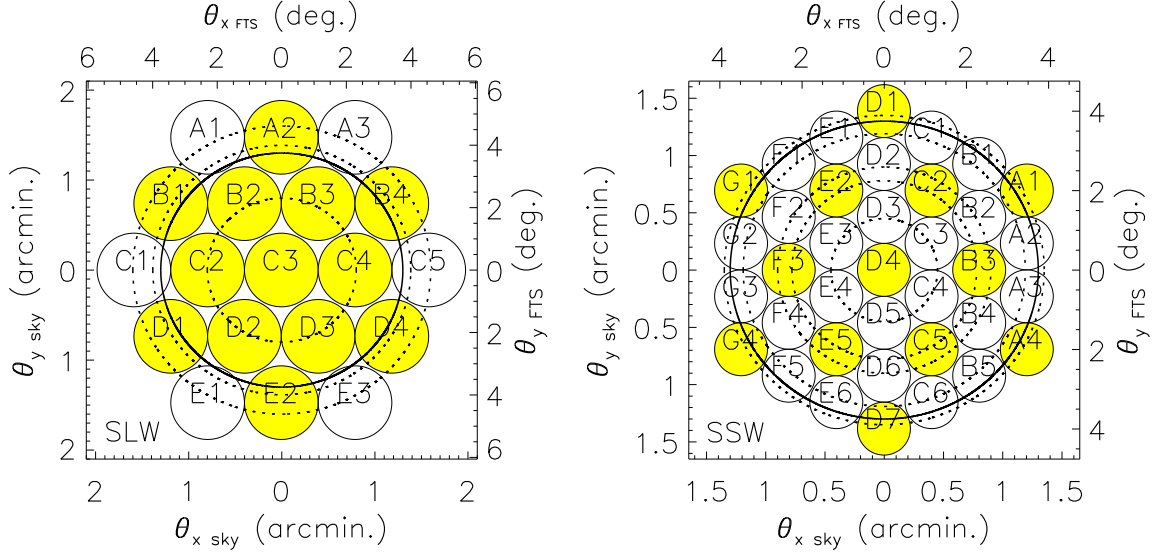


Figure 4.9: Angular position of SLW & SSW detectors on the sky (left and bottom axes) and the divergence angle within the FTS (top and right axes) for both detector arrays. The shaded pixels represent those that are co-aligned in both arrays. The  $2.6'$  diameter circle (solid) represents the SPIRE instrument FOV, outside of which partial vignetting occurs on the detectors. The dashed circles represent the off-axis concentric rings about which the HCP detectors are aligned (SLW – 3, SSW – 5).

has 37 detectors arranged in a HCP configuration distributed in five concentric rings about the central detector. The SSW beams are  $\sim 27''$  apart on the sky, while the FOV of each detector is frequency dependent and varies between  $\sim 15.5''$  near the band centre and  $\sim 17.4''$  near the band edges [152]. A nominal FOV half-angle of  $8''$  will be used for the SSW array. The layout of both detector arrays, including the  $2.6'$  instrument FOV (solid curve) and the off-axis concentric rings (dashed curves), is shown in Figure 4.9.

The conversion between sky angles ( $\theta_{\text{sky}}$ ) and off-axis angles within the SPIRE IFTS ( $\theta_{\text{FTS}}$ ) may be determined through the Lagrangian invariant [124], between the entrance and exit pupils as follows [154]

$$\theta_{\text{FTS}} = \theta_{\text{sky}} \left( \frac{D_{\text{tel}}}{D_{\text{pup}}} \right), \quad (4.13)$$

Table 4.2: SPIRE IFTS obliquity angle design specifications [13].

Array	$\alpha$		$\beta$		Detectors
	$\alpha_{\text{sky}}$	$\alpha_{\text{FTS}}$	$\beta_{\text{sky}}$	$\beta_{\text{FTS}}$	
SLW	20''	.96°	0''	0°	C3
			48''	2.3°	B2, B3, C2, C4, D2, D3
			83''	4.0°	A2, B1, B4, D1, D4, E2
			96''	4.6°	A1, A3, C1, C5, E1, E3
SSW	8''	0.4°	0''	0°	D4
			27''	1.3°	C3, C4, D3, D5, E3, E4
			47''	2.2°	B3, C2, C5, E2, E5, F3
			54''	2.6°	B2, B4, D2, D6, F2, F4
			71''	3.4°	A2, A3, B1, B5, C1, C6, E1, E6, F1, F5, G2, G3
			81''	3.9°	A1, A4, D1, D7, G1, G4

where  $D_{\text{tel}}$  and  $D_{\text{pup}}$  represent the pupil diameters of the telescope and FTS, respectively, resulting in a scaling of the off-axis angles seen within the SPIRE IFTS. Equation 4.13 is another way of stating that, in a well designed optical system, throughput or *étendue* is conserved. Table 4.2 shows expected values of detector FOV ( $\alpha_{\text{sky/FTS}}$ ) and angular offset ( $\beta_{\text{sky/FTS}}$ ) for both spectrometer arrays. Table 4.3 compares the expected  $\beta_{\text{sky}}$  with values calculated using PFM calibration test data. On-sky angles are derived assuming nominal Herschel telescope characteristics; actual in-flight values will not be determined accurately until the Herschel commissioning phase following the telescope launch [152].

#### 4.4.2 The Theoretical SPIRE IFTS ILS

The theoretical ILS functions determined with Equation 4.7, corresponding to the angles shown in Table 4.2 and infinite spectral resolution, are shown in Figure 4.10 for the SLW array, and in Figure 4.11 for the SSW array. The on-axis/central detector for each array has a rectangular ILS (normalized to unity amplitude) similar to that shown in

Table 4.3: SPIRE IFTS expected and measured on-sky  $\beta$ .

Array	$\beta_{\text{sky}}$	
	expected	measured
SLW	0''	0.2''
	48''	47.9'' $\pm$ 1.1''
	83''	83.0'' $\pm$ 2.3''
	96''	96.3'' $\pm$ 2.4''
SSW	0''	0''
	27''	27.0'' $\pm$ 0.6''
	47''	46.7'' $\pm$ 1.6''
	54''	54.0'' $\pm$ 2.1''
	71''	71.4'' $\pm$ 2.8''
	81''	81.2'' $\pm$ 3.9''

Figure 4.4. The off-axis detectors exhibit an ILS which deviates from the on-axis rectangular structure. Although the integrated area of the ILS (neglecting vignetting) is conserved for both the on- and off-axis cases, the amplitude of the off-axis ILS is reduced and the width is broadened. The inability of the instrument to see beyond  $1.3'$  on the sky from the optical axis, corresponding to a  $3.75^\circ$  divergence angle within the FTS (Equation 4.13), causes the modulation of each spectral component to be limited also (Equation 4.6). As shown by the dashed lines in Figures 4.10 & 4.11, the ILS for the vignetted detectors is truncated. This serves to reduce the obliquity induced frequency shift of a spectral feature, and causes a reduction in the integrated area of the ILS, i.e. energy is no longer conserved. The effect of vignetting on the measured data has been confirmed, as is shown in Figures 4.17 & 4.18.

Although the infinite spectral resolution ILS functions clearly change with axial position, the widths of each ILS remain significantly less than any practical spectral resolution, i.e.  $\sigma_o(\cos \theta_{min} - \cos \theta_{max}) \ll \Delta\sigma$ . Figures 4.12 & 4.13 illustrate the expected ILS for finite spectral resolutions, evaluated at the spectral band centre of each array and for

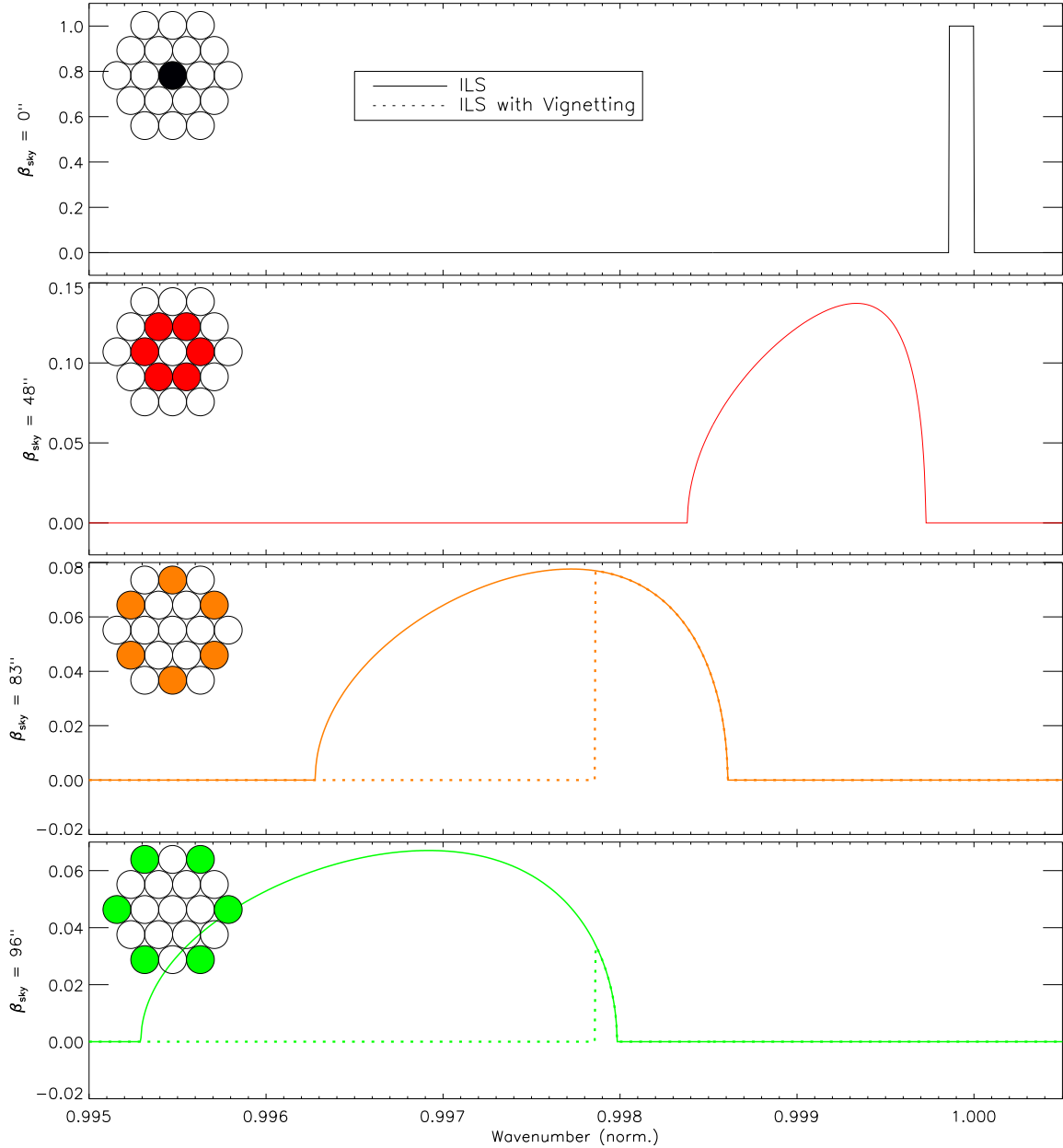


Figure 4.10: The ILS functions (Equation 4.7) for the SPIRE SLW array corresponding to the infinite spectral resolution case. Dashed curves show the theory including vignetting for on-sky angles greater than  $1.3'$ .



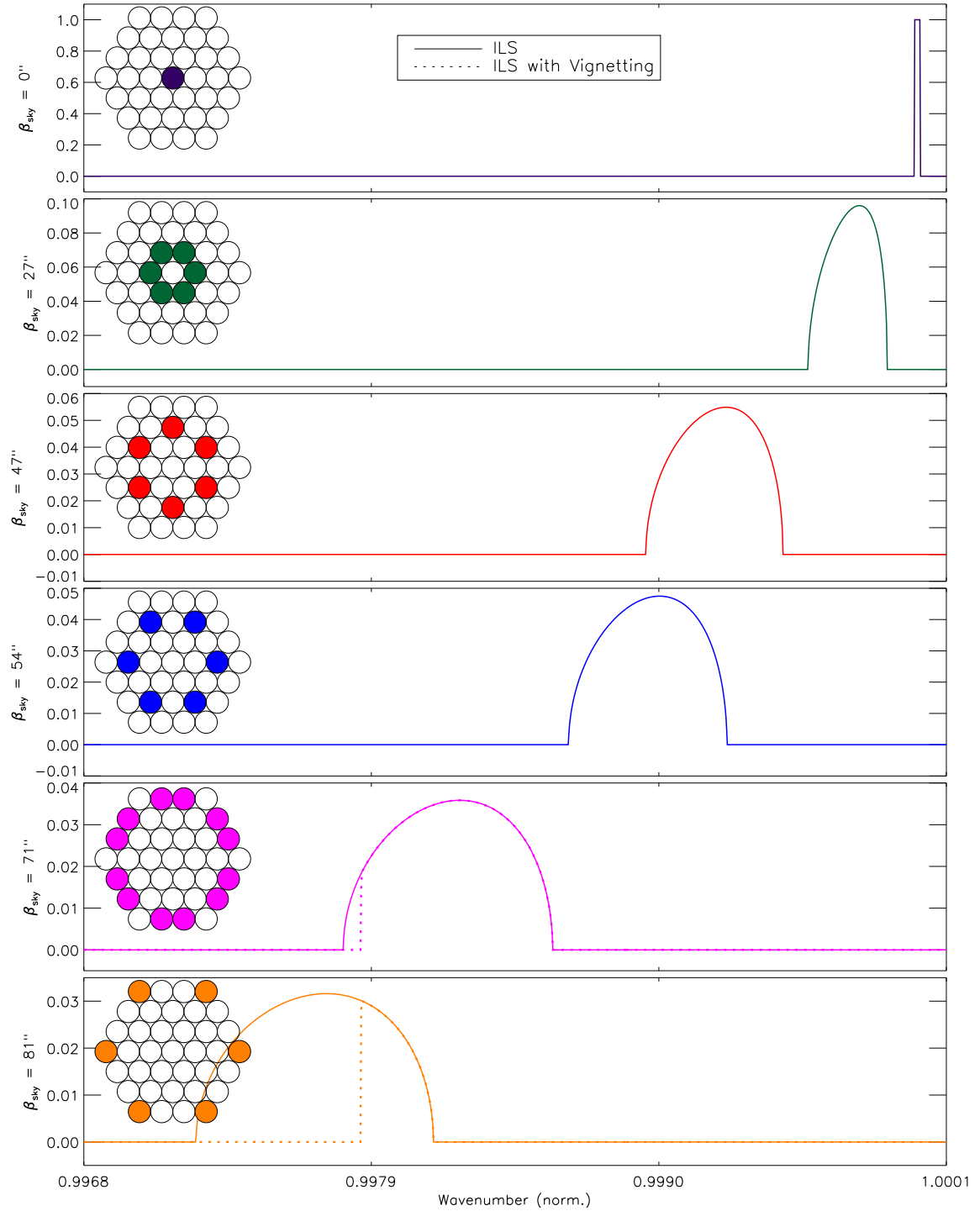


Figure 4.11: The ILS functions (Equation 4.7) for the SPIRE SSW array corresponding to the infinite spectral resolution case. Dashed curves show the theory including vignetting for on-sky angles greater than  $1.3'$ .

---

all SPIRE IFTS astronomical observation template (AOT) spectral resolutions. Although the true off-axis/finite FOV ILS is a sinc convolved with some other function, the observed ILS for an IFTS can be reasonably approximated by a sinc of modified width and centre frequency, as is demonstrated in Figures 4.12 & 4.13. As the individual ILS functions corresponding to finite spectral resolutions (low, medium, and high) are difficult to isolate within Figures 4.12 & 4.13, the axial ILS functions for the high-resolution case have been normalized in Figures 4.14 & 4.15 for SLW and SSW, respectively. In these figures, the ILS functions for each axial detector position have been frequency normalized after a frequency shift up to the centre frequency of the on-axis ILS was performed. The ILS width is seen to increase as detectors are moved away from the optical axis.

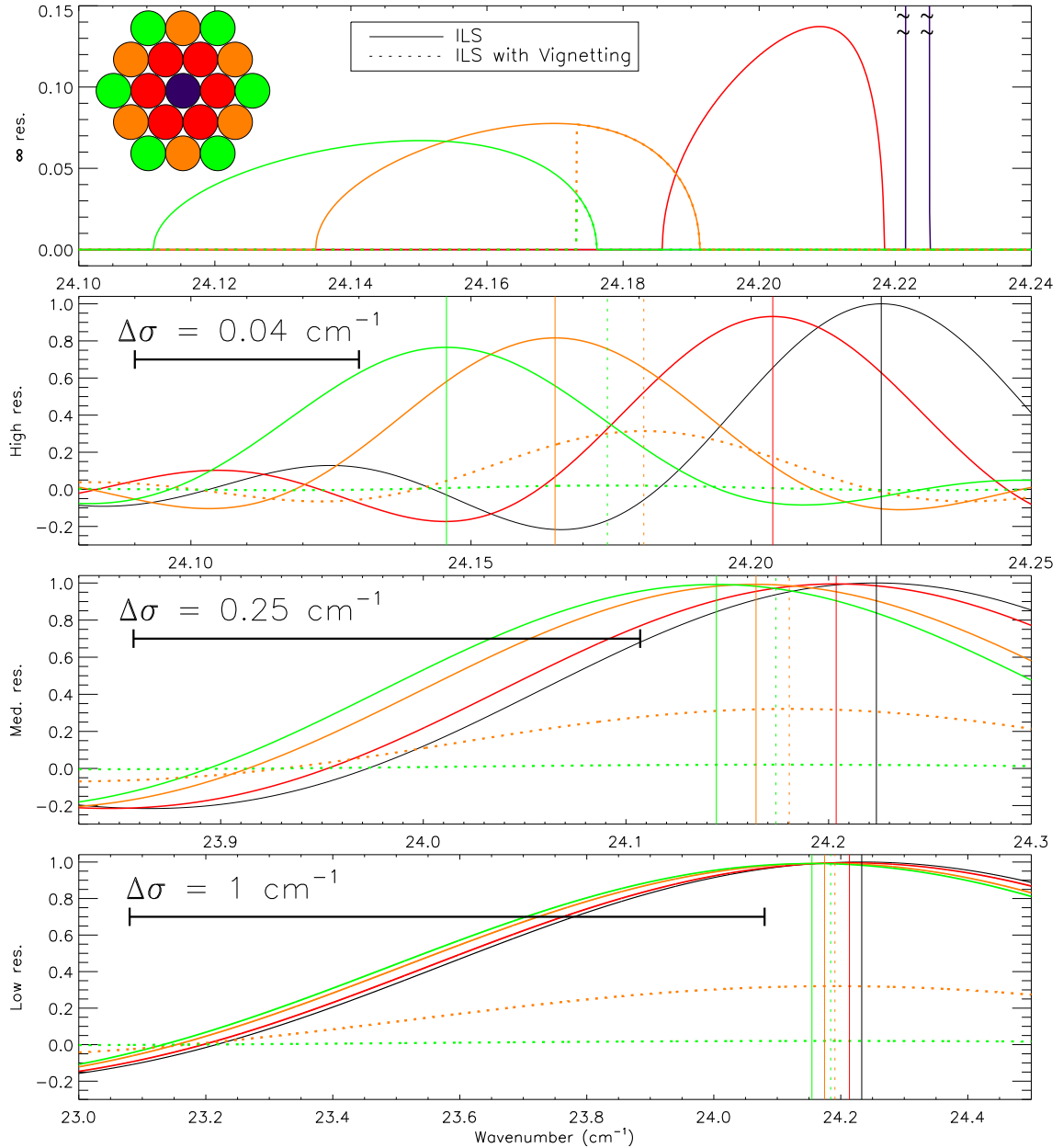


Figure 4.12: The ILS functions for the SPIRE SLW array for infinite (top), high (second row), medium (third row), and low (bottom) spectral resolutions. Dashed curves show the theory including vignetting for on-sky angles greater than  $1.3'$ . Vertical bars represent the line centre of each case. The frequency offset between the unvignetted (solid vertical bars) and vignetted (dashed) cases is clearly significant for high spectral resolution as it is on the order of a resolution element. The frequency shift between the vignetted and unvignetted case is less significant for medium-resolution scans, and barely perceptible compared to a resolution element for low spectral resolution.

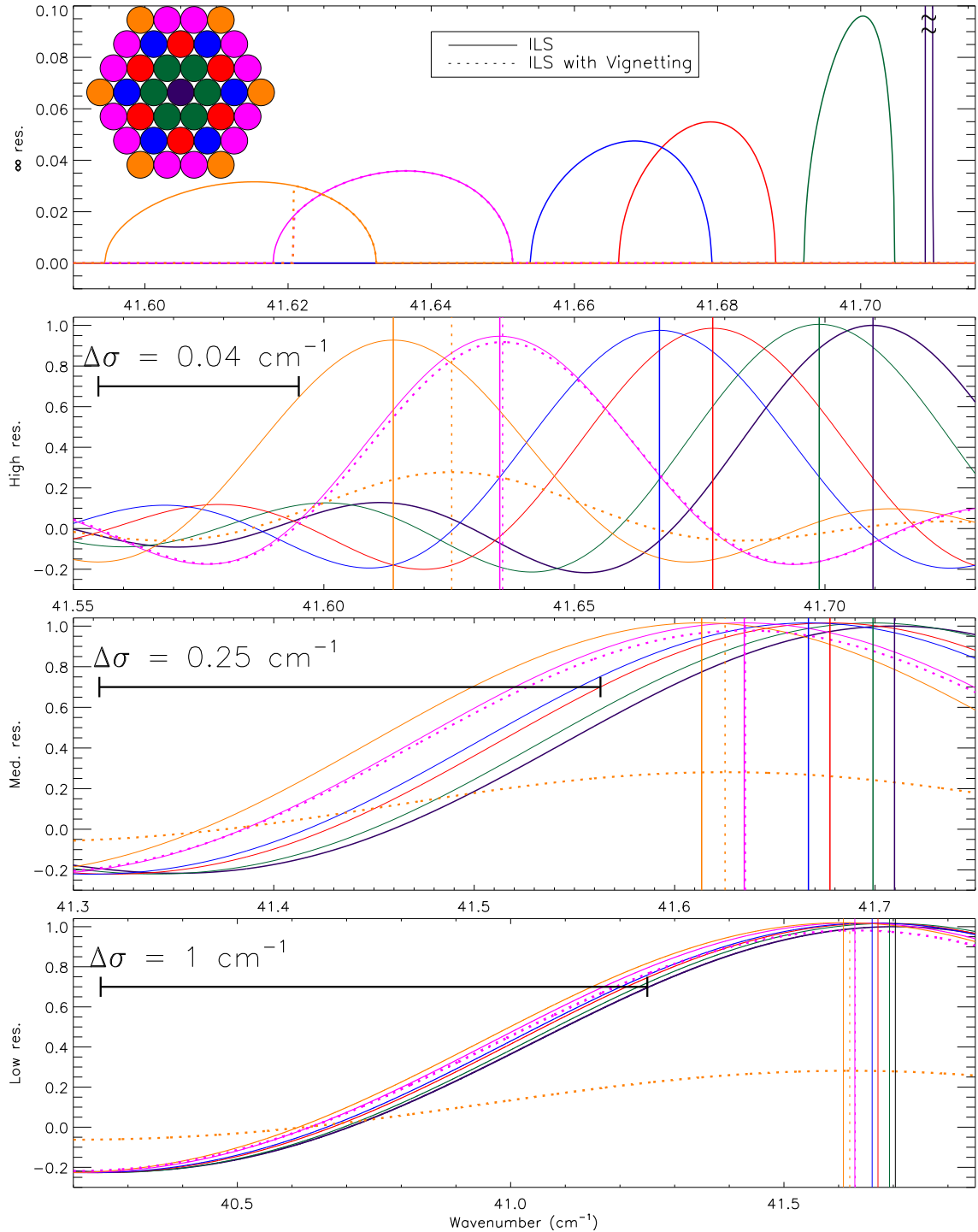


Figure 4.13: The ILS functions for the SPIRE SSW array for infinite (top), high (second row), medium (third row), and low (bottom) spectral resolutions. Dashed curves show the theory including vignetting for on-sky angles greater than  $1.3'$ . As in Figure 4.12, the difference in line centre for the vignettted and unvignettted cases is significant for high spectral resolution. Conversely, the vignetting frequency shift is not significant for medium- and low-resolution scans.

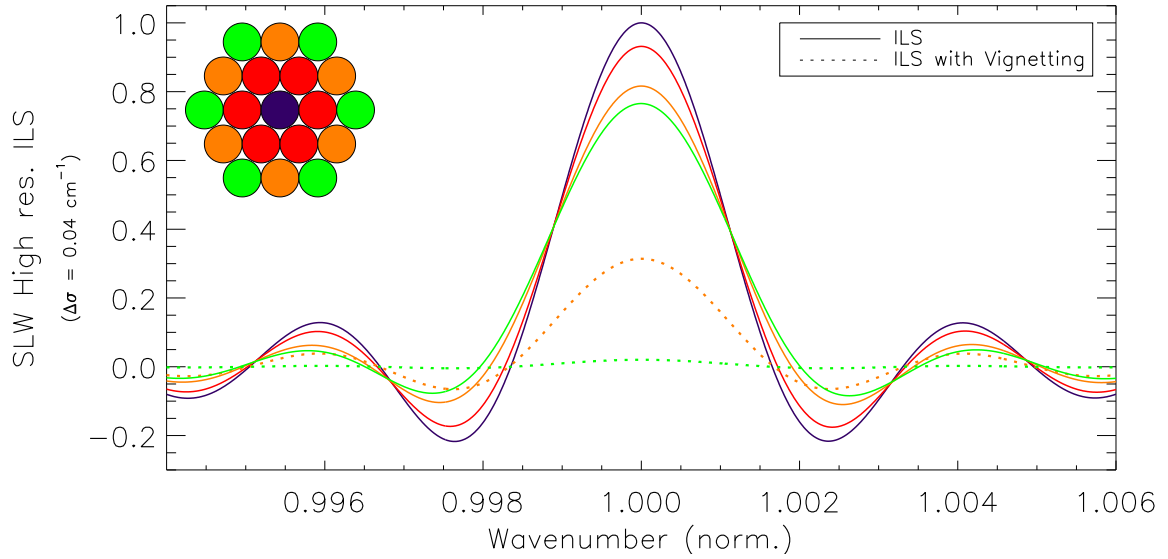


Figure 4.14: Frequency normalized high-resolution ILS functions for all axial detector positions of the SPIRE SLW array. In order of decreasing amplitude, the ILS functions correspond to the rows of Figure 4.10. The dashed curves represent the vignettted case.

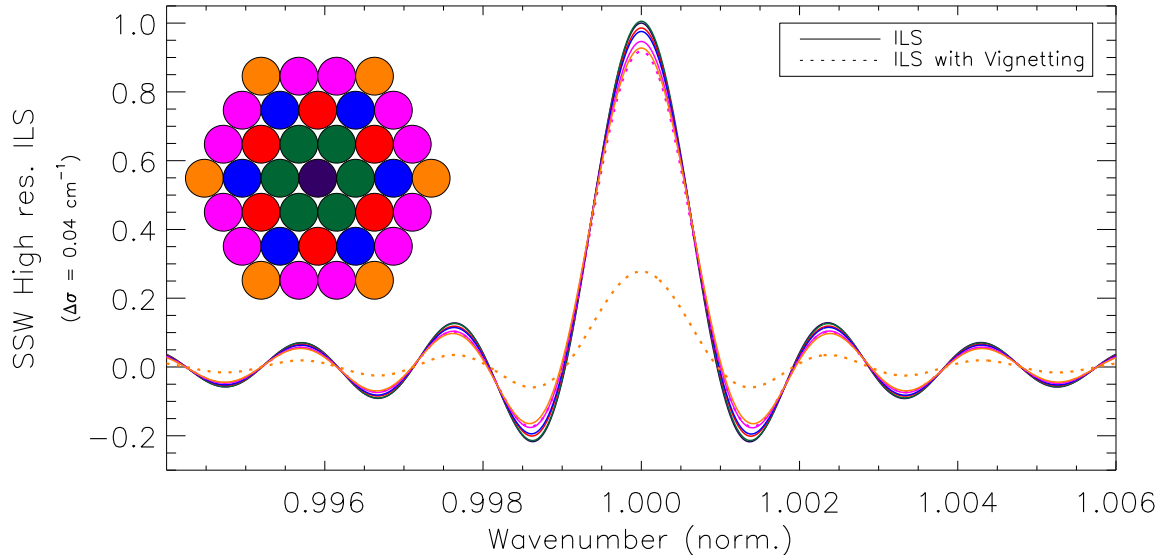


Figure 4.15: Frequency normalized high-resolution ILS functions for all axial detector positions of the SPIRE SSW array. In order of decreasing amplitude, the ILS functions correspond to the rows of Figure 4.11. Dashed curves represent the vignettted case.

## 4.5 Spectral Line Sources for Ground Testing

As discussed in §4.1, the simplest way to determine the ILS of an FTS is to use an unresolved spectral line source. The unresolved spectral line sources used in the PFM test campaigns were a molecular laser and a photonic mixer [155, 156]. This section will discuss the use of the molecular laser to characterize the SPIRE IFTS. The photonic mixer will be discussed in greater detail in §5.5.1.

One of the SPIRE test facility subsystems is a molecular laser (Edinburgh Instruments model 295 FIR). In operation, the laser is optically pumped by a CO<sub>2</sub> laser, which is tuned to match the pumping transition of a particular molecular gas in the laser resonant cavity. A beamsplitter placed in the output path of the molecular laser directs a portion of the beam towards a pyroelectric detector, which monitors and records the laser output power. With the selection of CO<sub>2</sub> pump lines, variable cavity length, and the lasing molecular gas, the resonant cavity is capable of providing a variety of laser lines throughout the far-infrared. Table 4.4 lists the pump states and transition lines used during PFM testing of the SPIRE spectrometer for either methanol (CH<sub>3</sub>OH) or formic acid (HCOOH) as the lasing molecular gas. Each of these transitions has been well studied and the corresponding frequencies are documented in the literature [157].

I was stationed at RAL in late 2006 for the duration of the PFM-4 test campaign (see Table 1.1). Between 21 November and 8 December of 2006, approximately 154 up/down high-resolution interferogram scan pairs were recorded with the molecular laser tuned to output one of the transitions listed in Table 4.4. This constitutes over six hours of observation time (excluding instrument overheads and the significant time taken to prepare,

tune, and maintain the laser) and resulted in ~1 GB of raw data (~6631 kB per scan pair). Including intermediate data products such as detector signal timelines, FTS translation stage position timelines, pre- and post- phase correction interferograms, spectra, averaged spectra, etc., the PFM-4 molecular laser observations occupy ~7 GB of disk space (~49 MB per scan pair).

The spectra resultant from the laser observations were analyzed to determine the observed line centre and corresponding uncertainty. These results were used to compare the observed axial frequency shift with that expected from the theory discussed above (§4.4.2).

Table 4.4: Summary of FTS laser spectra taken during PFM test campaigns.

Gas	CO <sub>2</sub> Pump line	laser line (cm <sup>-1</sup> )
HCOOH	9R 28	19.4925817(6)
		19.4930921(2)
HCOOH	9R 20	23.1124893(7)
		23.1143706(8)
HCOOH	9R18	25.4045183(4)
HCOOH	9R 4	33.0821464(5)
CH <sub>3</sub> OH	9R 10	42.9296823(7)
CH <sub>3</sub> OH	9P36	49.407(1) [158]

## 4.6 SPIRE ILS Characterization Results

During the SPIRE IFTS characterization portion of PFM testing, interferograms of unresolved spectral sources (e.g. various HCOOH or CH<sub>3</sub>OH transition lines of the molecular laser), directed towards individual pixels within both the SLW and the SSW arrays, were recorded. While the spectrometer views the line sources, it is also subject to ambient radiation from the test laboratory environment. Thus, the measured interferograms contain

both interference fringes from the unresolved line, which are observed as cosinusoidal oscillations throughout the length of the interferogram, and the broadband contribution from the background, which provides a large modulated signal component near ZPD. Standard FTS processing routines were used in the reduction of the data to generate spectra; this included phase correction using the Forman method [20] to remove interferogram asymmetries, and multiple scan averaging to reduce noise. A least-squares fitting routine is used to determine the amplitude, width, and central frequency of the sinc ILS for each spectral line. An example of the observed SPIRE IFTS ILS is provided in Figure 4.16. This figure shows a spectrum of an unresolved spectral feature from the photonic mixer in the SPIRE test facility laboratory after the laboratory background continuum had been removed (see §5.5.1). The circles represent the measured data and the solid line represents the sinc fit. There is excellent agreement between the observed and theoretical ILS for the SPIRE IFTS. This level of agreement is especially important when weak lines are in close proximity to strong spectral lines.

The uncertainty in the spectral line is related to the ILS width (i.e.  $\Delta\sigma$ ) and S/N by [159]

$$\delta\sigma_o \propto \frac{\Delta\sigma}{S/N} \quad [\text{cm}^{-1}]. \quad (4.14)$$

The measured frequencies are compared to their theoretical values with the resulting frequency shift shown against on-sky angular position in Figures 4.17 (SLW) & 4.18 (SSW).

The vignetting in the theoretical model is assumed to be a complete cut-off of anything outside of the allowed 1.3' radius FOV, equivalent to a divergence angle of 3.75° within the interferometer. This example was selected to demonstrate an upper limit estimate



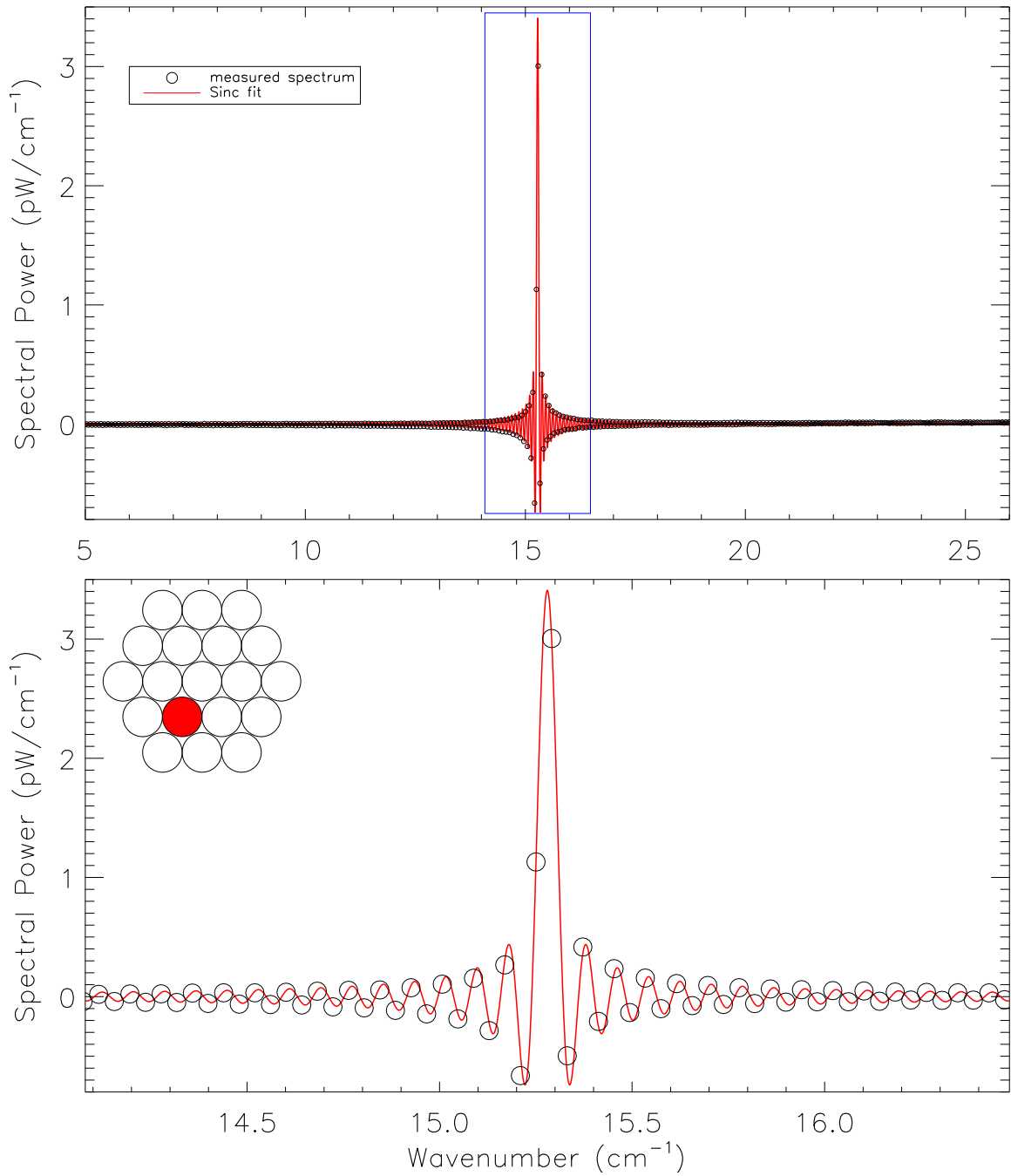


Figure 4.16: Measured ILS function for the SPIRE SLW-D2 detector determined through observations viewing an unresolved spectral source, i.e. the photonic mixer. The solid curve shows the theoretical sinc function and the circles represent measured data.

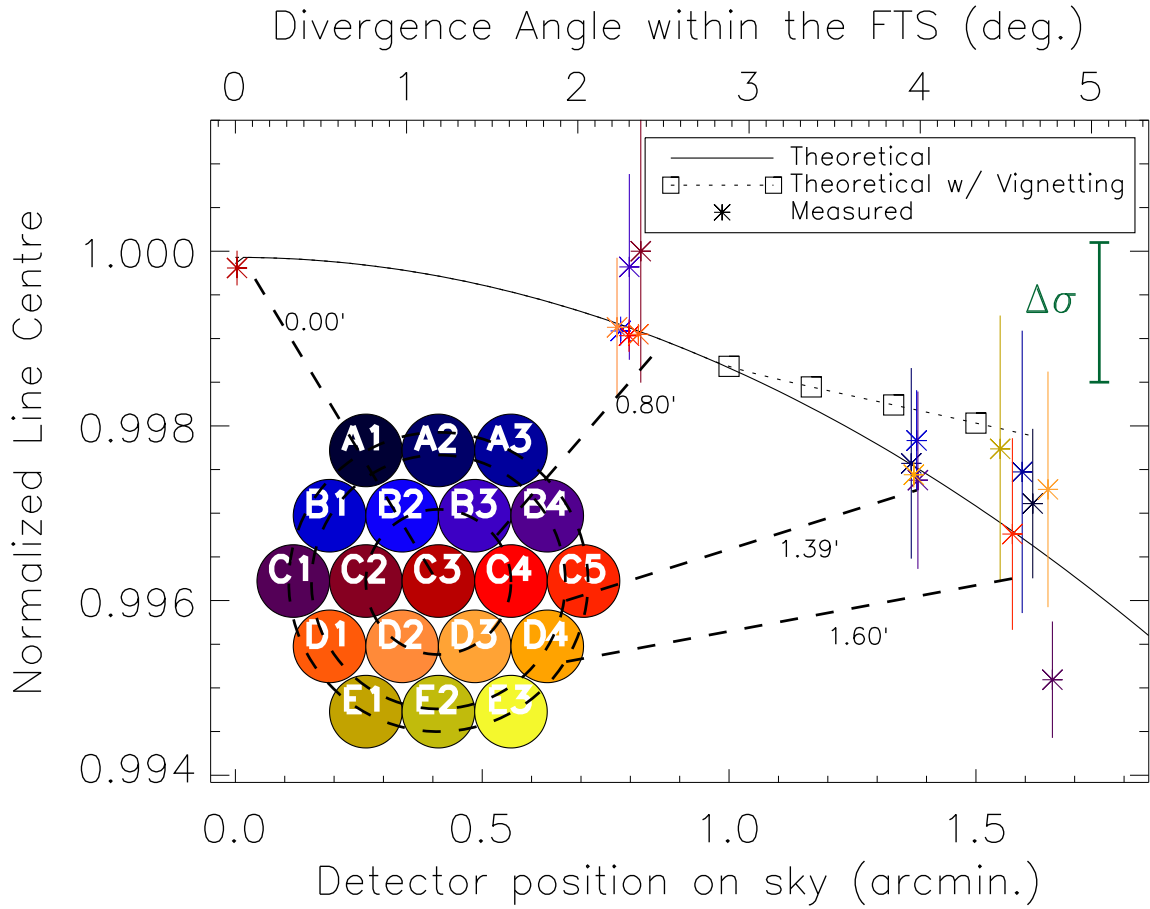


Figure 4.17: The observed shift in spectral frequency  $\sigma'_o$  (asterisks) for detector on-sky position (bottom axis) or FTS divergence angle (top axis). Also shown is the theoretical expectation, both with vignetting (dashed curve with squares), and without (solid curve), for the SLW array.

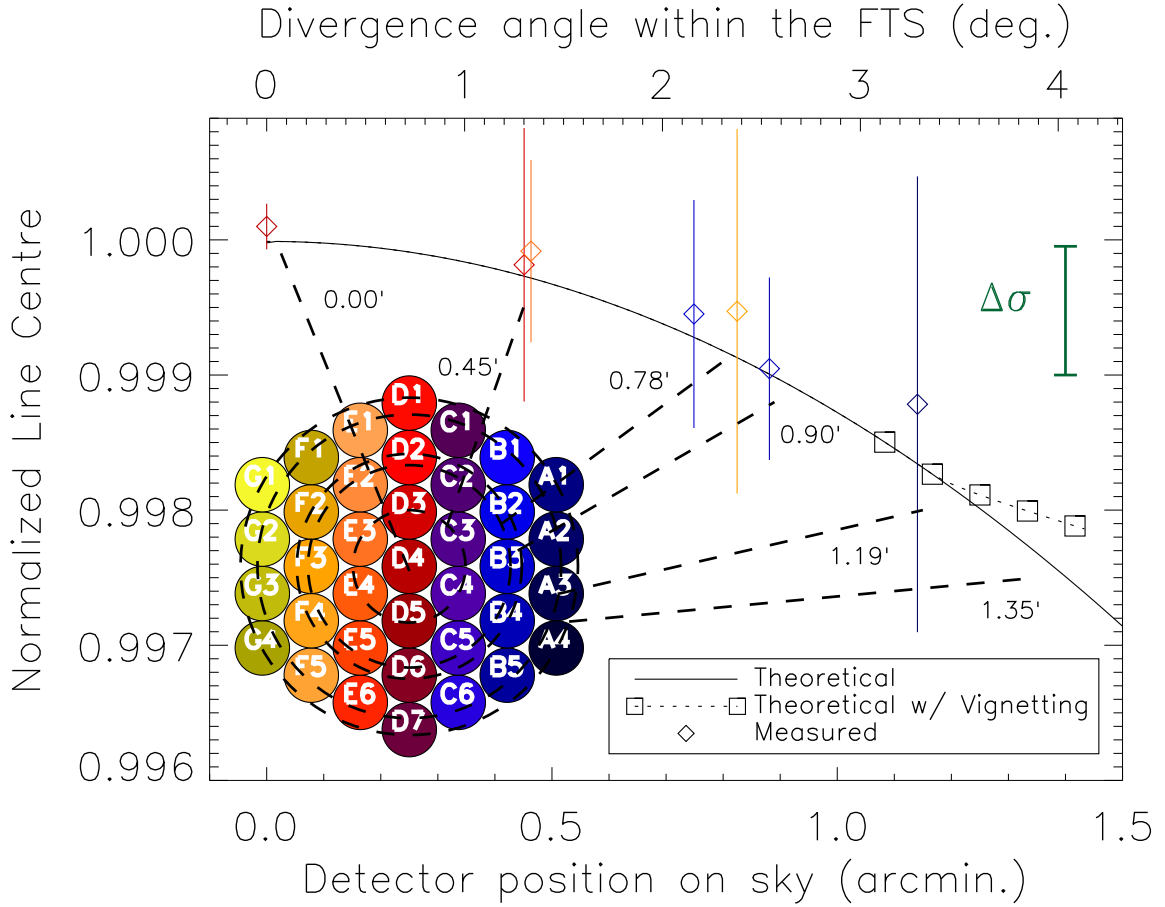


Figure 4.18: The observed shift in spectral frequency  $\sigma'_o$  (diamonds) for detector on-sky position (bottom axis) or FTS divergence angle (top axis). Also shown is the theoretical expectation, both with vignetting (dashed curve with squares), and without (solid curve), for the SSW array.

on axial line centre shift while the unvignetted case illustrates the lower limit. In practice, vignetting caused by the SPIRE IFTS instrument FOV will not likely be an instantaneous cut-off and is expected to vary with frequency. Therefore, the expected line centre shift is somewhere between the vignetted and un-vignetted case, as is observed in Figure 4.17 for measured data.

There is good agreement between the expected and observed axial frequency shift for the SPIRE IFTS. As the obliquity ILS shift approaches the size of a spectral resolution element, correct interpretation of the associated spectra must account for obliquity effects, otherwise errors in the interpretation of the astronomical source under study will result [160]. For high-resolution SPIRE IFTS scans, the frequency shifts in the ILS for off-axis detectors approaches the width of a spectral resolution element. The following section (§4.7) discusses the importance of correct frequency shift interpretation in the context of a case study of M82 [161].

## 4.7 A Case Study of IFTS in Astronomy

Spectroscopy is of fundamental importance in astronomy and astrophysics as it provides information on the composition and physical conditions of astronomical sources. Emission and absorption lines are the fingerprints of atoms and molecules. Spectra provide information on source composition, temperature, density, relative linear motion, and rotation. These parameters are often used as inputs to complicated astrophysical models to obtain estimates of star formation rates, lifetimes, etc. The goal of imaging spectroscopy is to provide accurate spectral information for every resolved spatial component of a scene.

Hence, all of the advantages of spectroscopy are applied to every pixel in an image. The advantages of IFTS can only be realized, however, if all systematic sources of error, such as instrumental obliquity factors, have been taken into account. This section discusses the importance of understanding the axial variation within an IFTS instrument and highlights some related implications.

Obliquity related frequency shifts in IFTS spectra may potentially masquerade as Doppler shifts. Small frequency shifts which are significantly less than the instrument spectral resolution will not have a noticeable effect, however, shifts comparable to or greater than the instrument resolution must be taken into account. This effect will not be easily measured for nearby (i.e. galactic) sources where the associated Doppler widths in molecular clouds are  $\sim 30$  km/s [162]. In this case, it is difficult to distinguish Doppler line widths from instrumental effects. More distant sources, e.g. extragalactic, where radial velocities are greater, will have lines exhibiting a combination of Doppler and instrumental effects. For the large scale velocities associated with the rotation of galaxies, the resolution of the SPIRE IFTS is in the regime where the associated velocity rotational curves will be evident. Such information is fundamental in the determination of galactic masses, which in turn are key in the understanding of the formation and evolution of galaxies.

Figure 4.19 illustrates the minimum resolvable redshift velocity for SPIRE observations as a function of frequency. The effective Doppler velocity due to ILS induced line shift is shown for both SPIRE arrays in Table 4.5. Not only do obliquity effects potentially increase the uncertainty of the spectral line centre, but they also vary across the detector image plane. This variation across an image is a potential source of error, which, if left

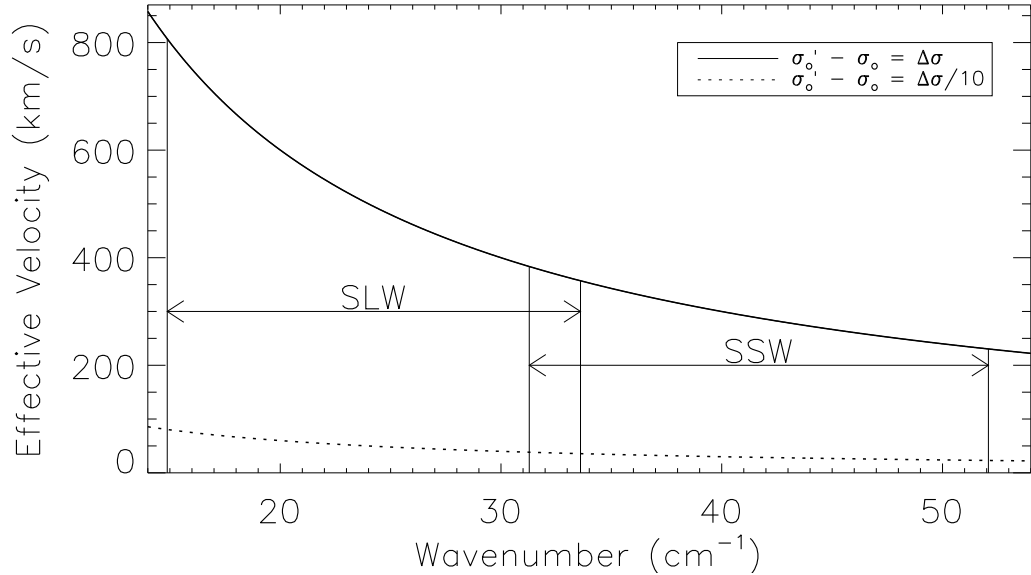


Figure 4.19: The minimum resolvable velocity shift for SPIRE using the highest available spectral resolution ( $0.04 \text{ cm}^{-1}$ ) and assuming that the minimum resolution is given by  $\Delta\sigma$  (solid) or  $\Delta\sigma/10$  (dotted).

uncorrected, will be interpreted in terms of scene dynamics. The effective Doppler shifts shown in Table 4.5 indicate that, for an extended stationary source of frequency  $\sigma_o$  observed with an IFTS, the outer-most off-axis detectors will observe a line shift equivalent to several hundred km/s, while the on-axis detector equivalent redshift is on the order of tens of km/s (42 km/s for SLW and 7 km/s for SSW). This is further complicated for Nyquist sampled (spatial) maps which require several chop/jiggle positions about a pointing, or for large maps constructed as mosaics of several imaging observations concatenated together. In such cases, uncorrected obliquity effects will introduce spatially periodic systematic velocity errors into a hyper-spectral image. Correction of the obliquity ILS broadening, therefore, is necessary to ensure accuracy in many aspects of the interpretation of spectral data.

Table 4.5: Effective Doppler velocity for uncorrected SPIRE ILS obliquity line shift.

Array	$\beta_{\text{sky}}$	$v_{\text{effective}}$ (km/s)
SLW	0''	42
	48''	264
	83''	750
	96''	993
SSW	0''	7
	27''	80
	47''	234
	54''	311
	71''	542
	81''	696

#### 4.7.1 The Starburst Galaxy M82

An infrared galaxy converting ISM into stars at an unsustainable rate is known as a starburst galaxy [163]. Stellar radiation emitted within a star forming region is reprocessed into infrared radiation by dust within surrounding molecular clouds. M82 (also known as NGC 3034) is one of the most well-studied starburst galaxies in the local Universe, and is one of the scheduled sources for SPIRE SAG-2 GTKP observations. In fact, SPIRE FTS observations of M82 are scheduled during the Herschel science demonstration phase due to SPIRE's high sensitivity in the submm region where M82 is known to exhibit a wealth of spectral content. The close proximity ( $\sim 3.63$  Mpc [164]) and moderate infrared luminosity of M82 make it the brightest infrared galaxy in our sky. Our edge-on perspective of the galaxy yields an optical angular size of  $11.2' \times 4.3'$ . The nuclear region of M82 is  $\sim 4' \times 2'$  and contains numerous point sources and concentrations of emission, some of which are massive star clusters and supernovae [165]. Observations have shown the central region to contain over 100 groupings of over  $10^5$  stars in star clusters, dusty molecular clouds,

filaments of ionized gas, and different regions of varying star formation environments [166]. Tidal interactions with nearby M81 and dwarf starburst galaxy NGC 3077 are suspected to have triggered a large burst of star formation in M82 approximately  $10^7 - 10^8$  years ago [167], explaining much of the activity presently observed. Figure 4.20 shows a multi-wavelength (IR – visible – X-ray) image of M82 comprised of Spitzer, Hubble, and Chandra observations with superimposed Submillimetre Common User Bolometer Array (SCUBA) submm contours.

In addition to the central region of M82, which hosts a variety of IR/submm processes, the proximity of M82 allows observations of the outer regions. This includes study of the interaction of star forming regions with the ISM and PDRs. Fine structure emission lines of O I, O III, N II, N III, and C II, within ISO LWS observations of M82, reveal a 225 km/s redshift [168]. SED analysis of the nucleus of M82, and regions  $15''$  North and South provides cooler temperatures and higher emissivities than the central region [165]. SCUBA observations of M82 reveal a single emission peak centred  $9''$  west of the galactic nucleus in the  $850 \mu\text{m}$  band resolved into two distinct spatial peaks in the  $450$  and  $350 \mu\text{m}$  bands,  $10''$  East and  $6''$  West, respectively, of the galactic nucleus [169].

The size and distribution of M82 make it small enough to be mapped by SPIRE (see beam sizes on Figure 4.20), but large enough to resolve internal details. SPIRE will provide, for the first time, uninterrupted broadband spectral coverage in the submm region of this galaxy. Even low-resolution spectra will allow distinction between continuum and line emission, which is currently yielding SED uncertainties on the order of 50% [165]. With the SPIRE IFTS detectors spatially separated by  $27''$  and  $48''$  on the sky, for SSW and SLW



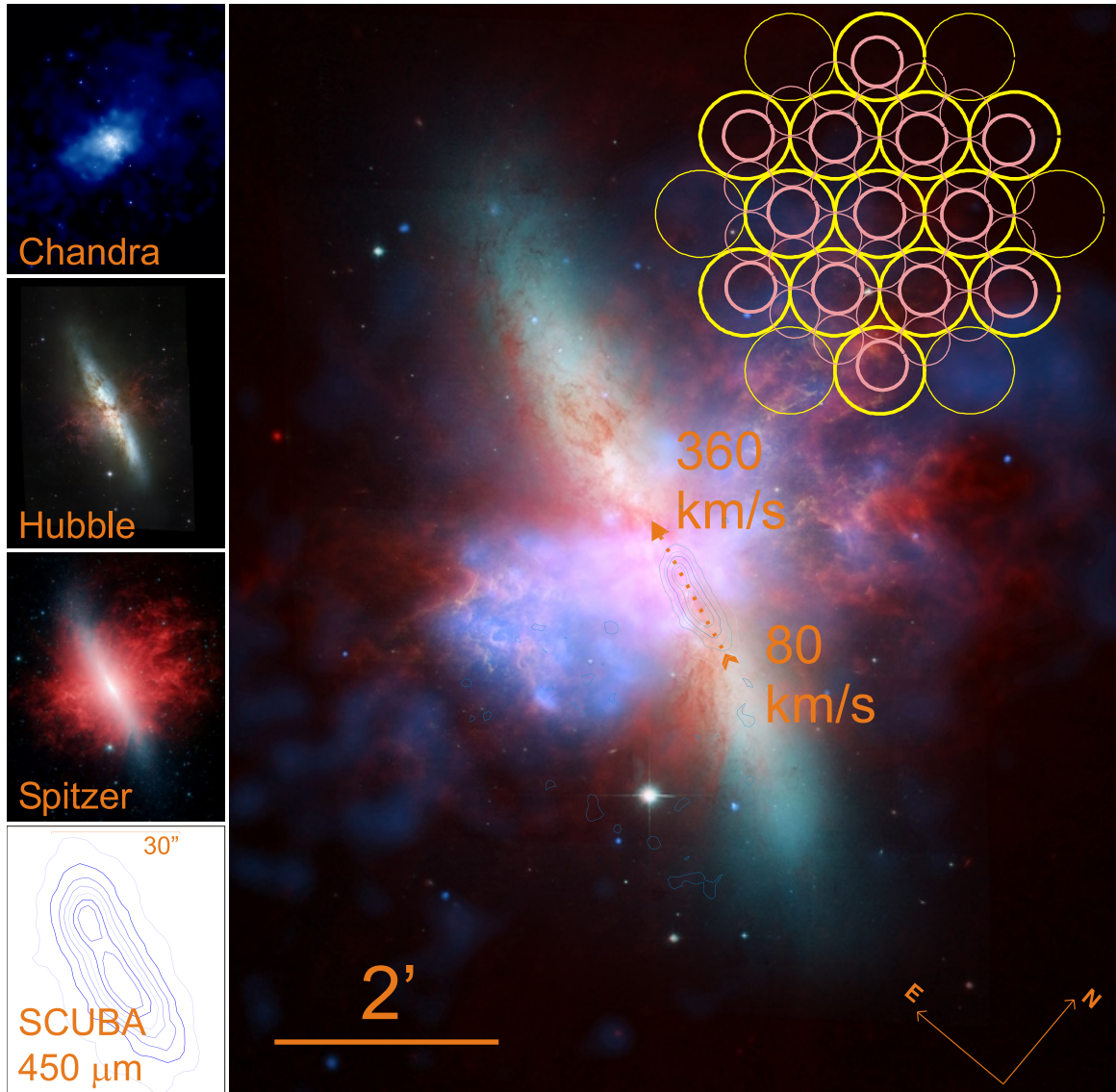


Figure 4.20: Multi-wavelength view of the starburst galaxy M82. The main image is a composite of NASA Chandra (X-ray, top-left), Hubble (visible, upper centre-left), and Spitzer (infrared, lower centre-left) space telescope observations. The contours shown are 450  $\mu\text{m}$  SCUBA continuum measurements ranging from 6.8 (center) – 0.5 (edge)  $\pm$  0.2 Jy/beam [165]. The image from each observatory is shown separately on the left. Observations of M82 in the submm reveal CO rotation dynamics between the NE and SW lobes [161] ( $\sim$ 80 km/s lower right to  $\sim$ 360 km/s upper left of image as indicated by the arrow). The SPIRE detector beam sizes are shown in the upper right of the figure. *Images – X-ray: NASA/CXC/JHU/D.Strickland; Optical: NASA/ESA/STScI/AURA/The Hubble Heritage Team; IR: NASA/JPL-Caltech/Univ. of AZ/C. Engelbracht; submm: CADC.*

respectively (see Figure 4.20), and the finest spectral resolution available being  $0.04 \text{ cm}^{-1}$ , M82 observations will exploit the utility of the SPIRE IFTS for extragalactic observations. By comparison, ground-based observations of M82, through narrow atmospheric windows in the submm, require weeks of observation time, whereas SPIRE observations will provide high quality observations of both line and continuum spectra in relatively little time, on the order of minutes (see §5.5.3).

Removal of the off-axis obliquity effect is critical to a correct understanding of the galactic dynamics of a source such as M82. For example, the CO lobes observed to be in rotation with respect to each other by Mao [161] are positioned such that they will be observed on adjacent SLW detectors. Although the lobe radial velocities are observed to be  $\sim 80$  and  $\sim 360$  km/s for the SW and NE lobes, respectively, the uncorrected observed velocities will be different because of obliquity effects. Table 4.6 lists the observed velocities expected for observation of CO rotation on neighboring SLW C detectors. The apparent rotation between the C1-C2 and C3-C4 observations is of approximately the same magnitude, but in the opposite direction. The range of velocity shifts shown in Table 4.6 emphasize the need to correct for obliquity effects as discussed in detail in this chapter. Fully spatially resolved SPIRE IFTS maps require a chop/jiggle raster which will further confuse the apparent dynamics in a scene if obliquity frequency shifts are not corrected. Isolation and removal of instrumental effects from observations is thus crucial to a correct interpretation of observations of M82 and other extragalactic sources.

Table 4.6: Resultant CO Doppler velocities for M82 without obliquity frequency shift correction.

Detector pair	$v_{\text{observed}}$ (km/s)	
	SW lobe	NE lobe
actual [161]	80	360
C1 & C2	1073	624
C2 & C3	344	402
C3 & C4	122	624
C4 & C5	344	1352

## 4.8 Conclusions

A discussion of the advantages and practical considerations for IFTS has been provided. The theoretical IFTS instrument response has been calculated including obliquity effects which involve modifications to the well-known FTS ILS sinc function. The SPIRE PFM qualification test measurements of the SPIRE IFTS, performed over several months at RAL, have verified the expected instrument performance. A general discussion of obliquity effects in IFTS measurements has been included. A detailed analysis of the implication of these effects for the SPIRE FTS has been presented from a theoretical and observational standpoint. Finally, it has been shown that, while obliquity corrections may not be of importance for galactic observations where the dominant velocity is determined by the rotation of our solar system, obliquity corrections are crucial for extragalactic observations. Indeed, for observations of M82, galactic dynamics could be *reversed* if obliquity effects are not considered.

## Chapter 5

# Signal and Noise in the SPIRE Fourier Transform Spectrometer

I have always believed that astrophysics should be the extrapolation of laboratory physics, that we must begin from the present Universe and work our way backward to progressively more remote and uncertain epochs.

---

Hannes Alfvén [170]

The accuracy of parameters derived from FTS spectra (e.g. line centre, line width, line profile, line intensity, temperature, SED, etc.) depends upon the conditions under which the corresponding interferograms are measured. Several factors affect the recorded signal amplitude and noise level, and hence the observed S/N, in an FTS observation. These factors include: the nature of the source under study and its surroundings, the optical path between the astronomical source and the science instrument package, including: pre-optics (i.e. telescope primary and secondary mirror), the FTS instrument itself and its associated optics, post-optics (i.e. field lens, detector feedhorns, etc.), and, finally, the characteristics of the radiation detectors and post detection read out electronics. A comprehensive understanding of the instrument, with particular regard to all potential sources of noise, is necessary to ensure optimal instrument performance. This is particularly important in space missions with a finite lifetime; such is the case for the Herschel telescope which has a limited supply of liquid Helium to maintain the required instrumentation operating temperatures.

This chapter discusses the performance characteristics of the composite, spider-web, bolometer detectors [11, 12] employed in the SPIRE IFTS, and compares their theoretical and experimental performance. In particular, I have studied the noise performance of the SPIRE FTS as determined through analysis of FTS interferograms obtained during PFM testing, using techniques similar to those that will be used in the analysis of FTS observations during flight. From this analysis, I have been able to predict the in-flight performance of the SPIRE IFTS.

A review of general bolometer theory is provided in §5.1. The SPIRE instrument optics are discussed in §5.2. The PFM observations are categorized as either viewing the

test facility or the CBB, i.e. the SPIRE instrument is either allowed to view sources within the ~300 K laboratory environment through a cryostat entrance window, or cold sources within the cryostat itself. The pre-optics both during the PFM tests and flight are discussed in §5.3. Modeling of the SPIRE FTS bolometer detectors is discussed in §5.4. In the theoretical bolometer model, each input configuration of the SPIRE instrument (§5.3) is modeled separately. The differences in expected instrument performance during PFM testing and in-flight are provided in §5.4. The observed performance of the SPIRE FTS during PFM testing is discussed in §5.5.1 & §5.5.2. The expected noise performance of the SPIRE detectors is given in §5.5.3. In this section I have modeled CO emission spectra from the starburst galaxy M82, and I have also used previous measurements from the literature [161], where available, to predict the in-orbit performance of SPIRE.

## 5.1 Bolometer Theory

Although the technology involved in designing state of the art bolometric systems is highly sophisticated, at a fundamental level, a bolometer is nothing more than a very sensitive thermometer. Radiant power absorbed by a bolometer causes a temperature change, which in turn causes a change in the resistance of the device, ultimately allowing a measure of the incident radiation on the detector. The theory presented in this section is distilled from that of Jones [171], Low [172], Mather [173,174], Griffin and Holland [175], and Sudiwala et al. [176]. A bolometer, of temperature  $T$ , is thermally coupled to a heat sink, of temperature  $T_o$ , by a thermal conductance,  $G(T, T_o)$ . Incident radiation absorbed by the bolometer causes an increase in temperature, and changes the dynamics of heat flow to the

sink, so as to restore the bolometer to its equilibrium operating temperature. Although the physical response to the incident radiation is a temperature change in the bolometer, it is the bolometer resistance,  $R(T)$ , that is the measurable quantity in practice. A typical bolometer circuit is shown in Figure 5.1 where the bolometer is connected in series with a load resistor,  $R_L$ , and a bias voltage,  $V_b$ , is applied across the network. While a bias current  $I$  is passed through the bolometer, the potential difference across the bolometer,  $V$ , which is a function of bolometer resistance, is measured. Thus, changes in the absorbed radiant power result in changes in the dissipated electrical power in the bolometer. Consequently, bolometer resistance varies both with changes in the absorbed radiant power, and as a result of the electrical power dissipated within the bolometer.

The dissipation of electrical power through the bolometer is  $P = VI$ , and the total power absorbed by the device is comprised of both optical and electrical components as follows

$$W = P + Q \quad [\text{W}] . \quad (5.1)$$

Figure 5.1 illustrates a schematic diagram of a SPIRE bolometer and its equivalent electrical circuit. The submm detectors on the SPIRE instrument are composite spider-web bolometers [107], with neutron transmutation doped germanium as the thermistor element bonded to a Silicon Nitride micromesh spider-web substrate [10,11] as the absorbing layer, coated with a metallic film to match the impedance of free space.

Over its operating temperature range, the resistance of a bolometer may be expressed as

$$R(T) = R^* \exp [(T_g/T)^n] \quad [\Omega] , \quad (5.2)$$

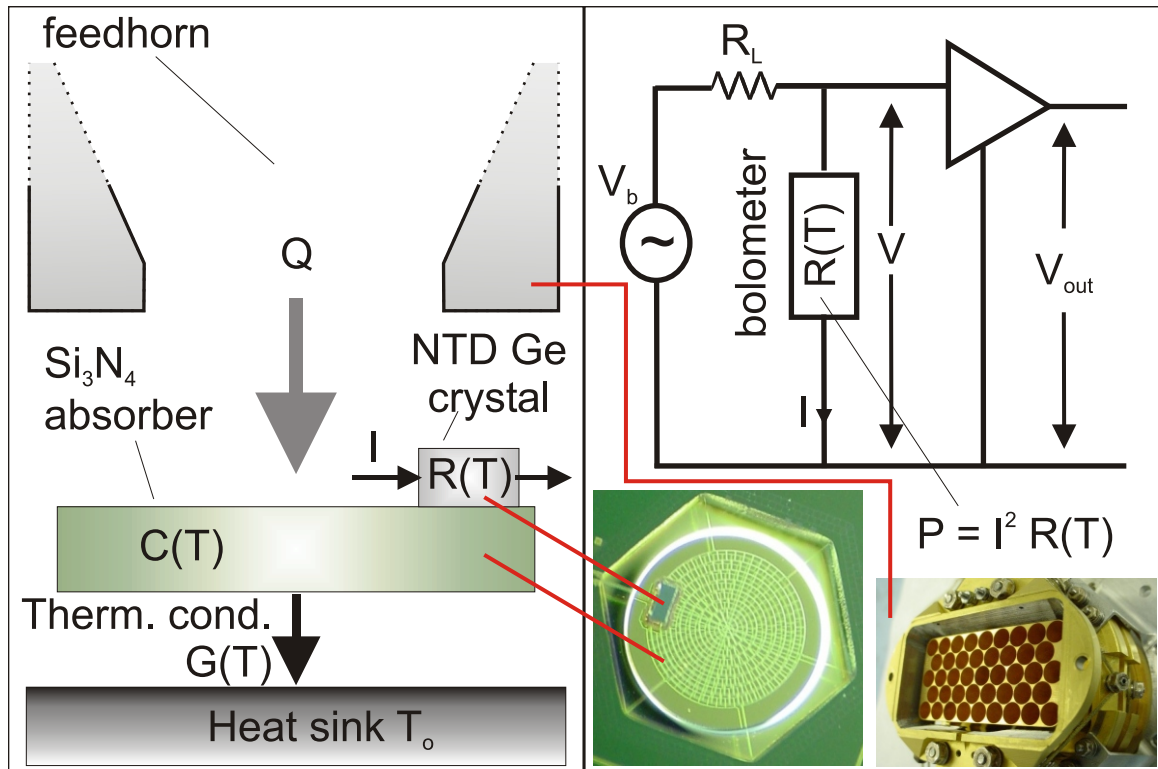


Figure 5.1: Schematic diagram of a SPIRE bolometric detector (left) and its equivalent electrical circuit (right). Incident radiant power,  $Q$ , and bias current,  $I$ , are absorbed by the bolometer, leading to an increase in the bolometer temperature dictated by the heat capacity,  $C(T)$ . A thermal gradient conducts energy from the bolometer to the heat sink. The bolometer resistance changes as a function of temperature, and a measure of the voltage across a bolometer can be used to determine the incident radiant power. *Inset Photos: SPIRE Consortium*



where  $T_g$  and  $n$  are material constants, and  $R^*$  is a device specific constant.  $T_g$  is the material bandgap temperature,  $n$  is the  $R$ - $T$  power law index, another material constant, and  $R^*$  is the resistance parameter for a specific bolometer. For SPIRE,  $n=1/2$  and  $T_g \approx 42$  K. The temperature coefficient of resistance for a bolometer is given by

$$\alpha = \frac{1}{R(T)} \frac{dR}{dT} = -\frac{nT_g^n}{T^{n+1}} \quad [\text{K}^{-1}] . \quad (5.3)$$

The bolometer heat capacity  $C(T)$  is given by

$$C(T) = C_o \left( \frac{T}{T_o} \right)^\rho \quad [\text{J/K}] , \quad (5.4)$$

where  $C_o$  is the heat capacity at a reference heat sink temperature  $T_o$ , and  $\rho$  is the heat capacity index; both  $C_o$  and  $\rho$  are material constants. The energy balance of a bolometer is given by

$$C(T) \frac{dT}{dt} + G(T, T_o)(T - T_o) = W \quad [\text{W}] , \quad (5.5)$$

where  $G(T, T_o)$  is the bolometer thermal conductance at temperature  $T$  and heat sink temperature  $T_o$ . Under steady state conditions, the energy balance is expressed as

$$W = P + Q = G_S(T, T_o)(T - T_o) \quad [\text{W}] , \quad (5.6)$$

where  $G_S(T, T_o)$  is the static thermal conductance of the bolometer, and is given by (see §D.1 for further details)

$$G_S(T, T_o) = \frac{G_{S_o}}{(\beta + 1)T_o^\beta} \frac{(T^{\beta+1} - T_o^{\beta+1})}{(T - T_o)} \quad [\text{W/K}] . \quad (5.7)$$

The dynamic thermal conductance,  $G_D(T, T_o) = dW/dT$ , is given by

$$G_D(T, T_o) = G_{S_o} \left( \frac{T}{T_o} \right)^\beta \quad [\text{W/K}] . \quad (5.8)$$

The power dissipation of a bolometer to a heat sink is also effected by the temperature dependence of the electrical bias in the circuit. The effective thermal conductance,  $G_E(T, T_o)$ , includes the effect of electrothermal feedback [176] in the dynamic thermal conductance as follows (see §D.2 for further details)

$$G_E(T, T_o) = \frac{dW}{dT} - \frac{dP}{dT} = G_D(T, T_o) - \alpha P(T, T_o) \left[ \frac{R_L - R(T)}{R_L + R(T)} \right] \quad [\text{W/K}] . \quad (5.9)$$

### 5.1.1 Determination of Incident Optical Power, $Q$

Although the goal of using a bolometer in an FTS spectrometer is to measure the incident radiant power on the detector, in practice, the measurable quantity is the voltage across a current biased bolometer as a function of OPD, i.e.  $V(z)$ . The incident radiant power on the detectors can be determined from a bolometer model based on knowledge of the bolometer voltage, the load resistance, the bias voltage, and the heat sink temperature. From Figure 5.1, the bolometer resistance can be expressed as

$$R(z) = \frac{V(z)R_L}{V_b - V(z)} \quad [\Omega] , \quad (5.10)$$

where  $V_b$  is the bias voltage and  $R_L$  is the load resistance. The bolometer bias current,  $I$ , can be expressed as

$$I(z) = \frac{V(z)}{R(z)} \quad [\text{A}] , \quad (5.11)$$

and the bolometer temperature is given by

$$T(z) = \frac{T_g}{\left[ \ln \left( \frac{R(z)}{R^*} \right) \right]^{1/n}} \quad [\text{K}] , \quad (5.12)$$

where  $R^*$ ,  $T_g$ , and  $n$  are material constants as described earlier. The electrical power dissipated in the bolometer is given by

$$P(z) = V(z)I(z) \quad [\text{W}] . \quad (5.13)$$

The key parameter of interest in bolometer operation is the bolometer temperature,  $T$ , which is critical in determining other desired quantities. The total power dissipated across the bolometer,  $W(z)$ , depends upon the temperatures of the bolometer and the heat sink,  $T(z)$  and  $T_o$ , and is given by

$$W(z) = \frac{T(z) - T_o}{G_E(T(z), T_o)} \quad [\text{W}] , \quad (5.14)$$

and the radiant optical power,  $Q(z)$ , is the difference between the total and electrical powers

$$Q(z) = W(z) - P(z) \quad [\text{W}] . \quad (5.15)$$

Alternatively, the measured bolometer voltage can be converted into total absorbed power directly using the bolometer responsivity  $S$  [V/W] (Equation 5.17 in §5.1.2). The task of separating the optical and electrical power components still remains, however. The responsivity,  $S$ , is a nonlinear function of power and is sensitive to the heat sink temperature, which places stringent requirements on the thermal stability of the heat sink. Converting the measured voltage into a temperature difference, as described above, provides a more direct connection to the thermal stability requirements of the heat sink than converting a measured voltage into an incident radiant power using the responsivity. In order to obtain noise performance in accordance with the derivations below, the noise equivalent power (NEP) (§5.1.3) may be converted into a noise equivalent temperature using the dynamic

thermal conductance. To give an example of the thermal stability required for SPIRE, the temperature stability of the heat sink must be better than  $\sim 1 \mu\text{K}/\sqrt{\text{Hz}}$  ( $\text{NEP}/G_D$ ) if the NEP is  $10^{-16} \text{ W}/\sqrt{\text{Hz}}$  (§5.5).

### 5.1.2 Bolometer Dynamic Response

The dynamic impedance of a bolometer element,  $Z_D = dV/dI$ , is given by (see §D.3 for further details)

$$Z_D = R \left[ \frac{G_D + \alpha P}{G_D - \alpha P} \right] \quad [\Omega]. \quad (5.16)$$

Bolometer responsivity,  $S$ , is a measure of the variation in the output voltage measured across a bolometer as a function of the incident radiant power, i.e.  $S = dV/dQ$ . The DC detector responsivity is dependent upon bolometer bias conditions and optical loading, and can be expressed as (details of this derivation are provided in §D.4)

$$S = \left[ \frac{Z_D - R}{2V} \right] \left[ \frac{R_L}{Z_D + R_L} \right] = \frac{\alpha V}{G_E} \left[ \frac{R_L}{Z_D + R_L} \right] \quad [\text{V/W}]. \quad (5.17)$$

The speed of a bolometer response to changing input (either optical or electrical input) is often represented by two time constants, one being thermal and the other being electrical. An effective time constant  $\tau_E$ , which takes electrothermal feedback into account, is given by

$$\tau_E = \frac{C(T)}{G_E(T, T_o)} \quad [\text{s}], \quad (5.18)$$

and a physical/thermal time constant  $\tau_D$  given by

$$\tau_D = \frac{C(T)}{G_D(T, T_o)} \quad [\text{s}]. \quad (5.19)$$

One advantage of electrothermal feedback is that it reduces the effective time constant. Mather [173] has shown, however, that the Johnson noise NEP depends on the real physical time constant  $\tau_D$  rather than the effective time constant  $\tau_E$ .

It is evident from Equations 5.18 & 5.19 that the detector response time (i.e. the detector time constant) is inversely proportional to the thermal conductance. As will be shown in §5.1.3, Johnson noise is linearly proportional to the thermal conductance (Equation 5.20). Thus, there is a trade-off between detector speed and noise; increases in the thermal conductance produce a smaller time constant, and thus a faster detector response, but come at the cost of increased noise.

### 5.1.3 Sources of Noise

As discussed in §2.7.2, there are many sources of noise present in a bolometric measurement. Noise sources include: the photon noise due to the statistical nature of photon arrival from the source under study, Johnson noise from the resistive bolometer element and load resistor, phonon noise from the thermal contact with the heat sink, and noise from the detector electronics (e.g. lock-in amplifier). A useful measure of noise in an infrared detection system is the NEP, which is defined as the radiant power required to produce a S/N of unity, normalized to half a second of integration time [76]. For example, a detection system with an overall NEP of  $10^{-16} \text{ W}/\sqrt{\text{Hz}}$  requires a radiant signal power of 0.1 fW and an integration time of 0.5 s to obtain an S/N of unity. The term noise equivalent power is a misnomer because the SI units of power are W and the units of NEP are  $\text{W}/\sqrt{\text{Hz}}$ . Assuming that noise sources are uncorrelated, the total NEP is the quadrature sum of the individual sources. This section discusses the main sources of noise in the SPIRE FTS and

derives the overall noise performance of the instrument.

**Johnson noise** Johnson noise is due to the thermal motion of charge carriers in a resistive device. Following the non-equilibrium theory of Mather [173], the DC Johnson noise NEP is given by

$$\text{NEP}_J = \sqrt{\frac{4k_b T G_D^2(T, T_o)}{\alpha^2 P(T)}} \quad [\text{W}/\sqrt{\text{Hz}}], \quad (5.20)$$

where  $k_b$  is the Boltzmann constant. The Johnson noise associated with the load resistor is included below (Equation 5.22).

**Phonon noise** Phonons are quantized lattice vibrations within any solid state device. The statistical variation in phonon distribution effects the thermal conductivity, and thus the bolometer operating point. Any variations in phonon flux are thus sensed by the bolometer circuit, and result in another electrical noise component [109, 110]. The DC phonon noise NEP is given by [176] (details of this derivation are provided in §D.5)

$$\text{NEP}_{\text{phonon}} = \sqrt{\frac{4k_b G_{So}}{T_o^\beta} \frac{(T^{2\beta+3} - T_o^{2\beta+3})(\beta + 1)}{(T^{\beta+1} - T_o^{\beta+1})(2\beta + 3)}} \quad [\text{W}/\sqrt{\text{Hz}}]. \quad (5.21)$$

**Load resistor Johnson noise** The noise associated with the load resistor is also Johnson noise due to thermal motions of its electric charge carriers. The DC load resistor NEP is given using the bolometer responsivity,  $S$ , as follows [173]

$$\text{NEP}_{\text{load}} = \sqrt{\frac{4k_b T_o}{R_L}} \left| \frac{Z_D R_L}{Z_D + R_L} \right| \frac{1}{S} \quad [\text{W}/\sqrt{\text{Hz}}]. \quad (5.22)$$

**Electronic amplifier noise** The electronic pre-amplifier will also contribute to the electrical noise. The amplifier rms noise voltage, i.e.  $V_{A-rms}$ , typically given in units of  $\text{nV}/\sqrt{\text{Hz}}$ , is converted into an amplifier NEP as follows

$$\text{NEP}_{amp} = \frac{V_{A-rms} 10^{-9}}{S} \quad [\text{W}/\sqrt{\text{Hz}}] . \quad (5.23)$$

For the case in which the above noise sources are not correlated, the combined effect of all non-optical sources becomes

$$\text{NEP}_{elec} = \sqrt{\text{NEP}_J^2 + \text{NEP}_{phonon}^2 + \text{NEP}_{load}^2 + \text{NEP}_{amp}^2} \quad [\text{W}/\sqrt{\text{Hz}}] . \quad (5.24)$$

**Photon noise** In addition to the noise sources presented above, there is also source noise associated with the radiation incident on the detectors. For each radiation source, a full radiative transfer analysis is required. Emission from each component preceding the detectors, and its propagation through all subsequent components down the optical chain must be taken into account. Incident radiation from a source, e.g. source  $i$  with a blackbody/greybody emission at temperature  $T_i$  and emissivity  $\epsilon_i$ , results in an absorbed radiant power  $Q_i$  as follows

$$Q_i = \int_{\sigma_{min}}^{\sigma_{max}} \epsilon_i(\sigma) P(\sigma, T_i) t_i(\sigma) \eta_i(\sigma) A \Omega(\sigma) d\sigma \quad [\text{W}] , \quad (5.25)$$

where  $\epsilon_i(\sigma) P(\sigma, T_i)$  [ $\text{W}/(\text{m}^2 \text{ sr cm}^{-1})$ ] represents the blackbody spectral radiance,  $t_i(\sigma)$  represents the transmission through the optical path from source to detector,  $A \Omega(\sigma)$  [ $\text{m}^2 \text{ sr}$ ] is the instrument throughput, and  $\eta_i(\sigma)$  represents the net efficiency of the optical system. The parameter  $\eta_i(\sigma)$  has several components including aperture efficiency, feed efficiency,

etc. This efficiency parameter changes depending on the source of the radiation, e.g. stray light from within an instrument c.f. blackbody emission from a telescope primary mirror, and will be discussed in greater detail in §5.2, §5.3, and §5.4. The total background power,  $Q$ , exposed to a detector, is the sum of the individual components

$$Q = \sum_{i=0}^n Q_i \quad [\text{W}] . \quad (5.26)$$

The NEP due to a source of photon noise is determined as follows [173]

$$\text{NEP}_{\nu-i} = \sqrt{4h^2c^3 \int_{\sigma_{min}}^{\sigma_{max}} \left[ \left( \frac{A\Omega\epsilon_i t_i \eta_i \sigma^4}{\exp\left(\frac{hc\sigma}{k_b T_i}\right) - 1} \right) \left( 1 + \frac{\epsilon_i t_i \eta_i}{\exp\left(\frac{hc\sigma}{k_b T_i}\right) - 1} \right) \right] d\sigma} \quad [\text{W}/\sqrt{\text{Hz}}] , \quad (5.27)$$

where  $h$  is Planck's constant, and  $A\Omega$ ,  $\epsilon$ ,  $t$ , and  $\eta$  are all frequency dependent variables as above (details of this derivation are provided in §D.6). The total optical NEP, for incoherent sources, is obtained via the quadrature summation of the individual components as follows

$$\text{NEP}_{photon} = \sqrt{\sum_{i=0}^n \text{NEP}_{\nu-i}^2} \quad [\text{W}/\sqrt{\text{Hz}}] . \quad (5.28)$$

## 5.2 SPIRE Optical Efficiencies

In order to model the performance of the SPIRE instrument, the reflection, transmission, absorption and emission of each optical element, all potentially frequency dependent, must be taken into account. This section outlines the main optical components of the SPIRE FTS. The parameter values presented here are based upon those found within the SPIRE Sensitivity Models document [6].



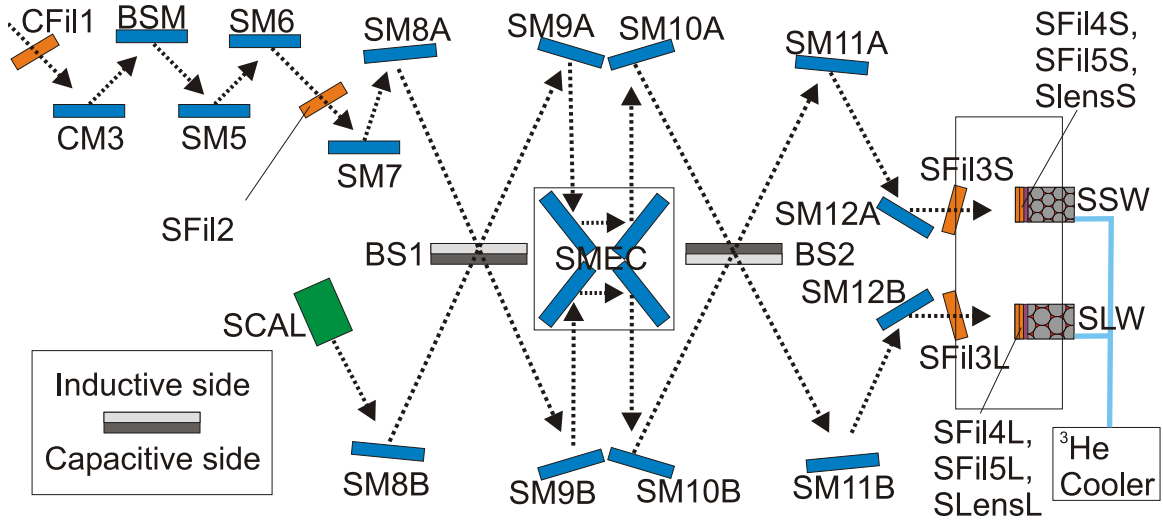


Figure 5.2: Optical configuration of the SPIRE FTS. There are several optical filters (CFil1, SFil2, SFil3L/S, SFil4L/S, SFil5L/S), mirrors (CM3, BSM, SM5–12, and the rooftop mirrors within the SMEC), two beamsplitters (BS1/2), and field lenses (SLensL/S) in the optical path between the source and the two detector arrays.

The Herschel/SPIRE optics train consists of several mirrors and filters between the primary mirror and the cryogenically cooled detectors, constituting the pre-optics (i.e. the Herschel primary and secondary mirrors), instrument optics, and post-optics. This work accounts for the pre-optics separately, as they are not part of the SPIRE instrument itself, and were not present during PFM testing. A schematic of the optical path through the SPIRE spectrometer is shown in Figure 5.2. In addition to the radiative transfer of source radiation processed by the various optical components of SPIRE, another source of radiation is straylight, originating from either within or outside of the instrument. The reflection/transmission efficiency ( $\eta$ ), emissivity ( $\epsilon$ ), and temperature ( $T$ ) assumed for each optical component of the SPIRE FTS are listed in Table 5.1.

In addition to component specific efficiencies, several coupling efficiency terms

Table 5.1: Assumed reflection/transmission efficiencies for components of the SPIRE FTS for which test data were not available.

Component	$T$ (K)	$\eta$	$\epsilon$
fold mirror (CM3, SM5-SM12)	5.5	0.995	0.05
BSM	5.5	0.95	0.012
SMEC rooftop	5.5	$(0.95)^2 \simeq 0.9$	0.05
BS1/2	5.5	$(0.487/0.5)^2 \simeq 0.95$	0.03
Field lens (SLensL/S)	0.310	0.9	N/A

must also be taken into account. These factors include: instrument throughput ( $A\Omega$ ), feed efficiency ( $\eta_{feed}$ ), aperture efficiency ( $\eta_A$ ), spillover efficiency ( $\eta_S$ ), and FTS modulation efficiency ( $\eta_{mod}$ ). These factors are discussed below and values for SPIRE are summarized in Table 5.2.

The product of the per-mode throughput and the feedhorn/cavity efficiency (i.e. allowed spectral mode content) determines the coupling of background power to the detector [9]. The feedhorn geometry dictates the allowed modes and their respective cut-on frequencies [11], and the throughput per mode is inversely proportional to the square of the frequency. Theoretically, the overall mode content appears as a series of steps in frequency as additional modes cut-on. In practice, however, the variation is not so discontinuous [6], and a linear approximation of the mode content starting at unity at the lower frequency band edge, and ending at  $n$  at the upper band edge, where  $n = 4$  for SLW and  $n = 3$  for SSW, has been used in this analysis. The product of the mode content and throughput per mode gives the feedhorn throughput  $A\Omega(\sigma)$ . The mode content and throughput for each array of the SPIRE FTS is shown in Figure 5.3.

The feed efficiency represents the absorption efficiency of various modes of incident radiation with respect to the combination of the feedhorn, cavity, and bolometer element.

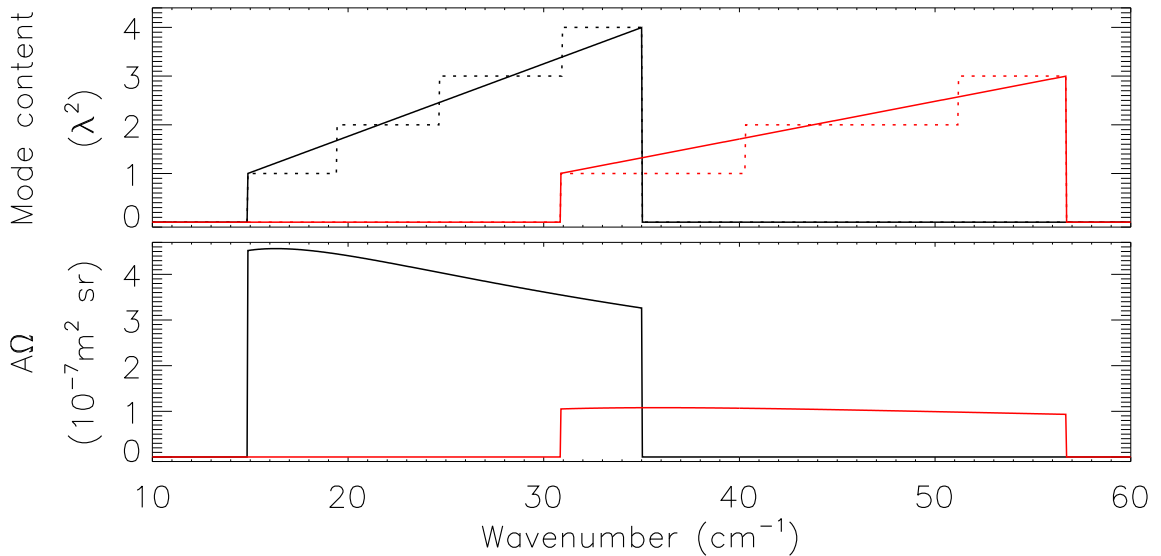


Figure 5.3: Optical throughput of the SPIRE FTS. The upper plot shows the  $\lambda^2$  mode content (dashed - discrete cut-on, solid - linear approximation) for the SLW array (left) and SSW array (right). The lower plots illustrates the resultant  $A\Omega$  throughput, shown here in units of  $\text{m}^2 \text{sr}$ . The throughput shown here does not take into account coupling to the telescope.

Although there are different theoretical feed efficiencies for each mode based upon the feedhorn and mode geometry [11], the variation of the theoretical coupling efficiency of each mode is small. During PFM testing, attempts were made to describe the modal content of observed data recorded with the SPIRE FTS; no simple relationship between observed spectra and theoretical mode content and mode coupling efficiency was found. Therefore, the average value of all expected mode coupling efficiencies is used for simplicity.

Spillover efficiency is a measure of the detector throughput illuminated by the telescope. The remainder (i.e.  $1 - \eta_S$ ) is assumed to terminate on the inside of the 2 K detector box. The same uniform spillover efficiency is assumed for both bands.

The FTS modulation efficiency is due to the interferogram modulation amplitude

Table 5.2: Estimated SPIRE FTS detector coupling efficiency factors.

Parameter	Array	
	SLW	SSW
$A\Omega$ (mm <sup>2</sup> sr)	0.32 – 0.46	0.09 – 0.11
$\eta_{feed}$	0.70	0.73
$\eta_S$	0.75	0.75
$\eta_{mod}$	0.5	0.5

of  $\sim \pm I_o/2$  about a DC offset of  $I_o/2$ , where  $I_o$  is the unmodulated signal amplitude. Although the modulated amplitude is reduced, it is important to note that the photon noise is related to the total signal level and not just the modulated portion, so  $\eta_{mod}$  is not used in the background noise determination.

The fraction of the total power from a point source diffraction pattern coupled to a detector which is centred on the source is known as the aperture efficiency. This reduction of intensity is not observed for extended sources as the detector is effectively exposed to the superposition of a dense spatial distribution of point sources, and therefore the diffraction pattern is flat.

The overall transmission of an extended greybody source ( $\epsilon = \epsilon_i$ ,  $T = T_i$ ) observed with SPIRE is given by

$$Q_i(\sigma) = \epsilon_i(\sigma) P(\sigma, T_i) A\Omega(\sigma) \text{Filt}(\sigma) \eta_S \eta_{feed} \eta_{mod} \quad [\text{W}], \quad (5.29)$$

$$\times (0.95) (0.995)^9 (0.95)^2 \left(\frac{0.487}{0.5}\right)^2 (0.9) d\sigma$$

where  $P(\sigma, T_i)$  is the Planck function,  $\text{Filt}(\sigma)$  is the overall filter profile, and the optical component efficiencies are taken from Table 5.1. While this analysis of the SPIRE FTS is based upon the best estimates of the expected operating conditions and the combined effect of propagation through all of the individual components, the performance of the

fully configured system, at its operating temperature, must be obtained through calibration observations of well known astronomical point and extended sources; this type of observation will not be possible until after launch. Measurements made with SPIRE during PFM testing were conducted with the instrument in an evacuated cryostat at cryogenic temperatures, however, it was impossible to simulate the expected in-flight conditions fully. The following section outlines the differences between operating conditions during PFM testing and flight, and discusses corresponding modifications of the bolometer model which account for these differences.

### 5.3 SPIRE Optical Input Configurations

In PFM testing of SPIRE, space-like conditions for the instrument were simulated in a laboratory setting. Although many factors are well controlled within the SPIRE cryostat, such as the various temperature stages (i.e. 77 K, 10 K, 5 K, 2 K, 0.3 K), the infrared input wavefront curvature and optical background levels present during instrument testing will vary from in-flight conditions. As it was not feasible to house a 3.5 m diameter mirror in the SPIRE test facility, a telescope simulator [177,178], consisting of a series of powered mirrors manipulated by linear actuators, was used to reproduce the wavefront expected from the SPIRE pre-optics. In addition to the telescope simulator (which is outside of the SPIRE test cryostat) the pre-instrument filters in the cryostat include a high density polyethylene (HDPE) cryostat window, three low-pass filters [127], and two neutral density filters (9.2% and 3.7% transmission), all tilted or wedged to avoid interference caused by multiple reflections, in place to bring the background radiation intensity from the laboratory

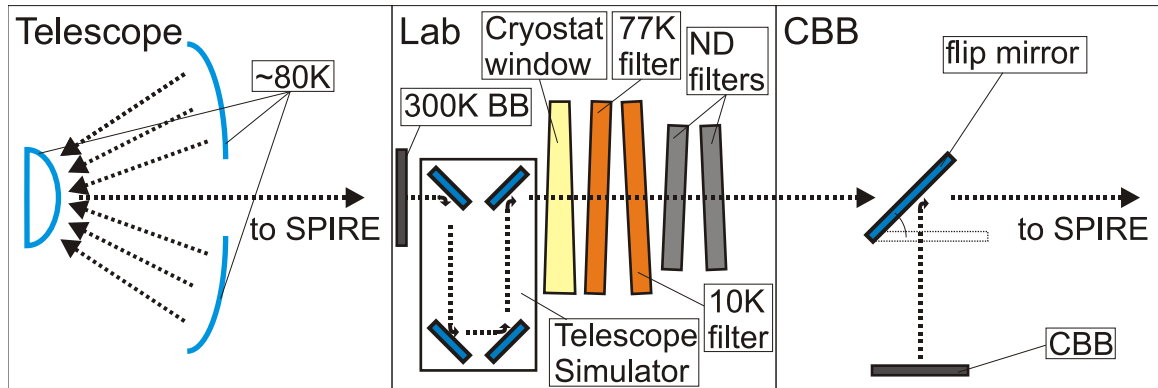


Figure 5.4: The input configuration for the SPIRE FTS in-flight (left) and during PFM testing (centre and right). The centre illustration shows a  $T \sim 300$  K,  $\epsilon \sim 1$  background source, a representation of the additional mirrors of the telescope simulator, the cryostat window, and the various filters inside the cryostat (and outside of the SPIRE instrument). The right illustration shows the CBB source and flip mirror used to switch the internal view from the lab to the CBB.

to representative levels [179]. In addition to radiation sources outside of the SPIRE cryostat, an internal blackbody source (i.e. the CBB [179]), thermally linked to the 4 K stage, was placed inside the cryostat just outside of the SPIRE instrument. The CBB is placed on the interior of all of the additional cryostat filters and windows mentioned above. A flip mirror allowed SPIRE to alternately view the CBB or the cryostat window/laboratory. Each of these input configurations is illustrated in Figure 5.4. Labeled photographs of each of the input sources in Figure 5.4 are shown in Figures 5.5 (the Herschel primary mirror), 5.6 (the laboratory background and telescope simulator), and 5.7 (the CBB). The principle uncertainties in the sensitivity performance estimation of Herschel/SPIRE, which will only be known after Herschel is launched, are the temperature and emissivity of the telescope primary mirror. The internal blackbody source, SCAL, in place at the secondary FTS input port to compensate for the background emission from the primary input port (largely

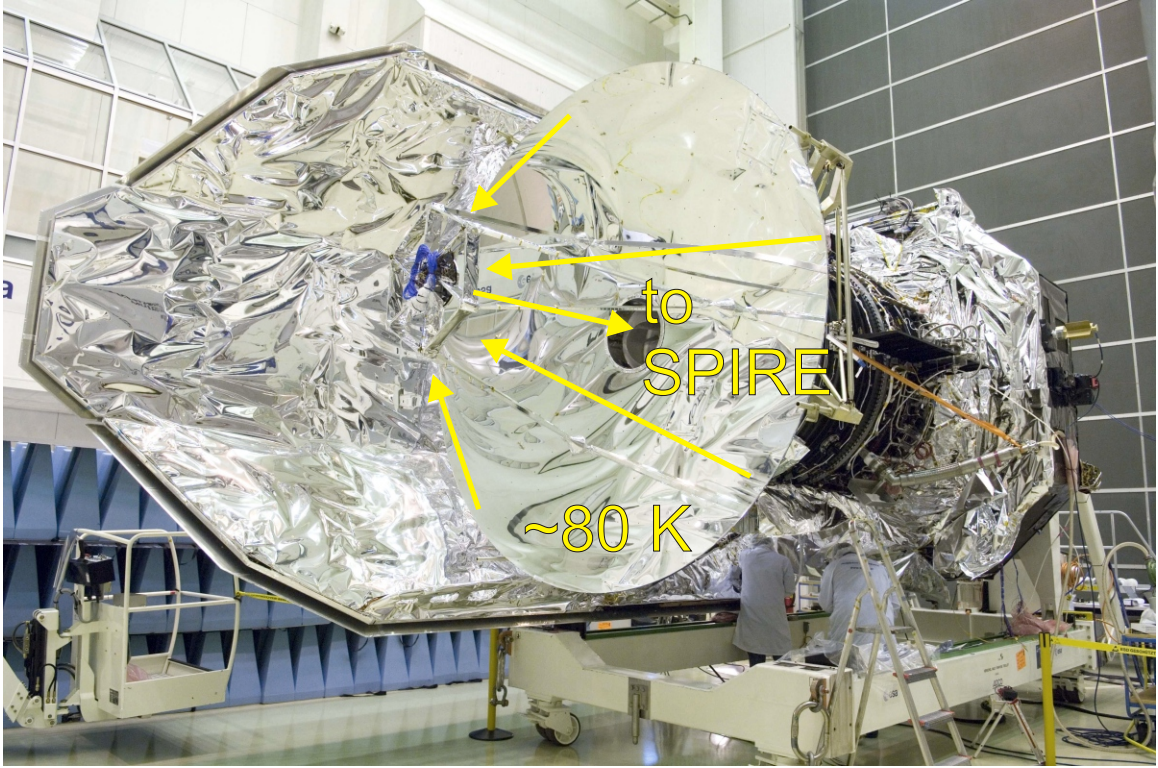


Figure 5.5: Image of the fully constructed Herschel telescope. The arrows show the telescope primary and secondary mirrors as sources of  $\sim 80$  K background radiation. *Photo: ESA.*

emission from the primary mirror), was designed for a  $\sim 60$  K,  $\epsilon \approx 0.04$  primary mirror [13]. Mirror development occurred in parallel with instrument testing, and it is now expected that the Herschel telescope will have a lower total emissivity  $\epsilon \approx 0.02$ , corresponding to a temperature of  $T \sim 80$  K [8]. The final mirror temperatures and emissivities, which vary inversely with respect to each other, will only be known after the in-flight performance verification phase which follows shortly after Herschel is launched, however, and may range from  $\epsilon \approx 0.04 - 0.005$  ( $T \approx 60 - 90$  K) [19]. The expected incident radiant power for each instrument configuration, i.e. viewing the CBB, the laboratory, or the telescope primary mirror in flight, including all optical efficiencies, is shown in Figure 5.8. The background



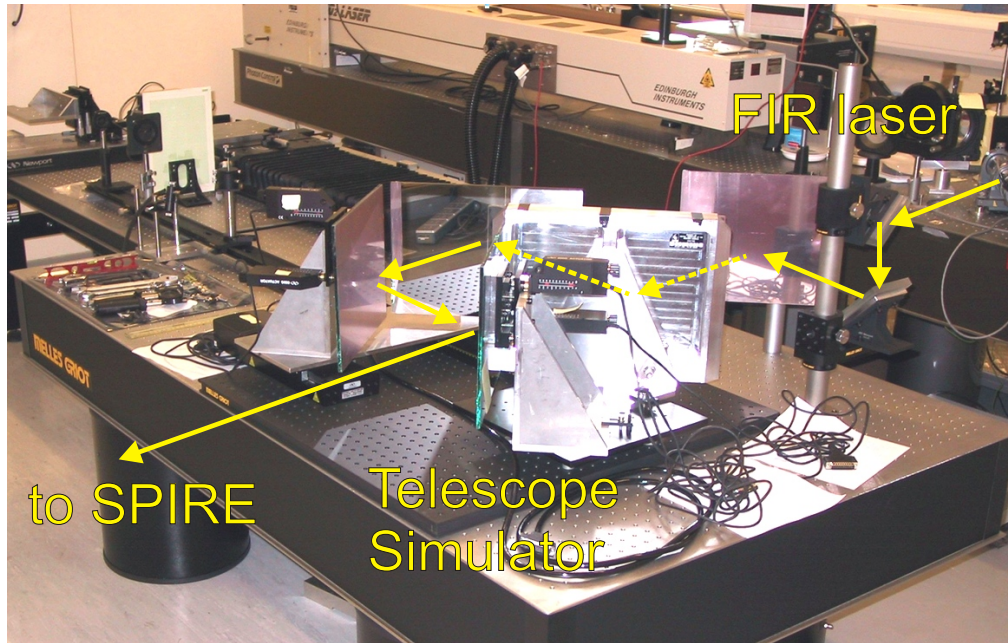


Figure 5.6: Image of the telescope simulator in the SPIRE test facility clean room at RAL. The arrows indicate the path of light from the laser optical bench through the simulator towards the SPIRE cryostat. When in use, the photonic mixer was positioned on the laser optical bench. *Photo: RAL.*

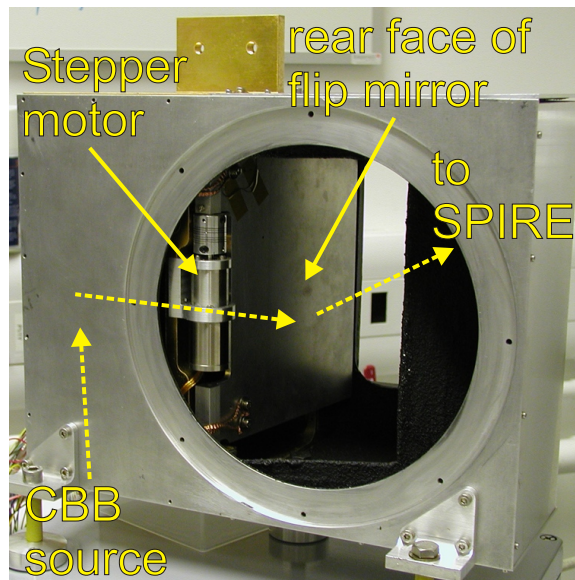


Figure 5.7: Image of the CBB inside of its housing. A stepper motor switches the flip mirror such that SPIRE views the CBB or the laboratory. *Photo: Cardiff AIG.*



Table 5.3: Incident background radiant power levels for the SPIRE FTS for each case presented in Figure 5.8.

Input Configuration	Q (pW)	
	SLW	SSW
CBB	8.82	1.12
Lab	5.46	2.78
Sky, $T = 60$ K, $\epsilon = 4\%$	4.40	3.31
Sky, $T = 80$ K, $\epsilon = 1\%$	5.01	4.15
Sky, $T = 90$ K, $\epsilon = 0.5\%$	5.44	4.58

optical power levels for each of the cases in Figure 5.8 are determined by integrating across the spectral bands and are shown in Table 5.3.

## 5.4 SPIRE Bolometer Models

Each of the background power conditions shown in Figure 5.8 is associated with a different bias condition that optimizes detector performance in terms of sensitivity and noise. This section uses the bolometer theory presented in §5.1 to explore the effect of varying input optical power and bias condition on the detector responsivity and NEP. The material parameter constants, and other input variables, for the SPIRE FTS bolometers of each detector array are listed in Table 5.4 [6, 180].

As discussed in §5.1, the bolometer bias conditions depend upon the background radiant power incident on the bolometer,  $Q$ , and the bolometer equilibrium operating temperature,  $T$ . The bolometer bias current can be expressed as a function of  $Q$  and  $T$  as follows

$$I(Q, T, T_o) = \sqrt{\frac{G_S(T, T_o)(T - T_o) - Q}{R^* \exp[(T_g/T)^n]}} \quad [\text{A}] . \quad (5.30)$$

It is instructive to determine the expected background power level,  $Q$ , and subsequently

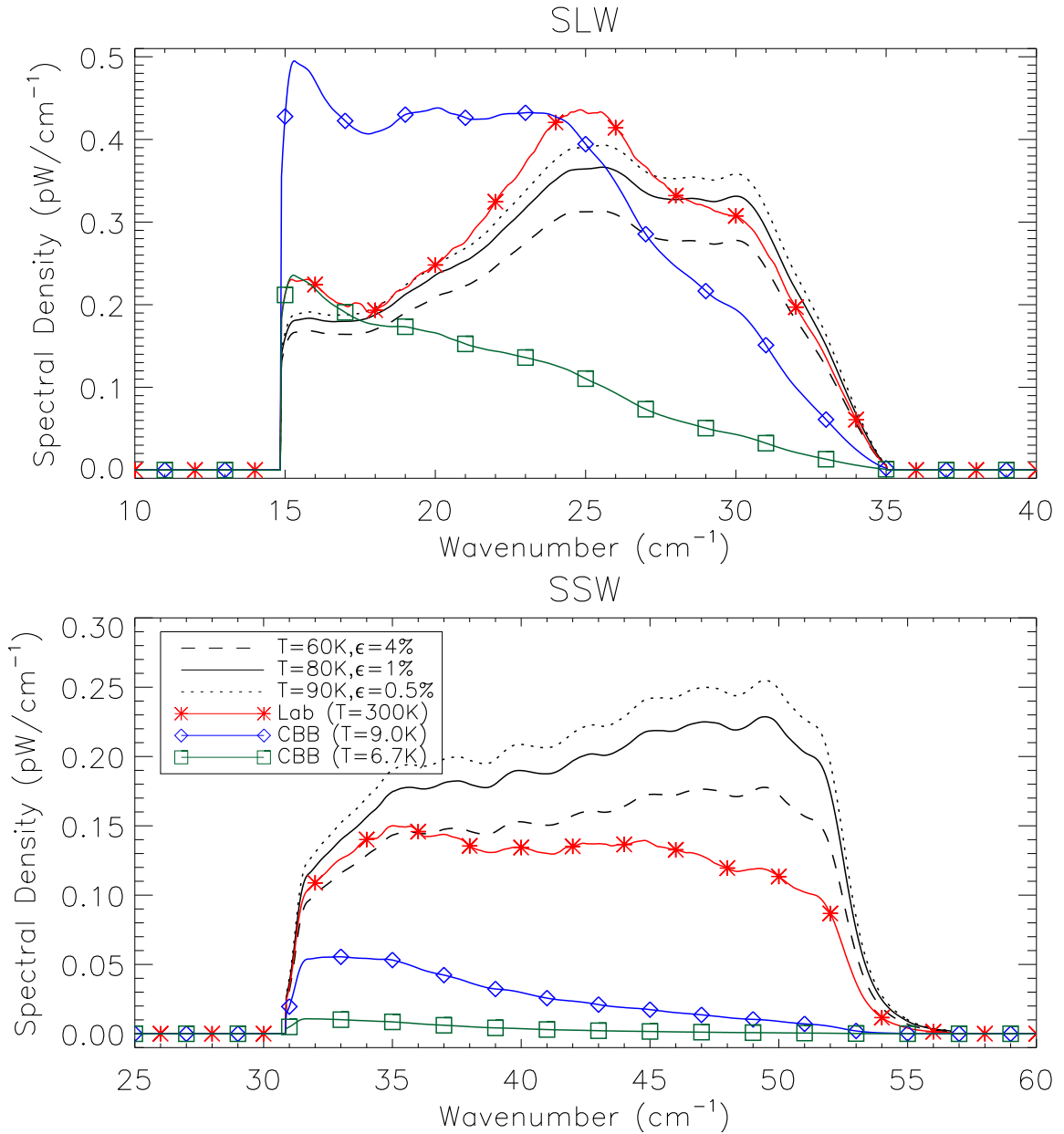


Figure 5.8: The spectral density of the incident background power for in-flight and laboratory configurations of the SPIRE FTS. The nominal (i.e.  $T \sim 80\text{K}$ ,  $\epsilon \sim 1\%$  – solid curve) and extreme cases (i.e.  $T \sim 60\text{K}$ ,  $\epsilon \sim 4\%$  – long dashes,  $T \sim 90\text{K}$ ,  $\epsilon \sim 0.5\%$  – short dashes) of the expected in-flight radiation background from the telescope primary optics are shown. The lab background is shown with asterisks and represents a  $T \sim 300\text{K}$ ,  $\epsilon \sim 100\%$  background, with the additional filters in place in the cryostat. The background power for the SPIRE instrument viewing the CBB ( $T \sim 10\text{K}$ ,  $\epsilon \sim 100\%$ ) is shown in diamonds. All of the spectra shown include optical throughput and transmission efficiencies.

Table 5.4: Input parameters for SPIRE FTS bolometer simulations.

Parameter	Description	Array	
		SLW	SSW
$T_o$ (K)	Bolometer heat sink temperature	0.31	0.31
$T_{L0}$ (K)	Detector array housing (Level-0) temp.	1.8	1.8
$T_{L1}$ (K)	Instrument temp. (Level-1)	5.5	5.5
$V_{A-rms}$ (nV/ $\sqrt{\text{Hz}}$ )	JFET plus amplifier noise	10	10
$T_G$ (K)	Bolometer band-gap temp.	41.0	42.1
$R^*$ ( $\Omega$ )	Bolometer resistance parameter	92.2	79.3
$R_L$ (M $\Omega$ )	Load resistor	23.2	19.2
$G_{So}$ (pW/K)	Static thermal conductance at 0.3 K	163	194
$\beta$	Thermal conductivity index	1.23	1.30
$n$	R-T power law index	0.5	0.5
$C_o$ (pJ/K)	Heat capacity at 0.3 K	1.00	1.02
$\rho$	Heat capacity index	1	1

determine the detector responsivity and NEP for a variety of bias currents. The desired bias current is that which results in optimum values for noise performance and sensitivity for a given  $Q$ ; this leads to the selection of load resistor,  $R_L$ , and bias voltage,  $V_b$ . An example of the bolometer model NEP results is shown for the 9.0 K CBB configuration in Figure 5.9, which illustrates the DC NEP values from the various noise sources in the model. Similar results were determined for the other input configurations (e.g. laboratory and expected telescope primary mirror).

The NEP contributions for the other input configurations were also modeled and used to determine the overall DC NEP in each case. The overall DC NEP results for each configuration modeled are shown in Figure 5.10. The vertical bars on the figure represent the bias current for which there is a minima in the total NEP. These results will be used in §5.5 to compare the expected instrument noise performance with that observed during PFM testing. The detector responsivity for each case shown in Figure 5.10 is illustrated

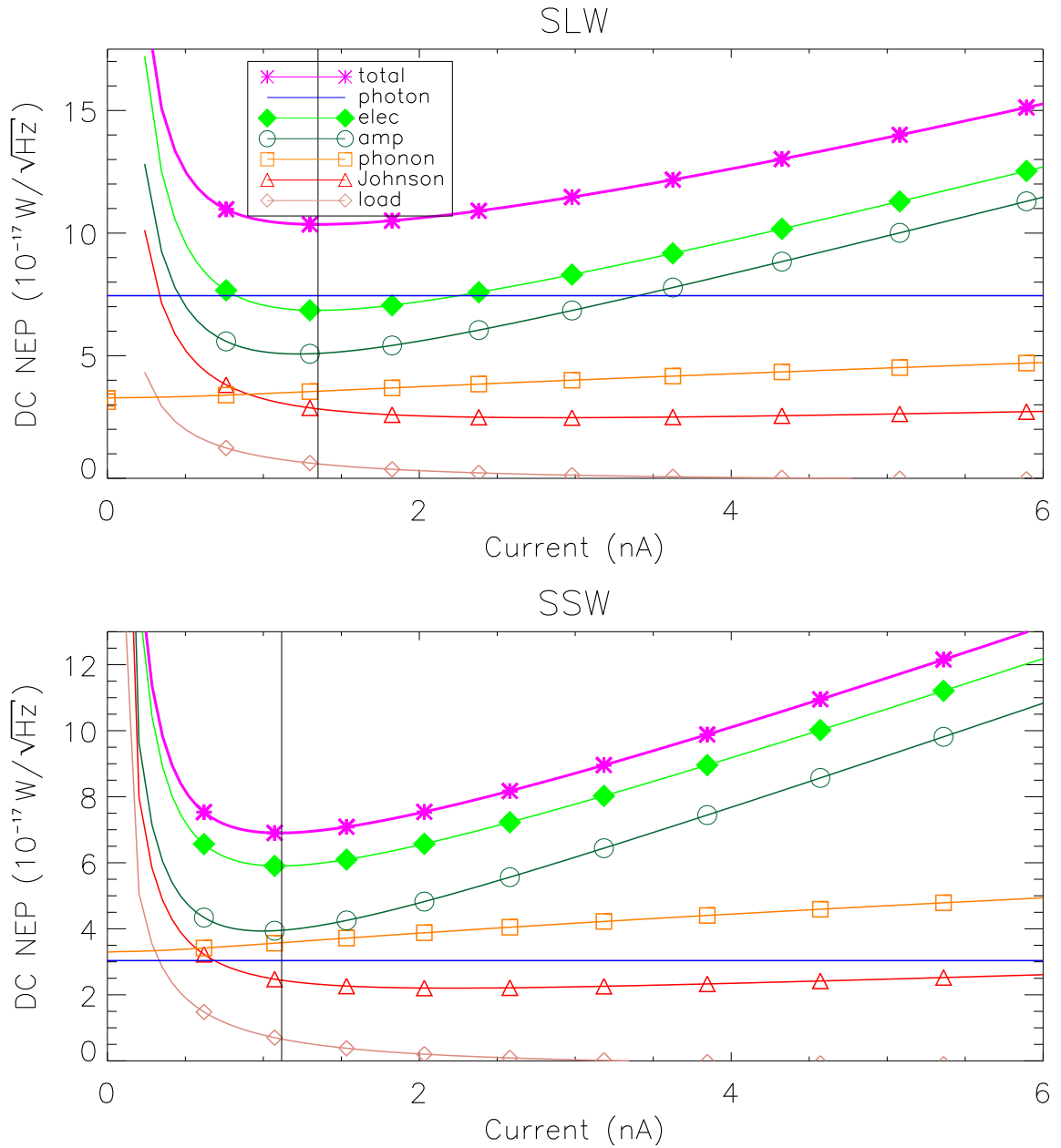


Figure 5.9: The DC NEP contributions for the SPIRE FTS viewing a 9.0 K CBB for both the SLW and SSW detector arrays. The vertical bar represents the minimum total NEP case, and thus the desired bias current. The NEP contributions shown are the total NEP (asterisks), total non-optical NEP (filled diamonds), amplifier NEP (circles), phonon NEP (squares), Johnson NEP (triangles), load resistor NEP (diamonds), and photon NEP (solid curve). It is evident that photon noise is the dominant unique noise source for the SLW array, whereas other noise sources are greater than the photon NEP for the SSW array.

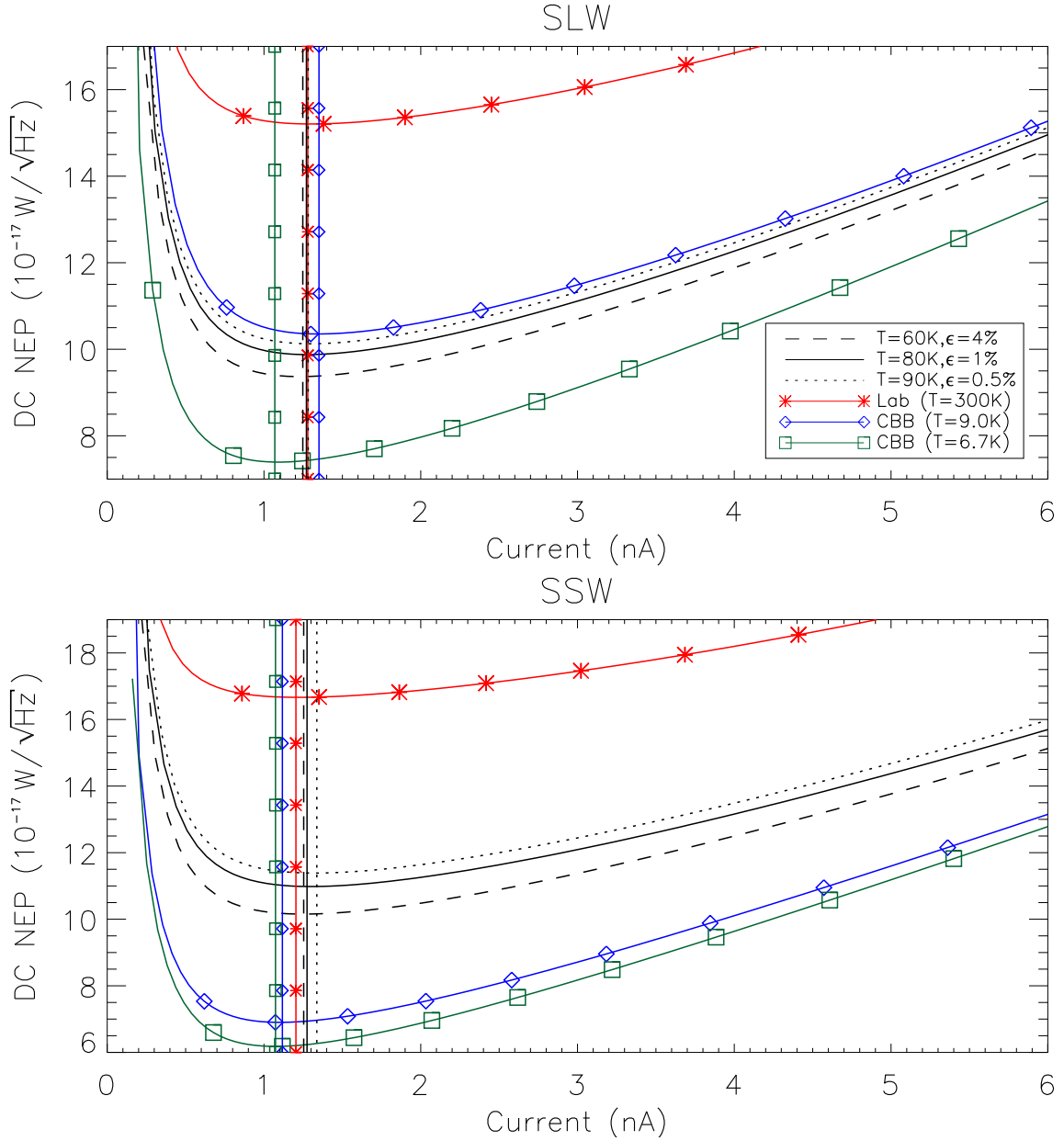


Figure 5.10: The total DC NEP for the SPIRE FTS viewing the lab during PFM testing (asterisks), the CBB (9.0 K – diamonds, 6.7 K – squares), and the expected performance in-flight (nominal – solid, low  $\epsilon$  primary – dashed, high  $\epsilon$  primary – dotted). The vertical bars represent the NEP minima, and thus the ideal bias current.

in Figure 5.11. The vertical bars in this figure represent the minimum NEP operating point, and are observed to be slightly offset from the responsivity maxima. The minimum noise bias current,  $I$ , and the value of other bolometer performance indicators such as bolometer voltage,  $V$ , input bias voltage,  $V_b$ , NEP, detector responsivity,  $S$ , and overall rms noise voltage,  $V_{rms-total}$ , at the minimum noise bias current are given for both detector arrays in Table 5.5. Although the input radiant power levels are similar (Table 5.3), it is readily evident that there are differences between a uniformly attenuated high emissivity, high temperature, source (i.e. the ~300 K test facility); an unattenuated high emissivity cold source (i.e. the CBB); and a low emissivity intermediate source (i.e. the telescope pre-optics) in terms of NEP. In particular, note the differences between the background power and photon NEP for room and CBB viewing configurations. For the SLW array, although  $Q_{room} < Q_{CBB}$ , it seems to be the opposite relationship for the NEP, i.e.  $NEP_{photon-room} > NEP_{photon-CBB}$ .

A study of Figure 5.8 shows, especially for the SLW array, that the spectral power density associated with observing the room through the cryostat filters is equivalent to that expected from the telescope primary optics in flight; despite this apparent close agreement, the photon NEP values for the two cases are dissimilar. This serves to illustrate that the optical/spectral simulation of the space-based environment of a far-infrared instrument in a laboratory setting is challenging!

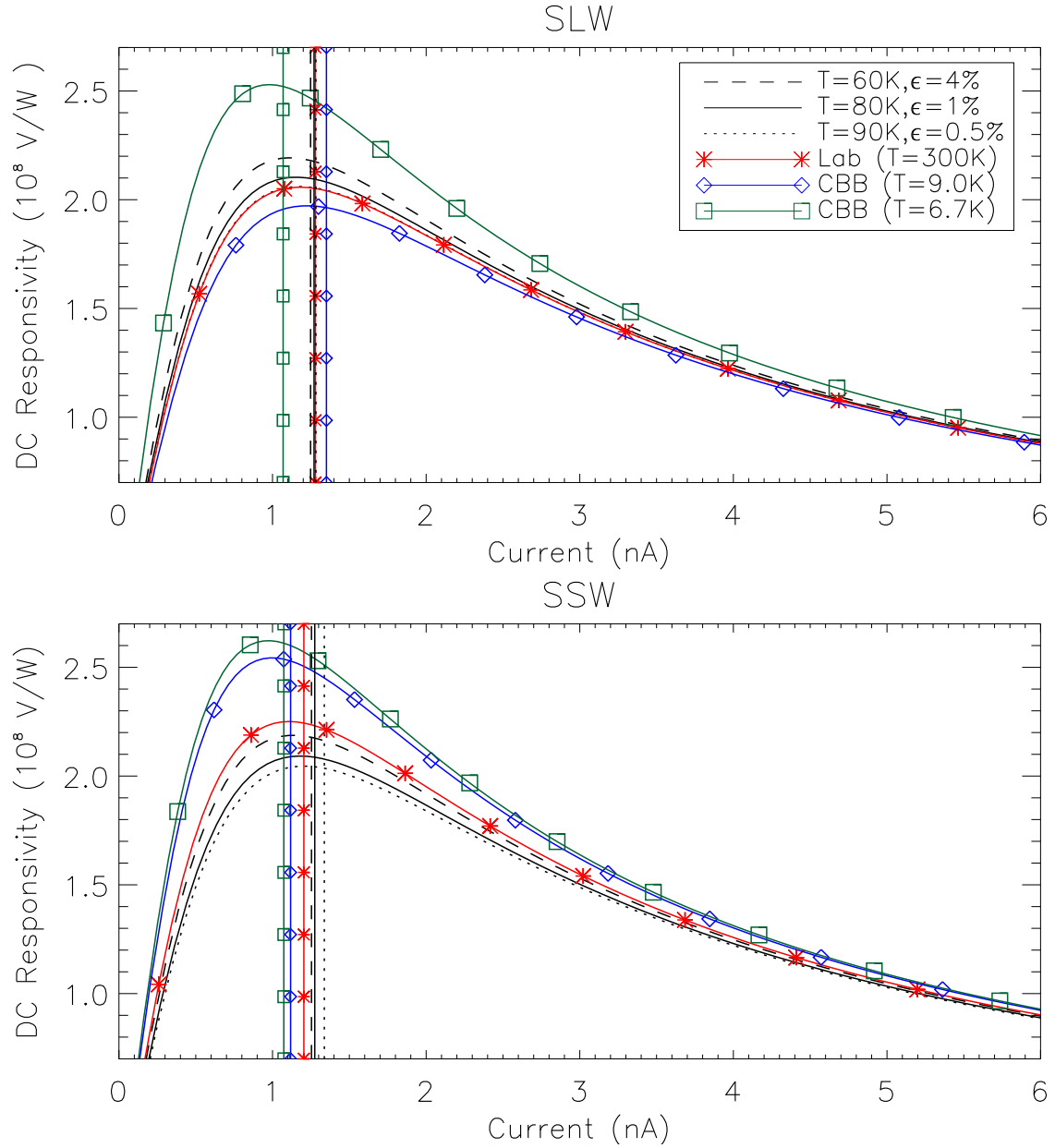


Figure 5.11: Simulation of the total DC detector responsivity,  $S$ , for the SPIRE FTS for various optical input configurations: viewing the lab during PFM testing (asterisks), viewing the CBB during PFM testing (diamonds), and the expected performance in-flight (nominal-solid, low  $\epsilon$  primary-dashed, high  $\epsilon$  primary-dotted). The vertical bars again represent the bias current level associated with the minima for the total NEP.

Table 5.5: Results from SPIRE FTS bolometer simulations at various input configurations.

Input Configuration		$T \sim 80$ K	$T \sim 90$ K	$T \sim 60$ K	Lab (300 K)	CBB (9.0 K)	CBB (6.7 K)
SLW	$I$ (nA)	1.27	1.28	1.25	1.28	1.35	1.07
	$V$ (mV)	4.54	4.48	4.66	4.47	4.42	4.92
	$V_b$ (mV)	34.01	34.22	33.61	34.15	35.75	29.72
	$Q$ (pW)	5.01	5.44	4.40	5.46	6.20	2.13
	$\text{NEP}_{\text{photon}}$ ( $10^{-17}\text{W} \sqrt{\text{Hz}}$ )	7.10	7.35	6.58	13.51	7.45	4.24
	$\text{NEP}_{\text{elec}}$ ( $10^{-17}\text{W} \sqrt{\text{Hz}}$ )	6.87	6.97	6.67	6.98	7.19	6.05
	$\text{NEP}_{\text{total}}$ ( $10^{-17}\text{W} \sqrt{\text{Hz}}$ )	9.88	10.13	9.37	15.21	10.35	7.39
	$S$ ( $10^8$ V/W)	2.10	2.06	2.19	2.06	1.97	2.53
	$V_{\text{rms-total}}$ (nV $\sqrt{\text{Hz}}$ )	20.69	20.80	20.43	31.20	20.33	18.64
SSW	$I$ (nA)	1.27	1.34	1.25	1.20	1.12	1.07
	$V$ (mV)	5.16	5.16	5.32	5.35	5.76	5.82
	$V_b$ (mV)	29.63	30.84	29.38	28.47	27.22	26.43
	$Q$ (pW)	4.15	4.58	3.31	2.78	0.61	0.09
	$\text{NEP}_{\text{photon}}$ ( $10^{-17}\text{W} \sqrt{\text{Hz}}$ )	8.41	8.84	7.50	15.25	3.04	1.12
	$\text{NEP}_{\text{elec}}$ ( $10^{-17}\text{W} \sqrt{\text{Hz}}$ )	7.06	7.17	6.85	6.72	6.20	6.08
	$\text{NEP}_{\text{total}}$ ( $10^{-17}\text{W} \sqrt{\text{Hz}}$ )	10.98	11.39	10.15	16.67	6.90	6.18
	$S$ ( $10^8$ V/W)	2.09	2.05	2.19	2.25	2.54	2.62
	$V_{\text{rms-total}}$ (nV $\sqrt{\text{Hz}}$ )	22.92	23.18	22.12	37.40	17.46	16.14



## 5.5 Performance of the SPIRE FTS

As mentioned in §5.4, it was impossible to simulate the flight environment of SPIRE. Therefore, the measured performance of the SPIRE FTS during PFM testing cannot provide a direct indication of the expected in-flight performance of the instrument. The observed instrument performance can, however, be compared to theoretical models which have been developed specifically for the laboratory conditions present during testing. This section evaluates the observed noise performance of the SPIRE FTS during PFM testing, and compares these results with the expectations dictated by the theoretical bolometer simulations. The results of the comparison between the observed and expected NEP for the PFM observations are then used to predict the in-flight noise performance of the SPIRE FTS.

### 5.5.1 Observations Viewing the SPIRE Test Facility

As mentioned in §4.5, a photonic mixer [155,156] was used during PFM testing as an additional unresolved spectral line source. The photonic mixer accepts two compact near-infrared lasers operating at a wavelength of  $\sim 1.55 \mu\text{m}$  (standard in the telecom industry) as input via a polarization maintaining fibre. The laser inputs are tuned to wavelengths chosen such that they are spectrally separated from each other by several hundred gigahertz (GHz), where the difference frequency output by the mixer forms the desired infrared/submm signal. Although the specific frequency of the photonic mixer source is not as precisely defined as is the energy/frequency of the transitions in a molecular laser, the photonic mixer provides a continuous range of tunable, stable, output frequencies which is much less limited than

the discrete transitions available from a molecular laser.

The unresolved spectral feature from the photonic mixer is isolated by obtaining the difference between PFM FTS observations recorded in rapid succession with and without the photonic mixer included in the input. Fitting and removal of this line from the residual spectrum, even under conditions where the continuum background is two orders of magnitude greater than the unresolved line source (8.5 pW cf. 0.01 – 0.1 pW for these observations), provides isolation of the noise present within a derived spectrum. This section presents results from the extraction of the spectral noise from PFM observations with the laboratory (i.e. ~300 K background) as a background. The spectral noise is used to determine an effective NEP which is in turn compared to the simulation results presented in §5.4.

At a fundamental level, the FTS is a spectrum analyzer and can thus be used to evaluate the spectral nature of noise sources. To understand instrument performance better, it is instructive to evaluate the spectral noise distribution, specifically comparing in and out of band spectral regions. A region below the spectral band will give an indication of the total noise, excluding photon noise, which is heavily effected by  $1/f$  noise (§2.7.2). A spectral region above the spectral passband will provide an estimate of the overall noise excluding photon noise that is well isolated from  $1/f$  noise. The spectral region within the spectral passband provides an estimate of the total overall noise present. Since SPIRE FTS data is four times oversampled, a spectral region well above the high optical frequency cut-off is available to be used for determination of the system noise excluding photon noise. The frequency bands used in this evaluation are 15 – 33  $\text{cm}^{-1}$  (in-band), and 150 – 180  $\text{cm}^{-1}$

(out-of-band) for SLW, and  $32 - 53 \text{ cm}^{-1}$  (in-band), and  $165 - 190 \text{ cm}^{-1}$  (out-of-band) for SSW.

In Fourier transform spectroscopy, the NEP can be expressed in terms of instrument parameters as follows [181]

$$\text{NEP}_{\text{measured}} = \varsigma \sqrt{\frac{\Delta\sigma}{2v_{\text{stage}}}} \quad [\text{W}/\sqrt{\text{Hz}}], \quad (5.31)$$

where  $\varsigma$  ( $\text{W}/\text{cm}^{-1}$ ) is the spectral noise,  $v_{\text{stage}}$  ( $\text{cm OPD}/\text{s}$ ,  $0.2 \text{ cm}/\text{s}$  for SPIRE) is the velocity of the FTS translation stage, and  $\Delta\sigma$  ( $\text{cm}^{-1}$ ) is the spectral resolution (see §D.7 for further details of this relation). In this analysis, Equation 5.31 is used with the residual spectral noise estimates to obtain a measure of the NEP for every spectral data point. Thus, the average in-band NEP gives an estimate of the total NEP, including  $\text{NEP}_{\text{photon}}$ , and an average of the above band NEP values gives an estimate of  $\text{NEP}_{\text{elec}}$ . The photon NEP is determined by the quadrature subtraction of  $\text{NEP}_{\text{elec}}$  from the  $\text{NEP}_{\text{total}}$ .

In order to compare the measured noise performance with that expected from simulations, an estimate of the noise present must be extracted from experimental observations. The spectral noise estimate is obtained by first subtracting the background only observation from the spectrum, fitting a sinc function to the residual spectrum, and then subtracting the best-fit sinc from the residual spectrum. Let  $B(\sigma)$  represent the background continuum from the laboratory, and  $A \text{ sinc}(\sigma_o, \delta\sigma_o)$  represent the unresolved source from the photonic mixer while the interferograms were recorded. For an individual scan, e.g. scan  $i$ , the spectral noise is assumed to be  $\varsigma_i$ . The background-only scan ( $j$ ) ideally contains the same background spectrum,  $B(\sigma)$ , while the noise,  $\varsigma_j$ , is independent. Assuming that both scans are recorded under similar conditions, and thus the noise amplitudes are equivalent, the

overall noise present in the residual noise spectrum will be  $\sqrt{\zeta_i^2 + \zeta_j^2} = \sqrt{2}\zeta$ . Since the photonic mixer only illuminated a few detectors per observation, the detectors which did not observe the photonic mixer during the observation did not need a sinc function subtracted from the residual spectrum; the difference between the two observations provided the residual spectral noise.

Figure 5.12 shows the process of noise extraction from one of the photonic mixer spectra recorded by the SPIRE FTS during PFM testing. The upper plot of the figure contains the original spectrum including the continuum background from the laboratory in addition to the unresolved feature due to the photonic mixer. The central plot shows the spectrum after the subtraction of a complementary scan where the photonic mixer was blocked, i.e. the removal of the background continuum. The lower plot shows the residual noise spectrum where the unresolved spectral feature (sinc fit, if applicable) and background continuum have been removed.

The NEP from spectra recorded viewing the laboratory is illustrated for SLW-D2 in Figure 5.13. Values of  $\text{NEP}_{elec}$  as derived from out of band NEP averaging for both SLW & SSW arrays are shown in Figure 5.14.  $\text{NEP}_{elec}$  is determined to be  $13 \pm 5 \cdot 10^{-17} \text{ W}/\sqrt{\text{Hz}}$  across the SLW array, and  $8 \pm 2 \cdot 10^{-17} \text{ W}/\sqrt{\text{Hz}}$  for the SSW array; both of these values are in good agreement with the model predictions listed in Table 5.6.  $\text{NEP}_{total}$  for both arrays is also shown in Figure 5.14 where the average value is  $98 \pm 72 \cdot 10^{-17} \text{ W}/\sqrt{\text{Hz}}$  for SLW and  $49 \pm 33 \cdot 10^{-17} \text{ W}/\sqrt{\text{Hz}}$  for SSW. These values are not in agreement with the bolometer model. It is important to note that the laboratory is not a passive environment and is not well represented by a perfect blackbody at a constant

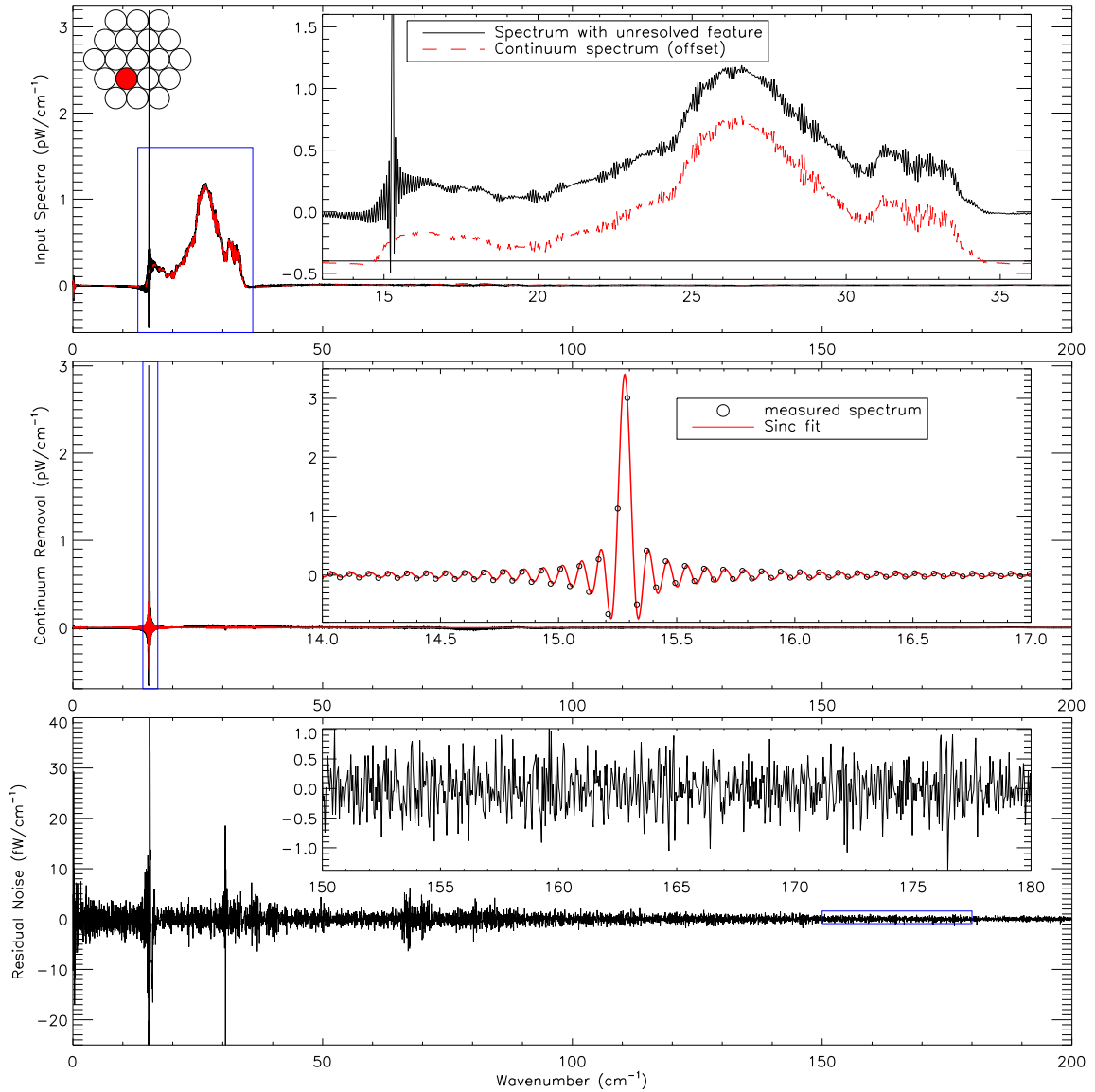


Figure 5.12: Determination of NEP from laboratory SPIRE FTS spectra for detector SLW-D2. The top figure illustrates spectra taken with the laboratory continuum background and with (solid) and without (dashed) the photonic mixer signal. The middle plot shows the continuum subtraction (solid in figure, circles in inset), and fit (solid in figure and inset), of the unresolved spectral feature. The lower figure shows the residual noise used to determine the NEP after both the continuum and unresolved feature have been subtracted. The boxed regions in each plot show the area plotted within the insets.

temperature. During the acquisition of these data, there were scientists operating test equipment and controls in the control room facility adjacent to the clean-room test facility and in the clean-room facility itself. Since the  $NEP_{elec}$  values are within agreement with the bolometer model, the excess noise in these data is assumed to be due to fluctuations of the laboratory continuum background. Temperature fluctuations on the order of a few tenths of a degree and humidity fluctuations on the order of a few percent may provide a partial explanation for the background continuum variation. Additionally, variations in the background scene (e.g. air currents, varying optical paths and sources) may be the result of the experimentalist operating the photonic mixer within the clean room test facility. The observed noise values for the SPIRE FTS viewing the laboratory, along with results for the CBB scans (to be discussed in §5.5.2), are presented in Table 5.6.

### 5.5.2 Observations Viewing the CBB

To evaluate the performance of the detectors while viewing a more stable thermal environment, a low temperature continuum source inside the cryostat, i.e. the CBB, was used during PFM testing of the SPIRE instrument. The CBB was designed as an ideal blackbody source of emissivity  $\epsilon = 1$  [179]. A flip mirror inside the SPIRE test cryostat allowed the SPIRE FOV to alternately view the laboratory external to the cryostat and the CBB within the cryostat (see Figure 5.2). Since in this configuration, while the flip mirror is set to view the CBB all of the emission incident upon the detectors originates from within the cryostat under space-like conditions, it is expected that these results will provide a more reliable measure of the FTS noise performance. A series of high-resolution ( $\Delta\sigma \sim 0.04 \text{ cm}^{-1}$ ) interferograms were recorded with the CBB set to 6.7, 7.2, 7.7, 8.2, 8.7,

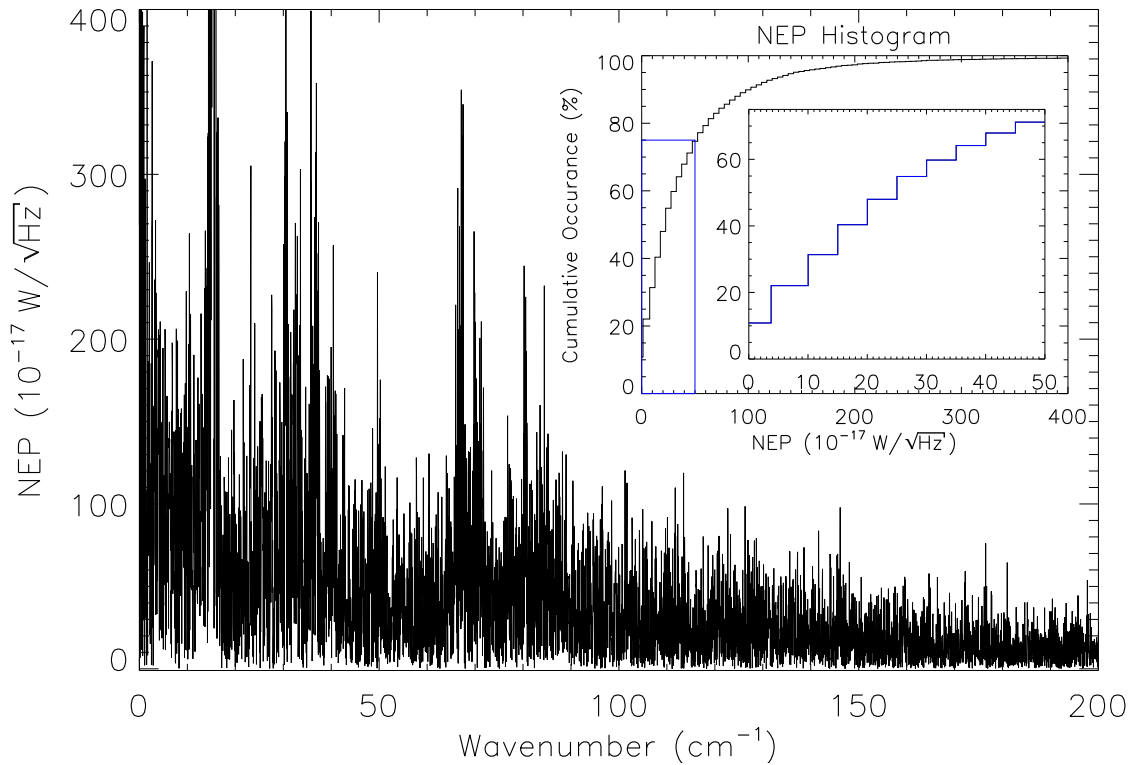


Figure 5.13: Spectral NEP derived from SPIRE FTS spectra of the photonic mixer and laboratory background for detector SLW-D2. An average within the band is used to determine  $\text{NEP}_{total}$  while an out of band average is used to estimate  $\text{NEP}_{elec}$ . The insets show a cumulative histogram representation of the spectral NEP data points with a box outlining the zoomed region of the second inset.

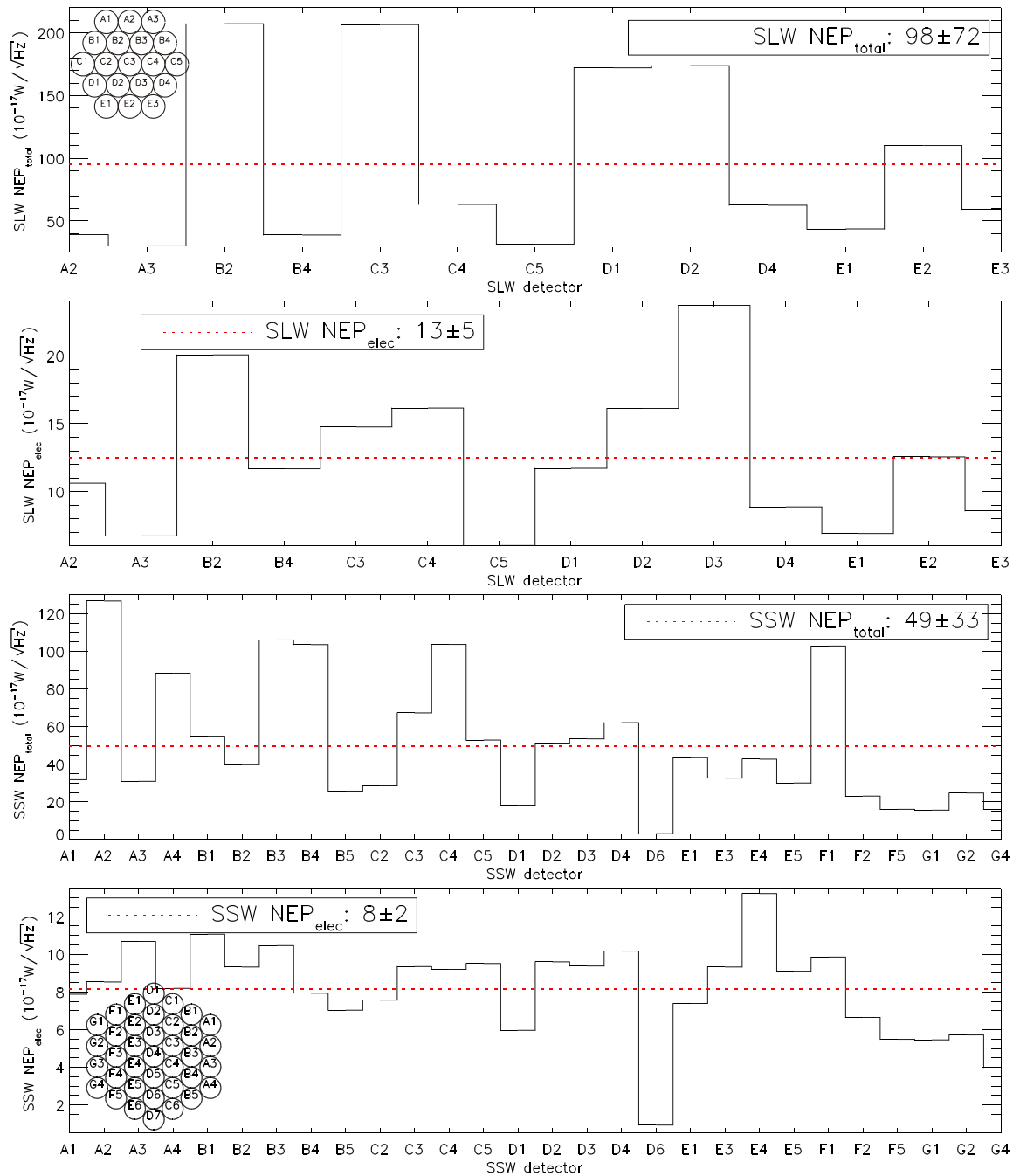


Figure 5.14: NEP<sub>elec</sub> and NEP<sub>total</sub> for both SPIRE FTS detector arrays while viewing the laboratory. NEP<sub>elec</sub> estimates are determined by averaging out of band spectral NEP values for each bolometer. NEP<sub>total</sub> estimates are obtained by averaging the in-band spectral NEP values for each bolometer.



and 9.0 K and SCAL switched off at the ambient instrument temperature ( $\sim 5$  K).

The analysis for these observations is similar to the analysis outlined in §5.5.1, where the difference between successive spectra derived from a series of high-resolution interferograms provides an estimate of the residual noise in a given spectrum. The noise of the CBB discussed in this section is derived from the difference between a single spectrum and the average of the spectra recorded under the same observation; between eight and sixteen scans were averaged in each case for these data. Figure 5.15 illustrates the noise extraction and NEP derivation for detector SLW-C4. The total NEP for each detector in the SPIRE arrays for the 6.7 K and 9.0 K CBB temperature settings is shown in Figure 5.16. These results are in excellent agreement with the performance predicted from the theoretical bolometer model (Table 5.5).

The CBB noise measurements were taken under such controlled conditions that it is possible to compare the noise observations at varying CBB temperatures with the expected theoretical change in photon noise over the same range of CBB temperatures. The variation of observed photon NEP as a function of CBB temperature is illustrated in Figure 5.17. Each data point in this figure is determined from averaging sixteen high-resolution scans; thus,  $\sim 1600$  interferograms were analyzed for the SLW array, and  $\sim 2800$  for the SSW array. Although the large error bars reflect the uncertainty in the nature of a noise measurement, the observed photon NEP is in agreement with theoretical expectations. There is excellent agreement found in the SLW array, and the agreement in the SSW array falls off at lower CBB temperatures. This is primarily due to the extremely low signal levels in this band causing errors in the extraction of photon noise from the total noise observed. Figure 5.8

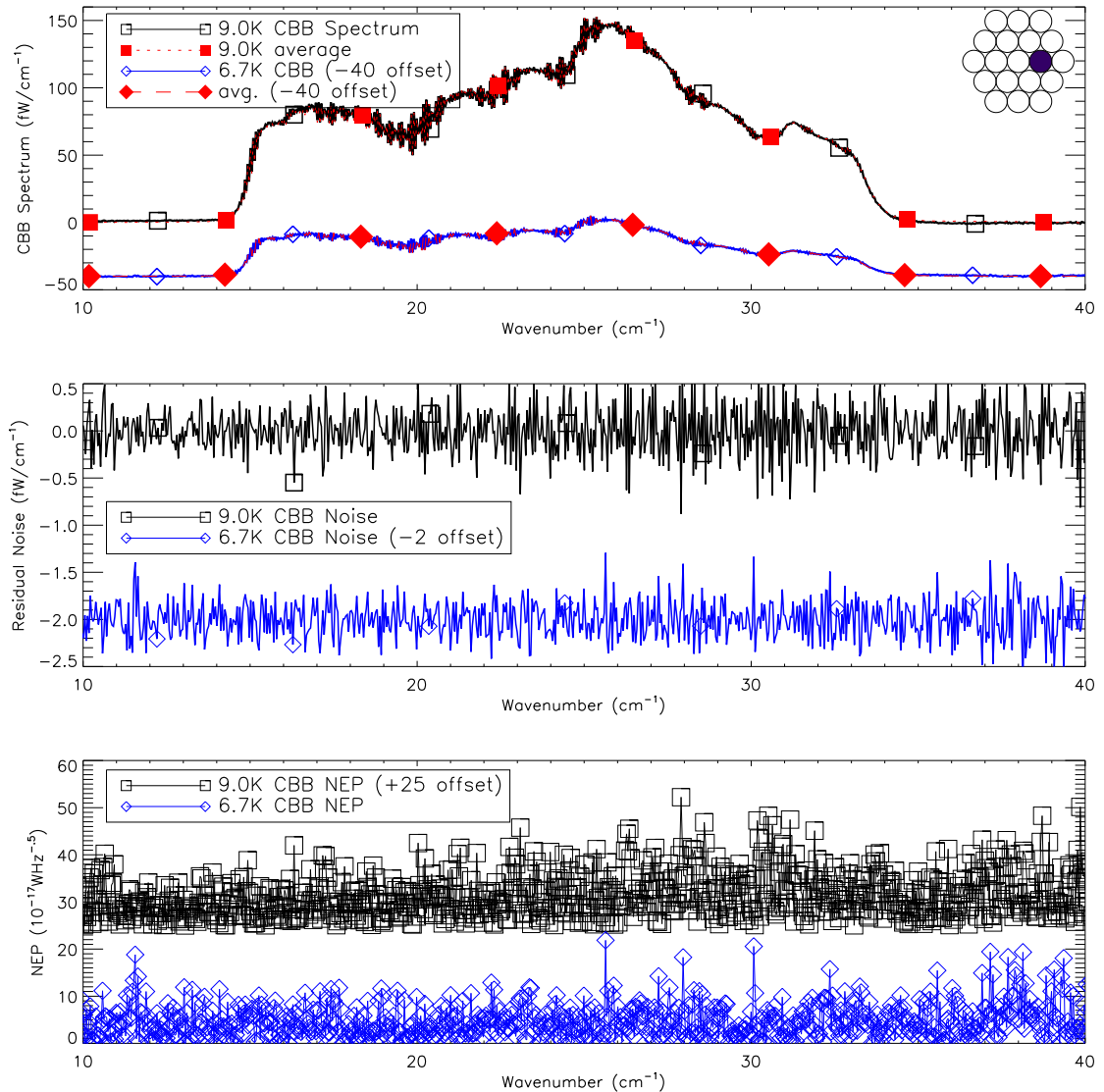


Figure 5.15: Determination of SPIRE FTS NEP for spectra recorded while viewing the CBB for detector SLW-C4. The upper plot shows individual spectra and the average of several spectra over-plotted for the 6.7 K and 9.0 K CBB temperature cases. The centre plot shows the difference between the individual spectrum and the corresponding average. The lower plot shows the resultant spectral NEP for each case.

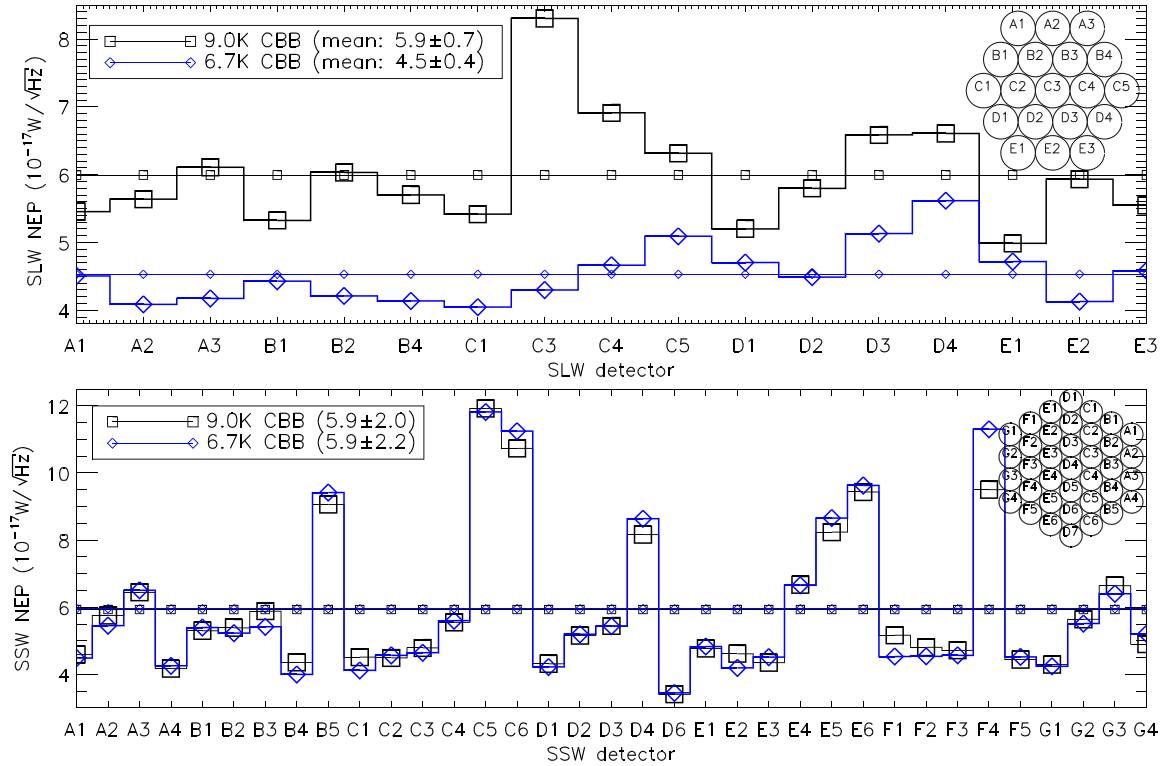


Figure 5.16: The NEP for the SPIRE FTS detectors viewing the CBB for both the 6.7 K and 9.0 K observations.

illustrates the spectral input for a 6.7 K and 9.0 K CBB. It is clear that the radiant power from the CBB falls off dramatically at low CBB temperatures and high frequencies.

A summary of  $NEP_{total}$  for the CBB scans, and both  $NEP_{total}$  and  $NEP_{elec}$  for the laboratory scans, is provided in Table 5.6. With the exception of the photon noise observed with SPIRE viewing the laboratory, all noise observations are in agreement with that predicted by theoretical bolometer models. Although it was not possible to do a full end to end test of the SPIRE instrument, including a cooled 3.5 m diameter telescope primary mirror within a laboratory setting, the series of tests which have been conducted support the theoretical bolometer model. The sensitivities predicted by the bolometer model for PFM

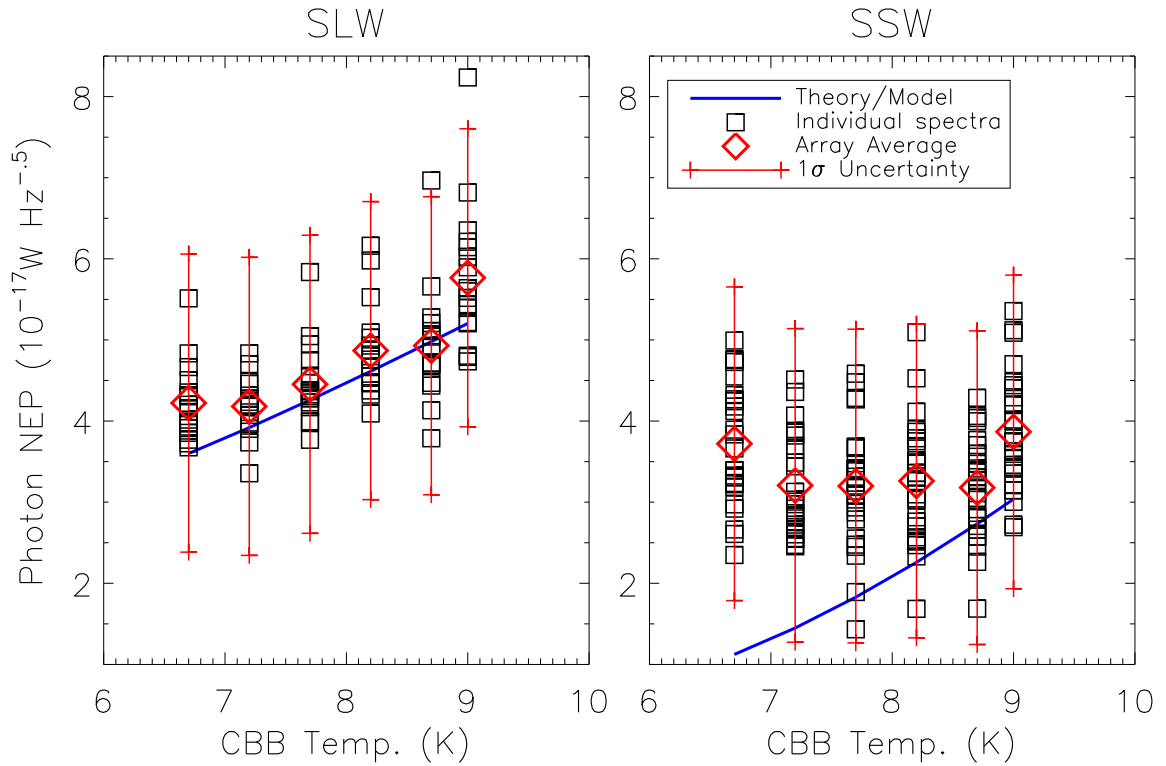


Figure 5.17: Variation of  $\text{NEP}_{\text{photon}}$  with CBB temperature. The squares illustrate the average photon NEP per detector at each temperature while the diamonds show the array average at each CBB temperature. The solid line shows the theoretical variation of detector  $\text{NEP}_{\text{photon}}$  with CBB temperature. The SLW array shows excellent agreement with theory. As photon noise is not the dominant noise source in the SSW array at these temperatures, the extraction of  $\text{NEP}_{\text{photon}}$  from  $\text{NEP}_{\text{total}}$  is less reliable.

Table 5.6: Comparison of average NEP values determined from SPIRE PFM interferograms for each SPIRE FTS array and predicted results from the theoretical bolometer model.

Input Configuration		NEP ( $10^{-17} \text{W}/\sqrt{\text{Hz}}$ )	
		measured	theoretical model
SLW	CBB (9.0 K)	$6 \pm 1$	8.2
	CBB (6.7 K)	$4.5 \pm 0.5$	6.8
	Lab ( $\text{NEP}_{elec}$ )	$13 \pm 5$	7.0
	Lab ( $\text{NEP}_{total}$ )	$98 \pm 72$	15.2
	Sky, $T = 80 \text{ K}$	N/A	9.9
SSW	CBB (9.0 K)	$6 \pm 2$	6.9
	CBB (6.7 K)	$5 \pm 2$	6.2
	Lab ( $\text{NEP}_{elec}$ )	$8 \pm 2$	6.7
	Lab ( $\text{NEP}_{total}$ )	$49 \pm 33$	16.7
	Sky, $T = 80 \text{ K}$	N/A	11.0

testing were confirmed and there is strong evidence that photon noise was measured for the CBB at 9.0 K, which in turn supports the utility and accuracy of the theoretical bolometer model used in this analysis. Thus, this same confidence may now be placed in the accuracy of the predictions of the theoretical model for the SPIRE FTS detectors in flight configuration with the telescope primary mirror as the dominant source of background emission once the in-flight operating environment parameters are known. Additionally, the verification of the accuracy of this bolometer model also places confidence in its application towards other applications of SPIRE data analysis such as absolute calibration of astronomical sources and detector non-linear responsivity correction (Figure 5.11) [33].

### 5.5.3 In-Flight Sensitivity Predictions

As shown in Table 5.5, and as verified by the analysis shown in §5.5.1 & §5.5.2, the total NEP for the SPIRE FTS detector arrays is expected to be 9.88 and  $10.98 \cdot 10^{-17} \text{ W}/\sqrt{\text{Hz}}$

Table 5.7: Observed M82 CO line intensities ( $\int T dv$  [K km/s]) [161, 182].

Line	Region		
	NE-Lobe	Centre	SW-Lobe
CO $J = 7 - 6$ ( $\sigma_o = 29.90701 \text{ cm}^{-1}$ )	$132.3 \pm 5.8$	$177.7 \pm 5.4$	$167.2 \pm 6.4$
CO $J = 4 - 3$ ( $\sigma_o = 15.37866 \text{ cm}^{-1}$ )	$465.3 \pm 12.9$	$493.3 \pm 12.1$	$503.0 \pm 12.6$

for the SLW and SSW arrays, respectively. In this section, the expected NEP values for the SPIRE FTS detector arrays are used in conjunction with astronomical observation data to estimate the time required to obtain observations with a desired S/N. The examples in this section use CO emission lines in M82 [161] as sources.

Table 5.7 lists the integrated line intensities,  $\int T dv$ , from Mao et al. [161] for the CO  $J = 7 - 6$  and  $J = 4 - 3$  rotational transitions for the centre, north-east lobe, and south-west lobe of M82. The intensities are given in units of K km/s, i.e. the antenna temperature integrated across the Doppler-shifted velocity profile. The line intensity is converted into an effective FTS-observed temperature,  $T_{eff}$ , distributed across an FTS resolution element as follows

$$T_{eff} = \frac{\int T dv}{\Delta v} \quad [\text{K}] , \quad (5.32)$$

where  $\Delta v$  is the FTS resolution in velocity units, e.g. km/s, and is given by

$$\Delta v = \frac{c\Delta\sigma}{\sigma} \quad [\text{km/s}] . \quad (5.33)$$

It is important to verify that all of the integrated line intensity falls within a single FTS resolution element, i.e. that the lines under observation are unresolved, otherwise the effective antenna temperature must be scaled to the appropriate resolution.

The S/N for FTS observations in the case of source power given in units of antenna

temperature,  $T_A$ , is given by [183]

$$S/N_T = \frac{k_b T_A c \Delta \sigma}{2 \text{NEP}} \sqrt{t}, \quad (5.34)$$

where  $t$  is the total observation time. The effective noise temperature,  $\varsigma_T$ , is given by [181]

$$\varsigma_T = \frac{4 \text{NEP}}{k_b c \Delta \sigma \sqrt{t}} \quad [\text{K}]. \quad (5.35)$$

Thus, the required observation time,  $t_{req}$ , can be expressed as a function of the desired S/N and effective antenna temperature as follows

$$t_{req} = \left[ \frac{4 \text{NEP} (S/N)}{k_b c \Delta \sigma T_{eff}} \right]^2 \quad [\text{s}]. \quad (5.36)$$

The astronomical observation template for high-resolution SPIRE FTS scans requires that interferograms be recorded in multiples of two (i.e. the FTS translation stage starts and ends at the same place). Although it is possible to observe a single up/down interferogram scan pair of a source, the associated telescope overheads make this measurement very inefficient [18]; the recommended minimum number of up/down scan pairs,  $N$ , is eight. Table 5.8 lists the resultant spectral S/N for observations of the CO lines observed by Mao [161] for one ( $N = 1$ ) and eight ( $N = 8$ ) up/down scan pairs. Table 5.9 shows the approximate number of scans required to obtain an S/N greater than 1000 for each of the above CO transitions. Approximate observation times, excluding any telescope overheads, are also shown for the  $S/N > 1000$  case in Table 5.9.

Not all of the CO lines within the SPIRE bands have been observed thus far as water vapour in the earth's atmosphere is highly absorptive at these frequencies. Observations of a family of transitions simultaneously using the broadband spectral coverage provided by an FTS will prove useful in providing constraints to temperature profiles used in theoretical

Table 5.8: Predicted S/N in terms of number of interferogram scan pairs ( $N$ ) for SPIRE FTS observations of M82. The uncertainty in brightness temperature,  $\delta T$ , is 2.5 mK for  $N = 1$ , and 0.89 mK for  $N = 8$ .

N	CO Line	Position		
		NE-Lobe	Centre	SW-Lobe
1	CO $J = 7 - 6$	$262.8 \pm 11.5$	$352.9 \pm 10.7$	$332.1 \pm 12.7$
	CO $J = 4 - 3$	$475.2 \pm 13.2$	$503.8 \pm 12.4$	$513.7 \pm 12.9$
8	CO $J = 7 - 6$	$743.2 \pm 32.6$	$998.2 \pm 30.3$	$939.2 \pm 36.0$
	CO $J = 4 - 3$	$1344.1 \pm 37.3$	$1424.9 \pm 35.0$	$1453.0 \pm 36.4$

Table 5.9: Integration time ( $t_{req}$ , seconds) required to achieve S/N greater than 1000 for SPIRE FTS observations of M82. Also shown are the corresponding number of interferograms,  $N$ , and uncertainty in brightness temperature,  $\delta T$ .

CO Line	Position		
	NE-Lobe	Centre	SW-Lobe
CO $J = 7 - 6$	S/N = $3621 \pm 317$	S/N = $2007 \pm 122$	S/N = $2267 \pm 174$
	$N \sim 29$	$N \sim 16$	$N \sim 18$
	$\delta T = 0.66$ mK	$\delta T = 0.89$ mK	$\delta T = 0.83$ mK
CO $J = 4 - 3$	S/N = $1107 \pm 61$	S/N = $985 \pm 48$	S/N = $947 \pm 47$
	$N \sim 9$	$N \sim 8$	$N \sim 8$
	$\delta T = 1.19$ mK	$\delta T = 1.26$ mK	$\delta T = 1.29$ mK



Table 5.10: Expected integrated CO line intensities for SPIRE FTS observations of a molecular cloud similar to M82.

		Line [182] ( $\text{cm}^{-1}$ )	$\int Id\sigma$ (fW)	
			$T_{CO} = 70$ K	$T_{CO} = 100$ K
SLW		15.37866 ( $J = 4 - 3$ )	0.80	1.02
		19.22223 ( $J = 5 - 4$ )	1.68	2.39
		23.06506 ( $J = 6 - 5$ )	3.35	5.50
		26.90701 ( $J = 7 - 6$ )	3.49	6.78
		30.74793 ( $J = 8 - 7$ )	2.55	5.99
SSW		34.58767 ( $J = 9 - 8$ )	0.98	2.84
		38.4261 ( $J = 10 - 9$ )	0.65	2.39
		42.26305 ( $J = 11 - 10$ )	0.41	1.95
		46.09839 ( $J = 12 - 11$ )	0.23	1.44
		49.93197 ( $J = 13 - 12$ )	0.11	0.91
		53.76364 ( $J = 14 - 13$ )	0.01	0.07

models. A simulation of CO in M82 was performed in order to estimate the S/N that would be achieved with a single pair of high-resolution SPIRE FTS spectra for each CO transition within the SPIRE FTS band. A CO column density of  $10^{18} \text{ cm}^{-2}$  was used [184] for CO rotation temperatures in the range of 70 – 100 K [161]. The continuum emission from dust has been reported to have temperatures ranging from 27 K [165] to 48 K [168], while the CO temperatures are thought to be between 70 K and 130 K [161]. The integrated line intensities for two CO temperatures, 70 K and 100 K, are shown for each CO line in Table 5.10. Figure 5.18 shows the simulation results for a single SPIRE FTS high-resolution observation. Many of the CO lines in the SLW array will be observed with high S/N with one high-resolution scan pair.

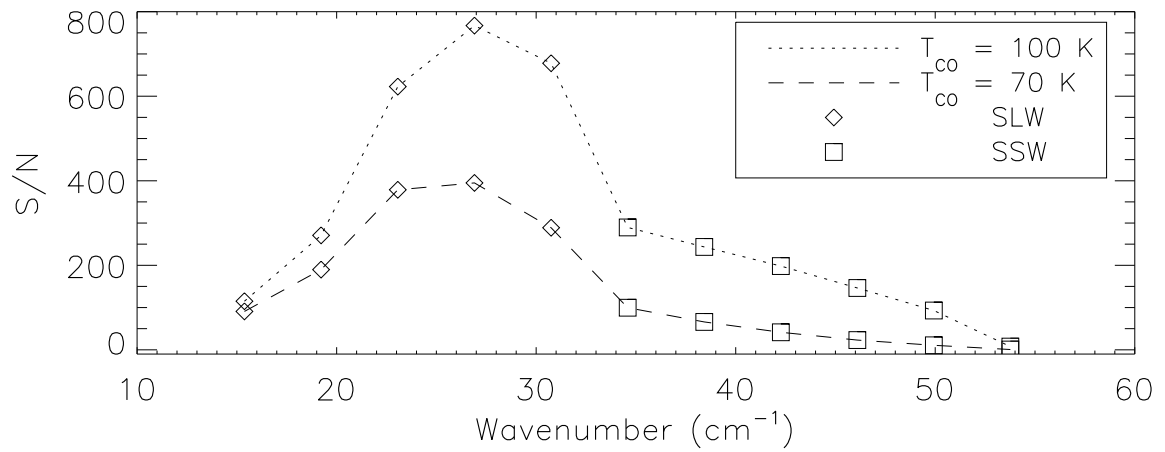


Figure 5.18: Expected S/N of CO lines for a single pair of high-resolution interferograms of a source such as M82. Results are shown for both a 100 K and 70 K CO gas temperature [161].

## 5.6 Conclusions

Bolometer theory relevant to the detectors employed within the SPIRE FTS instrument was introduced. The theoretical performance of the SPIRE instrument was determined by a combination of parameters of all of the subsystems. Although it was not possible to perform a full end to end test with the complete telescope under flight conditions, an extensive series of tests were conducted with the SPIRE instrument in the test facility cryostat viewing either the laboratory background external to the cryostat or the CBB within the cryostat.

As expected, the noise observed during observations of the laboratory background was greater than the noise observed during observations of the CBB. While the noise present during laboratory observations was not inconsistent with that predicted by the theoretical model, the laboratory background is not well synthesized by a stable, single temperature, blackbody source. The CBB observations, on the other hand, which used a blackbody source placed under near-flight conditions within the evacuated SPIRE test cryostat operating at cryogenic temperatures, produced estimates of the spectral noise which agree well with the theoretical model.

The observed variation in noise as a function of increasing CBB temperature (6.7 – 9.0 K) is shown to agree with the photon noise predicted by the theoretical model. Thus photon noise from the ~9.0 K CBB was measured directly; this serves to illustrate the superb performance of the SPIRE bolometer detectors.

Since the current instrument theoretical model has been shown to reliably predict the noise performance of the SPIRE instrument in the laboratory, it will accurately pre-

dict the performance of SPIRE once the final temperature and emissivity of the Herschel telescope primary mirror are known. Under nominal flight conditions the SPIRE FTS is expected to have total noise corresponding to DC NEP values of  $9.88 \cdot 10^{-17} \text{ W}/\sqrt{\text{Hz}}$  for the SLW array, and  $10.98 \cdot 10^{-17} \text{ W}/\sqrt{\text{Hz}}$  for the SSW array.

It is expected that the CO lines in M82 will be observed with S/N values of 250 – 500 (SLW), and 50 – 150 (SSW), for a single up/down high-resolution interferogram scan pair. A single high-resolution scan pair corresponds to less than 3 minutes of observation time (there is an additional ~5 minutes of telescope overhead time [18]), compared to the several days required to scan multiple transitions individually, to similar S/N levels, with a heterodyne spectrometer from a ground-based observatory [161, 181, 185].

## Chapter 6

# Conclusions

The vastness of the heavens stretches my imagination - stuck on this carousel my little eye can catch one-million-year-old light. A vast pattern - of which I am a part ... What is the pattern, or the meaning, or the why? It does not do harm to the mystery to know a little more about it. For far more marvelous is the truth than any artists of the past imagined!

---

Richard Feynman [113, p. 3-6]

This thesis has presented experiments, and related analyses, which were conducted to verify the performance of an IFTS system from a space based platform, specifically the SPIRE IFTS within the Herschel space observatory. Although it was not possible to test SPIRE in a true space environment prior to launch, attempts were made to simulate near-flight conditions within the laboratory at RAL. Results from PFM tests of SPIRE, and related follow-up investigations, have been presented. This thesis, and the work performed during its completion, provides important information regarding the performance verification, calibration, and use of the SPIRE IFTS and should prove invaluable in the analysis of SPIRE IFTS astronomical observations, especially for those not familiar with FTS instrumentation. This chapter reviews the work presented in this thesis and presents the current status of Herschel/SPIRE.

## 6.1 FTS Beamsplitter Phase

As discussed in Chapter 3, the SPIRE FTS uses an internal calibration source to compensate for emission from the telescope primary mirror. Under conditions of port compensation, recorded interferograms have been shown to have components of both even and odd symmetry. Emission from the FTS beamsplitter is one of the potential asymmetric interferogram components. Beamsplitter phase deviations from the ideal ( $\phi = \pi/2$ ) have been shown to produce an odd interferogram component resulting from one of the FTS input ports. Although beamsplitter phase has been noted as a source of spectral errors [133], this work illustrates that it cannot be corrected using standard FTS phase correction methods. Simulations and laboratory experiments investigating beamsplitter emission have

been performed and corresponding results were presented.

As a result of this characterization of the asymmetries in SPIRE port compensation interferograms, calibration measurements to correct for this effect are not needed as frequently while SPIRE is operating, yielding a savings in telescope observation time. This work will be incorporated into correction algorithms for the SPIRE FTS data processing pipeline [65], once in-flight telescope conditions are known after launch.

## 6.2 IFTS Obliquity Corrections

A study of the obliquity effects related to detector axial position and divergence within the SPIRE IFTS was presented in Chapter 4. The ILS in IFTS instruments was given for infinite and finite spectral resolutions. Although similar approaches relating detector geometry to ILS are found in the literature [151], this work is unique in that it presents an analytical expression for the ILS as a function of detector position on the sky. The PFM qualification test measurements of the SPIRE IFTS, performed over several months at RAL, have verified the expected instrument performance. A detailed analysis of the implication of obliquity effects for the SPIRE IFTS has been presented from both a theoretical and observational standpoint, using observational data of the starburst galaxy M82 as a case study.

This work will prove useful in the analysis and interpretation of the hyper-spectral data provided by the SPIRE IFTS in-flight. While obliquity corrections may not be of importance for observations of our own galaxy, correction of these effects is crucial for extragalactic observations. Indeed, for observations of M82, as shown in Table 4.6, the

internal galactic dynamics could be *reversed* if obliquity effects are not considered.

### 6.3 SPIRE Bolometer Detector Performance

Bolometer theory relevant to the detectors employed within the SPIRE FTS instrument was introduced in Chapter 5. Although it was not possible to perform a full end to end test with the complete telescope under flight conditions, a theoretical bolometer model was adapted to include the SPIRE instrument configuration within the laboratory test facility at RAL. For observations viewing the CBB, there is excellent agreement between the observed bolometer performance and that predicted by the theoretical model. The observed variation in noise as a function of increasing CBB temperature (6.7 – 9.0 K) is shown to agree with the photon noise predicted by the theoretical model. Thus photon noise from the ~9.0 K CBB was measured directly; this serves to illustrate the superb performance of the SPIRE bolometer detectors and instills confidence in the predictions made by the theoretical model.

The SPIRE instrument theoretical bolometer model will thus accurately predict the performance of SPIRE once the final temperature and emissivity of the Herschel telescope primary mirror are known shortly after launch. The accuracy of the bolometer model will also be important in determining the overall instrument calibration, and is necessary for correction of detector nonlinearity in recorded interferograms [33].

It is expected that the CO lines in M82 will be observed with S/N values of 250 – 500 (SLW), and 50 – 150 (SSW), for a single up/down high-resolution interferogram scan pair. This corresponds to less than 3 minutes of observation time, compared to the



several days required to scan multiple transitions individually, to similar S/N levels, with a ground-based heterodyne spectrometer [161, 181, 185].

## 6.4 Current Status of Herschel

Although there have been several changes to Herschel's official launch date, starting with a projected launch date of early 2007, Herschel was finally launched at 13:12 UTC on 14 May 2009 from the Guiana Space Centre in French Guiana. The launch was successful and Herschel is making good progress as it is in transit to its mission orbit. As of 1 June 2009, both Herschel and Planck separated as planned, the SMEC survived launch and performed smoothly during its first use in zero-gravity, various electronics and engineering tests have been performed, the ~300 mK SPIRE detector cooler has been recycled three times, and the first SPIRE interferograms (of the instrument cryo-cover) were recorded on 29 May 2009. It will take approximately two months from launch for Herschel to reach its operational orbit at L2 and enough liquid Helium cryogen should remain for 3 – 5 years of telescope observation. Herschel is poised to perform ground-breaking science in the sparsely explored FIR/submm region of the electromagnetic spectrum in areas including star and galaxy formation and evolution, and the molecular chemistry of the Universe.

The instrument PV phase will start on operational day 64 (OD64, the 64th day after launch) after Herschel has reached its L2 orbit. The first spectrometer AOT interferograms of the dark sky will be recorded on OD68. PV sources for the SPIRE spectrometer include dark sky, Uranus, Ceres, NGC 6543 (the Cat's Eye Nebula), NGC 7027 (a white dwarf centred planetary nebula [186]), Gamma Dra, and Sagittarius A [187]. Following

the PV phase will be the science demonstration phase in which, in addition to many other sources, M82 will be observed with the SPIRE FTS.

As 2009 is the international year of astronomy, celebrating both the 400th anniversary of Galileo pointing his telescope towards the sky, and the 150th anniversary of the discovery of the relationship between laboratory emission lines and solar absorption lines by Bunsen and Kirchoff, the launch of Herschel early in the year is a very appropriate event.

## 6.5 Future Work

Calibration of the SPIRE FTS and subsequent analysis of the science demonstration phase data will be top priority as data become available. As Herschel is in many ways its own pathfinder, initial observations must be analyzed quickly to allow for the execution of follow-up observations during Herschel's finite lifetime. As mentioned in Chapter 1, I have been awarded associate scientist status on the SAG-4 interstellar medium GTKP observation program. In addition to participating in instrument calibration and performance verification work, and comparing instrument performance during flight to that of ground based calibration measurements from an instrumentation perspective, I will become involved in the analysis of SPIRE science data with an astronomy perspective. A knowledge of both astronomy and instrumentation is important to the development of future telescopes and related instrumentation, paving the way for future missions such as SPICA [90], FIRI [91], SPIRIT [112], and many others [87–94].

## Bibliography

- [1] C. A. Lubbock. *The Herschel chronicle; the life-story of William Herschel and his sister, Caroline Herschel*. New York, The Macmillan company; Cambridge, Eng., The University press, 1933.
- [2] J. W. Cooley and J. W. Tukey. An algorithm for the machine calculation of complex fourier series. *Math. Comput.*, 19:297, 1965.
- [3] Stopford Augustus Brooke. *The poetry of Robert Browning*. T.Y. Crowell & Co., 1902.  
from the poem “Andrea del Sarto”.
- [3.14159 26535 89793 23846 26433 83279 50288 41971 69399 37510 58209 74944 59230]  $\pi$
- [4] G. L. Pilbratt. Herschel Mission Overview and Key Programmes. *Proc. SPIE: Space Telescopes and Instrumentation I - Optical, Infrared, and Millimeter Wave*, 7010:701002–1–12, 2008.
- [5] V. Minier, L. Olmi, P.-O. Lagage, L. Spinoglio, G. A. Durand, E. Daddi, D. Galilei, H. Gallée, C. Kramer, D. Marrone, E. Pantin, L. Sabbatini, N. Schneider, N. F. H. Tothill, L. Valenziano, and C. Veyssi ere. Submm/FIR Astronomy in Antarctica: Potential for a large telescope facility. In H. Zinnecker, N. Epchtein, and H. Rauer,

- editors, *EAS Publications Series*, volume 33 of *EAS Publications Series*, pages 21–40, 2008.
- [6] M. J. Griffin. Spire sensitivity models. Technical Report SPIRE-QMW-NOT-000642, Cardiff University, Cardiff, Wales, May 2007.
- [7] <http://herschel.jpl.nasa.gov/lagrange.shtml>.
- [8] Matt Griffin, Bruce Swinyard, Laurent Vigroux, Alain Abergel, Peter Ade, Philippe André, Jean-Paul Baluteau, James Bock, Alberto Franceschini, Walter Gear, Jason Glenn, Maohai Huang, Douglas Griffin, Ken King, Emmanuel Lellouch, David Naylor, Seb Oliver, Göran Olofsson, Ismael Perez-Fournon, Mat Page, Michael Rowan-Robinson, Paolo Saraceno, Eric Sawyer, Gillian Wright, Annie Zavagno, Asier Abreu, George Bendo, Alan Dowell, Darren Dowell, Marc Ferlet, Trevor Fulton, Peter Hargrave, Glenn Laurent, Sarah Leeks, Tanya Lim, Nanyao Lu, Hien Nguyen, Alan Pearce, Edward Polehampton, Davide Rizzo, Bernhard Schulz, Sunil Sidher, Dave Smith, Locke Spencer, Ivan Valtchanov, Adam Woodcraft, Kevin Xu, and Lijun Zhang. Herschel-SPIRE: design, ground test results, and predicted performance. *Proc. SPIE: Space Telescopes and Instrumentation I - Optical, Infrared, and Millimeter Wave*, 7010:701006–1–12, 2008.
- [9] Matthew J. Griffin, James J. Bock, and Walter K. Gear. Relative performance of filled and feedhorn-coupled focal-plane architectures. *Applied Optics*, 41(31):6543–6554, 2002.
- [10] P. D. Mauskopf, J. J. Bock, H. Del Castillo, W. L. Holzapfel, and A. E. Lange. Com-

- posite infrared bolometers with Si<sub>3</sub>N<sub>4</sub> micromesh absorbers. *Appl. Opt.*, 36(4):765–771, 1997.
- [11] G. Chattopadhyay, J. Glenn, J. J. Bock, B. K. Rownd, M. Caldwell, and M. J. Griffin. Feed horn coupled bolometer arrays for SPIRE – design, simulations, and measurements. *IEEE Transactions on Microwave Theory and Techniques*, 51(10):2139 – 2146, October 2003.
- [12] Anthony D. Turner, James J. Bock, Jeffrey W. Beeman, Jason Glenn, Peter C. Hargrave, Voktor V. Hristov, Hien T. Nguyen, Faiz Rahman, Srinivasan Sethuraman, and Adam L. Woodcraft. Silicon nitride micromesh bolometer array for submillimeter astrophysics. *Applied Optics*, 40:4921–31, 2001.
- [13] Douglas Griffin, Matt Griffin, and Bruce Swinyard. SPIRE Design Description. Technical Report SPIRE-RAL-PRJ-000620, Rutherford Appleton Laboratory, May 2003.
- [14] Bruce M. Swinyard, P. A. R. Ade, M. J. Griffin, K. Dohlen, J. Baluteau, D. Pouliquen, D. Ferand, P. Dargent, G. Michel, J. Martignac, L. Rodriguez, D. Jennings, M. Caldwell, A. Richards, P. Hamilton, and David A. Naylor. The FIRST-SPIRE Spectrometer: A Novel Imaging FTS for the Sub-Millimetre. *Proc. SPIE: UV, Optical, and IR Space Telescopes and Instruments*, 4013:196–207, 2000.
- [15] P. A. R. Ade, P. A. Hamilton, and David A. Naylor. An absolute dual beam emission spectrometer. In *FTS Topical Meeting*, Santa Barbara, California, June 1999. Optical Society of America.
- [16] Locke D. Spencer, Baoshe Zhang, David A. Naylor, Peter Davis-Imhof, Trevor R.

- Fulton, Jean-Paul Baluteau, Marc J. Ferlet, Tanya L. Lim, Edward T. Polehampton, and Bruce M. Swinyard. Performance Evaluation of the Herschel/SPIRE Instrument Flight Model Imaging Fourier Transform Spectrometer. In *Space Telescopes and Instrumentation I: Optical, Infrared, and Millimeter Wave 2008*, volume 7010. Proceedings of the International Society for Optical Engineering, 2008.
- [17] Bruce Swinyard, Kjetil Dohlen, Didier Ferand, Jean Paul Baluteau, Dominique Pouliquen, Pascal Dargent, Guy Michel, Jerome Martignac, Peter Ade, Peter Hargrave, Matthew Griffin, Donald Jennings, and Martin Caldwell. The Imaging FTS for Herschel SPIRE. In *IR Space Telescopes and Instruments, Proc. SPIE*, volume 4850, pages 698–709, Mar 2003.
- [18] The European Space Agency. SPIRE Observers’ Manual. Technical Report 1.2, The European Space Agency, 2007. HERSCHEL-HSC-DOC-0789.
- [19] The European Space Agency. Herschel Observers’ Manual. Technical Report 2.1, The European Space Agency, 2007. HERSCHEL-HSC-DOC-0876.
- [20] Locke Dean Spencer. Spectral Characterization of the Herschel SPIRE Photometer. Master’s thesis, University of Lethbridge, Lethbridge, AB, 2005.
- [21] Kris Dyke, Peter Davis, David Naylor, Trevor Fulton, Ian Chapman, Locke Spencer, and John Lindner. University of Lethbridge Data Processing Toolkit Architecture Design Document. Technical report, Astronomical Instrumentation Group, University of Lethbridge, 2003.
- [22] Bruce M. Swinyard and Locke D. Spencer. Instrument Throughput. Technical Re-

- port SPIRE-RAL-REP-002564, Rutherford Appleton Laboratory, January 2006. SVR Technical Report.
- [23] Bruce M. Swinyard and Locke D. Spencer. Instrument Throughput. Technical Report SPIRE-RAL-REP-002564iss2, Rutherford Appleton Laboratory, September 2006. SVR Technical Report.
- [24] Bruce M. Swinyard and Locke D. Spencer. SPIRE ILT Report: Instrument Throughput. Technical Report SPIRE-RAL-REP-002977, Rutherford Appleton Laboratory, October 2007. SPIRE Science Verification Review 3, Stockholm 29-30 October 2007.
- [25] Locke D. Spencer, David A. Naylor, Bruce M. Swinyard, Asier A. Aramburu, Trevor R. Fulton, Tanya L. Lim, Samuel D. Ronayette, and Ian S. Schofield. A Fourier Transform Spectrometer for Ground Testing of the Herschel/SPIRE Instrument. In *Proc. SPIE: Astronomical Telescopes and Instrumentation*, volume 5487, pages 501 – 512, Jun 2004.
- [26] Locke D. Spencer, David A. Naylor, and Bruce M. Swinyard. A comparison of the theoretical and measured performance of the Herschel/SPIRE imaging Fourier transform spectrometer. In *Space Telescopes and Instrumentation I: Optical, Infrared, and Millimeter*, volume 6265, page 62652Z. Proceedings of the International Society for Optical Engineering, 2006.
- [27] Tanya Lim, Bruce Swinyard, A. A. Aramburu, J. Bock, M. Ferlet, Doug Griffin, Matt J. Griffin, Peter Hargrave, Ken King, Sarah Leeks, David Naylor, Samuel Ronayette, Eric Sawyer, Bernhard Schulz, Sunil Sider, Locke Spencer, Dave Smith, and

- Adam Woodcraft. First Results from Herschel - SPIRE performance tests. In *Optical, Infrared, and Millimeter Space Telescopes, Proc. SPIE*, volume 5487, pages 460 – 468, Jun 2004.
- [28] D.A. Naylor, T.R. Fulton, P.W. Davis, I.M. Chapman, B.G. Gom, Locke D. Spencer, J.V. Lindner, N.E. Nelson-Fitzpatrick, M.K. Tahic, and G.R. Davis. Data processing pipeline for a time-sampled imaging fourier transform spectrometer. In *Proc. SPIE Imaging Spectrometry X*, pages 61–72, August 2004.
- [29] T. Lim, B. Swinyard, M. Griffin, A. Aramburu, J.-P. Baluteau, J. Bock, M. Ferlet, T. Fulton, D. Griffin, S. Guest, P. Hargrave, K. King, S. Leeks, D. Naylor, E. Polehampton, D. Rizzo, E. Sawyer, B. Schulz, S. Sidher, L. Spencer, D. Smith, H. T. Nguyen, I. Valtchanov, T. Waskett, and A. Woodcraft. Preliminary results from Herschel-SPIRE flight model testing. In *Space Telescopes and Instrumentation I: Optical, Infrared, and Millimeter*, volume 6265, page 62650F. Proceedings of the International Society for Optical Engineering, 2006.
- [30] Locke D. Spencer and David A. Naylor. Optimization of FTS Phase Correction Parameters. In *Fourier Transform Spectroscopy/ Hyperspectral Imaging and Sounding of the Environment*, page FTuD12. Optical Society of America, 2005.
- [31] Locke D. Spencer and David A. Naylor. A novel technique for the metrology calibration of a fourier transform spectrometer. In *Fourier Transform Spectroscopy/ Hyperspectral Imaging and Sounding of the Environment*, page FTuB4. Optical Society of America, 2007.



- [32] Locke D. Spencer, David A. Naylor, Peter A. R. Ade, and Jin Zhang. Beamsplitter Emission in the Herschel/SPIRE Fourier Transform Spectrometer. In *Spring Optics and Photonics Congress Fourier Transform Spectroscopy Topical Meeting*, page FTuC4. Optical Society of America, 2009.
- [33] David A. Naylor, Brad G. Gom, Scott C. Jones, and Locke D. Spencer. Non-Linear Behaviour of Bolometric Detectors in Fourier Spectroscopy. In *Spring Optics and Photonics Congress Fourier Transform Spectroscopy Topical Meeting*, page JTuB15. Optical Society of America, 2009.
- [34] L.D. Spencer, D.A. Naylor, T.R. Fulton, J.P. Baluteau, P.A.R. Ade, and B.M. Swinyard. Port Compensation Using the Herschel/SPIRE Imaging Fourier Transform Spectrometer. *32nd International Conference on Infrared and Millimetre Waves*, 2:718–719, 2007.
- [35] D.A. Naylor, L.D. Spencer, and P.A.R. Ade. The Effects of Beamsplitter Emission in a Balanced Fourier Transform Spectrometer. In *Proc. IRMMW-THz 33*, page 1633, Pasadena, CA, September 2008. IEEE.
- [36] Locke D. Spencer and David A. Naylor. Herschel/SPIRE Imaging Fourier Transform Spectrometer. In *Future Directions & Science with the Next Generation of International Telescopes*, page P95. Canadian Astronomy Society (CASCA), June 2006. CASCA Annual Meeting.
- [37] Locke D. Spencer and David A. Naylor. Herschel Interstellar Dust Evolution Guar-

- anteed Time Proposal. In *CASCA 2007 : Big Science in Small Packages*. Canadian Astronomy Society (CASCA), June 2007. CASCA Annual Meeting.
- [38] Locke D. Spencer, David A. Naylor, B. Zhang, P.W. Davis-Imhof, T.R. Fulton, J.P. Baluteau, M.J. Ferlet, T.L. Lim, E.T. Polehampton, and B.M. Swinyard. The Herschel/SPIRE Instrument Flight Model Imaging Fourier Transform Spectrometer Performance Evaluation. In *The Scientific Impact of Canadian Astronomical Facilities and Instrumentation CASCA 2008*, page O12B2. Canadian Astronomy Society (CASCA), May 2008. CASCA Annual Meeting.
- [39] Locke D. Spencer and David A. Naylor. Far-infrared Imaging Fourier Transform Spectroscopy. *Bridging Excellence – The 30<sup>th</sup> Canadian Symposium on Remote Sensing, June 22-25, Lethbridge, Alberta, Canada*, page 546, June 2009.
- [40] Scott C. Jones, David A. Naylor, Brad G. Gom, and Locke D. Spencer. Spectral Line Fitting of an Astronomical Source. *Bridging Excellence – The 30<sup>th</sup> Canadian Symposium on Remote Sensing, June 22-25, Lethbridge, Alberta, Canada*, page 556, June 2009.
- [41] Alain Abergel, Jean-Paul Baluteau, Peter Ade, Philippe Andre, Chas Beichman, Jean-Philippe Bernard, Sylvain Bontemps, Francois Boulanger, Martin Cohen, Pierre Cox, Emmanuel Dartois, Gary Davis, Roger Emery, Cecile Gry, Emilie Habart, Mark Halpern, Christine Joblin, Jason Kirk, Guilaine Lagache, Tanya Lim, Suzanne Maden, Peter Martin, Marc-Antoine Miville-Deschenes, Sergio Molinari, Harvey Moseley, Frederique Motte, David Naylor, Koryo Okumura, Francois Orioux, Edward Pole-

- hampton, Thomas Rodet, Delphine Russeil, Paolo Saraceno, Marc Sauvage, Sunil Sidher, Locke Spencer, Bruce Swinyard, Derek Ward-Thompson, Glenn J. White, and Annie Zavagno. Evolution of Interstellar Dust: Proposal for a Guaranteed Time Key Project of SPIRE, April 2007.
- [42] Locke D. Spencer and David A. Naylor. Technique for the metrology calibration of a Fourier transform spectrometer. *Applied Optics*, 47(32):6009–6013, 2008.
- [43] David A. Naylor and Margaret K. Tahic. Apodizing functions for fourier transform spectroscopy. *J. Opt. Soc. Am. A*, 24(11):3644–3648, 2007.
- [44] Robin R. Phillips, Vic Haynes, David A. Naylor, and Peter Ade. Simple method for antireflection coating ZnSe in the 20  $\mu\text{m}$  wavelength range. *Applied Optics*, 47(7):870–873, 2008.
- [45] Göran L. Pilbratt. ESA FIRST cornerstone mission. volume 4013, pages 142–151. SPIE, 2000.
- [46] The Infrared Astronomical Satellite. <http://irsa.ipac.caltech.edu/IRASdocs/iras.html>.
- [47] R. J. Laureijs, F. O. Clark, and T. Prusti. *IRAS* Detection of Very Cold Dust in the Lynds 134 Cloud Complex. *The Astrophysical Journal*, 372:185–193, May 1991.
- [48] E. Dwek, R. G. Arendt, M. G. Hauser, D. Fixsen, T. Kelsall, D. Leisawitz, Y. C. Pei, E. L. Wright, J. C. Mather, S. H. Moseley, N. Odegard, R. Shafer, R. F. Silverberg, and J. L. Weiland. The Cobe Diffuse Infrared Background Experiment Search For The Cosmic Infrared Background. Iv. Cosmological Implications. *The Astrophysical Journal*, 508:106–122, November 1998.

- [49] The Infrared Space Observatory. <http://www.iso.vilspa.esa.es/>.
- [50] M. F. Kessler, J. A. Steinz, M. E. Anderegg, J. Clavel, G. Drechsel, P. Estaria, J. Faelker, J. R. Riedinger, A. Robson, B. G. Taylor, and S. Ximénez de Ferrán. The infrared space observatory (iso) mission. *Astronomy and Astrophysics*, 315:L27 – L31, 1996.
- [51] E. Habart, L. Verstraete, F. Boulanger, G. Pineau des Forêts, F. Le Peintre, and J. P. Bernard. Photoelectric effect on dust grains across the L1721 cloud in the  $\rho$  Ophiuchi molecular complex. *Astronomy & Astrophysics*, 373:702–713, 2001.
- [52] David B. Gallagher, William R. Irace, and Michael W. Werner. The development and mission of the space infrared telescope facility (sirtf). In *Optical, Infrared, and Millimeter Space Telescopes, Proc. SPIE*, volume 5487, pages 13 – 25, Jun 2004.
- [53] A. P. Jones, A. G. G. M. Tielens, and D. J. Hollenbach. Grain shattering in shocks: The interstellar grain size distribution. *The Astrophysical Journal*, 469:740–764, October 1996.
- [54] E. Falgarone and J.-L. Puget. The intermittency of turbulence in interstellar clouds: implications for the gas kinetic temperature and decoupling of heavy particles from the gas motions. *Astronomy & Astrophysics*, 293:840–852, 1995.
- [55] F. Boulanger, M. L. Prévot, and C. Gry. The contribution of small particles to the extinction curve. *Astronomy & Astrophysics*, 284:956–970, 1994.
- [56] A. Abergel, J. P. Bernard, F. Boulanger, D. Cesarsky, E. Falgarone, A. Jones, M.-A. Miville-Deschenes<sup>1</sup>, M. Perault, J.-L. Puget, M. Hultgren, A. A. Kaas, L. Nordh,

- G. Olofsson, P. André, S. Bontemps, M. M. Casali, C. J. Cesarsky, M. E. Copet, J. Davies, T. Montmerle, P. Persi, , and F. Sibille. Evolution of very small particles in the southern part of Orion B observed by ISOCAM. *Astronomy & Astrophysics*, 389:239–251, 2002.
- [57] E. Habart, A. Abergel, C. M. Walmsley, D. Teyssier, and J. Pety. Density structure of the Horsehead nebula photo-dissociation region. *Astronomy & Astrophysics*, 437:177–188, 2005.
- [58] N. A. Ridge, J. Di Francesco, H. Kirk, D. Li, A. A. Goodman, J. F. Alves, H. G. Arce, M. A. Borkin, P. Caselli, J. B. Foster, M. H. Heyer, D. Johnstone, D. A. Kosslyn, M. Lombardi, J. E. Pineda, S. L. Schnee, and M. Tafalla. The COMPLETE Survey of Star-Forming Regions: Phase I Data. *The Astronomical Journal*, 131:2921–2933, June 2006.
- [59] M. A. Reid and C. D. Wilson. High-Mass Star Formation. I. The Mass Distribution of Submillimeter Clumps in NGC 7538. *The Astrophysical Journal*, 625:891–905, June 2005.
- [60] M. A. Reid and C. D. Wilson. High-Mass Star Formation. II. The Mass Function of Submillimeter Clumps in M17. *The Astrophysical Journal*, 644:990–1005, June 2006.
- [61] M. A. Reid and C. D. Wilson. High-Mass Star Formation. III. The Functional Form of the Submillimeter Clump Mass Function. *The Astrophysical Journal*, 650:970–984, October 2006.
- [62] Matthew Griffin, Bruce Swinyard, and Laurent Vigroux. SPIRE - Herschel’s Submil-

- limetre Camera and Spectrometer. In *IR Space Telescopes and Instruments, Proc. SPIE*, volume 4850, pages 686–697, Mar 2003.
- [63] M. L. Enoch, J. Glenn, N. J. Evans, II, A. I. Sargent, K. E. Young, and T. L. Huard. Comparing Star Formation on Large Scales in the c2d Legacy Clouds: Bolocam 1.1 mm Dust Continuum Surveys of Serpens, Perseus, and Ophiuchus. *The Astrophysical Journal*, 666:982–1001, September 2007.
- [64] P. F. Goldsmith. The Astrophysics of Spectroscopic Studies with the Herschel Space Observatory. In L. Pagani and M. Gerin, editors, *EAS Publications Series*, volume 34 of *EAS Publications Series*, pages 89–105, 2009.
- [65] Trevor R. Fulton, David A. Naylor, Jean-Paul Baluteau, Matthew Griffin, Peter Davis-Imhof, Bruce Swinyard, Tanya L. Lim, Christian Surace, David Clements, Pasquale Panuzzo, Rene Gastaud, Edward T. Polehampton, Steve Guest, Nanyao Lu, Arnold Schwartz, and Kevin Xu. The data-processing pipeline for the Herschel/SPIRE Fourier Transform Spectrometer. In *Space Telescopes and Instrumentation I: Optical, Infrared, and Millimeter Wave 2008*, volume 7010. Proceedings of the International Society for Optical Engineering, 2008.
- [66] Richard Rhodes. *The Making of the Atomic Bomb*. Simon and Schuster, New York, 1988.
- [67] H. Rubens and R. W. Wood. Focal isolation of long heat-waves. *Philosophical Magazine*, 21:249–261, 1911.
- [68] J. Connes, P. Connes, and J. P. Maillard. *Atlas des spectres dans le proche infrarouge*

- de Venus, Mars, Jupiter et Saturn.* Paris: Centre National de la Recherche Scientifique, 1969.
- [69] Ivor Grattan-Guinness. *Joseph Fourier, 1768-1830.* Cambridge: MIT Press, 1972.  
A survey of his life and work, based on a critical edition of his monograph on the propagation of heat, presented to the Institut de France in 1807.
- [70] John Herivel. *Joseph Fourier. The man and the Physicist.* Oxford University Press, 1975.
- [71] Jean Baptiste Joseph Fourier. *Théorie Analytique De La Chaleur.* F. Didot, 1822.  
Title translation: The Analytical Theory of Heat.
- [72] Michael T. Heideman, Don H. Johnson, and C. Sidney Burrus. Gauss and the history of the fast fourier transform. *Archive for History of Exact Sciences*, 34(3):265 – 277, September 1985.
- [73] Albert A. Michelson. *Light Waves and Their Uses.* University of Chicago Press, Chicago, Illinois, 1902.
- [74] A.A. Michelson and E.W. Morley. On the Relative Motion of the Earth and the Luminiferous Ether. *American Journal of Science*, 34(203):333 – 345, November 1887.
- [75] R. J. Bell. *Introductory Fourier Transform Spectroscopy.* Academic Press, New York, 1972.

- 
- [76] Sumner P. Davis, Mark C. Abrams, and James W. Brault. *Fourier Transform Spectroscopy*. Academic Press, first edition, 2001.
- [77] P. R. Griffiths and J. A. Haseth. *Fourier Transform Infrared Spectrometry*. John Wiley and Sons, New York, 1986.
- [78] Albert A. Michelson. Determination of Periodicities by the Harmonic Analyzer with an Application to the Sun-Spot Cycle. *Astrophysical Journal*, 38:268–275, October 1913.
- [79] A. A. Michelson. Radiation in a Magnetic Field. *Astrophysics Journal*, 7:131–139, February 1898.
- [80] P. Fellgett. A propos de la theorie du spectrometre interferentiel multiplex. *Journal of Physics Radium*, 19:187, 1958.
- [81] P. Jacquinot. New developments in interference spectroscopy. *Rep. Prog. Phys.*, 23:267–312, 1960.
- [82] Michael L. Forman. Fast Fourier-Transform Technique and its Application to Fourier Spectroscopy. *Journal of the Optical Society of America*, 56(7):978, July 1966.
- [83] G. C. Danielson and C. Lanczos. Some improvements in practical Fourier analysis and their application to X-ray scattering from liquids. *Journal of the Franklin Institute*, 233(4):365 – 380, 1942.
- [84] G. C. Danielson and C. Lanczos. Some improvements in practical fourier analysis



- and their application to X-ray scattering from liquids (Continued from April issue).  
*Journal of the Franklin Institute*, 233(5):435 – 452, 1942.
- [85] C. Runge and H. König. *Vorlesungen ueber numerisches Rechnen*. 1924.
- [86] J. W. Cooley, P. A. Lewis, and P. D. Welch. Historical Notes on the Fast Fourier Transform. *IEEE Trans. Audio Electroacoust.*, (2):76–79, August 1967.
- [87] M. Griffin, P. Ade, P. André, J.-P. Baluteau, J. Bock, A. Franceschini, W. Gear, J. Glenn, M. Huang, K. King, E. Lellouch, D. Naylor, S. Oliver, G. Olofsson, M. Page, I. Perez-Fournon, M. Rowan-Robinson, P. Saraceno, E. Sawyer, B. Swinyard, L. Vigroux, G. Wright, and A. Zavagno. The SPIRE Instrument. In *EAS Publications Series*, volume 34 of *EAS Publications Series*, pages 33–42, 2009.
- [88] J. R. Graham, M. Abrams, C. Bennett, J. Carr, K. Cook, A. Dey, J. Najita, and E. Wishnow. The Performance and Scientific Rationale for an Infrared Imaging Fourier Transform Spectrograph on a Large Space Telescope. *Publications of the Astronomical Society of the Pacific*, 110:1205–1215, October 1998.
- [89] M. Kawada, H. Takahashi, N. Murakami, H. Matsuo, Y. Okada, A. Yasuda, S. Matsuura, M. Shirahata, Y. Doi, H. Kaneda, T. Ootsubo, T. Nakagawa, and H. Shibai. Performance of an Imaging Fourier Transform Spectrometer with Photoconductive Detector Arrays: An Application for the AKARI Far-Infrared Instrument. *Publications of the Astronomical Society of Japan*, 60:389–397, December 2008.
- [90] B. M. Swinyard et. al. The space infrared telescope for cosmology and astrophysics:

- SPICA A joint mission between JAXA and ESA. *Experimental Astronomy*, pages 7–25, May 2008.
- [91] F. P. Helmich and R. J. Ivison. FIRI – A far-infrared interferometer. *Experimental Astronomy*, pages 245 – 276, July 2008.
- [92] Donald E. Jennings, J. C. Brasunas, R. C. Carlson, F. M. Flasar, V. G. Kunde, A. A. Mamoutkine, C. A. Nixon, J. C. Pearl, P. N. Romani, A. A. Simon-Miller, G. L. Bjoraker, and CIRS Team. Thermal Infrared Spectroscopy of Saturn and Titan from Cassini. In *Spring Optics and Photonics Congress Fourier Transform Spectroscopy Topical Meeting*, page FMA3. Optical Society of America, 2009.
- [93] J. C. Brasunas, F. M. Flasar, and Donald E. Jennings. CIRS-*lite*: A Fourier Transform Spectrometer for a Future Mission to Titan. In *Spring Optics and Photonics Congress Fourier Transform Spectroscopy Topical Meeting*, page FTuA1. Optical Society of America, 2009.
- [94] Jean-Pierre Maillard. Wide-Field Imaging FTS at High Spectral Resolution. In *Spring Optics and Photonics Congress Fourier Transform Spectroscopy Topical Meeting*, page FThA4. Optical Society of America, 2009.
- [95] Leonhard Euler. *Introductio in analysin infinitorum*. M. M. Bousquet, Lausannae, 1748. Title translation: Introduction to the Analysis of Infinities.
- [96] Peter Gustav Lejeune Dirichlet, Richard Dedekind, and John Stillwell. *Lectures on Number Theory*. American Mathematical Society, 1999. translated from original

- title “Vorlesungen über Zahlentheorie” (1863) compiled and published shortly after Dirichlet’s death in 1859.
- [97] J. S. Walker. *Fourier Analysis*. Oxford University Press, 1988.
- [98] E. O. Brigham. *The Fast Fourier Transform*. Prentice-Hall Inc., 1974.
- [99] Ronald Bracewell. *The Fourier Transform and Its Applications*. McGraw-Hill Book Company, New York, 1965.
- [100] B. P. Lathi. *Signal Processing & Linear Systems*. Berkeley-Cambridge Press, Carmichael, 1998.
- [101] Graham Woan. *The Cambridge Handbook of Physics Formulas*. Cambridge University Press, New York, 2003.
- [102] Eugene Hecht. *Optics*. Addison Wesley, fourth edition, 2002.
- [103] D. B. Chase. Phase Correction in FT-IR. *Applied Spectroscopy*, 36(3):240–244, 1982.
- [104] J. Connes. Le filtrage mathématique dans la spectroscopie par transformation de fourier. *Rev. Opt.*, 40:45, 116, 171, 233, 1961. English translation as document AD 409869, Clearinghouse for Federal Scientific and Technical Information, Cameron Station, VA.
- [105] H. Nyquist. Certain topics in telegraph transmission theory. *Transactions of the American Institute of Electrical Engineers*, 47:617 – 644, 1928.
- [106] C. E. Shannon. A mathematical theory of communication. *The Bell System Technical Journal*, 27:379 – 423, 1948.

- 
- [107] E. L. Dereniak and D. G. Crowe. *Optical radiation detectors*. Wiley Series in Pure and Applied Optics, New York: Wiley, 1984.
- [108] M. Menat. The continuity of Bose-Einstein photon noise statistics and Fermi electron statistics. *Optics Communications*, 1(9):463 – 464, 1970.
- [109] D. A. Naylor, B. G. Gom, P. A. R. Ade, and J. E. Davis. Design and performance of a dual polarizing detector system for broadband astronomical spectroscopy at sub-millimetre wavelengths. *Review of Scientific Instruments*, 70(10):4097–4109, 1999.
- [110] Charles Kittel. *Introduction to Solid State Physics*. John Wiley & Sons, Inc., seventh edition, 1996.
- [111] B. Gom, D. Naylor, and B. Zhang. Integration and testing of FTS-2: an imaging Fourier transform spectrometer for SCUBA-2. *Proc. Society of Photo-Optical Instrumentation Engineers (SPIE)*, 7020:70201W, August 2008.
- [112] D. Leisawitz, T. T. Hyde, S. A. Rinehart, and M. Weiss. The Space Infrared Interferometric Telescope (SPIRIT): the mission design solution space and the art of the possible. *Proc. Society of Photo-Optical Instrumentation Engineers (SPIE)*, 7010:701028, August 2008.
- [113] Richard P. Feynman, Robert B. Leighton, and Matthew Sands. *The Feynman Lectures on Physics*, volume I. Addison-Wesley, 1963.
- [114] David A. Naylor, Brad A. Gom, Ian S. Schofield, Greg J. Tompkins, and Gary R. Davis. Mach-Zehnder Fourier Transform Spectrometer for astronomical spectroscopy

- at submillimeter wavelengths. *Proc. SPIE: Millimeter and Submillimeter Detectors for Astronomy*, 4855:540–51, 2002.
- [115] Kjetil Dohlen, Alain Origné, Dominique Pouliquen, and Bruce Swinyard. Optical Design of the SPIRE Instrument for FIRST. *SPIE Proceedings: UV, Optical and IR Space Telescopes*, 4013:119–28, 2000.
- [116] B. Carli, L. Palchetti, and P. Raspollini. Effect of beam-splitter emission in Fourier-transform emission spectroscopy. *Applied Optics*, 38:7475–7480, December 1999.
- [117] Peter Hargrave and Matt Griffin. Spectrometer Calibrator (SCAL) Subsystem Design Description. Technical Report SPIRE-QMW-PRJ-001104, Cardiff University, Cardiff, Wales, U.K., September 2001.
- [118] Maurice Hamy. Fringes by reflection from silvered glass. *J. Phys. Radium*, 5:789 – 809, 1906.
- [119] Bruno Carli. Reflectivity of metallic films in the infrared. *JOSA*, 67(7):908 – 910, July 1977.
- [120] Charles Dufour. Application aux couches minces de la theorie de l’etalon interferentiel par reflexion. *J. Phys. Radium*, 11:327 – 331, 1950.
- [121] Allan R. Cownie. Phase condition for light incident normally on a semireflecting film. *JOSA*, 47(2):132 – 136, February 1957.
- [122] Yu. V. Troitskii. The Energy Conservation Law for Optical Two-Port Devices. *Optics and Spectroscopy*, 92(4):555 – 559, 2002.

- [123] Yu. V. Troitskii. Limits of variation of the composite phase parameter of dielectric multilayer systems. *Optics and Spectroscopy*, 66(1):105 – 107, 1989.
- [124] M. Born and E. Wolf. *Principles of Optics: Electromagnetic Theory of Propagation, Interference and Diffraction of Light*. Cambridge University Press, seventh edition, 1999.
- [125] D. J. Fixsen, E. S. Cheng, J. M. Gales, J. C. Mather, R. A. Shafer, and E. L. Wright. The Cosmic Microwave Background Spectrum from the Full COBE FIRAS Data Set. *The Astrophysical Journal*, 473:576–588, December 1996.
- [126] 3D Full-wave Electromagnetic Field Simulation, Ansoft Corporation. High frequency structural simulator. [www.ansoft.com/products/hf/hfss/](http://www.ansoft.com/products/hf/hfss/).
- [127] P. A. R. Ade, G. Pisano, C. Tucker, and S. Weaver. A review of metal mesh filters. *Proc. SPIE: Millimeter and Submillimeter Detectors and Instrumentation for Astronomy III*, 6275:6275OT–1–9, July 2006.
- [128] J. C. Brasunas. Phase anomalies in Fourier-transform spectrometers: an absorbing beam splitter is neither sufficient nor necessary. *Applied Optics*, 41:2481–2487, May 2002.
- [129] Minco Corporation. Minco flexible electronic heaters. [www.minco.com](http://www.minco.com).
- [130] Epoxy Technology. Epo-tek-920 thermal epoxy resin. [www.epotek.com](http://www.epotek.com).
- [131] Dupont Corporation. Delrin acetal resin. [www2.dupont.com](http://www2.dupont.com).
- [132] Flir systems inc. [www.flir.com/thermography/](http://www.flir.com/thermography/).

- 
- [133] H. E. Revercomb, W. L. Smith, H. Buijs, H. B. Howell, and D. D. Laporte. Radiometric calibration of IR Fourier transform spectrometers - Solution to a problem with the High-Resolution Interferometer Sounder. *Applied Optics*, 27:3210–3218, August 1988.
- [134] J. Schreiber, T. Blumenstock, and H. Fischer. Effects of the self-emission of an IR Fourier-transform spectrometer on measured absorption spectra. *Applied Optics*, 35(31):6203–6209, 1996.
- [135] G. Bianchini, L. Palchetti, and B. Carli. Vectorial combination of signals in Fourier transform spectroscopy. *Infrared Physics & Technology*, 2008. doi:10.1016/j.infrared.2008.09.004.
- [136] O. Trieschmann and C. Weddigen. Thermal Emission from Dielectric Beam Splitters in Michelson Interferometers: a Schematic Analysis. *Applied Optics*, 39:5834–5842, November 2000.
- [137] Frank Hase, Olaf Trieschmann, and Christian Weddigen. Response of Fourier-transform spectrometers to absorption and emission in a homogeneous single-layered beam splitter. *Applied Optics*, 40(28):5078 – 5087, October 2001.
- [138] Jean-Marc Thériault. Modeling the responsivity and self-emission of a double-beam fourier-transform infrared interferometer. *Applied Optics*, 38(3):505–515, 1999.
- [139] Jean-Marc Thériault. Beam splitter layer emission in Fourier-transform infrared interferometers. *Applied Optics*, 37(36):8348 – 8351, December 1998.

- [140] Jules Henry Poincaré and George Bruce Halsted. *The Foundations of Science*. The Scientific Press, New York, first edition, 1913.
- [141] Henry Buijs. An Historical Perspective on the Development of Fourier Transform Spectrometry. In *Spring Optics and Photonics Congress Fourier Transform Spectroscopy Topical Meeting*, page FMA1. Optical Society of America, 2009.
- [142] A. Rogalski. Competitive Technologies of Third Generation Infrared Photon Detectors. *Opto-Electronics Review*, 14(1):84–98, 2006.
- [143] Chih-Cheng Hsieh, Chung-Yu Wu, Far-Wen Jih, and Tai-Ping Sun. Focal-plane-arrays and CMOS readout techniques of infrared imaging systems. *Circuits and Systems for Video Technology, IEEE Transactions on*, 7(4):594–605, Aug 1997.
- [144] Pantazis Mouroulis, Robert O. Green, and Thomas G. Chrien. Design of pushbroom imaging spectrometers for optimum recovery of spectroscopic and spatial information. *Applied Optics*, 39(13):2210–2220, 2000.
- [145] Mark H. Stockett, Michael P. Wood, Satyakumar Nagarajan, and James E. Lawler. Echelle spectrograph optimized for a diffuse interstellar band carrier search using synchrotron radiation. *Applied Optics*, 47(29):5390–5393, 2008.
- [146] J. M. Vaughan. *The Fabry-Perot Interferometer, History, Theory, Practice, and Applications*. The Adam Hilger Series on Optics and Optoelectronics. Adam Hilger, Bristol, 1989.
- [147] Charles L. Bennett, Michael R. Carter, David J. Fields, and John Hernandez. Imaging



- Fourier Transform Spectrometer. In *Proc. SPIE*, volume 1937. The international society for optical engineering, 1993.
- [148] K. I. Salonen, I. K. Salomaa, and J. K. Kauppinen. Diffraction in a fourier-transform spectrometer. *Applied Optics*, 34(7):1190–1196, 1995.
- [149] Jérôme Genest and Pierre Tremblay. Diffraction and line shape of fourier-transform spectrometers. *Applied Optics*, 42(22):4541–4548, 2003.
- [150] Pekka Saarinen and Jyrki Kauppinen. Spectral line-shape distortions in Michelson interferometers due to off-focus radiation source. *Applied Optics*, 31(13):2353–2359, 1992.
- [151] Jérôme Genest and Pierre Tremblay. Instrument Line Shape of Fourier Transform Spectrometers: Analytic Solutions for Nonuniformly Illuminated Off-Axis Detectors. *Applied Optics*, 38(25):5438–5446, 1999.
- [152] Marc J. Ferlet. SPIRE ILT Report: Instrument Optical Performances. Technical Report SPIRE-RAL-REP-002963 1.3, Rutherford Appleton Laboratory, Stockholm, October 2007. SPIRE Science Verification Review – 3.
- [153] Marc J. Ferlet, Glenn Laurent, Bruce Swinyard, Jason Glenn, James J. Bock, and Kjetil Dohlen. Characterization of Herschel/SPIRE Flight Model Optical Performances. In *Space Telescopes and Instrumentation I: Optical, Infrared, and Millimeter Wave 2008*, volume 7010. Proceedings of the International Society for Optical Engineering, 2008.

- [154] Kjetil Dohlen and Bruce M. Swinyard. SPIRE Optical System Design Description. Technical report, Laboratoire d'Astrophysique de Marseille, Rutherford Appleton Laboratory, December 2000. SPIRE-LAM-PRJ-000447.
- [155] P.G. Huggard, B.N. Ellison, P. Shen, N.J. Gomes, P.A. Davies, W.P. Shullue, A. Vaccari, and J.M. Payne. Efficient Generation of Guided Millimeter-Wave Power by Photomixing. *IEEE Photonics Technology Letters*, 14(2):197 – 199, February 2002.
- [156] P.G. Huggard, B.N. Ellison, P. Shen, N.J. Gomes, P.A. Davies, W.P. Shullue, A. Vaccari, and J.M. Payne. Generation of Millimetre and Sub-millimetre Waves by Photomixing in 1.55  $\mu\text{m}$  Wavelength Photodiode. *Electronics Letters*, 38(7):327 – 328, March 2002.
- [157] M. Inguscio, G. Moruzzi, K. M. Evenson, and D. A. Jennings. A review of frequency measurements of optically pumped lasers from 0.1 to 8 THz. *Journal of Applied Physics*, 60:161, December 1986.
- [158] G. Moruzzi, J. C. Silos Moraes, and F. Strumia. Far Infrared Laser Lines and Assignments of  $\text{CH}_3\text{OH}$ : A Review. *International Journal of Infrared and Millimeter Waves*, 13(9):1269 – 1312, 1992.
- [159] J. W. Brault. High Precision Fourier Transform Spectrometry: The Critical Role of Phase Corrections. *Mikrochimica Acta*, 3:215–227, 1987.
- [160] Raphaël Desbiens, Pierre Tremblay, Jérôme Genest, and Jean-Pierre Bouchard. Matrix form for the instrument line shape of fourier-transform spectrometers yielding a fast integration algorithm to theoretical spectra. *Applied Optics*, 45(3):546–557, 2006.

- [161] R. Q. Mao, C. Henkel, A. Schulz, M. Zielinsky, R. Mauersberger, H. Storzer, T. L. Wilson, and P. Gensheimer. Dense gas in nearby galaxies. *Astronomy and Astrophysics*, 358:433 – 450, 2000.
- [162] M. Crosas and K. M. Menten. Physical Parameters of the IRC +10216 Circumstellar Envelope: New Constraints from Submillimeter Observations. *The Astrophysical Journal*, 483:913–924, July 1997.
- [163] Bradley W. Carroll and Dale A. Ostlie. *An Introduction to Modern Astrophysics*. Addison Wesley Publishing, 1996.
- [164] W. L. Freedman, S. M. Hughes, B. F. Madore, J. R. Mould, M. G. Lee, P. Stetson, R. C. Kennicutt, A. Turner, L. Ferrarese, H. Ford, J. A. Graham, R. Hill, J. G. Hoessel, J. Huchra, and G. D. Illingworth. The Hubble Space Telescope Extragalactic Distance Scale Key Project. 1: The discovery of Cepheids and a new distance to M81. *The Astrophysical Journal*, 427:628–655, June 1994.
- [165] L. L. Leeuw and E. I. Robson. Submillimeter Continuum Properties of Cold Dust in the Inner Disk and Outflows of M 82. *The Astronomical Journal*, 137:517–527, January 2009.
- [166] Richard de Grijs. Star formation timescales in M82. *Astronomy & Geophysics*, 42(4):12 – 17, August 2001.
- [167] Natascha M. Förster Schreiber. The nature of starburst activity in M 82. *New Astronomy Reviews*, 44(4-6):263 – 267, 2000.

- [168] J. W. Colbert, M. A. Malkan, P. E. Clegg, P. Cox, J. Fischer, S. D. Lord, M. Luhman, S. Satyapal, H. A. Smith, L. Spinoglio, G. Stacey, and S. J. Unger. ISO LWS Spectroscopy of M82: A Unified Evolutionary Model. *The Astrophysical Journal*, 511:721–729, February 1999.
- [169] L. L. Leeuw, E. I. Robson, and D. H. Hughes. Submillimetre Continuum Imaging of Large-scale Outflows in Nearby Starburst Galaxies. In P. Whitelock and R. Cannon, editors, *The Stellar Content of Local Group Galaxies*, volume 192 of *IAU Symposium*, pages 330–333, January 1999.
- [170] Hannes Alfvén. Plasma universe. *Physica Scripta*, T18:20–28, 1987.
- [171] R. Clark Jones. The general theory of bolometer performance. *J. Opt. Soc. Am.*, 43(1):1–10, 1953.
- [172] Frank J. Low. Low-Temperature Germanium Bolometer. *Journal of the Optical Society of America*, 51(11):1300–1304, November 1961.
- [173] John C. Mather. Bolometer noise: nonequilibrium theory. *Applied Optics*, 21(6):1125–1129, 1982.
- [174] John C. Mather. Bolometers: ultimate sensitivity, optimization, and amplifier coupling. *Applied Optics*, 23(4):584–588, 1984.
- [175] M. J. Griffin and W. S. Holland. The Influence of Background Power on the Performance of an Ideal Bolometer. *International Journal of Infrared and Millimeter Waves*, 9(10):861 – 875, 1988.

- [176] R. V. Sudiwala, M. J. Griffin, and A. L. Woodcraft. Thermal Modelling and Characterisation of Semiconductor Bolometers. *International Journal of Infrared and Millimeter Waves*, 23(4):545 – 573, April 2002.
- [177] Patrick A. Collins, Peter A. R. Ade, M. Caldwell, M. Ferlet, M. J. Griffin, Pete C. Hargrave, M. R. Harman, Dave L. Smith, and Bruce M. Swinyard. A Ground Calibration Facility for Herschel - SPIRE. In *IR Space Telescopes and Instruments, Proc. SPIE*, volume 4850, Mar 2003.
- [178] W. D. Duncan, T. J. Norton, D. J. Robertson, J. M. D. Strachan, J. E. Harris, C. R. Cunningham, P. A. R. Ade, and W. S. Holland. Long Wavelength (Sub-mm) Telescope Simulator. *Infrared Physics*, 34(1):1–15, 1993.
- [179] D. Smith, M. Caldwell, M. Ferlet, M. R. Harman, and G. Toplis. Plans for the Spire Instrument AIV and Calibration. In B. Schürmann, editor, *Fourth International Symposium Environmental Testing for Space Programmes*, volume 467 of *ESA Special Publication*, pages 191–196, 2001.
- [180] Bolometer Detector Assembly Centre, NASA Jet Propulsion Laboratory. SPIRE Bolometer End Item Data Packages (EIDPs). Pasadena, California, <http://www.ipac.caltech.edu/Herschel/index.shtml>.
- [181] E. Serabyn and E. W. Weisstein. Fourier Transform Spectroscopy of the Orion Molecular Cloud Core. *The Astrophysical Journal*, 451:238–251, September 1995.
- [182] California Institute of Technology Jet Propulsion Laboratory. Molecular spectroscopy catalog, 2004. <http://spec.jpl.nasa.gov/>.

- 
- [183] E. Serabyn and E. W. Weisstein. Surface figure measurements of radio telescopes with a shearing interferometer. *Applied Optics*, 30(10):1227–1241, April 1991.
- [184] P. Schilke, J. E. Carlstrom, J. Keene, and T. G. Phillips. Atomic Carbon in M82. *The Astrophysical Journal*, 417:L67–L70, November 1993.
- [185] E. R. Seaquist and J. Clark. Observations of CO  $J = 32$  in the Outflow of the Starburst Galaxy M82. *The Astrophysical Journal*, 552:133–143, May 2001.
- [186] K. Justtanont, M. J. Barlow, A. G. G. M. Tielens, D. Hollenbach, W. B. Latter, X.-W. Liu, R. J. Sylvester, P. Cox, and N.-Q. Rieu. ISO-LWS observations of rotational CO lines from C-rich objects: AFGL 2688, AFGL 618 and NGC 7027. *Astronomy & Astrophysics*, 360:1117–1125, August 2000.
- [187] Tanya Lim. SPIRE Commissioning and PV Timeline. [www.herschel.be/twiki](http://www.herschel.be/twiki).
- [188] K. M. van Vliet. Noise limitations in solid state photodetectors. *Applied Optics*, 6(7):1145–1169, 1967.

## Appendix A

# Off-Axis Optical Path Difference Correction

Section 2.7.3 cites the off-axis correction factor for an FTS to be  $\cos(\alpha)$  for collimated light which is off-axis by an angle  $\alpha$  without a derivation. This section provides that derivation.

Figure A.1 illustrates off-axis light traversing an FTS (with the transmissive path reflected onto the reflective path for clarity) at an angle  $\alpha$  with respect to the optical axis. All marked angles represent  $\alpha$ . The optical path difference in this configuration will be the difference between the two total paths traveled. It is clear that on-axis light would experience an OPD of  $\pm(2z_2 - 2z_1)$  within the FTS. Off-axis light traveling through the  $z_2$  arm of the FTS travels a revised distance of

$$z'_2 = 2 \frac{z_2}{\cos(\alpha)} .$$

The same for the  $z_1$  arm is given as follows

$$z'_1 = 2 \frac{z_1}{\cos(\alpha)} + d_1 ,$$

where  $d_1$  is determined below. The length of  $d_o$ , i.e. the hypotenuse for the triangle in Figure A.1 involving  $d_1$ , is given as

$$d_o = 2z_2 \tan(\alpha) - 2z_1 \tan(\alpha) .$$

$d_1$  is then given by  $\sin(\alpha)d_o$  as follows

$$d_1 = 2 \tan(\alpha)(z_2 - z_1) \sin(\alpha) = \frac{2 \sin^2(\alpha)(z_2 - z_1)}{\cos(\alpha)} .$$

The overall OPD for off-axis light in an FTS is thus given by

$$\begin{aligned} z' &= z'_2 - z'_1 \\ z' &= \left[ \frac{2z_2}{\cos(\alpha)} \right] - \left[ \frac{2z_1}{\cos(\alpha)} + \frac{2 \sin^2(\alpha)(z_2 - z_1)}{\cos(\alpha)} \right] \\ z' &= \left[ \frac{2(z_2 - z_1)}{\cos(\alpha)} \right] - \left[ \frac{2 \sin^2(\alpha)(z_2 - z_1)}{\cos(\alpha)} \right] \\ z' &= \frac{2(z_2 - z_1) - 2 \sin^2(\alpha)(z_2 - z_1)}{\cos(\alpha)} , \tag{A.1} \\ z' &= \frac{2(z_2 - z_1)[1 - \sin^2(\alpha)]}{\cos(\alpha)} \\ z' &= \frac{2(z_2 - z_1)[\cos^2(\alpha)]}{\cos(\alpha)} \\ z' &= z \cos(\alpha) \end{aligned}$$



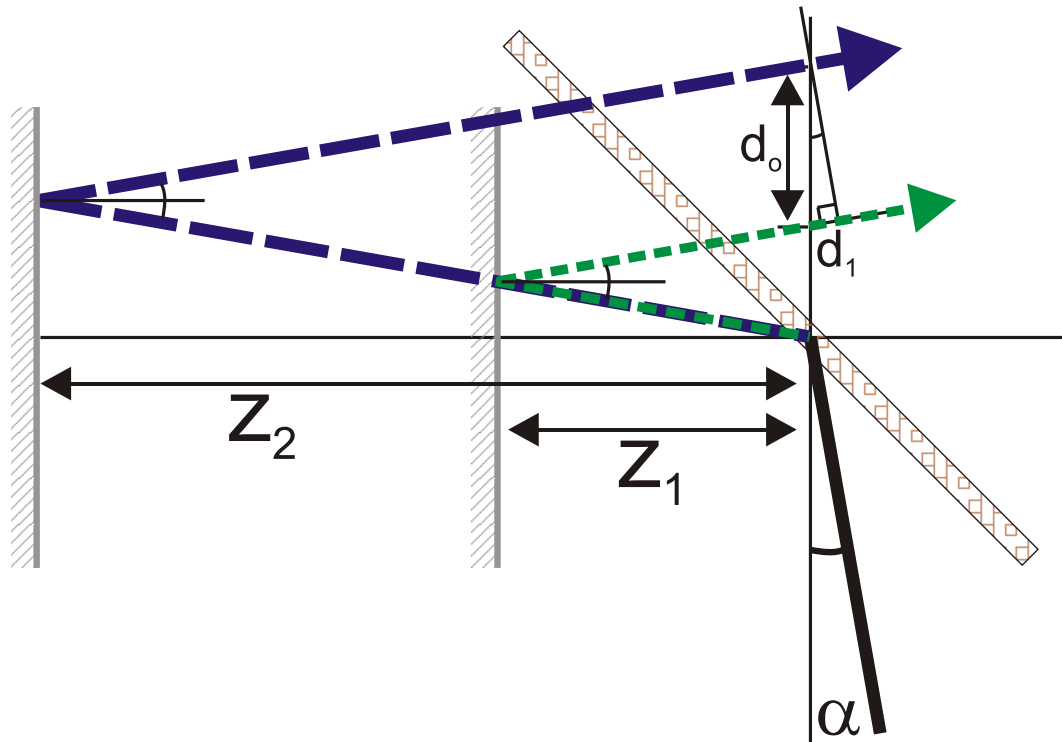


Figure A.1: Diagram of off-axis light to derive the FTS obliquity correction term.

where  $z = 2(z_2 - z_1)$ .

## Appendix B

# Derivation of Beamsplitter Phase $\Phi$

In the interests of brevity, several equations are given in Chapter 3 without a detailed derivation. This section provides further detail on some of these relations.

### B.1 Derivation of Dual Input Interferogram Outputs, Eq.

#### 3.1 & 3.2

For the following derivations, let  $z_1$  represent one optical path through the spectrometer,  $z_2$  represent the other optical path, and  $z_1 - z_2 = z$  represent the OPD. As time variations cancel out when the intensity is calculated they are omitted. The beamsplitter reflection is given by  $re^{i\rho}$ , with reflectance  $R = r^2$ . The beamsplitter transmission is given by  $te^{i\tau}$ , with transmittance  $T = t^2$ . Recall that  $\Phi = \rho - \tau$ .

Consider a monochromatic source of frequency  $\sigma_o$  incident on an MZ-FTS. For an electric field intensity  $E_A$  in input A and  $E_B$  in input B of a MZ-FTS, there are four electric field components per output to consider. For output 1, let  $E_{1i}$ ,  $E_{1ii}$ ,  $E_{1iii}$ , and  $E_{1iv}$

represent each component as follows

$$E_{1i} = E_A r^2 e^{i2\rho} e^{i2\pi\sigma_o z_1} ,$$

$$E_{1ii} = E_A t^2 e^{i2\tau} e^{i2\pi\sigma_o z_2} ,$$

$$E_{1iii} = E_B r t e^{i(\rho+\tau)} e^{i2\pi\sigma_o z_1} , \text{ and}$$

$$E_{1iv} = E_B r t e^{i(\rho+\tau)} e^{i2\pi\sigma_o z_2} .$$

The total electric field at output 1 is given by the sum of all components

$$E_1 = E_{1i} + E_{1ii} + E_{1iii} + E_{1iv} .$$

The irradiance at output 1 is given by the total field multiplied by its complex conjugate.

$$I_1 = (E_{1i} + E_{1ii} + E_{1iii} + E_{1iv})^* (E_{1i} + E_{1ii} + E_{1iii} + E_{1iv})$$

As  $E_A$  and  $E_B$  are incoherent with respect to each other, only the terms above involving

$E_A^* E_A$  and  $E_B^* E_B$  are included resulting in

$$I_1 = (E_{1i} + E_{1ii})^* (E_{1i} + E_{1ii}) + (E_{1iii} + E_{1iv})^* (E_{1iii} + E_{1iv}) ,$$

where

$$\begin{aligned} (E_{1i} + E_{1ii})^* (E_{1i} + E_{1ii}) &= E_A^2 [R^2 + T^2 + RT e^{-i2(\rho-\tau)} e^{-i2\pi\sigma_o(z_1-z_2)} \\ &\quad + RT e^{i2(\rho-\tau)} e^{i2\pi\sigma_o(z_1-z_2)}] , \\ &= E_A^2 [R^2 + T^2 + 2RT \cos(2\pi\sigma_o z + 2\Phi)] \end{aligned}$$

and

$$\begin{aligned} (E_{1iii} + E_{1iv})^* (E_{1iii} + E_{1iv}) &= E_B^2 [2RT + RT e^{-i2\pi\sigma_o(z_1-z_2)} + RT e^{i2\pi\sigma_o(z_1-z_2)}] \\ &= 2E_B^2 RT [1 + \cos(2\pi\sigma_o z)] \end{aligned}$$

Therefore,

$$I_1(z, \sigma_o) = I_A[R^2 + T^2 + 2RT \cos(2\pi\sigma_o z + 2\Phi)] + 2I_B RT[1 + \cos(2\pi\sigma_o z)] \quad . \quad (\text{B.1})$$

Similarly, for output 2,

$$E_{2i} = E_B r^2 e^{i2\rho} e^{i2\pi\sigma_o z_2} \quad ,$$

$$E_{2ii} = E_B t^2 e^{i2\tau} e^{i2\pi\sigma_o z_1} \quad ,$$

$$E_{2iii} = E_A r t e^{i(\rho+\tau)} e^{i2\pi\sigma_o z_2} \quad , \text{ and}$$

$$E_{2iv} = E_A r t e^{i(\rho+\tau)} e^{i2\pi\sigma_o z_1} \quad .$$

$$I_2 = (E_{2i} + E_{2ii})^*(E_{2i} + E_{2ii}) + (E_{2iii} + E_{2iv})^*(E_{2iii} + E_{2iv}) \quad ,$$

where

$$\begin{aligned} (E_{2i} + E_{2ii})^*(E_{2i} + E_{2ii}) &= E_B^2 [R^2 + T^2 + RT e^{-i2(\rho-\tau)} e^{i2\pi\sigma_o(z_1-z_2)} \\ &\quad + RT e^{i2(\rho-\tau)} e^{-i2\pi\sigma_o(z_1-z_2)}] \quad , \\ &= E_B^2 [R^2 + T^2 + 2RT \cos(2\pi\sigma_o z - 2\Phi)] \end{aligned}$$

and

$$\begin{aligned} (E_{2iii} + E_{2iv})^*(E_{2iii} + E_{2iv}) &= E_A^2 [2RT + RT e^{i2\pi\sigma_o(z_1-z_2)} + RT e^{-i2\pi\sigma_o(z_1-z_2)}] \\ &= 2E_A^2 RT [1 + \cos(2\pi\sigma_o z)] \end{aligned} \quad .$$

Therefore,

$$I_2(z, \sigma_o) = I_B [R^2 + T^2 + 2RT \cos(2\pi\sigma_o z - 2\Phi)] + 2I_A RT [1 + \cos(2\pi\sigma_o z)] \quad . \quad (\text{B.2})$$

## B.2 Derivation of Ideal Beamsplitter Phase Difference $\Phi$ , Eq.

### 3.6

Start by evaluating Equation 3.5 for  $E_B = 0$ .

$$I_1(z)|_{E_B=0} = I_A[R^2 + T^2 + 2RT \cos(2\pi\sigma_o z + 2\Phi)] ,$$

and

$$I_2(z)|_{E_B=0} = 2I_A RT[1 + \cos(2\pi\sigma_o z)] .$$

$$I_A = I_A[R^2 + T^2 + 2RT \cos(2\pi\sigma_o z + 2\Phi)] + 2I_A RT[1 + \cos(2\pi\sigma_o z)]$$

Divide by  $I_A$  as follows

$$1 = R^2 + T^2 + 2RT \cos(2\pi\sigma_o z + 2\Phi) + 2RT + 2RT \cos(2\pi\sigma_o z)$$

$$1 = R^2 + 2RT + T^2 + 2RT \cos(2\pi\sigma_o z + 2\Phi) + 2RT \cos(2\pi\sigma_o z) .$$

$$1 = (R + T)^2 + 2RT \cos(2\pi\sigma_o z + 2\Phi) + 2RT \cos(2\pi\sigma_o z)$$

For zero absorption,  $R + T = 1$ . Subtract 1 from both sides and divide by  $2RT$ .

$$\cos(2\pi\sigma_o z) = -\cos(2\pi\sigma_o z + 2\Phi)$$

$$2\pi\sigma_o z = 2\pi\sigma_o z + 2\Phi - (2n + 1)\pi , \quad \text{where } n \text{ is any integer} \quad (\text{B.3})$$

$$\Phi = n\pi + \pi/2 .$$

## Appendix C

# Off-Axis Natural Apodization

## Integral

§4.3.3 discusses the effect of natural apodization for detectors of a finite FOV which are centred off-axis. The following is the derivation for Equation 4.5.

Assume that a detector has a field-of-view of half angle  $\alpha$  centred off of an optical axis by angle  $\beta$  as is shown in Figure C.1. For convenience the angle  $\beta$  is selected to be in the  $y - z$  plane, i.e. a counter clockwise rotation about the x axis. The generic integral for ILS given in Equation 2.30 is valid for both on axis, and off axis cases provided the integration with respect to  $\Omega_M$  is determined correctly. Recall

$$I(z) = \int_{\Omega_M} \cos(2\pi\sigma z \cos \gamma) d\Omega ,$$

where  $\gamma$  is the off-axis angle of the finite element  $d\Omega$ .

If the integration across  $\Omega_M$  were performed with respect to  $\theta$  and  $\phi$  the following

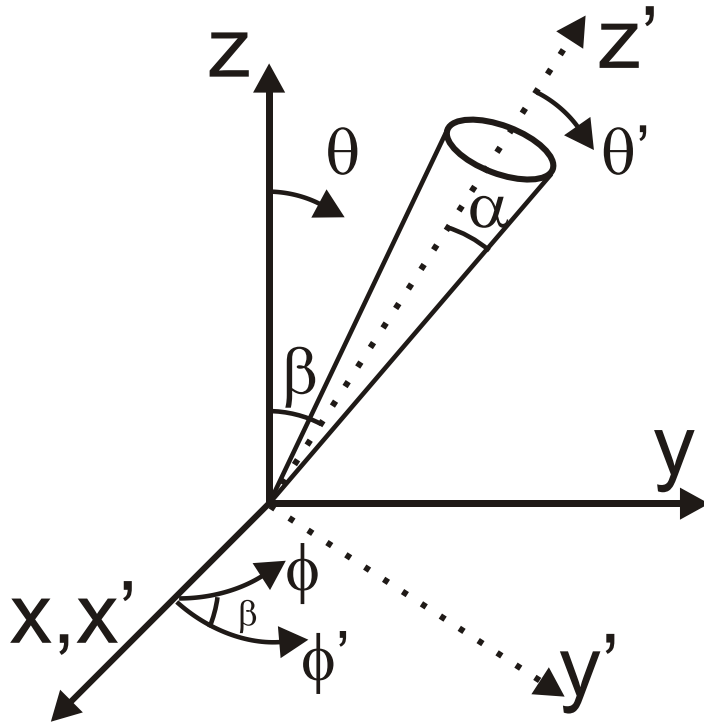


Figure C.1: Diagram of off-axis coordinate system used to derive the IFTS ILS.

is true

$$d\Omega = \sin \theta d\theta d\phi .$$

It is evident from Figure C.2 that for each incremental step  $d\theta$ ,  $\gamma$  is equivalent to  $\theta$  and  $\cos(2\pi\sigma z \cos \gamma) = \cos(2\pi\sigma z \cos \theta)$ . There is no  $\phi$  dependence on  $\gamma$  and the integration limits for  $\phi$  change with  $\theta$  as is demonstrated by the constant  $\theta$ /rotating  $\phi$  slices shown in the figure.

In the  $\theta, \phi$  coordinate system of Figures C.1 & C.2, the  $\theta$  integration limits are  $\theta \in [\beta - \alpha, \beta + \alpha]$  and the  $\phi$  integration limits are determined by some function  $f(\theta, \alpha, \beta)$ .

It is the goal of this section to explore this function and identify integrable solutions.

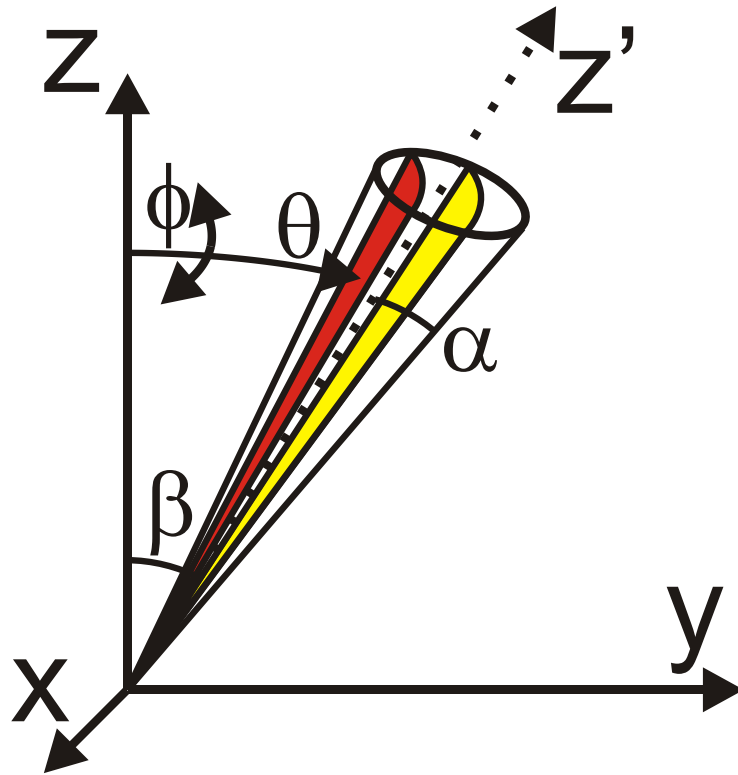


Figure C.2: Diagram of constant  $\theta$  slices through the solid angle integral.

In terms of the  $x', y', z'$  coordinate system also shown in Figure C.1, the detector FOV boundary is given by the equation

$$r^2 = x'^2 + y'^2 + r^2 \cos^2(\alpha) ,$$

where  $r$  is the distance from the origin to the surface of interest. A rotation matrix is defined to translate from  $x, y, z$  to  $x', y', z'$  as follows

$$R_\beta = \begin{bmatrix} 1 & 0 & 0 \\ 0 & \cos \beta & -\sin \beta \\ 0 & \sin \beta & \cos \beta \end{bmatrix} ,$$



where

$$(x', y', z') = [R_\beta] \begin{pmatrix} x \\ y \\ z \end{pmatrix} .$$

This results in the following relations

$$x' = x = r(\sin \theta)(\cos \phi)$$

$$y' = (\cos \beta)y - (\sin \beta)z = (\cos \beta)r(\sin \theta)(\sin \phi) - (\sin \beta)r(\cos \theta)$$

$$z' = (\sin \beta)y + (\cos \beta)z = (\sin \beta)r(\sin \theta)(\sin \phi) + (\cos \beta)r(\cos \theta)$$

With the above relations, the detector FOV boundary can be described in terms of  $\theta, \beta$ , and  $\alpha$  rather than  $x', y', z'$ . The overall expression to be simplified and solved for  $\phi$  is as follows

$$\begin{aligned} r^2 &= x'^2 + y'^2 + z'^2 \cos^2 \alpha \\ 1 &= \left(\frac{x'}{r}\right)^2 + \left(\frac{y'}{r}\right)^2 + \left(\frac{z'}{r}\right)^2 \cos^2 \alpha \\ 1 &= (\sin^2 \theta \cos^2 \phi) \\ &\quad + (\cos^2 \beta \sin^2 \theta \sin^2 \phi + \sin^2 \beta \cos^2 \theta \\ &\quad - 2 \sin \beta \cos \beta \sin \theta \cos \theta \sin \phi) \\ &\quad + \cos^2 \alpha \end{aligned}$$

The above relation may be reduced to a quadratic equation in  $\sin \phi$  of the form

$$a \sin^2 \phi + b \sin \phi + c = 0$$

where

$$a = \sin^2 \beta \sin^2 \theta ,$$

$$b = 2 \sin \beta \cos \beta \sin \theta \cos \theta ,$$

and

$$c = \cos^2 \beta \cos^2 \theta - \cos^2 \alpha .$$

The solution to the above quadratic equation is

$$\sin \phi = \frac{-\cos \beta \cos \theta \pm \cos \alpha}{\sin \beta \sin \theta} .$$

Given that practical values of the angles  $\alpha, \beta,$  and  $\theta$  all are within 0 and  $\pi/2$ , it is expected that  $\sin \phi > 0$  for at least a portion of the integration of Equation 2.30. This means that only the  $+\cos \alpha$  case is a valid solution

$$\sin \phi = \frac{\cos \alpha - \cos \beta \cos \theta}{\sin \beta \sin \theta} . \tag{C.1}$$

The range of  $\phi$  in Equation 4.4 is symmetric about  $\pi/2$ . Therefore,  $\phi' = \phi - \pi/2$  is defined such that its origin is about the y-axis and

$$\cos \phi' = \frac{\cos \alpha - \cos \beta \cos \theta}{\sin \beta \sin \theta} . \tag{C.2}$$

## Appendix D

# Bolometer Theory Derivations

There are several equations used in Chapter 5 in which the equations presented do not necessarily follow intuitively from the previous step or explanation offered in the text. This chapter is intended to provide further details to the derivation of some of the less obvious equations. Further details are available in Jones [171], Low [172], Mather [173,174], Griffin and Holland [175], and Sudiwala et al. [176].

### D.1 Bolometer Static Conductance $G_S(T, T_o)$ , Equation 5.7

The thermal conductance of a bolometer is determined by the thermal link that it has to the heat sink. The thermal link is, in turn, determined not only through the geometry, i.e. length  $L$  and cross sectional area  $A$ , of the link, but also by the thermal conductivity of the link material. The thermal conductivity of the thermal link, can be expressed by a power law as follows [174,176]

$$k(T) = k_o \left( \frac{T}{T_o} \right)^\beta \quad \left[ \frac{\text{W}}{\text{m K}} \right], \quad (\text{D.1})$$

where  $k_o = k(T_o)$ . For a cross sectional area  $A(x)$  along the length of the thermal link  $x$ , the power dissipation,  $W$  is given by

$$W = \frac{\int_{T_o}^T k(T') dT'}{\int_0^L \frac{1}{A(x)} dx} \quad [\text{W}] .$$

Evaluation of the above expression, assuming a constant cross sectional area on the thermal link, results in the following

$$W = \frac{A k_o T_o}{L \beta + 1} \left( \frac{T^{\beta+1}}{T_o^{\beta+1}} - 1 \right) \quad [\text{W}] .$$

The above expression is combined with the steady state power dissipation (Equation 5.6) and results in Equation 5.7 as follows

$$\begin{aligned} G_S(T, T_o) &= \frac{A k_o}{L (\beta + 1)} \left( \frac{\frac{T^{\beta+1}}{T_o^{\beta+1}} - 1}{\frac{T}{T_o} - 1} \right) \quad [\text{W/K}] , \quad (\text{D.2}) \\ &= \frac{G_{S_o}}{(\beta + 1) T_o^\beta} \frac{(T^{\beta+1} - T_o^{\beta+1})}{(T - T_o)} \end{aligned}$$

where  $G_{S_o}(T, T_o) = k_o(A/L)$ .

## D.2 Bolometer Dynamic Conductance with Electrothermal Feedback $G_E(T, T_o)$ , Equation 5.9

$G_E(T, T_o)$  is determined by the evaluation of  $dW/dT - dP/dT$ . The result of  $dW/dT = G_D(T, T_o)$  is straightforward and provided in Equation 5.8, and will not be detailed here. The format of  $dP/dT$  as presented in Equation 5.9 is shown below. The

electrical power input to the bolometer is given by

$$P(T) = \frac{V(T)^2}{R(T)} \quad [\text{W}] ,$$

and the voltage divider across the bolometer and load resistor is used to relate the power to the bias voltage  $V_b$ , which does not vary with  $T$ .

$$P(T) = \frac{\left( V_b \left( \frac{R(T)}{R_L + R(T)} \right) \right)^2}{R(T)} = \frac{V_b^2 R(T)}{(R_L + R(T))^2} \quad [\text{W}] .$$

The only temperature dependent function in the above expression is now  $R(T)$  and the derivative with respect to temperature is as follows

$$\begin{aligned} \frac{dP(T)}{dT} &= V_b^2 \frac{d}{dT} \left( \frac{R(T)}{(R_L + R(T))^2} \right) \\ &= V_b^2 \left[ \frac{dR(T)}{dT} \left( \frac{1}{(R_L + R(T))^2} \right) - \left( \frac{2R(T)}{(R_L + R(T))^3} \frac{dR(T)}{dT} \right) \right] \\ &= V_b^2 \frac{1}{(R_L + R(T))^3} \frac{dR(T)}{dT} (R_L + R(T) - 2R(T)) \\ &= V_b^2 \frac{1}{(R_L + R(T))^3} \frac{dR(T)}{dT} (R_L - R(T)) \end{aligned} \quad [\text{W/K}] .$$

The bias current  $I$  is given by  $\frac{V_b}{R_L + R(T)}$  and Equation 5.3 allows  $dR/dT$  to be substituted with  $\alpha R(T)$ , yielding

$$\begin{aligned} \frac{dP(T)}{dT} &= I^2 \alpha R(T) \left( \frac{R_L - R(T)}{R_L + R(T)} \right) \\ &= \alpha P(T) \left( \frac{R_L - R(T)}{R_L + R(T)} \right) \end{aligned} \quad [\text{W/K}] .$$

This result can now be used to determine the electrothermal feedback dynamic conductance as follows

$$G_E(T, T_o) = \frac{dW}{dT} - \frac{dP}{dT} = G_D(T, T_o) - \alpha P(T, T_o) \left[ \frac{R_L - R(T)}{R_L + R(T)} \right] \quad [\text{W/K}] . \quad (\text{D.3})$$

### D.3 Bolometer Dynamic Impedance $Z_D$ , Equation 5.16

The dynamic impedance of the bolometer is given by

$$Z_D = \frac{dV}{dI} \quad [\Omega] .$$

Since all changes are to be traced to changes in temperature, the above differential will be related to changes in temperature as follows

$$Z_D = \frac{dV/dT}{dI/dT} \quad [\Omega] .$$

Recall that since  $P = W - Q$ , for constant  $Q$

$$\frac{dP}{dT} = \frac{dW}{dT} = G_D(T, T_o) \quad [\text{W/K}] ,$$

and

$$\frac{dR}{dT} = \alpha R(T) \quad [\Omega/\text{K}] .$$

Since  $V = \sqrt{P(T)R(T)}$ , it is true that

$$\begin{aligned} \frac{dV}{dT} &= \frac{1}{2} \frac{1}{\sqrt{P(T)R(T)}} \left( \frac{dP}{dT} R(T) + P(T) \frac{dR}{dT} \right) \\ &= \frac{1}{2} \sqrt{\frac{R(T)}{P(T)}} (G_D(T, T_o) + \alpha P(T)) \end{aligned} \quad [\text{V/K}] .$$

Similarly for  $I = \sqrt{P(T)/R(T)}$ ,

$$\begin{aligned} \frac{dI}{dT} &= \frac{1}{2} \sqrt{\frac{R(T)}{P(T)}} \left( \frac{dP}{dT} \frac{1}{R(T)} - \frac{P(T)}{R^2(T)} \frac{dR}{dT} \right) \\ & \quad \text{[I/K]} . \\ &= \frac{1}{2} \frac{1}{\sqrt{P(T)R(T)}} (G_D(T, T_o) - \alpha P(T)) \end{aligned}$$

Therefore,

$$\begin{aligned} Z_D &= \frac{dV/dT}{dI/dT} \\ &= \frac{\frac{1}{2} \sqrt{\frac{R(T)}{P(T)}} (G_D(T, T_o) + \alpha P(T))}{\frac{1}{2} \frac{1}{\sqrt{P(T)R(T)}} (G_D(T, T_o) - \alpha P(T))} \quad \text{[\Omega]} . \quad \text{(D.4)} \\ &= R(T) \left( \frac{G_D(T, T_o) + \alpha P(T)}{G_D(T, T_o) - \alpha P(T)} \right) \end{aligned}$$

## D.4 Bolometer Responsivity $S$ , Equation 5.17

Recall, as derived in §D.3, that

$$Z_D = R(T) \left( \frac{G_D(T, T_o) + \alpha P(T)}{G_D(T, T_o) - \alpha P(T)} \right) \quad \text{[\Omega]} .$$

A dimensionless parameter  $H(T)$ , called the slope parameter by Jones [171], may be defined

$$H(T) = \frac{G_D(T, T_o)}{\alpha P(T)} \quad \text{(D.5)}$$

such that

$$Z_D = R(T) \left( \frac{H(T) + 1}{H(T) - 1} \right) \quad \text{[\Omega]} .$$

It can also be shown [171] that

$$H(T) = \frac{1}{I^2(T)} \frac{dW}{dR} .$$

With an equivalent method to the derivation of the dynamic impedance above, using

$$\frac{dP}{dT} = \alpha P(T) \left( \frac{R_L - R(T)}{R_L + R(T)} \right) \quad [\text{W/K}] ,$$

and

$$\frac{dR}{dT} = \alpha R(T) \quad [\Omega/\text{K}] ,$$

it can be shown that

$$\frac{dV}{dT} = \alpha \sqrt{P(T)R(T)} \left( \frac{R_L}{R_L + R(T)} \right) \quad [\text{V/K}] ,$$

and

$$\frac{dI}{dT} = -\alpha \sqrt{P(T)R(T)} \left( \frac{1}{R_L + R(T)} \right) \quad [\text{A/K}] .$$

This produces the following result for  $dV/dI$

$$\frac{dV}{dI} = \frac{dV/dT}{dI/dT} = -R_L \quad [\Omega] . \quad (\text{D.6})$$

For a varying optical load, the slope parameter may be rearranged to give the bolometer responsivity.

$$\begin{aligned} H &= \frac{1}{I^2} \frac{dW}{dR} \\ &= \frac{1}{I^2} \frac{d(IV + Q)}{dR} \\ &= \frac{1}{I^2} \frac{d(IV + Q)}{d\left(\frac{V}{I}\right)} \end{aligned}$$



$$\begin{aligned}
H &= \frac{1}{I^2} \left( \frac{IdV + VdI + dQ}{\frac{dV}{I} - \frac{VdI}{I^2}} \right) \\
&= \frac{1}{I^2} \left( \frac{1}{1/I^2} \right) \left( \frac{(IdV)(1 + \frac{V}{I} \frac{dI}{dV} + \frac{dQ}{IdV})}{IdV - VdI} \right) \\
&= \frac{IdV}{IdV} \left( \frac{1 + \frac{V}{I} \frac{dI}{dV} + \frac{dQ}{IdV}}{1 - \frac{V}{I} \frac{dI}{dV}} \right) \\
&= \left( \frac{1 + R \frac{1}{dV/dI} + \frac{1}{IdV/dQ}}{1 - R \frac{1}{dV/dI}} \right)
\end{aligned}$$

The relation shown in Equation D.6 above, i.e.  $dV/dI = -R_L$ , is incorporated into the algebra involving  $H$  above, and the expression is rearranged to solve for  $S = dV/dQ$  as follows

$$H = \left( \frac{1 - \frac{R}{R_L} + \frac{1}{IS}}{1 + \frac{R}{R_L}} \right)$$

$$H + H \frac{R}{R_L} = 1 - \frac{R}{R_L} + \frac{1}{IS}$$

$$\frac{1}{IS} = H - 1 + \frac{R}{R_L}(H + 1)$$

$$IS = \frac{1}{H - 1 + \frac{R}{R_L}(H + 1)}$$

$$S = \frac{1}{I} \left( \frac{1}{H - 1 + \frac{R}{R_L}(H + 1)} \right) \quad [V/W].$$

Another equivalent expression for  $H$  given by Jones [171] is

$$H = \left( \frac{Z_D + R}{Z_D - R} \right),$$

which can be used to further simplify the expression for the detector responsivity above as follows

$$\begin{aligned} S &= \frac{1}{I} \left( \frac{1}{\frac{Z_D + R}{Z_D - R} - 1 + \frac{R}{R_L} \left( \frac{Z_D + R}{Z_D - R} + 1 \right)} \right) \\ &= \frac{1}{I} (Z_D - R) \frac{1}{(Z_D + R) - (Z_D - R) + \frac{R}{R_L} [(Z_D + R) + (Z_D - R)]} \\ &= \frac{1}{I} (Z_D - R) \frac{1}{2R + \frac{2RZ_D}{R_L}} \quad [V/W] . \\ &= \frac{(Z_D - R)}{2IR} \frac{1}{1 + Z_D/R_L} \\ &= \frac{(Z_D - R)}{2V} (R_L) \frac{1}{R_L + Z_D} \end{aligned}$$

This results in the following

$$S = \left( \frac{Z_D - R}{2V} \right) \left( \frac{R_L}{R_L + Z_D} \right) \quad [V/W] . \quad (D.7)$$

Equation D.7 can in turn be further reduced using the relation for the dynamic impedance,

namely  $Z_D = R \left( \frac{G_D + \alpha P}{G_D - \alpha P} \right)$ ,

$$\begin{aligned}
S &= \left( \frac{1}{2V} \right) \left( R \left[ \frac{G_D + \alpha P}{G_D - \alpha P} \right] - R \right) \left( \frac{R_L}{R_L + R \left[ \frac{G_D + \alpha P}{G_D - \alpha P} \right]} \right) \\
&= \left( \frac{1}{2V} \right) \left( \frac{1}{G_D - \alpha P} \right) (R(G_D + \alpha P) - R(G_D - \alpha P)) \\
&\quad \times (G_D - \alpha P) \left( \frac{R_L}{R_L(G_D - \alpha P) + R(G_D + \alpha P)} \right) \\
&= \left( \frac{1}{2V} \right) (2\alpha R P) \left( \frac{R_L}{G_D(R_L + R) - \alpha P(R_L - R)} \right) \quad [V/W] . \\
&= (\alpha V) \left( \frac{1}{R_L + R} \right) \left( \frac{R_L}{G_D - \alpha P \left( \frac{R_L - R}{R_L + R} \right)} \right) \\
&= (\alpha V) \left( \frac{R_L}{R_L + R} \right) \left( \frac{1}{G_E} \right) \\
&= \frac{\alpha V}{G_E} \left( \frac{R_L}{R_L + R} \right)
\end{aligned}$$

## D.5 Phonon NEP, Eq. 5.21

The nonequilibrium noise analysis of Mather [173] expresses the phonon NEP as

$$\text{NEP}_{\text{phonon}} = \sqrt{4k_b(\theta T)^2 G_D(T, T_o)} \quad [W/\sqrt{\text{Hz}}] ,$$

where  $\theta$  accounts for the temperature gradient between the heat sink and the bolometer element and is determined as follows

$$(\theta T)^2 = \frac{1}{G_D(T)} \frac{\int_{T_o}^T [TG_D(T)]^2 dT}{\int_{T_o}^T G_D(T) dT} \quad [\text{K}^2].$$

Solving the above relation for  $\theta^2$  results in the following

$$\begin{aligned} (\theta)^2 &= \frac{1}{T^2} \frac{T_o^\beta}{G_{S_o} T^\beta} \frac{\int_{T_o}^T G_{S_o}^2 \left(\frac{T^{2\beta+2}}{T_o^{2\beta}}\right) dT}{\int_{T_o}^T G_{S_o} \left(\frac{T^\beta}{T_o^\beta}\right) dT} \\ &= \frac{T_o^\beta}{G_{S_o} T^{\beta+2}} \frac{G_{S_o}^2 / T_o^{2\beta}}{G_{S_o} / T_o^\beta} \frac{\int_{T_o}^T G_{S_o}^2 (T^{2\beta+2}) dT}{\int_{T_o}^T (T^\beta) dT} \\ &= \frac{1}{T^{\beta+2}} \frac{\beta+1}{2\beta+3} \frac{T^{2\beta+3} - T_o^{2\beta+3}}{T^{\beta+1} - T_o^{\beta+1}} \end{aligned}$$

Substituting this back in the relation for  $\text{NEP}_{\text{phonon}}$  results in the following

$$\text{NEP}_{\text{phonon}} = \sqrt{\frac{4k_b G_{S_o}}{T_o^\beta} \frac{\beta+1}{2\beta+3} \frac{T^{2\beta+3} - T_o^{2\beta+3}}{T^{\beta+1} - T_o^{\beta+1}}} \quad [\text{W}/\sqrt{\text{Hz}}]. \quad (\text{D.8})$$

## D.6 Photon NEP, Eq. 5.27

Random fluctuations in the rate of radiation absorption give rise to photon noise.

The spectral density  $\chi$  of fluctuations in absorbed power is [188]

$$\chi = 2 \int Q_\nu h\nu [1 + \kappa(\nu)] \quad [\text{W}^2/\text{Hz}], \quad (\text{D.9})$$

where  $Q_\nu$  is the radiant power absorbed per unit optical bandwidth, and the effective photon mode occupation number is  $\kappa(\nu)$  [173]. The effective photon mode occupation is given by

$$\kappa(\nu) = \frac{\eta\epsilon t}{\exp\left(\frac{h\nu}{k_b T_S}\right) - 1}, \quad (\text{D.10})$$

where  $\epsilon$  is the source emissivity,  $t$  is the transmissivity of the optical system,  $\eta$  is the detector absorptivity, and  $T_S$  is the source temperature. The absorbed radiant power per unit bandwidth,  $Q_\nu$ , is given by

$$Q_\nu = 2(\eta\epsilon t)A\Omega(\nu)\frac{h\nu^3}{c^2} \frac{1}{\exp\left(\frac{h\nu}{k_b T_S}\right) - 1} \quad [\text{W/Hz}]. \quad (\text{D.11})$$

The photon NEP is related to  $\chi$  as follows

$$\begin{aligned} \text{NEP}_{\nu-i} &= \sqrt{\chi} \\ &= \sqrt{2 \int Q_\nu h\nu [1 + \kappa(\nu)] d\nu} \\ &= \sqrt{2 \int 2(\eta\epsilon t)A\Omega(\nu)\frac{h\nu^3}{c^2} \frac{1}{\exp\left(\frac{h\nu}{k_b T_S}\right) - 1} h\nu [1 + \kappa(\nu)] d\nu} \\ &= \sqrt{4 \int \frac{h^2 \nu^4}{c^2} \frac{(\eta\epsilon t)A\Omega(\nu)}{\exp\left(\frac{h\nu}{k_b T_S}\right) - 1} \left[1 + \frac{\eta\epsilon t}{\exp\left(\frac{h\nu}{k_b T_S}\right) - 1}\right] d\nu} \\ &= \sqrt{\frac{4h^2}{c^2} \int \frac{(\eta\epsilon t)A\Omega(\nu)\nu^4}{\exp\left(\frac{h\nu}{k_b T_S}\right) - 1} \left[1 + \frac{\eta\epsilon t}{\exp\left(\frac{h\nu}{k_b T_S}\right) - 1}\right] d\nu} \\ &\quad [\text{W}/\sqrt{\text{Hz}}], \end{aligned}$$

and substituting  $\nu = c\sigma$  and  $d\nu = c d\sigma$  results in the following

$$\text{NEP}_{\nu-i} = \sqrt{4h^2c^3 \int \frac{(\eta\epsilon t)A\Omega(\sigma)\sigma^4}{\exp(\frac{hc\sigma}{k_bT_S}) - 1} \left[ 1 + \frac{\eta\epsilon t}{\exp(\frac{hc\sigma}{k_bT_S}) - 1} \right] d\sigma} \quad [\text{W}/\sqrt{\text{Hz}}], \quad (\text{D.12})$$

where this relationship is equivalent to Equation 5.27 provided that  $\eta(\sigma)$  as used in §5.1.3 is equivalent to  $\eta(\sigma)$  as used in this section.

## D.7 Determination of NEP from FTS Observations, Equation 5.31

This section reviews the derivation of Equation 5.31. The noise present in an FTS spectrum is given by  $\varsigma$  [W/cm<sup>-1</sup>]. The noise power is determined by multiplying the spectral noise density by the spectral resolution as follows

$$\varsigma_{power} = \varsigma \Delta\sigma \quad [\text{W}].$$

NEP is determined by multiplying the signal noise (W) by the square root of the observation time required to obtain the measurement ( $\sqrt{s} = 1/\sqrt{\text{Hz}}$ ). The scanned OPD is related to the spectral resolution (Equation 2.25) via

$$L = \frac{1}{2\Delta\sigma} \quad [\text{cm OPD}],$$

and the time to record the scan is simply the OPD divided by the stage speed

$$t_{scan} = \left( \frac{1}{2\Delta\sigma} \right) / v_{stage} \quad [\text{s}].$$

Therefore, the measured NEP in an FTS spectrum is given as follows

$$\begin{aligned}
 \text{NEP}_{\text{measured}} &= (\varsigma \Delta \sigma) \sqrt{\frac{1}{\frac{2\Delta\sigma}{v_{\text{stage}}}}} \\
 &= (\varsigma \Delta \sigma) \sqrt{\frac{1}{2\Delta\sigma v_{\text{stage}}}} \quad [\text{W}/\sqrt{\text{Hz}}] . \quad (\text{D.13}) \\
 &= \varsigma \sqrt{\frac{\Delta\sigma^2}{2\Delta\sigma v_{\text{stage}}}} \\
 &= \varsigma \sqrt{\frac{\Delta\sigma}{2v_{\text{stage}}}}
 \end{aligned}$$